

Ulrich Weinbach

**Feasibility and impact of receiver clock modeling
in precise GPS data analysis**

München 2013

**Verlag der Bayerischen Akademie der Wissenschaften
in Kommission beim Verlag C. H. Beck**

ISSN 0065-5325

ISBN 978-3-7696-5104-1

**Diese Arbeit ist gleichzeitig veröffentlicht in:
Wissenschaftliche Arbeiten der Fachrichtung Geodäsie und Geoinformatik der Leibniz Universität Hannover
ISSN 0174-1454, Nr. 303, Hannover 2013**



DGK Deutsche Geodätische Kommission
bei der Bayerischen Akademie der Wissenschaften

Reihe C

Dissertationen

Heft Nr. 692

Feasibility and impact of receiver clock modeling in precise GPS data analysis

Von der Fakultät für Bauingenieurwesen und Geodäsie
der Gottfried Wilhelm Leibniz Universität Hannover
zur Erlangung des Grades
Doktor-Ingenieur (Dr.-Ing.)
genehmigte Dissertation

von

Dipl.-Ing. Ulrich Weinbach

München 2013

Verlag der Bayerischen Akademie der Wissenschaften
in Kommission bei der C. H. Beck'schen Verlagsbuchhandlung München

ISSN 0065-5325

ISBN 978-3-7696-5104-1

Diese Arbeit ist gleichzeitig veröffentlicht in:
Wissenschaftliche Arbeiten der Fachrichtung Geodäsie und Geoinformatik der Leibniz Universität Hannover
ISSN 0174-1454, Nr. 303, Hannover 2013

Adresse der Deutschen Geodätischen Kommission:



Deutsche Geodätische Kommission

Alfons-Goppel-Straße 11 • D – 80 539 München

Telefon +49 – 89 – 23 031 1113 • Telefax +49 – 89 – 23 031 -1283 / - 1100

e-mail hornik@dgfi.badw.de • <http://www.dgk.badw.de>

Prüfungskommission

Vorsitzender: Prof. Dr.-Ing. habil. Jürgen Müller

Hauptreferent: Prof. Dr.-Ing. Steffen Schön

Korreferenten: Prof. Dr. phil. nat. habil. Markus Rothacher

Prof. Dr.-Ing. habil. Christian Heipke

Tag der Einreichung der Arbeit: 20.6.2012

Eröffnung des Promotionsverfahrens durch den Fakultätsrat: 27.6.2012

Tag der mündlichen Prüfung: 25.9.2012

© 2013 Deutsche Geodätische Kommission, München

Alle Rechte vorbehalten. Ohne Genehmigung der Herausgeber ist es auch nicht gestattet,
die Veröffentlichung oder Teile daraus auf photomechanischem Wege (Photokopie, Mikrokopie) zu vervielfältigen

ISSN 0065-5325

ISBN 978-3-7696-5104-1

Summary

Today's Global Navigation Satellite Systems (GNSS) allow worldwide positioning with unprecedented precision and accuracy. When using precise carrier phase observations in post processing, a repeatability of daily coordinates below 5 mm in the horizontal position and better than 1 cm in height can be achieved everywhere on the Earth. The accuracy of kinematic, i.e. epoch-wise determined coordinates is generally at the level of 1 cm in the horizontal components and below 3 cm in height. Despite this already high level of accuracy, there is still room for improvement through advanced observation modeling.

All current GNSS are based on one-way ranging with L-band microwave signals. In order to recover the signal travel time, i.e. the distance divided by the speed of light, the transmitter and receiver clocks have to be synchronized. This is usually achieved by estimating epoch-wise independent clock offsets with respect to a common system time scale. Compared to other parameters of the GPS solution, modeling of the satellite and receiver clock corrections has not found much attention, although it is well known, that the receiver clock estimates exhibit pronounced mathematical correlations with the troposphere parameters and height coordinates. This correlation is one of the main reasons for the degraded height precision of GPS-based positioning. In addition, recent technological progress in the field of atomic frequency standards has led to the development of compact chip-scale atomic clocks and highly precise optical frequency standards. Such optical clocks are up to two orders of magnitude more stable than the best microwave clocks in use today.

In this work, the feasibility and the impact of advanced receiver clock modeling in precise GPS data analysis based on carrier phase observations is investigated. In particular, the requirements concerning oscillator frequency stability and electric hardware delay stability are addressed. Furthermore, functional and stochastic models for the estimation of the receiver clock in classical batch least-squares adjustment and Kalman filter are proposed and validated using simulated and real data. Based on simulated data it is shown that receiver clock modeling can improve the repeatability of kinematic height estimates in Precise Point Positioning by up to 75%, while the impact on static coordinate estimation is negligible. For real data, the improvement of the kinematic height estimates is typically around 50%. In analogy to the terrestrial case, the proposed clock modeling can also be applied to GPS-based kinematic orbit determination of Low Earth Orbiters. It is shown that the ultra-stable oscillators (USO) on board of the two GRACE satellites can be modeled by piece-wise linear functions with a parameter spacing of several tens of seconds. This allows position estimation even if only 3 GNSS satellites are observed and reduces the high-frequency noise in the radial component of the kinematic orbit.

keywords: *GPS, Precise Point Positioning, Clock Modeling, Frequency Transfer, GRACE*

Zusammenfassung

Globale Satellitennavigationssysteme (GNSS) erlauben heute die Positionsbestimmung in einem globalen Referenzrahmen mit noch nie da gewesener Genauigkeit. Die Wiederholbarkeiten täglicher Koordinatenlösungen ist im Allgemeinen besser als 5 mm in der Horizontalen und 10 mm in der Höhe. Die Genauigkeit kinematischer Koordinaten liegt typischerweise bei 1 cm in der Horizontalen und 3 cm in der Höhe. Trotz dieses hohen Genauigkeitsniveaus ist eine weitere Steigerung der Genauigkeit durch eine verbesserte Beobachtungsmodellierung zu erwarten.

GNSS basieren auf einem Einweg-Messverfahren, das eine Synchronisierung von Sender und Empfänger erforderlich macht. Diese wird in aller Regel durch die Bestimmung unabhängiger Uhrfehler für jede Beobachtungsepoche erreicht. Im Vergleich zu anderen Parametern der GNSS-Auswertung hat die Modellierung dieser Satelliten- und Empfängeruhrfehler bislang wenig Beachtung gefunden. Das ist in so fern erstaunlich, da beispielsweise der Empfängeruhrfehler bekanntermaßen stark mit den zu schätzenden Troposphärenparametern und der Höhenkoordinate korreliert ist. Diese Korrelation ist einer der Hauptgründe für die schlechtere Bestimmbarkeit der Höhenkomponente durch GNSS. Eine Untersuchung der Uhrmodellierung scheint auch deshalb interessant, da die Fortschritte im Bereich der präzisen Frequenznormale in den letzten Jahren zur Entwicklung stark miniaturisierter (engl.: chip-scale) Atomuhren sowie hochgenauer optischer Uhren geführt hat. Letztere sind bis zu zwei Größenordnungen stabiler als die besten heute verfügbaren Mikrowellen-Atomuhren (Wasserstoff-Maser).

In der vorliegenden Arbeit wurden die technische Realisierbarkeit und der Einfluss einer verbesserten Uhrmodellierung auf die präzise GPS-Datenanalyse untersucht. Im speziellen wurden die erforderlichen Voraussetzungen hinsichtlich der Frequenzstabilität des Oszillators und der Stabilität der Signalverzögerungen in der Elektronik analysiert. Des Weiteren wurden geeignete Parametrisierungen des Empfängeruhrfehlers für die Parameterschätzung im Rahmen einer klassischen Ausgleichung sowie in einem Kalman Filter vorgeschlagen und validiert. Basierend auf simulierten Daten konnte eine Verbesserung der Höhenkomponente für eine präzise kinematische Positionierung mittels Trägerphasen (engl.: Precise Point Positioning - PPP) von mehr als 70% gezeigt werden. Für Realdaten von GPS Stationen, die mit einem stabilen Wasserstoff-Maser als Frequenzquelle ausgerüstet sind, lag die Verbesserung im Allgemeinen bei etwa 50%.

Analog zur kinematischen Positionierung auf der Erde, kann eine Uhrmodellierung auch für die kinematische Bahnbestimmung niedrigfliegender Satelliten (engl.: Low Earth Orbiter - LEO) genutzt werden, falls dessen GPS-Empfänger mit einem hochpräzisen Oszillator ausgerüstet ist. Es wird gezeigt, dass die ultra-stabilen Quarzoszillatoren (engl.: Ultra-Stable Oscillator - USO) an Bord der beiden GRACE-Satelliten gut durch eine stückweise lineare Funktion mit Segmenten bis zu einer Länge von 100 s approximiert werden können. Dies ermöglicht eine Positionsbestimmung auch dann, wenn Beobachtungen von nur drei GPS-Satelliten vorliegen und führt zu einer Reduktion des hochfrequenten Rauschens in der Radialkomponente der kinematischen Satellitenpositionen.

Schlagwörter: *GPS, Precise Point Positioning, Uhrmodellierung, Frequenzübertragung, GRACE*

Contents

1	Introduction	11
2	GPS Data Processing	15
2.1	GPS and other GNSS	15
2.2	Basic principles of GNSS positioning and the role of the receiver clock	16
2.3	GNSS observables	18
2.3.1	Linear combinations of observations	20
2.3.2	Observation differencing	22
2.4	The International GNSS Service (IGS) and its analysis centers	23
2.5	Precise Point Positioning (PPP)	24
2.5.1	Observation modeling	24
2.5.2	Ambiguity fixing in PPP	31
3	Clock Characterization	37
3.1	Oscillator signal description	37
3.2	Measures of frequency stability in the Fourier frequency domain	38
3.3	Measures of frequency stability in the (averaging-) time domain	39
3.4	Relationship between Allan variance and power spectral density	41
3.5	High-precision frequency standards	42
3.5.1	Quartz oscillators	42
3.5.2	Microwave atomic clocks	43
3.5.3	Optical atomic clocks	45
3.5.4	High-precision oscillators for space applications	45
3.5.5	Summary of high-precision frequency standards	46
3.6	The time scales TAI, GPS Time and IGS Time	47
3.7	Clock time prediction and modeling errors	48
3.8	Simulation of power-law noise in precision oscillators	50
4	Parameter Estimation and Clock Modeling	53
4.1	Least-squares adjustment theory	53
4.2	Kalman filtering	58
4.2.1	Kalman filter theory	58
4.2.2	Numerical stability	61
4.2.3	Smoothing of the filter output	61
4.3	Continuous receiver clock modeling versus epoch-wise clock elimination	62
4.4	Functional and stochastic models for clocks in GNSS data analysis	66
4.4.1	A clock model for use in a batch least-squares adjustment	66
4.4.2	A clock model for use in a Kalman filter	68
4.5	Frequency stability requirements for clock modeling	70
4.6	Clock jump detection and modeling	71
5	Stability of Receiver Hardware Delays	75
5.1	Types of hardware delay variations	75
5.2	Antenna effects	76
5.3	Cables and distribution amplifiers	77
5.4	Receiver effects	78
5.5	Summary and recommendations	84

6	PPP-based Clock Comparisons	85
6.1	Fundamentals of GNSS time and frequency transfer	85
6.2	Achievable precision	86
6.3	Remaining error sources	88
6.4	The impact of ambiguity fixing	89
6.5	Summary and alternative time and frequency transfer methods	90
7	Analysis of the Impact of Receiver Clock Modeling	93
7.1	Empirical analysis of the parameter cofactor matrix	93
7.1.1	Static positioning	94
7.1.2	Kinematic positioning	96
7.1.3	Troposphere estimation in static positioning	97
7.1.4	Absolute versus relative positioning	99
7.2	PPP results with simulated data	99
7.2.1	Static PPP results with simulated data	100
7.2.2	Kinematic PPP results with simulated data	101
7.3	PPP results with real data	105
7.3.1	Static PPP results with real data	105
7.3.2	Kinematic PPP results with real data	106
7.4	Receiver clock modeling for a LEO	111
7.4.1	The GRACE mission	111
7.4.2	LEO data processing	113
7.4.3	Application of clock modeling to simulated GRACE GPS data	113
7.4.4	Application of clock modeling to real GRACE GPS data	117
8	Conclusions	127
	Bibliography	129
	Acknowledgments	137

List of abbreviations

AC	(IGS) Analysis Center
ACES	Atomic Clock Ensemble in Space
AIUB	Astronomical Institute, University of Berne
ANTEX	ANTenna EXchange Format
ARP	Antenna Reference Point
CODE	Centre for Orbit Determination in Europe
CSAC	Chip-Scale Atomic Clock
DCB	Differential Code Bias
ICRF	International Celestial Reference Frame
ITRF	International Terrestrial Reference Frame
ECEF	Earth Centered Earth Fixed (reference system)
ECI	Earth Centered Inertial (reference system)
EKF	Extended Kalman Filter
ESA	European Space Agency
FFM	Flicker Frequency Modulation
FPM	Flicker Phase Modulation
GMF	Global Mapping Functions
GLONASS	Globalnaya Navigatsionnaya Sputnikovaya Sistema
GNSS	Global Navigation Satellite System
GPS	Global Positioning System
GPST	GPS time
GPT	Global Pressure and Temperature model
GRACE	Gravity Recovery And Climate Experiment
IERS	International Earth Rotation Service
IGS	International GNSS Service
IGRT	IGS rapid timescale
IGST	IGS final timescale
IFE	Institut für Erdmessung, Hannover
JPL	Jet Propulsion Laboratory, Pasadena
L1B	GRACE Level 1B data
LC	Linear Combination
LEO	Low Earth Orbiter
LNA	Low-Noise Amplifier
LSQ	Least-Squares adjustment
NL	Narrow-Lane
NRL	U.S. Naval Research Laboratory
NWM	Numerical Weather Model
OCXO	Oven-Controlled quartz crystal oscillator
PCO	Phase Center Offset
PCV	Phase Center Variation
PPP	Precise Point Positioning
PPS	Pulse-Per-Second
PSD	Power Spectral Density
PTB	Physikalisch-Technische Bundesanstalt, Braunschweig
RINEX	Receiver INdependent EXchange format
RMS	Root Mean Square error
RWFM	Random-Walk Frequency Modulation

RWPM	Random-Walk Phase Modulation
SD	Single Difference
TIC	Time-Interval Counter
TAI	International Atomic Time
TCXO	Temperature-Compensated quartz crystal oscillator
TDOP	Time Dilution Of Precision
TT	Terrestrial Time
TWSTFT	Two-Way Satellite Time and Frequency Transfer
USO	Ultra-Stable Oscillator
UTC	Universal Time Coordinated
VLBI	Very Long Baseline Interferometry
VMF1	Vienna Mapping Functions 1
WFM	White Frequency Modulation
WL	Wide-Lane
WPM	White Phase Modulation
WVR	Water Vapor Radiometer
ZHD	(Tropospheric) Zenith Hydro-static Delay
ZWD	(Tropospheric) Zenith Wet Delay
XO	quartz crystal oscillator

1 Introduction

Today's Global Navigation Satellite Systems (GNSS) allow worldwide positioning with unprecedented precision and accuracy. When using precise carrier phase observations in post processing, a repeatability of daily coordinates below 5 mm in the horizontal position and better than 1 cm in height can be achieved everywhere on the Earth. The accuracy of kinematic, i.e. epoch-wise coordinates is generally at the level of 1 cm in the horizontal components and below 3 cm in height.

Despite this already high level of accuracy, there is still room for improvement through advanced observation modeling. In recent years the research focused mainly on troposphere modeling and the calibration of site-specific multipath and near-field effects. At the same time the modeling of the satellite and receiver clocks has not found much attention, although it is well known, that for example the receiver clock estimates exhibit pronounced mathematical correlations with the troposphere parameters and height coordinates (e.g. Rothacher and Beutler, 1998). In this work, the impact and the feasibility of advanced receiver clock modeling in precise GPS data analysis is going to be investigated.

All current GNSS are based on one-way ranging with L-band microwave signals. In order to recover the signal travel time, i.e. the distance divided by the speed of light, the transmitter and receiver clocks have to be synchronized. This is usually achieved by estimating clock offsets with respect to a common system time scale. For single-receiver point positioning at the centimeter level based on GNSS carrier phase observations the clock synchronization must be at the level of a few tens of picoseconds. Alternatively, observation double differences between pairs of receivers and satellites can be processed, which avoids the explicit estimation of clock offsets. However, this approach only allows the determination of relative positions with respect to a reference site and implicitly exhibits the same correlation problem.

At least for post processing, GNSS transmitter clock corrections with a precision of a few tens of picoseconds are readily available, thanks to the highly precise orbit products of the International GNSS Service (IGS) and its associated analysis centers. Even for real-time or near real-time applications precise clock corrections are provided in the framework of the IGS real-time pilot project, although not quite at the same level of accuracy yet. In addition, first experiences with the Galileo test satellite GIOVE-B and the GPS Block IIF satellites indicate a considerably increased frequency stability of the next generation of GNSS satellite clocks, that will significantly improve the predictability of the satellite clock synchronization errors.

In contrast to the transmitter clocks, the corrections for the receiver clocks in point positioning have to be determined by the user. Usually, this is done by estimating an additional parameter for every observation epoch that accounts for the synchronization error. In this way even low-quality clocks can be employed at the receiver side. Unfortunately, there are some drawbacks associated with the procedure of epoch-wise clock estimation or elimination. One of the consequences is the need to observe at least four satellites at the same time to compute a position because three coordinates and one clock offset have to be determined. Another effect is the degraded vertical position accuracy due to the fact that only satellites in the hemisphere above the receiver can be observed. This asymmetry of the observation geometry leads to pronounced mathematical correlations between the estimates of the receiver clock corrections, troposphere parameters, and the station height (Rothacher and Beutler, 1998). If we had a receiver clock that would be perfectly synchronized with the system time and ignore atmospheric and multipath errors, i.e. if we would measure true ranges rather than pseudo-ranges, the vertical station positions would be more precise than the horizontal positions (Kuang et al., 1996). In practice, physical synchronization or permanent external calibration of the receiver clock offset with respect to the system timescale would be extremely difficult to achieve, at the required level of accuracy. If, however, the internal oscillator of the receiver is replaced by a stable atomic clock one can attempt to model the receiver clock offset, e.g. by a low-order polynomial, instead of estimating it for every epoch independently. The validity interval

of the clock model then depends on the frequency stability of the oscillator, i.e. for an oscillator with better frequency stability, fewer clock parameters need to be determined. Generally, we expect that a reduction of the number of clock parameters in the estimation will improve the separability of receiver clock, troposphere and height parameters.

Apart from the frequency stability requirements concerning the receiver's oscillator, the stability of the electronic delays in the antenna-receiver chain is a prerequisite for clock modeling. Even the best oscillator would be useless for clock modeling if its frequency signal or the GNSS signals were significantly distorted on their way from the antenna to the GNSS receiver or inside the receiver unit itself. Various studies from the field of GNSS-based time transfer have shown that temperature influences on the antenna, cables and the receiver itself are generally the most important error sources, that limit the stability of the electronic delays in the receiver system. The magnitude of these errors depends on the antennas and cables in use as well as the receiver type and its configuration. Therefore, one of the goals of this work is to assess the hardware-delay stability of the entire receiver equipment.

The motivation for an investigation of advanced receiver clock modeling is twofold. On the one hand, many receivers of the global IGS reference station network are already connected to highly stable hydrogen maser frequency standards, but the additional knowledge about the frequency stability of these oscillators is presently neglected in the data processing by the IGS and its analysis centers. Therefore, an analysis of the impact of clock modeling is thought to provide valuable information for the development of future processing strategies. On the other hand, the current progress in the field of optical atomic clocks is very promising and may form the basis for a new generation of much more precise GNSS clocks on the ground and in space. In contrast to classical atomic clocks, that probe the characteristic transition frequency associated with certain hyperfine levels of the atom using a microwave signal, optical clocks use laser light at wavelengths of visible or ultra-violet light to interrogate the clock transition. Due to the much higher frequencies, oscillators operating in the optical regime can be much more accurate. In recent years, optical clocks have been developed that outperform the best microwave frequency standards by well over one order of magnitude. By means of a femtosecond frequency comb the stable optical frequency generated by these clocks can be conveniently converted to the microwave and radio frequencies that are used in GNSS.

In summary, the main objectives of this work can be expressed by the following key questions:

- What are the technical requirements for clock modeling at the carrier phase precision level in terms of oscillator performance and GNSS equipment?
- What are suitable functional and stochastic clock models in the parameter estimation?
- What is the benefit of clock modeling in different application scenarios?

The Precise Point Positioning (PPP) method has been chosen as the primary processing approach in this work. The PPP method is based on the processing of undifferenced dual frequency code and carrier phase observations in combination with precise satellite orbit and clock data. In contrast to differential processing approaches, the determination of the receiver clock offset is an integral part of the PPP method, making it particularly suitable to study the feasibility and the impact of advanced clock models. Furthermore, PPP has found applications in a multitude of different fields, including geophysics, surveying, navigation, time-keeping and meteorology. The almost complete independence of the inter-station distance makes PPP a very flexible analysis tool, e.g. precise clocks often need to be compared over inter-continental distances, where only few common satellites can be observed. Furthermore, the simple observation geometry facilitates the interpretation of the results and complex concepts of baselines and handling of networks involving 2 or more stations are avoided, at least for the user. Nevertheless, for long sessions (>12 h) the precision of a PPP solution is comparable to a classical network solution. With the latest developments even integer resolution of the carrier phase ambiguity can be applied in PPP. Despite the slightly more complex modeling of the observations, the PPP approach is computationally efficient because the data is processed independently station by station.

All results presented in this work were computed with a MATLAB-based Precise Point Positioning software developed by the author. The software is designed for high-precision, post-facto data analysis.

The parameter estimation can be performed either by classical batch least-squares adjustment (LSQ) or by an extended Kalman filter (EKF) with forward/backward smoothing.

Apart from few studies in the field of aircraft and automotive navigation (Sturza, 1983; Misra, 1996; Ramlall et al., 2011), research contributions in the area of advanced clock modeling are generally scarce. In particular, clock modeling for carrier phase based positioning, where frequency stability requirements are much more challenging, has hardly been investigated before. Lichten and Border (1987) mention improvements of a GPS carrier phase solution under certain conditions when a polynomial clock model is applied for receivers equipped with hydrogen maser frequency standards, but they do not provide any conclusive results. Furthermore, some authors discuss the modeling of receiver and satellite clocks in a Kalman filter in some detail (e.g. Wübbena, 1991). However, no systematic investigations regarding the technical feasibility and the impact of different clock models on the parameter estimates are reported.

The investigations presented in this work aim to close this gap. Based on simulated and real data the impact of clock modeling on the estimated position and troposphere parameters is investigated for both, static and kinematic positioning. The technical requirements for clock modeling are discussed and suitable functional and stochastic clock models for batch least-squares adjustment and Kalman filtering are proposed and validated. Furthermore, in the course of this work, GPS-based kinematic orbits for a Low Earth Orbiter (LEO) using carrier phase observations and receiver clock modeling have been computed for the first time. It could be shown that the ultra-stable oscillators (USO) on board of the two GRACE satellites can be modeled by a piece-wise linear function with a parameter spacing of several tens of seconds. This allows positioning estimation even if only three GNSS satellites are observed and reduces the high-frequency noise in the radial component of the kinematic orbit.

More recently a growing interest in clock modeling can be noted which is, e.g., reflected by an ESA project on GNSS satellite and station clock modeling with preliminary results shown in (Orliac et al., 2011).

A short outline of the structure of the thesis is given in the following:

Chapter 2 is devoted to the fundamentals of GNSS data processing. In particular, the observation types and linear combinations used at various stages in this work are introduced. The observation modeling is described in some detail because of the sensitivity of the PPP receiver clock estimates to any modeling deficiencies. In addition to the description of the standard PPP models, a method for ambiguity fixing is introduced, that was implemented for test purposes in the course of this work.

In Chapter 3 the characterization of the frequency stability of high-precision oscillators is reviewed. The most important state-of-the-art frequency sources applicable to GNSS are described and compared in terms of their frequency stability. In addition, the realization of the GNSS timescales used to align the transmitter and receiver oscillators are described and their importance for clock modeling is discussed.

Chapter 4 starts with a brief mathematical description of the employed parameter estimation approaches. In the sequel, the difference between continuous clock bias modeling and epoch-wise clock estimation is discussed based on an algebraic analysis of the normal equations for a simple static and kinematic point positioning problem with 2 observation epochs. Finally, functional and stochastic models for the receiver clock offset, applicable to Kalman filtering and classical batch least-squares adjustment are introduced.

An analysis of the stability of the hardware delays in the receiver system is presented in Chapter 5. In addition to a literature review with regard to the influences of antennas, cables and receivers, experimental results from common clock tests with a number of recent geodetic receiver models are presented.

In preparation of the practical application of the proposed receiver clock modeling approach, Chapter 6 covers important aspects of clock comparisons based on the PPP method. Several examples provide valuable insights into potential error sources and the variable clock performance at different IGS sites equipped with hydrogen maser frequency standards.

Finally, Chapter 7 contains an empirical analysis of the impact of GPS receiver clock modeling based on simulations and real data. In a first step the cofactor matrix for a simplified case of point positioning is studied. In the sequel static and kinematic PPP solutions with simulated and real observation data

are analyzed. In the last part of this chapter, the impact of receiver clock modeling on kinematic LEO orbit determination is investigated using the GRACE mission as a case study.

The work concludes with a summary of the most important findings and a discussion of the future prospects of clock modeling for GNSS applications.

2 GPS Data Processing

Continuously refined data analysis methods as well as the increase in the number of satellites and ground stations, have led to an ever increasing accuracy and precision of GPS positioning. For post processing applications, using GPS carrier phase observations in combination with the precise satellite clock corrections and orbits provided by the International GNSS Service (IGS), a repeatability of daily coordinates below 5 mm in the horizontal position and around 1 cm in height can be achieved (e.g. Ray and Senior, 2005). The average accuracy of kinematic, i.e. epoch-wise independent, coordinates is generally better than 2 cm in the horizontal components and below 5 cm in the vertical (e.g. Kouba, 2009a; Ray and Senior, 2003). At this level of accuracy, the modeling of the GNSS observations has to be done very carefully. This holds in particular when the observation data are processed in Precise Point Positioning (PPP) mode or when the distances between the observing sites are very large. In these cases the distant-dependent error sources such as satellite clock and orbit errors, atmospheric propagation delays and geophysical station displacements cannot or can only insufficiently be eliminated. The estimated receiver clock offsets are particularly sensitive to these modeling errors, because they are usually estimated with high temporal resolution and are strongly correlated with the station height and troposphere parameters. Therefore, precise modeling of the GPS observations is essential when clocks shall be compared with the highest possible precision or when the clock itself is to be modeled in order to improve other parameters in the GPS solution.

In this chapter, some fundamental aspects of the GPS and other GNSS are going to be discussed in order to provide the reader with the required background information. After a short review of the current status of the different GNSS, the basic principles of GNSS-based positioning are discussed with a focus on the role of satellite and receiver clock corrections. Subsequently, the GPS observation equations are described and various linear combinations of the observations, that are relevant for this work, are introduced. Furthermore, the products of the International GNSS Service and its analysis centers are described, because they are indispensable for the Precise Point Positioning (PPP) analysis strategy applied in this work. The major part of this chapter consists of a detailed description of the PPP approach and the observation models used therein. In addition to the description of the standard models, an approach for ambiguity fixing in PPP is outlined which has been implemented in the context of this work, in order to analyze the impact of float ambiguities in PPP-based time and frequency transfer and kinematic positioning.

2.1 GPS and other GNSS

At the time of writing, there are two fully operational *Global Navigation Satellite Systems* (GNSS), namely the US American *Global Positioning System* (GPS) and the Russian *Globalnaja Nawigazionnaja Sputnikowaja Sistema* (GLONASS). In addition, two other GNSS are currently under development, the European *Galileo* positioning system and the Chinese *Compass* positioning system. Both are scheduled to be fully operational around 2020.

Full operational capability of GPS was declared in July 1995. However, at that time it had already been a reliable service for several years. Today, the GPS space segment comprises around 30 active and several spare satellites. In contrast, GLONASS only briefly reached a full 24 satellite constellation in early 1996, but went through a long phase of limited availability afterwards. Due to funding problems and the short lifetime of the GLONASS satellites, the number of usable satellites dropped to only 6-8 satellites around 2001. Since 2005 the constellation has been steadily replenished with a new generation of satellites and by the end of 2011 a full 24 satellite constellation was in operation again. Nevertheless,

even today the GLONASS satellite orbits are significantly less accurate and the IGS still does not provide precise satellite clock corrections. Therefore, precise positioning with GLONASS is presently mainly done in relative mode. Only the IGS analysis center ESA has started to provide GLONASS satellite clock corrections a few years ago that are sufficiently accurate for precise point positioning. However, with the rebuilt satellite constellation and a greatly increased number of GLONASS receivers in the IGS tracking network, the accuracy of the orbit and clock products for GLONASS is likely to improve in the future. Nevertheless, in this work, however, the focus will be on GPS, but the basic findings will also hold for other GNSS. Technical details on the space and ground segment of the different GNSS can be found in various textbooks on the subject, e.g. Hofmann-Wellenhof et al. (2008) or Seeber (2003). In the following some fundamental aspects of GNSS-based positioning that are related to the role of clocks in the data analysis are going to be briefly discussed.

2.2 Basic principles of GNSS positioning and the role of the receiver clock

All GNSS are based on one-way ranging between the GNSS satellites and receivers. That means, satellites and receivers have their own local oscillator that is used to generate and track the navigation signals. In order to determine the travel time (time of arrival) of the navigation signals and thereby the ranges between a receiver and the satellites, the time of transmission and the time of reception have to be related to a common time scale. Consequently, GNSS data processing always involves time synchronization between satellite and receiver clocks. This synchronization is realized by introducing a system time scale, all satellite and receiver clocks are referenced to.

For autonomous positioning in real-time, predictions of their position and clock offsets are broadcasted by the GNSS satellites. In order to enable a sufficiently precise prediction of the satellite clock offsets with respect to the system time, the satellites use stable atomic frequency standards for the generation of the navigation signals. Nevertheless, the error of the clock prediction increases with the prediction interval, i.e. the further we move into the future. Therefore, regular updates of the clock correction coefficients are necessary. In GPS, the predicted satellite clock offsets contained in the broadcast navigation message are formally provided as a second-order polynomial but the quadratic term is always zero, so that the representation is actually linear. The clock polynomial is updated every 2 hours together with the orbital elements that describe the satellite positions. The average accuracy of these clock corrections when compared to the much more accurate IGS clock estimates is approximately 5 ns or 1.5 m (Senior et al., 2008). Thus, the satellite clock corrections transmitted in the GPS navigation message enable real-time positioning with meter-level accuracy based on pseudorange observations but are not accurate enough to take advantage of the precise carrier phase observations. For processing of the latter, either dedicated (near) real-time clock products which considerably reduce the clock prediction interval or precise post-processed satellite clock correction, e.g. provided by the IGS, have to be used. Alternatively, the data can be processed in differential mode, where satellite clock errors may be conveniently estimated or eliminated.

In contrast to the satellite clocks, the offset of the receiver clock with respect to the GPS system time cannot be obtained from an external source at the required level of accuracy. Therefore, it has to be determined always by the user. Usually, this is done by estimating an additional parameter for every observation epoch that accounts for the receiver synchronization error. In this way even low-quality clocks can be employed at the receiver side. In fact, one of the reasons for the success of today's GNSS architecture is the possibility to use small and inexpensive quartz crystal oscillators in the receivers. There are, however, some drawbacks associated with the epoch-wise clock estimation procedure, the most obvious being the need to observe at least 4 satellites at any time if kinematic, i.e. epoch-wise, positions are to be determined. In addition, the correlation between the receiver clock, the tropospheric delay parameters and the height coordinate causes a significant degradation of the positioning precision in the vertical direction. In combination with multipath effects and troposphere mismodeling, the amplification of systematic errors through the pronounced correlation of vertical position, receiver clock offset and

Equatorial site				
z_{min}	z_{max}	$\rho(h, \delta t_r)$	$\rho(zwd, \delta t)$	$\rho(h, zwd)$
0°	85°	0.949	-0.907	-0.802
0°	80°	0.975	-0.968	-0.907
0°	75°	0.985	-0.983	-0.943
0°	70°	0.990	-0.990	-0.964
Polar site				
z_{min}	z_{max}	$\rho(h, \delta t_r)$	$\rho(zwd, \delta t)$	$\rho(h, zwd)$
45°	85°	0.967	-0.946	-0.868
45°	80°	0.984	-0.980	-0.937
45°	75°	0.992	-0.990	-0.967
45°	70°	0.996	-0.995	-0.983

Table 2.1: Analytically derived correlation coefficients ρ between receiver clock, station height and tropospheric zenith delay for a given minimum and maximum zenith distance z of the observations as given by Dach et al. (2003) based on elevation-dependent observation weighting

troposphere parameters is one of the main limiting factors for accurate GNSS height determination (Rothacher and Beutler, 1998). This is unfortunate, because the height component is often the most important quantity in geophysical studies, e.g. for the determination of sea-level rise or tsunami detection.

The described correlation problem becomes obvious, if we look at the GPS observation equation. According to Rothacher and Beutler (1998), the linearized observation equation with respect to the receiver clock offset δt_r , the station height Δh and the tropospheric zenith delay Δzwd can be expressed as

$$\rho + v = \rho_0 + c \cdot \delta t_r - \cos z \cdot \Delta h + \frac{1}{\cos z} \Delta zwd, \quad (2.1)$$

where

- ρ is the raw observation of the receiver-satellite distance in meters,
- v the residual of the observation,
- ρ_0 the known approximate propagation distance (computed part),
- c the velocity of light, and
- z the zenith distance of the observation.

When inspecting (2.1) it becomes clear, that the separation of the three parameter types would be impossible if all satellites were observed at the same zenith distance. In turn, this means the *separability of the parameters* depends on the geometric diversity of the observations. Due to the fact that the geometric diversity is limited, because only satellites in the hemisphere above the receiver can be observed, the mathematical correlation between receiver clock, station height and troposphere parameters is typically above 90 %. Table 2.1, taken from Dach et al. (2003) lists analytically derived correlation coefficients between receiver clock δt_r , station height h and tropospheric zenith (wet) delay zwd estimates, for an equatorial and a near-polar observing site.

As shown by e.g. Rothacher and Beutler (1998) and Dach et al. (2003), the correlation between the parameters can be reduced when observations at elevation angles below 15° are included in the analysis (cf. Tab. 2.1). Unfortunately, observations at low elevations are less accurate, due to systematic errors caused by troposphere inhomogeneities and signal multipath. In addition, these observations exhibit an increased tracking noise level due to the lower signal-to-noise ratio. Therefore, the effective improvement by lowering the elevation mask is limited.

An alternative approach to improve the separability of the three parameter types is the introduction of external information for the values in (2.1). For example, the wet part of the tropospheric delay can, in

principle, be measured with adequate precision using Water Vapor Radiometers (WVR). However, these devices cannot generally replace zwd estimation, because they do not produce reliable results during rain and are delicate to calibrate (Elgered et al., 1991). On the other hand it is common practice to constrain consecutive troposphere parameters according to the typical temporal variability of the tropospheric zenith delay. Without such a constraint, the parameter estimates obtained with (2.1) would be extremely noisy.

In contrast to the tropospheric signal delays, the receiver clock offset can generally not be observed by alternative methods. However, in case the receiver is driven by a stable oscillator, the epoch-to-epoch change of the receiver clock may be predictable. Consequently, the temporal variation of the receiver clock offset may be constrained in the same - physically meaningful - way as it is done for the tropospheric zenith delay. The main difference is, that the receiver clock is allowed to have a frequency offset, so that a linear drift in time has to be taken into account. The amount by which this drift changes essentially depends on the oscillator in use and may be constrained according to its frequency stability.

The idea of using a stable oscillator and constrain the temporal variations of the GPS receiver clock in the parameter estimation is the topic of this work and we will refer to this approach generally as *clock modeling*. Based on the correlation considerations discussed above, it is expected that clock modeling can improve the separability of clock error, tropospheric zenith delay and station height and therefore improve the precision and accuracy of these parameters.

It is worth noting that a similar correlation problem as for the GNSS receiver clock occurs also at the GNSS satellites during precise orbit determination. Here, a pronounced correlation between radial orbit positions and the satellite clock corrections can be observed. The observation geometry at the satellite is even more unfavorable, because the maximum nadir angle at which the satellite signals are seen by terrestrial tracking stations is only about 14° . On the other hand, the dynamic force model used to describe the motion of the GNSS satellites is well known and imposes very strong constraints on the satellite trajectory. Nevertheless, periodic orbit errors may arise due to the correlation between the satellite clock corrections and empirical parameters that are required to account for the solar radiation pressure acting on the satellites. Corresponding investigations by Hugentobler et al. (2009) based on simulated Galileo data and a sparse tracking network indicate indeed a reduction of spurious once-per-revolution variations in the radial component of the satellite orbit when the satellite clock offsets were not estimated. However, this is a rather optimistic assumption because the true value of the satellite clock would need to be determined with few picoseconds precision outside the orbit determination procedure. More realistically, if the satellite oscillators were extremely stable, like e.g. optical clocks, they could be represented by a linear model over intervals as long as the revolution period and beyond. This would presumably reduce the ability of the clock corrections to compensate for once-per-revolution variation in the orbit. However, the impact of this mechanism remains to be investigated.

2.3 GNSS observables

The two fundamental observation types of all GNSS are pseudorange and carrier phase measurements on multiple frequencies. From the very beginning, the GPS satellites have broadcasted signals on two frequency, namely the L_1 frequency at 1575.42 MHz and the L_2 frequency at 1227.60 MHz. Only the two most recently launched Block IIF satellites transmit also on a third frequency at 1176.45 MHz denoted as L_5 . The observations can be processed directly or after forming linear combinations of the various observation types or differences between stations and satellites. More information concerning the GNSS signal structure and processing strategies based on observation differencing can be found, for example, in Hofmann-Wellenhof et al. (2008) or Seeber (2003). In this work, only undifferenced data analysis will be discussed. The basic observation equations for the undifferenced case, i.e. using the original measurements are given by

$$P_i = \rho + c \cdot \delta t_r - c \cdot \delta t^s + T - I_i + \delta t_{rel} + \varepsilon_{P_i}, \quad (2.2a)$$

$$L_i = \rho + c \cdot \delta t_r - c \cdot \delta t^s + T + I_i + \delta t_{rel} + \lambda_i(n_i + \alpha_{i,r} - \alpha_i^s) + \lambda_i \Delta \phi + \varepsilon_{L_i}, \quad (2.2b)$$

with

P_i	the pseudorange observation of frequency i in meters,
L_i	the carrier phase observation of frequency i in meters,
$\rho = \ \mathbf{X}_r - \mathbf{X}^s\ $	geometric distance between satellite \mathbf{X}^s and receiver position \mathbf{X}_r ,
c	the speed of light in vacuum,
T	the propagation delay in the neutral atmosphere, mainly the troposphere,
I_i	the frequency-dependent propagation delay caused by the ionosphere,
λ_i	the wavelength of the carrier phases on frequency i ,
n_i	the integer number of cycles of initial phase ambiguity i ,
$\alpha_{i,r}$	the receiver-specific fractional part of the initial phase ambiguity,
α_i^s	the satellite-specific fractional part of the initial phase ambiguity,
δt_r	the receiver clock error in seconds,
δt^s	the satellite clock error in seconds,
δt_{rel}	the conventional relativistic corrections,
$\Delta \phi$	the carrier phase wind-up effect in cycles,
ε_{P_i}	the pseudorange observation noise including multipath effects, and
ε_{L_i}	the carrier phase observation noise including multipath effects.

In the following, a few remarks regarding the elements of the observation equations (2.2) are going to be added. More details can be found in Section 2.5, where the observation modeling for the PPP approach is described.

The observations in (2.2) refer to the distance between the electric phase centers of the transmitter and receiver antennas. In practice, however, we want to relate the observations to a physical reference point of the receiving antenna and the center of mass of the GNSS satellite. Thus, frequency-dependent phase center offset (PCO) and phase center variation (PCV) corrections have to be applied for both receiver and satellite antennas. More details concerning the phase center modeling can be found in Section 2.5.1.

Furthermore the geometric distance contains the effects of receiver displacements due to deformations of the Earth's crust. In order to obtain receiver positions in ITRF the displacements of the observing site due to solid Earth tides and ocean loading need to be accounted for. Additional corrections, like e.g. for atmospheric loading and pole tides are also frequently applied if highest accuracy is sought for. It has to be kept in mind, however, that these models have to be consistent with the models used to generate the GNSS satellite orbits and clock offsets by e.g. the IGS analysis centers. A summary of the site displacement models applied for the data analysis in this work is given in Section 2.5.1.

Due to the frequency-dependence of the ionospheric propagation delay, it can be almost entirely eliminated by forming the ionosphere-free linear combination L_3 (cf. sec. 2.3.1). In contrast, the tropospheric delay is independent of the frequency and has to be modeled precisely. For high-precision applications based on carrier phase observations a slowly time-varying troposphere zenith delay parameter is usually estimated which is mapped to the elevation of a particular observation using an elevation-dependent mapping function (cf. Sec. 2.5.1).

The relativistic effects can be computed and removed from the observations using the conventional formulas given in Section 2.5.1.

If the data is processed in differential mode, many of the terms in (2.2) will be eliminated or largely reduced. For more details on the processing of observation differences we refer to section 2.3.2. In the following, several important linear combinations of the observations, used for parameter estimation and data screening, are introduced.

2.3.1 Linear combinations of observations

The original carrier phase and/or code observations of two or more frequencies can be combined into linear combinations (LC) in order to eliminate or largely reduce common biases and/or geometric information and to modify the effective carrier wavelength. For dual-frequency carrier phase observations, L_1 and L_2 , the linear combination L_x is expressed as

$$L_x = \kappa_{1,x}L_1 + \kappa_{2,x}L_2, \quad (2.3)$$

where $\kappa_{1,x}$ and $\kappa_{2,x}$ are the coefficients of the particular linear combination.

In the following discussion of the most important linear combinations of the observations a simplified observation model will be adopted, where the noise terms are omitted and all non-dispersive delays and clock biases are merged into a pseudo-distance term ρ' . Furthermore, the initial phase ambiguity is modeled by a non-integer quantity b that includes the fractional receiver and satellite-specific parts. Consequently, the four basic observables for dual-frequency code (P_1, P_2) and carrier phase (L_1, L_2) data can be written as

$$P_1 = \rho' + I_1, \quad (2.4a)$$

$$P_2 = \rho' + \frac{f_1^2}{f_2^2}I_1, \quad (2.4b)$$

$$L_1 = \rho' - I_1 + \lambda_1 b_1, \quad (2.4c)$$

$$L_2 = \rho' - \frac{f_1^2}{f_2^2}I_1 + \lambda_2 b_2. \quad (2.4d)$$

with

- ρ' a pseudo-distance term including clock errors and frequency-independent delays,
- I_i the frequency-dependent propagation delay caused by the ionosphere,
- f_i the carrier frequency i ,
- λ_i the wavelength of the carrier signal on frequency i , and
- b_i the non-integer initial carrier phase ambiguity on frequency i .

The wide-lane linear combination (L_w)

The so called wide-lane linear combination of the carrier phase observations

$$L_w = \frac{f_1}{f_1 - f_2}L_1 - \frac{f_2}{f_1 - f_2}L_2 = \rho' - \frac{f_1}{f_2}I_1 + \frac{c}{f_1 - f_2}(b_1 - b_2) \quad (2.5)$$

contains the full geometric information along with a differential ionospheric delay and the difference of the L_1 and L_2 carrier phase ambiguities $b_1 - b_2$, also referred to as wide-lane ambiguity b_w . The factor $c/(f_1 - f_2)$ determines the wide-lane wavelength λ_w which is approximately 86 cm. Due to this relatively large wavelength, the wide-lane linear combination plays an important role for carrier phase ambiguity resolution.

The ionosphere-free linear combinations (L_3 and P_3)

The ionosphere is the most important error source affecting the GNSS signals on the way from the satellite to the Earth. The ionospheric delay is highly variable in space and time which makes modeling a complex task and prediction almost impossible. Fortunately, however, the ionosphere is a dispersive

medium for microwaves, i.e. the ionospheric delay depends on the frequency of the transmitted signal. Consequently, it can be eliminated to first order by forming the following linear combination of two signals at different frequencies

$$P_3 = \frac{f_1^2}{f_1^2 - f_2^2} P_1 - \frac{f_2^2}{f_1^2 - f_2^2} P_2 = \rho', \quad (2.6a)$$

$$L_3 = \frac{f_1^2}{f_1^2 - f_2^2} L_1 - \frac{f_2^2}{f_1^2 - f_2^2} L_2 = \rho' + \frac{f_1^2}{f_1^2 - f_2^2} \lambda_1 b_1 - \frac{f_2^2}{f_1^2 - f_2^2} \lambda_2 b_2. \quad (2.6b)$$

This simple and efficient elimination of the ionospheric delays makes the L_3 linear combination the most widely used observable for precise GNSS data analysis of large scale networks. Parameter estimation performed in this work is based exclusively on this observable. The disadvantages of the L_3 LC are the need for dual-frequency receivers, an increased observation noise level and the fact, that the integer nature of the ambiguities is lost. According to the laws of error propagation and neglecting correlations between L_1 and L_2 observations, the noise level of the ionosphere-free linear combination can be computed from the following expression

$$\sigma_{L_3} = \sqrt{(2.546)^2 \sigma_{L_1}^2 + (-1.546)^2 \sigma_{L_2}^2} \quad (2.7)$$

Assuming furthermore an identical noise level of the observation on the individual frequencies we obtain an amplification factor of approximately 3 for the noise of the ionosphere-free linear combination with respect to the individual carrier phase (or pseudorange) signals. Moreover, (2.6) implies, that frequency-dependent systematic measurement errors, such as multipath, are also amplified.

For carrier phase ambiguity resolution, the ionosphere-free linear combination of the carrier phase observations can be expressed in terms of wide-lane ($b_w = b_1 - b_2$) and L_1 (b_1) ambiguities. Assuming the wide-lane ambiguity to be known, we may replace the L_2 ambiguity b_2 in (2.6b) by $b_1 - b_w$, i.e.

$$L_3 = \rho' + \frac{f_1^2}{f_1^2 - f_2^2} \lambda_1 b_1 - \frac{f_2^2}{f_1^2 - f_2^2} \lambda_2 b_1 + \frac{f_2^2}{f_1^2 - f_2^2} \lambda_2 b_w, \quad (2.8)$$

or simplified

$$L_3 = \rho' + \frac{c}{f_1 + f_2} b_1 - \frac{f_2^2}{f_1^2 - f_2^2} \lambda_2 b_w = \rho' + \lambda_c b_1 - \frac{f_2^2}{f_1^2 - f_2^2} \lambda_2 b_w. \quad (2.9)$$

This formulation is particularly useful for ambiguity resolution because the effective wavelength of the remaining, so called narrow-lane, ambiguity λ_c is approximately 10.7 cm. In contrast, the largest effective wavelength of the ionosphere-free linear combination expressed by integer multiples of the original L_1 and L_2 ambiguities is only 0.6 cm. Generally, the wide-lane and L_1 ambiguities b_w and b_1 can only be fixed to integers at the double difference level. However, if the fractional parts of the ambiguities originating at the satellite are known from a network solution, b_w and b_1 can also be fixed to integers at the level of single differences between satellites. This approach using also (2.9) is discussed in more detail in Section 2.5.2.

Following early works, e.g., by Brunner and Gu (1991), higher-order ionosphere influences on GNSS signals have been a major research topic over the past decade. It was shown that second- and third-order effects can cause positioning errors at the few mm level, especially during periods of high ionospheric activity (Fritsche et al., 2005; Hoque and Jakowski, 2007). Nevertheless, at the time of writing higher-order ionospheric corrections are only used at the IGS AC CODE in routine processing.

The geometry-free linear combination (L_4)

As the name implies, the geometry-free linear combination

$$L_4 = L_1 - L_2 = \left(1 - \frac{f_1^2}{f_2^2}\right) I_1 + (\lambda_1 b_1 - \lambda_2 b_2) \quad (2.10)$$

does not depend on station and satellite clocks, orbits, station coordinates or tropospheric propagation delays. In fact, it only contains carrier phase ambiguities and the differential ionospheric delay between the L_1 and L_2 frequency. Due to the elimination of the geometry and the very low noise, this linear combination is frequently used for ionospheric delay estimation and screening of the carrier phase observations for cycle slips, i.e. sudden jumps in the ambiguities. The latter is usually done by analyzing the differences between consecutive L_4 observations. Due to the high temporal and spatial variability of the ionospheric delays, the time differences between the observations should be small. For 1 Hz data, the detection of cycle slips based on time-differenced L_4 observations is straight forward in almost all cases. For static receivers even 30-second and 5-minute observation intervals are usually sufficient during times of moderate ionospheric activity. Note, however, that only the difference of cycle slips on L_1 and L_2 can be tested. Thus, certain linear combinations of simultaneous cycle slips on L_1 and L_2 cannot be detected using this observable but have to be revealed by other tests.

The Melbourne-Wübbena linear combination (L_{MW})

Forming the difference of the wide-lane linear combination of the phase observations (2.5) and the following linear combination of the pseudo-range observations

$$\frac{f_1}{f_1 + f_2} P_1 + \frac{f_2}{f_1 + f_2} P_2 = \rho' - \frac{f_1}{f_2} I_1, \quad (2.11)$$

a dual-frequency code and carrier phase linear combination is obtained that eliminates the influence of the geometry, the troposphere and the ionosphere, thus containing only the wide-lane phase ambiguity and noise

$$L_{MW} = \frac{f_1 L_1 - f_2 L_2}{f_1 - f_2} - \frac{f_1 P_1 + f_2 P_2}{f_1 + f_2} = \frac{c}{f_1 - f_2} (b_1 - b_2) = \lambda_w b_w. \quad (2.12)$$

This linear combination was first employed for double difference wide-lane ambiguity resolution independently by Melbourne (1985) and Wübbena (1985). The success of this approach mainly depends on the noise of the pseudorange observations. With modern receivers, however, generally few observations are sufficient to resolve the wide-lane ambiguities. In this work, the Melbourne-Wübbena linear combination is used to determine undifferenced integer wide-lane ambiguities which are required for the ambiguity fixing of ionosphere-free observations in PPP.

2.3.2 Observation differencing

The most popular strategies for high-precision GNSS data processing are based on observation differencing. This is due to the fact that many common errors can be eliminated or at least strongly reduced with this approach. The most efficient error reduction is achieved by forming *single differences* between simultaneous observations of two stations to the same satellite. This eliminates the satellite clock error and - depending on the distance between the two stations - reduces the impact of satellite orbit errors and atmospheric propagation delays. Strictly speaking, the satellite clock error is not completely eliminated, because the time of transmission of the signal received by the two stations differs slightly. However, due to the frequency stability of the satellite oscillators the remaining differential satellite clock error is generally negligible.

Product	code	latency	orbit accuracy	clock accuracy	clock precision
final	IGS	2 weeks	2.5 cm	75 ps	20 ps
rapid	IGR	18 hours	2.5 cm	75 ps	25 ps
ultra rapid (obs. half)	IGU	3 hours	3 cm	150 ps	50 ps
ultra rapid (pred. half)	IGU	0 hours	5 cm	3 ns	1.5 ns

Table 2.2: GPS ephemeris and clock products provided by the IGS (IGS, 2012). The clock precision values are obtained by taking a station and satellite-specific bias into account

By forming the difference between single differences of simultaneously observed satellites, a new observable is obtained, which is commonly referred to as *double difference*. The main advantages of this observable are that the single difference receiver clock term is eliminated and that carrier phase ambiguities are turned into integer values. Since in this thesis clock parameters are to be studied, we will focus on an undifferenced processing method, namely the Precise Point Positioning (PPP) approach, which is described in detail in Section 2.5.

2.4 The International GNSS Service (IGS) and its analysis centers

Most precise GNSS applications at global and regional scales rely on highly accurate satellite orbit and clock information. This is particularly true for the Precise Point Positioning approach as we shall see in Section 2.5. The International GNSS Service (IGS) plays a key role in providing and distributing precise orbits and clock corrections for the GNSS satellites. The IGS is a voluntary international federation of research institutions and governmental agencies. It coordinates a global GNSS reference station network and uses its data to compute highly precise orbits and clocks for the GPS and GLONASS satellites (Dow et al., 2009). The computation of the IGS products is performed by the IGS analysis center coordinator (IGS ACC), who is responsible for the rigorous combination of the orbit and clock solutions of currently up to 11 IGS analysis centers (IGS AC). Three product lines differing in timeliness and accuracy are provided (Tab. 2.2). In addition to the combination products also the products of the individual analysis centers are available from the IGS data centers. An overview of the current ACs contributing to the final IGS satellite clock corrections and their individual clock products is given in Table 2.3.

By combining the solutions of different analysis centers, the IGS products are usually more precise and reliable than the products of any AC alone. However, it has to be kept in mind that the AC solutions are not statistically independent, because they usually share a large amount of common observation data. Furthermore, some minor differences in the observation modeling, e.g. modeling of the yaw-attitude of the GNSS satellites or consideration of higher-order ionosphere effects exist, which may cause a degradation of the combined solution. Further inconsistencies can occur in the combination procedure itself. A specific problem for the analysis presented in this work is an inconsistency of the 30-s IGS final clock product and the corresponding orbits (Kouba, 2009b; Montenbruck et al., 2009). This problem is related to the fact that only 3 ACs contribute to the 30s satellite clocks but typically 6 ACs to the 5 min clocks and orbits. The resulting bias between 5-minute and 30-second clocks has been removed in the products starting with GPS week 1517 (Jan, 2009) by adjusting the 30 s clocks through interpolation of the biases at the 5 min epochs (IGS Mail #5902).

In view of these potential pitfalls, it has been decided to generally use products of a single IGS analysis center. If not indicated otherwise, ephemerides and clock corrections of the Center for Orbit Determination in Europe (CODE), located at the Astronomical Institute of the University of Berne (AIUB), are used in this work.

Analysis Center (AC)	ID	rapid	final clocks
Centre for Orbit Determination in Europe	COD	30 s	30 s / 5 s
Natural Ressources Canada	EMR	5 min	30 s
European Space Operations Center	ESA	5 min	30 s
Deutsches GeoForschungszentrum	GFZ	5 min	5 min
Jet Propulsion Laboratory	JPL	5 min	5 min
Massachusetts Institute of Technology	MIT	-	30 s

Table 2.3: IGS analysis centers that contribute to the final IGS satellite clock corrections and their individual clock products as of December 2011

2.5 Precise Point Positioning (PPP)

Precise Point Positioning (PPP) is a rather new approach, that combines the processing of undifferenced GNSS code and carrier phase data with accurate satellite orbit and clock information for precise absolute position determination (Zumberge et al., 1997). For long observation sessions (>6h), the accuracy of PPP is comparable to that of carrier phase based relative positioning, i.e. at the 1-2 centimeter level in the vertical and below one centimeter horizontally (e.g. Kouba, 2009a). Initially introduced as a method to reduce the computational burden for the processing of networks with many stations, it quickly became a popular alternative to classical baseline or network processing strategies with applications in geophysics, surveying, navigation, time-keeping and meteorology.

PPP is made possible through the availability of highly precise satellite orbits and clock corrections provided, e.g., by the IGS. Since no differences with respect to a reference station need to be formed, precise positioning of an isolated receiver is possible. Moreover, the resulting coordinates directly refer to the International Terrestrial Reference Frame (ITRF) that was used to generate the satellite orbits and clocks. Thus, PPP provides access to the ITRF with cm accuracy anywhere on the Earth without the need to process data of a reference station with known ITRF coordinates. Other reasons for the great success of the PPP method are the conceptual simplicity and interpretability of the results, e.g. geophysical effects can be studied on a station-by-station basis and atmospheric propagation delays on a line-of-sight basis.

The main limitation of the current PPP algorithms are the long observation times that are required to determine the unknown carrier phase ambiguities. This problem is partly overcome by variants of PPP that allow integer ambiguity fixing at the undifferenced or between-satellites single difference level. However, the convergence is generally still slower than for differential methods with short inter-station distances, e.g. Real-Time Kinematic (RTK) methods. This is mainly because in PPP tropospheric delays have to be estimated which requires a certain minimum time span of observation data, while for relative positioning on short baselines troposphere effects can be eliminated.

Since the PPP algorithm is used throughout this work and fundamental for its understanding, a short introduction to the employed corrections and the adjustment model is given below. For additional information on the PPP approach, the involved models and achievable accuracies, the reader is referred to Zumberge et al. (1997), Kouba and Héroux (2001), and Kouba (2009a).

2.5.1 Observation modeling

In classical PPP, first-order effects of the ionosphere are eliminated by forming the ionosphere-free linear combinations P_3 and L_3 of the observations, according to Equations 2.6. Precise satellite orbits and clock corrections, e.g. provided by the IGS or one of its analysis centers, are introduced. The hydrostatic part of the tropospheric propagation delay is usually approximated by an a priori model while the wet part is estimated as a slowly time-varying zenith delay parameter zwd , that is projected onto the elevation e of an individual observation using a corresponding mapping function $m_{f_w}(e)$. The L_3 linear combination of the integer initial carrier phase ambiguities is combined with the fractional receiver and satellite

parts in a non-integer carrier phase ambiguity term b . Finally, all a priori known signal delays, satellite clock offsets and reference point displacements are merged into the distance term ρ' . Consequently, the observation equations can be written as

$$P_3 = \rho' + c \cdot \delta t_r + m f_w(e) \cdot zwd + \varepsilon_{P_3}, \quad (2.13)$$

$$L_3 = \rho' + c \cdot \delta t_r + m f_w(e) \cdot zwd + b + \varepsilon_{L_3}, \quad (2.14)$$

with

ρ'	the propagation distance between satellite and receiver including the effects of satellite clock offsets, reference point displacements, and hydrostatic troposphere delays,
$m f_w(e)$	the mapping function for the wet part of the tropospheric delay,
zwd	the wet tropospheric delay in zenith direction,
δt_r	the receiver clock error in seconds,
b	the float L_3 phase ambiguity including fractional receiver and satellite biases,
ε_{P_3}	the P_3 observation noise including multipath effects,
ε_{L_3}	the L_3 observation noise including multipath effects, and
c	the speed of light in vacuum.

In order to achieve centimeter-level accuracy it is absolutely essential to apply the same correction models as the IGS analysis centers. Therefore, the required observation corrections are briefly introduced in the following paragraphs.

Displacements of the observing sites In a global coordinate frame every observing site undergoes periodic and secular movements due to the deformation of the Earth's crust. While the secular movements are mainly driven by plate tectonics and geophysical phenomena such as post-glacial rebound, the periodic displacements are primarily caused by the gravitational forces of the Sun and the Moon as well as varying surface loads. The following periodic displacement effects have been modeled according to the IERS conventions 2010 (Petit and Luzum, 2010) in order to be consistent with the current IGS solutions.

The site displacements caused by the *solid Earth tides*, are computed using the Fortran subroutine `dehanttidein1.f` which is provided by the IERS. In order to maintain consistency with the ITRF, which is conventional tide-free, the permanent tidal displacement is not removed from the model (Petit and Luzum, 2010).

Ocean loading corrections are computed according to the model FES2004 (Lyard et al., 2006). The computation is carried out using the Fortran subroutine `hardisp.f` also available through the IERS with the amplitude and phase coefficients of the model obtained from the on-line ocean loading service (<http://www.oso.chalmers.se/loading/>) maintained by Machiel Bos and Hans-Georg Scherneck. The corrections for the center of mass motion of the solid Earth due to the ocean tides are not included.

Solid Earth pole tides are modeled according to the IERS conventions 2010 (Petit and Luzum, 2010). The required pole coordinates are taken from the IGS weekly solution of the Earth rotation parameters.

Note that site displacements due to *atmospheric loading* and the effect of *ocean pole tides* are not considered, because they are not yet adopted by the IGS analysis centers for their routine processing. The impact of both, atmospheric loading displacement and ocean pole tide are largest for the station height, reaching maximum displacements of 4 mm and 2 mm, respectively (Petit and Luzum, 2010).

Troposphere modeling The electromagnetic signals broadcasted by the GNSS satellites are subject to significant delays in the neutral part of the Earth's atmosphere, mainly the troposphere. The delay depends on the length of the signal path in the troposphere, thus it increases at low elevation angles.

Typical values are 2.4 m for an observation in zenith direction and up to 24 m at an elevation angle of 5° . Since the delay induced by the troposphere is the same for all GNSS signals, it cannot be eliminated by using multiple frequencies as it is the case for the ionospheric delay. In addition, the delay is highly variable in space and time, due to the varying distribution of the water vapor in the troposphere. This severely limits the accuracy of a priori tropospheric delay models. In PPP and other precise GNSS processing approaches with large inter-station distances or large height differences the tropospheric delay is therefore usually estimated as a time-varying zenith delay parameter that is related to the slant delay of a certain observation by a so called mapping function. All mapping functions in use today assume azimuthal symmetry, i.e. they depend only on the elevation angle of the observed satellite. The total tropospheric zenith delay is usually expressed as the sum of a *hydrostatic* (zhd) and a so called *wet* (zwd) part, with individual mapping functions mf_h and mf_w , respectively. The complete expression for the tropospheric slant delay T for an observation at an elevation angle e reads (Bevis et al., 1992):

$$T(e) = mf_h(e) \cdot zhd + mf_w(e) \cdot zwd. \quad (2.15)$$

The hydrostatic part of the tropospheric zenith delay primarily depends on the partial pressure of dry air and varies slowly in space and time. Thus, it can be determined accurately using pressure values observed at the GNSS antenna site. The zhd amounts to approximately 2.3 m at sea level and makes up around 90 % of the total tropospheric delay (Bevis et al., 1992). Various models have been established to derive the hydrostatic zenith delay from surface pressure or a standard atmosphere, with the one by Saastamoinen (1973) being the most popular and recommended by the IERS (Petit and Luzum, 2010). More recently, zhd from ray-tracing through numerical weather models (NWM) have been made available (Boehm et al., 2006b), that allow the determination of accurate zhd values when no pressure observations are available. Accurate zhd are required if the water vapor in the atmosphere shall be derived from the estimated wet zenith delay. For positioning purposes the accuracy of the a priori hydrostatic zenith delay is less critical, since the hydrostatic and the wet mapping function are very similar, so that the effect of residual hydrostatic zenith delay errors is largely compensated by the estimated wet zenith delays.

In contrast to the hydrostatic part of the tropospheric delay, the wet component cannot be estimated from surface meteorological data at the level of accuracy required. Sophisticated and expensive monitoring devices, like Water Vapor Radiometers (WVR) or Raman Lidars, which can sense the amount of precipitable water vapor in the troposphere would have to be used to get an accurate value for the zwd . However, the accuracy of WVRs is strongly degraded by rainfall and Raman Lidars can only operate in clear sky conditions preferably during night time. In addition, the calibration of these devices is difficult (Elgered et al., 1991; Bosser et al., 2010). Thus for all high-precision GNSS applications, except for differential positioning with very short baselines and small height differences, the wet part of the tropospheric zenith delay has to be estimated within the least-squares adjustment. The parameterization needs to take into account the time-varying nature of the zenith delay for example through piece-wise linear modeling or the addition of process noise in a Kalman filter (cf. Section 4.2).

If not indicated otherwise, the Global Mapping Function (GMF) (Boehm et al., 2006a) is used in this work to map the hydrostatic and the wet part of the tropospheric delay to the elevation of the observations. The hydrostatic zenith delay zhd is computed according to the model of Saastamoinen using meteorological data taken from the Global Pressure and Temperature (GPT) model (Boehm et al., 2007) as recommended in the latest IERS standards (Petit and Luzum, 2010).

For high-precision static positioning, azimuthal asymmetries of the tropospheric delay at low elevations are commonly accounted for by estimating *horizontal troposphere gradients* in north-south and east-west directions. This gradient estimation can be interpreted as a tilting of the zenith direction that is used in the tropospheric mapping functions. The largest improvement is usually achieved for the horizontal coordinates ($\approx 30\%$), while the impact on the vertical position is rather small ($\approx 10\%$) (Meindl et al., 2004). Since the mathematical correlation between the receiver clock parameters and the horizontal coordinates is much lower than the correlation between the receiver clock and the height component, also the impact of estimating troposphere gradients on the receiver clock estimates is expected to be

small. For the sake of simplicity, the estimation of horizontal troposphere gradients is therefore not considered in this work.

Precise ephemerides and satellite clock corrections The PPP approach relies on the availability of highly precise satellite positions and satellite clock corrections. The primary source of precise satellite ephemerides and clock corrections for the GPS and GLONASS satellites for post processing are the IGS and its analysis centers.

Nowadays, the precise ephemerides are provided almost exclusively in the SP3c-Format, with a spacing of typically 900 s. Between these epochs the satellite positions have to be interpolated. Popular interpolation techniques are based on Lagrange, Newton and Neville interpolation polynomials. When choosing a suitable degree of the polynomial the error of the interpolation is at the few mm level (e.g. Remondi, 1991; Yousif and El-Rabbany, 2007). Of course, this precision can only be achieved around the center of the interpolated points, thus if a complete day is to be processed, ephemeris data from the days before and after have to be used. Because precise post-processing GNSS data analysis is usually done in daily batches, there may be small discontinuities in the orbit and clock products at the day boundaries. This can cause a small degradation of the interpolated positions at the beginning and the end of the day. In the PPP software developed for this work, satellite positions are interpolated with a 9th-order Newton interpolation. The coefficients for this type of interpolation can be computed very efficiently using divided differences.

Ideally, the ephemerides should be interpolated by a satellite orbit, that fulfills the equation of motion of the satellite. This would yield an orbit with homogeneous precision even at the boundaries of the ephemeris file. However, much care has to be taken to apply exactly the same force modeling that was used to generate the ephemerides. If this consistency cannot be guaranteed, a good fit may still be achieved by fitting several shorter orbital arcs to the ephemerides (Dach et al., 2007). For most applications, however, simple numerical interpolation techniques, as applied in this work, are entirely sufficient.

Although the computation of satellite positions is a standard procedure, two potential pitfalls are going to be briefly discussed in the following, because they are a frequent cause of confusion.

The satellite positions have to be interpolated for the time of signal transmission in the GPS time scale. The GNSS satellites move with a velocity of approximately 4 km/s and the maximum rate of change of the receiver satellite distance is approximately 800 m/s. Thus, the signal transmission time must be known with μs accuracy in order to keep the computational error of the receiver-satellite distance below 1 mm. If the receiver position is known a priori within a hundred meters, which is often the case, the signal transmission time $t - \tau^j$ can be computed non-iteratively using the pseudorange observations according to

$$t - \tau^j = t_r(t) - \frac{P_r^j}{c} - \delta t^i(t - \tau^j), \quad (2.16)$$

with

t	the signal reception time in the GPS time scale,
τ^j	the signal propagation time of satellite j ,
$t_r(t)$	the signal reception time in the receiver time scale (RINEX observation epoch),
P_r^j	the pseudorange observation of satellite j ,
c	the speed of light in vacuum, and
$\delta t^i(t - \tau^j)$	the clock offset of satellite j with respect to the GPS time scale.

Strictly speaking the satellite clock error at the time of signal transmission ($t - \tau^j$) should be used. Within the required accuracy limits, however, the satellite clock offset at the signal reception time $t_r(t)$ can be used.

Another remark is related to the coordinate system that is used for the computation of the geometric distance between satellite and receiver. Even if we ignore the impact of atmospheric refraction, only in an inertial coordinate system electromagnetic signals propagate in straight lines and with constant velocity. Thus, the geometric distance must be evaluated in an Earth-centered inertial (ECI) system. When computing satellite positions in a rotating Earth-centered and Earth-fixed (ECEF) coordinate system, care has to be taken to correct for the effect of the Earth's rotation (Sagnac effect). By choosing the ECI that coincides with the ECEF at the time of signal reception, the Sagnac effect can be taken into account simply through a rotation of the interpolated satellite positions by the angle the Earth has rotated during the signal propagation time τ^j around the Z-axis common to the ECI and ECEF systems, i.e.

$$\mathbf{X}_{ECI(t)}^j = \begin{bmatrix} \cos(\dot{\Omega}_{\oplus}\tau^j) & \sin(\dot{\Omega}_{\oplus}\tau^j) & 0 \\ -\sin(\dot{\Omega}_{\oplus}\tau^j) & \cos(\dot{\Omega}_{\oplus}\tau^j) & 0 \\ 0 & 0 & 1 \end{bmatrix} \mathbf{X}_{ECI(t-\tau^j)}^j \quad (2.17)$$

with

$\dot{\Omega}_{\oplus}$ the Earth's rotation rate ($7.2921151467 \cdot 10^{-5}$ rad/s).

The propagation time τ^j , required in (2.17), can be computed from the geometric distance between the satellite and the receiver with sufficient accuracy, again provided that the receiver coordinates are accurate to within 100 m. Due to the small time interval τ^j on the order of 65 to 90 ms, other changes between the ECEF and the ECI during the signal propagation as for example polar motion and length of day variations can be safely neglected.

In contrast to the satellite positions, satellite clock corrections can generally not be interpolated over intervals larger than a few seconds, if highest accuracy is required. This is due to the limited frequency stability of the atomic clocks on board of the GPS satellites, which causes high-frequency variations exceeding the carrier phase observation noise. For post-processing applications this is not a severe limitation, since satellite clock corrections with 30 s spacing are provided by the IGS and several of its analysis centers. The IGS analysis center CODE at AIUB even provides GPS satellite clock corrections with 5 s spacing. These clock corrections can be linearly interpolated with almost no loss of accuracy (Bock et al., 2009). For the Galileo satellites which will carry passive hydrogen maser clocks and the latest GPS Block IIF satellites that use a new generation of improved Rubidium frequency standards, interpolation and modeling of the satellite clocks at the level of precision of the GNSS carrier phase observations over longer intervals will be possible in the future (Hauschild et al., 2012).

A final remark concerns the *attitude modeling* of the GPS satellites. In nominal attitude, the antenna z-axis of the GPS satellite points towards the center of the Earth, the y-axis points along the solar-panel-axis and is perpendicular to the Sun-satellite vector and the x-axis points either towards the Sun for the Block IIA and IIF satellites or away from the Sun for the Block IIR satellites and completes a right-hand coordinate system. Departures from this nominal orientation can affect the satellite orbit and clock corrections. Critical situations typically arise when the GPS satellites cross the Earth's shadow and when the vectors satellite-Sun and satellite-Earth are close to collinearity. In the latter situation rapid yaw rotations, known as noon and midnight turns, are required to maintain the nominal attitude. Due to the limited maximum yaw rotation rate of the satellites, they cannot keep up with the nominal orientation and temporary attitude errors are the consequence. According to Kouba (2009a), mainly observations of GPS Block IIA satellites are affected by such attitude problems because the transmitter antenna of this block type is offset by about 20 cm from the center of mass in the x-direction of the satellite body frame. In addition, the Block IIA satellites do not keep nominal attitude while being in the Earth's shadow and it can take up to half an hour after shadow exist until these satellites regain nominal attitude. Significant departures from the nominal attitude also exist for the Block IIF satellites during midnight and noon turns, if the angle β between the vector Earth-Sun and the orbital plane is smaller than 8° . In this situation the limited maximum yaw rotation rate does not allow to maintain the

nominal attitude. This causes modeling errors of several centimeters, because the offset of the antenna from the center of mass in the x-direction of the IIF satellites is even larger than for the Block IIA satellites. However, the errors can be largely reduced with a simple model of the actual attitude based on the maximum yaw rotation rates for noon and midnight turns (Dilßner, 2010).

Usually, attitude modeling problems can be detected in the post-fit residuals and the affected data can be removed. However, under certain conditions the detection may fail. Therefore, the observations of Block IIA satellites during shadow transit and 30 minutes after shadow exit have been excluded automatically from the processing. The required times of shadow entry and exit are determined using a simple cylindrical shadow model (Seeber, 2003, p.104).

Differential code biases GPS satellites broadcast different ranging codes on multiple frequencies. Due to different signal delays in the satellite hardware each of the code signals has its own time offset which also varies with time. All currently operating GPS satellites transmit the un-encrypted C/A-code on the L_1 frequency and the protected P-code on both, L_1 and L_2 frequencies. According to the RINEX 2 terminology (Gurtner and Estey, 2007), we refer to these pseudorange observations as C1, P1 and P2. Geodetic GPS receivers employ sophisticated algorithms to track the P-codes despite the encryption. Depending on the receiver type either C1, P1 and P2 or only C1 and P2 are provided. In addition some older receiver types based on cross correlation techniques provide C1 and P2'= $C1+(P2-P1)$ (e.g. Dach et al., 2007). By convention, the GPS broadcast satellite clock corrections as well as the IGS analysis center and combined satellite clock products refer to the ionosphere-free linear combination of the P-codes P1 and P2 (IGS Mail #2744). Consequently, if PPP is to be performed for a receiver that does not provide P1, the C1 observations have to be corrected for the difference P1-C1 of the individual satellite (Kouba, 2009a). Such offsets are commonly referred to as Differential Code Biases (DCB). The term “differential” indicates that only the difference between codes and between satellites can be determined. In practice, the latter singularity is typically removed by forcing the average DCB of all satellites to be equal to zero. Consequently, DCB for each satellite can be provided. In addition to the P1-C1 bias also the P1-P2 difference is sometimes required, e.g., for single-frequency positioning. The P1-C1 DCB can be as large as 2 ns or 0.6 m and are normally stable in time. DCB values are determined regularly by the IGS AC CODE and are provided as monthly mean values. These corrections have been used in this work in cases when no P1 observations were available.

Satellite and receiver antenna phase center variations GPS observations refer to the distance between the electric phase centers of the transmitter and receiver antennas. In practice, however, we need to relate the observations to some physical reference point of the receiving antenna, the so called antenna reference point (ARP), and the center of mass of the GNSS satellite, respectively. This is achieved by applying frequency-dependent phase center offset (PCO) and phase center variation (PCV) corrections for both, the receiver and satellite antennas. As the name implies, the PCO is a 3D offset vector, while the PCV are usually provided on a $5^\circ \times 5^\circ$ grid in azimuth and elevation. Consequently, the range correction $\Delta\rho$ for an observation at elevation e and azimuth α can be computed as

$$\Delta\rho(\alpha, e) = \mathbf{x}_{PCO}^T \cdot \mathbf{e}_r^s - PCV(\alpha, e), \quad (2.18)$$

with the PCO-vector \mathbf{x}_{PCO} and the receiver-satellite unit vector \mathbf{e}_r^s in the antenna coordinate system

$$\mathbf{e}_r^s = [\cos e \cos \alpha \quad \cos e \sin \alpha \quad \sin e]^T. \quad (2.19)$$

The PCO and PCV values required to compute these corrections can be taken, e.g., from the IGS antenna file in ANTEX format (Rothacher and Schmid, 2010). In this way, the compatibility with the IGS orbit and clock products is ensured. While receiver antennas can be calibrated for each individual frequency by means of a robot rotating and tilting the antenna in a short baseline configuration (Wübbena et al., 2000) or in an anechoic chamber (Zeimet and Kuhlmann, 2008), the phase center offsets and variations of the transmitter antennas are estimated from a global network solution and are therefore only available for the ionosphere-free linear combination (2.6) of the observations (Schmid and Rothacher, 2003).

Carrier phase wind-up Due to the circular polarization of the GPS signals, a carrier phase delay or advance is introduced if either the transmitting or the receiving antenna is rotated around its bore axis. When processing carrier phase data of large networks or in PPP mode, the effect of this *phase wind-up* effect needs to be taken into account. According to Wu et al. (1993) the effective dipole vectors of the receiver and transmitter antennas can be defined as

$$\mathbf{D}_r = \mathbf{e}_{x,r} - \mathbf{k}(\mathbf{k} \cdot \mathbf{e}_{x,r}) + \mathbf{k} \times \mathbf{e}_{y,r} \quad (2.20)$$

and

$$\mathbf{D}_s = \mathbf{e}_x^s - \mathbf{k}(\mathbf{k} \cdot \mathbf{e}_x^s) - \mathbf{k} \times \mathbf{e}_y^s, \quad (2.21)$$

with

- \mathbf{k} the unit vector pointing from the satellite to the receiver,
- $\mathbf{e}_{x,r}, \mathbf{e}_{y,r}$ the unit vectors pointing into the x and y direction of the receiver antenna coordinate system, and
- $\mathbf{e}_x^s, \mathbf{e}_y^s$ the unit vectors pointing into the x and y direction of the transmitter antenna coordinate system.

Using these vectors, the phase wind-up effect can be computed as

$$\Delta\phi = \text{sign}(\zeta) \arccos \frac{\mathbf{D}_s \cdot \mathbf{D}_r}{\|\mathbf{D}_s\| \cdot \|\mathbf{D}_r\|}, \quad (2.22)$$

where

$$\zeta = \mathbf{k} \cdot (\mathbf{D}_s \times \mathbf{D}_r). \quad (2.23)$$

Note, that the arccos function in (2.22) is limited to the interval $[0, 2\pi]$. In order to avoid jumps of 2π in (2.22), the difference between consecutive $\Delta\phi$ is checked and integer multiples of 2π are introduced as required. However, for large rotations of the receiver antenna in combination with low observation rate, additional information about the size and direction of the rotations may be required.

In GNSS analysis solely based on carrier phase observations only the phase wind-up effect caused by the rotation of the GNSS satellites has to be taken into account. This is due to the fact that the phase wind-up caused by a rotation of the receiving antenna is identical for all satellites. Thus the effect can conveniently be absorbed by the estimated receiver clock offsets or be eliminated by forming single differences between satellites. However, this property does not hold for conventional PPP solutions because code and carrier phase observations are processed simultaneously, assuming that the receiver clock error is identical for both observation types. Consequently, the phase wind-up effect will introduce an inconsistency between code and carrier phases which grows with the number and size of rotations. Due to the different weighting of the code and carrier phase observations, the PPP solution exhibits a certain degree of tolerance with respect to antenna rotations. However, as the antenna rotations, e.g. in a navigation application, accumulate, a degradation of the solution will be inevitable (Banville and Tang, 2010). Finally, if modeling of the receiver clock is intended, receiver antenna rotations have to be considered even more carefully. Since a 360° rotation of the antenna will cause a phase shift of 10.7 cm in the L_3 linear combination, the attitude of the antenna should be known to better than 30° (4°) in order to correct for the effect with sub-centimeter (sub-millimeter) range accuracy.

Relativistic corrections By convention, the IGS has adopted the same relativistic correction for the GPS satellite clocks as the GPS control segment (IS-GPS-200D, 2004). The correction Δt_{PerRel} accounts for the periodic frequency variations of the satellite oscillators caused by the varying altitude and velocity of the GNSS satellites with respect to an Earth-bound clock and can be expressed (in seconds) by

$$\Delta t_{PerRel} = \frac{2}{c^2} \sqrt{a \cdot GM} e \sin E, \quad (2.24)$$

with

- c speed of light in vacuum,
- a semi-major axis of the satellite orbit,
- GM the Earth's gravitational constant,
- e numerical eccentricity of the satellite orbit,
- E eccentric anomaly of the satellite orbit,

or equivalently

$$\Delta t_{PerRel} = \frac{2}{c^2} \mathbf{x} \cdot \mathbf{v}, \quad (2.25)$$

with

- c speed of light in vacuum,
- \mathbf{x} position vector of the satellite,
- \mathbf{v} velocity vector of the satellite.

Mainly depending on the orbit eccentricity, the correction for GPS satellites can exceed 30 nanoseconds (9 meters) and needs to be applied by all users of IGS products as well as broadcast satellite clock corrections for consistency purposes. At the required accuracy level, the computation of (2.25) may be performed both with Earth-centered inertial and Earth-centered Earth-fixed position and velocity vectors. Note, however, that (2.25) does not take into account the influence of the Earth's oblateness or any higher-order coefficients of the Earth's gravity potential.

In addition to the relativistic satellite clock correction (2.25), most IGS analysis centers correct for the general relativistic time delay of the GNSS signals on their way through the Earth's gravity field, also known as *Shapiro effect* or gravitational time delay. According to the IERS standards, the effect (in seconds) can be computed and corrected by the following expression

$$\Delta t_{Shapiro} = \frac{2GM}{c^3} \ln \frac{r^s + r_r + \rho_r^s}{r^s + r_r - \rho_r^s}, \quad (2.26)$$

with

- GM the Earth's gravitational constant,
- c speed-of-light in vacuum,
- r^s geocentric distance of the satellite,
- r_r geocentric distance of the receiver and
- ρ_r^s distance between satellite and receiver.

The impact on individual ranges may reach up to 19 mm (Hofmann-Wellenhof et al., 2008, p. 145). If neglected in the PPP solutions computed for this work, the Shapiro effect caused a pure scale bias of approximately 0.7-0.8 ppb, i.e. a common height offset of all stations of approximately 4.5-5 mm. This is in reasonable agreement with the maximum value of 1 ppb stated by Zhu and Groten (1988).

2.5.2 Ambiguity fixing in PPP

One of the drawbacks of the conventional PPP approach can be seen in the fact, that the carrier phase ambiguities are float values. Consequently, they cannot be constrained to integer values as it is possible

in relative data processing at the level of double differences. The main difference between relative and point positioning, that prohibits integer ambiguity recovery for an isolated receiver, is the possibility to eliminate the satellite clock errors and hardware biases by forming observation differences between receivers. That means, if ambiguities shall be fixed for a single receiver, the satellite clock corrections have to be adjusted in a way that ensures the integer nature of the carrier phase ambiguities. Over the past years, several approaches have been developed that allow to generate satellite clock corrections with such integer properties (Ge et al., 2008; Collins et al., 2008; Laurichesse et al., 2009). In order to study the impact of carrier phase ambiguity resolution on clock estimation and clock modeling, the method presented by Laurichesse et al. (2009) has been implemented and will be briefly outlined in the following.

In the first step, the integer wide-lane ambiguities N_w are determined using the Melbourne-Wübbena linear combination (2.12). In practice, the undifferenced wide-lane ambiguity b_w is not naturally an integer but contains fractional receiver μ_i and satellite μ^j biases. The key to consistently isolate the individual components is the temporal stability of these fractional wide-lane delays. In fact, the satellite fractional wide-lane delays μ^j are usually constant over days and weeks (Ge et al., 2008; Loyer et al., 2012), while the receiver fractional wide-lane delays μ_i for geodetic receivers may change slowly, typically by less than 1 wide-lane cycle per day (Mercier and Laurichesse, 2007).

By averaging the Melbourne-Wübbena observable for each phase coherent observation arc we obtain the following quantity

$$L_{MW} = \lambda_w b_w + \varepsilon = \lambda_w N_w + \mu_i + \mu^j + \varepsilon. \quad (2.27)$$

with

L_{MW}	the Melbourne-Wübbena linear combination of the observations,
λ_w	the wide-lane wavelength,
b_w	the complete float wide-lane ambiguity,
N_w	the integer part of the wide-lane ambiguity,
μ_i, μ^j	the fractional satellite and receiver wide-lane delays, and
ε	the observation noise of the Melbourne-Wübbena linear combination.

Obviously, there is an infinite number of combinations of μ_i , μ^j and N_w fulfilling (2.27). One way to remove this singularity is to select a reference station for which all fractional receiver wide-lane delays μ_i are assumed to be zero. After removing the integer part N_w of (2.27) by rounding we are left with a first set of values of the fractional wide-lane delays of the GPS satellites μ_0^j . These values can then be used to compute the corresponding fractional wide-lane delays of other receivers. In this way, a consistent set of μ_i , μ^j and integer N_w values can be identified for an entire network. During this procedure, differences of +1 or -1 wide-lane cycle for individual observation arcs may occur, which can be easily identified and corrected by comparing the resulting fractional part with other observation arcs of the receiver in question. Finally, a least-squares adjustment can be performed to derive an optimized set of μ^j , but usually the initial set of satellite fractional wide-lane delays μ_0^j is accurate enough to enable a reliable N_w determination. Figure 2.1 shows the fractional N_w ambiguity biases in wide-lane cycles for the Russian IGS station ARTU, that are obtained during the N_w identification process. The figure shows that the fractional receiver wide-lane delay for this station is indeed changing very slowly.

Laurichesse et al. (2009) note that a different set of satellite fractional wide-lane delays μ^j has to be used for receivers that report C/A-code (C1) pseudoranges instead of P1-code pseudoranges, like e.g., Trimble and Novatel/Leica receivers. This is due to the fact that the C1-code exhibits an offset with respect to the P1-code. However, when the difference between the C1-code and the P1-code pseudorange observations is corrected using the P1-C1 differential code biases provided by the Center for Orbit Determination in Europe (CODE), no problems concerning the wide-lane ambiguity determination for the C1/P2 receivers using the same set of μ^j could be identified for the data processed in the context of this work. The second part of the ambiguity-fixed clock determination procedure consists of the identification of the L_1 integer ambiguities N_1 . For this step, precise estimates of the propagation distance between the receivers and the satellites as well as receiver clock offsets are required. Therefore, independent PPP solutions are first

computed for all receivers in the network. The resulting coordinate, receiver clock and zwd estimates for each station can then be used to compute approximate observations L^0 with an accuracy of a few centimeters. Eventually, using (2.9), a reduced ionosphere-free observable L'_3 can be formed as

$$L'_3 = L_3 - L^0 - \frac{f_2^2}{f_1^2 - f_2^2} \lambda_2 N_w = \lambda_c N_1 + h_i - h^j + \varepsilon. \quad (2.28)$$

where λ_c is the narrow-lane wavelength of 10.7 cm.

In Equation 2.28, only the N_1 ambiguity as well as the receiver and transmitter biases h_i and h^j are unknown. The structure of (2.28) is similar to (2.27) with the important difference that the clock-like biases h_i and h^j are neither constant nor slowly changing and thus must be identified for every epoch. Following Laurichesse et al. (2009) this was done by first fixing the h_i and N_1 values of a reference station to zero and computing a first set of fractional satellite clock corrections h^j . Using these values and inserting them into (2.28) for any nearby station, the N_1 ambiguities and receiver fractional biases for this station can be determined.

Figure 2.2 shows the fractional parts of the L_1 ambiguities in narrow-lane cycles for the IGS station ARTU, that are obtained during the N_1 identification process. The figure demonstrates that the fractional receiver narrow-lane bias of this station is very stable in time.

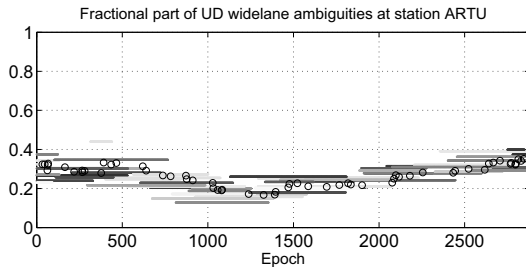


Figure 2.1: Receiver fractional parts of the undifferenced *wide-lane* ambiguities for the IGS station ARTU; the open circles indicate a moving average that is used to identify outliers

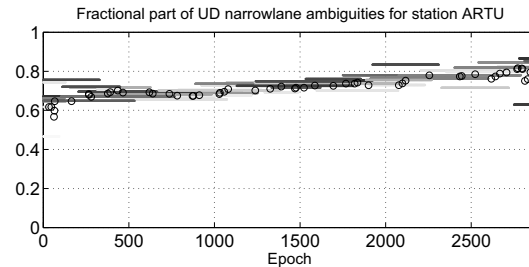


Figure 2.2: Receiver fractional parts of the undifferenced *narrow-lane* ambiguities for the IGS station ARTU; the open circles indicate a moving average that is used to identify outliers

Due to the requirement of significant common satellite observations the distance between consecutively processed stations should not exceed a certain threshold. Figure 2.3 shows an exemplary global network of 40 IGS reference stations, that was used to generate the integer satellite clock corrections for this work. Although, in this network inter-station distances are as large as 4000 km, no problems with the N_1 integer identification procedure were encountered.

After the integer N_1 ambiguities for the neighboring station have been determined, this information can be used to compute the satellite clock corrections, which could not or only badly be determined from the data of the previously processed stations. Of course, care must be taken, to not extend the constant N_1 ambiguities across a carrier phase cycle slip. After processing all stations of the network, which may be regional or global, a consistent set of integer N_1 ambiguities and corresponding satellite clock corrections h^j are obtained. Along with the constant fractional wide-lane ambiguities μ^j , these “integer” satellite clock corrections h^j contain all the information, that is required to fix the carrier phase ambiguities for any receiver within the area covered by the reference network.

Figure 2.4 shows the observation residuals in narrow-lane cycles for the IGS station ARTU, that are obtained after all conventional PPP corrections, ambiguity-fixed receiver clock h_i and satellite clock h^j corrections as well as integer ambiguities N_w and N_1 were subtracted. The residuals are correctly centered around zero and demonstrate the consistency of the derived satellite clock corrections and integer carrier phase ambiguities.

In the following, the incorporation of the ambiguity fixing procedure into the standard PPP processing will be explained. In a first step, the undifferenced wide-lane ambiguities are determined using the frac-

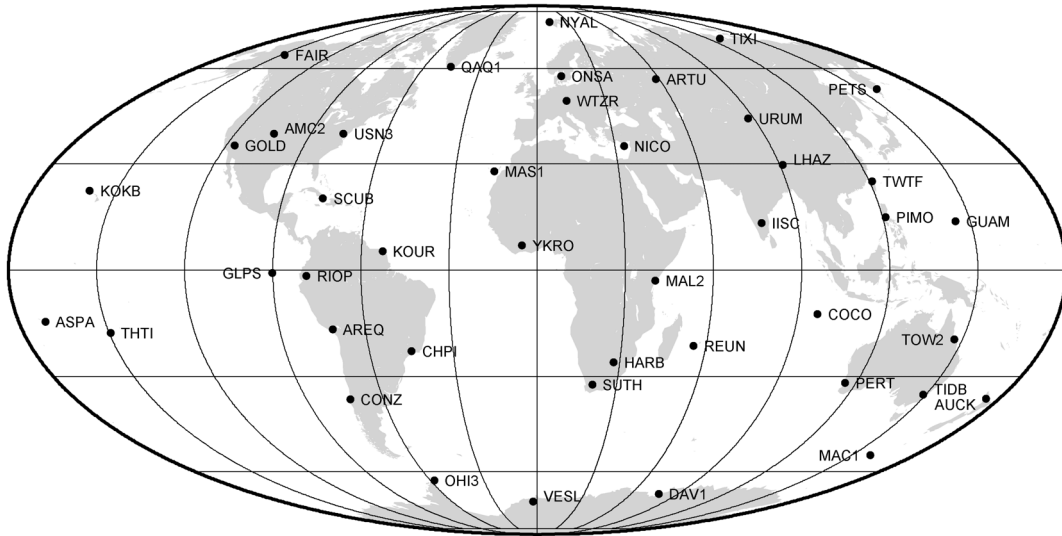


Figure 2.3: Typical global network (~ 40 stations) used for the narrow-lane integer clock generation

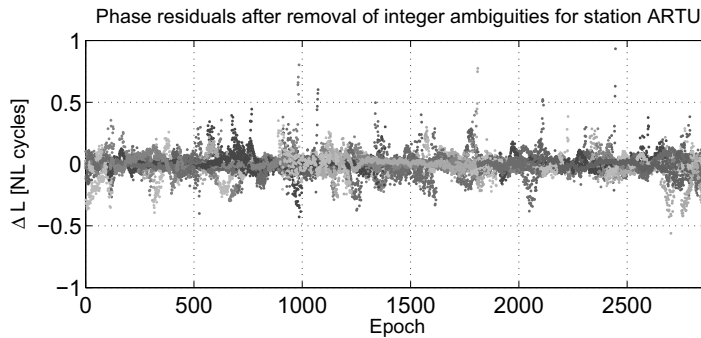


Figure 2.4: L_3 observation residuals of the IGS station ARTU after subtraction of the geometrical distance, integer clocks, fixed wide-lane and narrow-lane ambiguities and the estimated tropospheric delays

tional wide-lane ambiguities μ^j from the network processing outlined above and the Melbourne-Wübbena linear combination of the observations. The resulting integer wide-lane ambiguities are multiplied by the factor $\lambda_2 f_2^2 / (f_1^2 - f_2^2)$ and subtracted from the raw L_3 observations along with the ambiguity-fixed satellite clocks, the geometrical distance and the carrier phase wind-up effect. Using this “observed-minus-computed” vector, the PPP parameter estimation is carried out. The resulting ambiguity estimates are however not integers because they contain an unknown receiver bias. One way to solve this problem is to constrain the ambiguities at the level of single differences between satellites, i.e. not the ambiguities themselves are constrained but the difference with respect to a reference ambiguity. Note, that this approach differs from the one proposed by Laurichesse et al. (2009). The integer constraint imposed on the ambiguities is expressed by pseudo-observations of the following type

$$b_{1,i} - b_{1,ref} = \lambda_c (N_{1,i} - N_{1,ref}) + v, \quad D(v) = \sigma_v^2. \quad (2.29)$$

Note, that at this stage it is assumed, that the fractional narrow-lane delays are identical for all ambiguities. From the experience with the above procedure, it can be concluded that this assumption is usually valid for receivers in the IGS network. However, more work is required to confirm this finding and care must be taken when data of receivers of lower quality shall be processed with the described approach. During the fixing process the reference ambiguity can be tightly constrained to an arbitrary value. Therefore, this and all other ambiguities would not be determined by the pseudorange observations anymore

and the result can be considered as a phase-only solution. As a consequence, the computed clock offsets may exhibit an arbitrary offset with respect to GPS time. In practice, however, the “integer” clocks can be easily leveled to a reasonable value, only limited to integer multiples of the narrow-lane wavelength of 10.6 cm or 0.3 ns which is well below typical time transfer calibration uncertainties.

3 Clock Characterization

The primary goal of this chapter is to infer measures that allow a description of the predictability of the time indicated by different clock types. Therefore, the theory of oscillator frequency stability analysis is going to be reviewed. Starting with the description of a generic oscillator signal, measures of frequency stability in the Fourier frequency and the time domain are introduced.

Much of the fundamental work on oscillator frequency stability is due to Barnes and Allan and dates back to the sixties, e.g. Allan (1966); Barnes et al. (1971). A very good introduction to the time-domain characterization of precision oscillators is given by Allan (1987), while a more comprehensive overview of frequency stability analysis methods is given in Rutman (1978) and Stein (1985). An exhaustive reference with a special focus on practical aspects can be found in Riley (2008). The close relationship between the time-domain measures of frequency stability and n -th order structure functions is discussed by Lindsey and Chie (1976). After having introduced the methods for oscillator frequency stability characterization, some important types of high-precision frequency sources applicable to GNSS transmitters and receivers and the GNSS system time scales will be discussed. In addition the relationship between frequency stability and time prediction uncertainty is addressed. Finally, a widely used algorithm for the simulation of random clock errors proposed by Kasdin and Walter (1992) is described. Based on this algorithm, artificial clock offset time series have been generated, which are later on used to validate the proposed functional and stochastic oscillator models.

3.1 Oscillator signal description

Every clock consists of an oscillator generating a periodic signal and a counter counting the number of oscillations. The fundamental property characterizing the quality of a clock is its ability to produce ticks at precisely repeating intervals which is referred to as its frequency stability. The key features that determine the frequency stability of an oscillator are the periodic physical phenomenon and the techniques used to interrogate its signal. In order to understand the quantities, that are used to describe the frequency stability of an oscillator we have to start with a mathematical description of its signal. The sinusoidal output voltage of any precision oscillator V at a certain time t can be described by

$$V(t) = (V_0 + \epsilon(t)) \sin(2\pi\nu_0 t + \phi(t)), \quad (3.1)$$

where V_0 is the nominal voltage amplitude and ν_0 the nominal frequency; $\epsilon(t)$ and $\phi(t)$ are the time-dependent amplitude and phase fluctuations, respectively. For the following discussion amplitude fluctuations (AM noise) can be safely ignored. Thus, the instantaneous frequency can be defined as

$$\nu(t) = \nu_0 + \frac{1}{2\pi} \frac{d\phi(t)}{dt}, \quad (3.2)$$

where the second part is commonly referred to as instantaneous frequency fluctuation or simply frequency noise

$$\Delta\nu(t) = \frac{1}{2\pi} \frac{d\phi(t)}{dt}. \quad (3.3)$$

This leads to the important dimensionless quantity of normalized or *fractional frequency deviations* $y(t)$

$$y(t) = \frac{\Delta\nu(t)}{\nu_0} = \frac{\nu(t) - \nu_0}{\nu_0}. \quad (3.4)$$

Since the fractional frequency deviation is independent of the nominal frequency used by the specific oscillator or frequency distribution system, it greatly facilitates the comparison of different frequency sources. By integrating the fractional frequency deviations we obtain the phase deviations $x(t)$ in units of time

$$x(t) = \int_0^t y(t') dt', \quad (3.5)$$

i.e. fractional frequency is the derivative of phase (time)

$$y(t) = \frac{dx(t)}{dt}. \quad (3.6)$$

The relationship between the above quantities are summarized in Figure 3.1. In practice, we cannot measure instantaneous frequency but only an average frequency \bar{y} over a finite time interval τ . This is usually done by measuring phase or time differences $x(t)$ between clocks and differencing these observations

$$\bar{y}\tau = \frac{x(t+\tau) - x(t)}{\tau}, \quad (3.7)$$

where the numerator is often referred to as first difference or first increment of phase (time).

A final remark concerns the reference for the frequency deviations. Because there is no true reference time standard we can only measure differences between clocks. In case one of the clocks is much more precise than the other or one clock is compared to the mean of several clocks that are at least as precise, we may, however, still be able to characterize a single clock. We will come back to this issue in Section 3.6 when discussing the time scales related to GNSS.

Based on the quantities $x(t)$ and $y(t)$, measures of frequency stability can be defined. These are introduced in the following two sections.

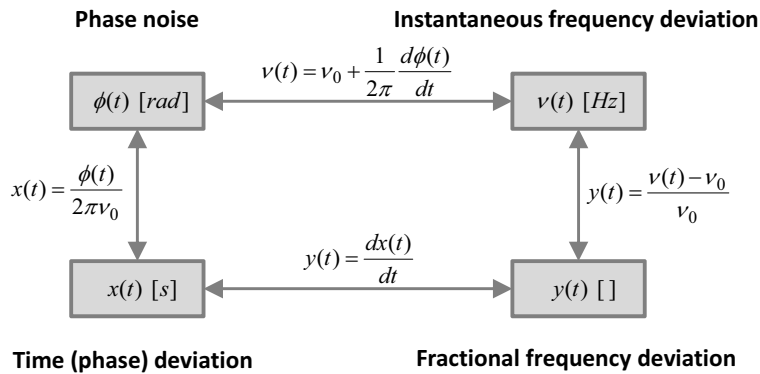


Figure 3.1: Relationship of quantities used to describe random clock instability

3.2 Measures of frequency stability in the Fourier frequency domain

The spectral density $S_y(f)$ of the random frequency fluctuations $y(t)$ for a precision oscillator can usually well be approximated by the sum of five *power-law noise types* with integer exponents α ranging from -2 to 2

$$S_y(f) = \sum_{\alpha=-2}^2 h_\alpha f^\alpha, \quad (3.8)$$

where f is the Fourier frequency and h_α is the intensity of the particular noise type (Barnes et al., 1971). The five power-law noise types are referred to as white phase noise or modulation (WPM), flicker phase noise (FPM), white frequency noise (WFM), flicker frequency noise (FFM) and random walk frequency noise (RWFN). If plotted on a double-logarithmic scale, every power-law noise process will result in a straight line with slope α , e.g. the power spectral density (PSD) of a white frequency noise process ($\alpha = 0$) is a constant, while the PSD of flicker frequency noise ($\alpha = -1$) varies as f^{-1} . The power-law noise model and the h_α coefficients allow a compact description of the frequency stability characteristics of high-precision oscillators and were used in this work as input values for noise simulation and the stochastic clock model in the Kalman filter. In Figure 3.2 typical time series of white, flicker and random walk noise are plotted. Note, that the random walk process is integrated white noise, i.e. white frequency noise $y(t)$ results in a random walk noise in phase $x(t)$. Similarly to the spectral density of the frequency fluctuations $S_y(f)$ we can define the spectral density of the phase or time fluctuations $x(t)$

$$S_x(f) = \frac{1}{4\pi^2} f^{-2} S_y(f) = \frac{h_\alpha}{4\pi^2} f^{\alpha-2} = \sum_{\beta=-4}^0 g_\beta f^\beta. \quad (3.9)$$

This representation is used, for example, in the derivation of the power-law noise simulation algorithm presented in Section 3.8.

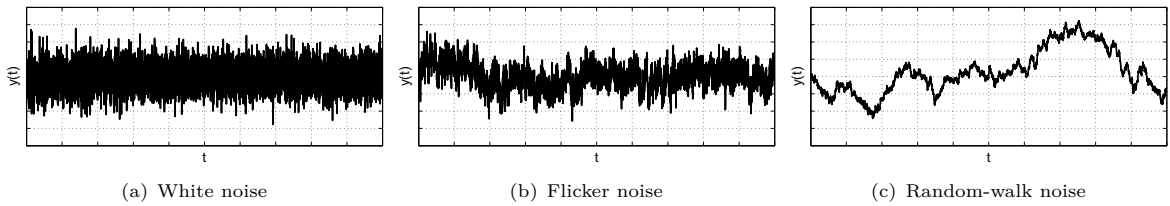


Figure 3.2: Typical time-domain behavior of power-law noise types

3.3 Measures of frequency stability in the (averaging-) time domain

In addition to the characterization of the clock frequency noise by means of the power spectral density, it is common to express the frequency stability in the time domain, or more precisely over a range of averaging times. Time-domain measures are typically used if the time interval of interest is larger than 1 second (Winkler, 1976). The most important of these measures is the so called *Allan variance* $\sigma_y^2(\tau)$. The Allan variance is defined as the infinite time average of the squared difference of consecutive fractional frequency values \bar{y}^τ averaged over a certain time interval τ , referred to as averaging time, i.e.

$$\sigma_y^2(\tau) = \frac{1}{2} \left\langle (\Delta \bar{y}^\tau)^2 \right\rangle, \quad (3.10)$$

where the brackets $\langle \dots \rangle$ denote an infinite time average. By varying the averaging time τ , different values of the Allan variance are obtained. Thus, the Allan variance is not a single value but rather a function of the averaging time τ .

It is interesting to note, that the Allan variance may be viewed as the Kolmogorov structure function of the fractional frequency deviations. Extending the concept of structure function to higher order, i.e. n -th differences, the Allan variance may also be denoted as the structure function of the 2nd differences of the time deviations or simply the 2nd structure function of time (phase) (Lindsey and Chie, 1976).

The advantage of analyzing higher-order differences, is that these may be stationary while the original process is not. This property is utilized e.g. in the Hadamard variance described below.

For a finite number of time differences N taken at the interval τ_0 an estimate of the Allan variance can be obtained using the following expression

$$\hat{\sigma}_y^2(\tau) = \frac{1}{2(N-2)} \sum_{k=1}^{N-2} (\bar{y}_{k+1}^\tau - \bar{y}_k^\tau)^2, \quad (3.11)$$

with \bar{y}_k^τ being adjacent fractional frequency values averaged over the interval $\tau = n\tau_0$, i.e.

$$\bar{y}_k^\tau = \frac{1}{n} \sum_{i=k}^{k+n-1} \bar{y}_i^{\tau_0} = \frac{x_{k+n} - x_k}{\tau}. \quad (3.12)$$

An equivalent form that uses the second differences of the time difference measurements $x(t)$ is given by

$$\hat{\sigma}_y^2(n\tau_0) = \frac{1}{2n^2\tau_0^2(N-2)} \sum_{i=1}^{N-2} (x_{i+2} - x_{i+1} + x_i)^2, \quad (3.13)$$

where x_i and x_{i+1} are spaced by $\tau = n\tau_0$. Sesia and Tavella (2008) show that (3.13) provides a much more robust estimate of $\sigma_y(\tau)$ in the presence of outliers and gaps in the data.

In order to increase the confidence of the Allan variance estimate, it can be computed from overlapping samples. The estimator of the overlapping Allan variance reads

$$\hat{\sigma}_y^2(n\tau_0) = \frac{1}{2n^2\tau_0^2(N-2n)} \sum_{i=1}^{N-2n} (x_{i+2n} - 2x_{i+n} + x_i)^2. \quad (3.14)$$

Although the overlapping samples are not statistically independent, the confidence of the estimate is increased. Therefore, the overlapping Allan variance is the recommended time-domain measure of frequency stability for most applications (Riley, 2008). Empirically derived expressions to compute confidence intervals for the overlapping Allan variance using noise-specific degrees of freedom can be found in e.g. Stein (1985).

As the well-known standard deviation is the square root of the variance, the Allan deviation $\sigma_y(\tau)$ is defined as the square root of the Allan variance $\hat{\sigma}_y^2(\tau)$ and is often the preferred quantity. The Allan variance and Allan deviation are not only convergent for all power-law noise types typically encountered in oscillator signals but also allow to identify the dominant noise type from their slope plotted on a double-logarithmic scale. Figure 3.3 shows a schematic representation of the 5 power-law noise types in the Allan deviation plot. Note, that the conventional Allan variance or Allan deviation yield the same slope for white phase and flicker phase noise. Although initially developed for the characterization of atomic clocks, the Allan deviation has been used in various applications in other field, e.g. bias stability characterization of gyroscopes (El-Sheimy et al., 2008).

In the past, other time-domain frequency stability measures have been proposed that resolve some of the limitations of the classical Allan variance. We want to briefly discuss two of them.

The modified Allan Variance In contrast to the conventional Allan variance, the modified Allan variance allows to distinguish between white phase noise and flicker phase noise. As can be seen from Table 3.1, flicker phase noise depends on the hardware bandwidth times the averaging times $f_h \cdot \tau$ whereas white phase noise depends only on f_h . This property can be used to define a modified Allan variance, that removes the ambiguity with respect to these two noise types by varying an artificial software bandwidth. The resulting stability measure $\text{Mod } \hat{\sigma}_y^2(n\tau_0)$ varies with τ^{-3} for white phase noise and τ^{-2} for flicker phase noise. The standard Allan variance exhibits a slope of -2 for both noise types. The modified Allan variance can be estimated using the following expression

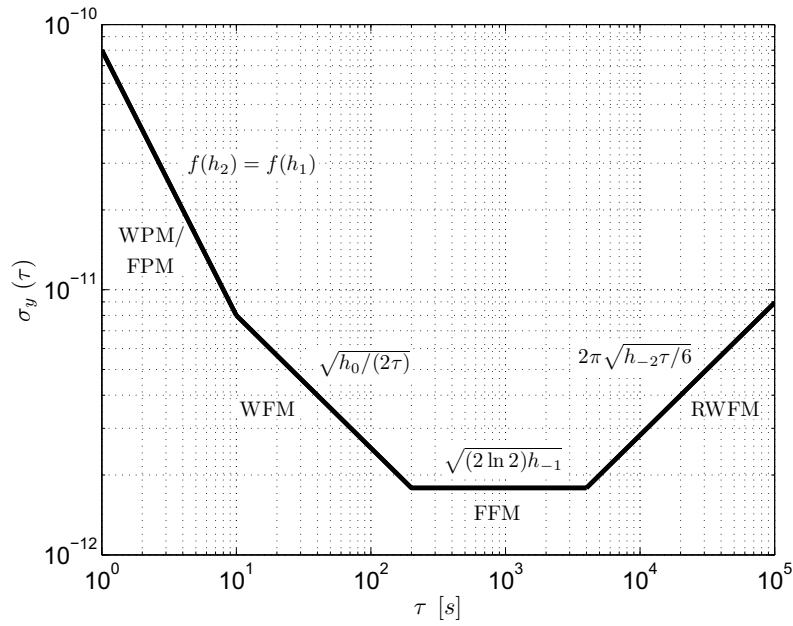


Figure 3.3: Schematic plot of the Allan deviation for common oscillator noise types: white phase (slope -1), flicker phase (slope -1), white frequency (slope -1/2), flicker frequency (slope 0) and random walk frequency modulation (slope +1/2)

$$\text{Mod } \hat{\sigma}_y^2(n\tau_0) = \frac{1}{2n^4\tau_0^2(N-3n+1)} \sum_{j=1}^{N-3n+1} \left(\sum_{i=j}^{j+n-1} (x_{i+2n} - x_{i+n} + x_i) \right)^2 \quad (3.15)$$

and equals the standard Allan variance for $n = 1$, i.e. $\tau = \tau_0$. For $n > 1$, the modified Allan variance is generally smaller than the conventional Allan variance and its primary purpose is the described distinction of white and flicker phase noise.

The Hadamard Variance is based on 2nd differences in frequency and 3rd differences in phase, respectively, making it insensitive to a constant frequency drift. This feature is often useful when analyzing rubidium atomic clocks (Riley, 2008). The formula of the (non-overlapping) Hadamard variance is

$$H\hat{\sigma}_y^2(n\tau_0) = \frac{1}{6n^2\tau_0^2(N-3)} \sum_{i=1}^{N-3} (x_{i+3} - 3x_{i+2} + 3x_{i+1} - x_i)^2, \quad (3.16)$$

where x_i and x_{i+1} are again spaced by $\tau = n\tau_0$.

3.4 Relationship between Allan variance and power spectral density

Although for our purpose the Allan deviation is the most widely used measure of frequency stability, it is at times useful to be able to convert from PSD to Allan deviation and vice versa, e.g., if PSD coefficients h_α are to be derived from a given Allan variance. The conversion formula from power spectral density to Allan variance is given e.g. by (Rutman, 1978) as

$$\sigma_y^2(\tau) = \int_0^\infty S_y(f) \frac{2 \sin^4 \pi \tau f}{(\pi \tau f)^2} df, \quad (3.17)$$

Noise type	$S_y(f)$ slope α	$S_y(f)$	$\sigma_y^2(\tau)$	$\sigma_y^2(\tau)$ slope	$\sigma_y(\tau)$ slope
White PM	2	$h_2 f^2$	$\frac{3h_2 f h}{4\pi^2 \tau^2}$	-2	-1
Flicker PM	1	$h_1 f^1$	$\frac{3h_1 \ln(2\pi f h \tau)}{4\pi^2 \tau^2}$	-2	-1
White FM	0	h_0	$\frac{h_0}{2\tau}$	-1	-1/2
Flicker FM	-1	$h_{-1} f^{-1}$	$2h_{-1} \ln 2$	0	0
Random walk FM	-2	$h_{-2} f^{-2}$	$\frac{2\pi^2}{3} h_{-2} \tau$	+1	+1/2

Table 3.1: Relationships between PSD $S_y(f)$ and Allan variance $\sigma_y^2(\tau)$ for different power-law noise types

whereas no general expression for the conversion from the time to the frequency domain is available. However, if we restrict ourselves to the specific power-law noise model (3.8), which is commonly used to describe the noise spectra of precision oscillators, simple conversion formulas can be obtained (cf. Barnes et al., 1971), that allow to convert in both directions. Table 3.1 summarizes the specific conversion formulas for the five noise types.

3.5 High-precision frequency standards

In the following sections an overview of the current state-of-the-art high-precision frequency sources is provided. In addition to the classical atomic clocks operating in the microwave domain, the promising developments in the area of optical atomic clocks will be discussed. A separate paragraph is devoted to high-precision clocks for space applications. Apart from some very basic technical characteristics, the focus in this section is on the frequency stability of the different oscillators and their suitability for an integration into GPS applications. The Allan deviation of the most important oscillators that are described below are shown in Figure 3.5. A compact introduction to the physics and technical realizations of the different atomic clocks can be found in, e.g., Bauch (2007) or McCarthy and Seidelmann (2009).

3.5.1 Quartz oscillators

Quartz crystal oscillators (XO) are the standard oscillators in GPS receivers and many other electronic devices. Quartz oscillators can be made extremely small and cheap while still providing satisfactory frequency stability for many applications including GNSS signal tracking. Due to their flicker frequency noise characteristic, temperature sensitivity and relatively large frequency aging, they are generally not classified as high-precision oscillators. Typical frequency stabilities of quartz oscillators used in GPS receivers are around $\sigma_y(\tau) \approx 1 \times 10^{-9}$ at $\tau = 1$ s (e.g. Brown and Hwang, 2005). However, certain types of sophisticated quartz oscillators exhibit short-term (<100 s) frequency stabilities comparable with or even superior to atomic frequency standards. For example commercial oven-controlled quartz oscillators (OCXO) offer frequency stability up to $\sigma_y \approx 1 \times 10^{-12}$ for averaging times between 1 and 100 s (Symmetricom Inc., 2012). So called ultra-stable oscillators may even reach a few parts in 10^{-13} up to 1000 s (Weaver et al., 2010). Unfortunately, no OCXO data was available for this investigation but the modeling of an USO is going to be discussed in the context of the GRACE mission (cf. Sections 3.5.4 and 7.4).

3.5.2 Microwave atomic clocks

Almost all current high-precision atomic clocks operate in the microwave domain. That means, the characteristic transition frequency that is emitted or absorbed when an electron changes between two hyperfine levels of an atomic species is interrogated with a microwave signal. Basically all of these clocks are using either Cesium-133, Rubidium-87 or Hydrogen-1 atoms. The basic mode of operation of all atomic clocks is the same in the sense that a microwave signal usually generated by a quartz oscillator is adjusted to be in resonance with the characteristic transition frequency. However, various technical realizations exist. While cesium standards are mostly beam devices, rubidium clocks typically employ the gas cell technology. Active hydrogen masers in turn are related to beam standards but make use of stimulated emission within a cavity that is precisely tuned to the wavelength of the resonant frequency. The potential frequency stability of an atomic oscillator is primarily determined by the employed *resonance frequency* and the *resonance width* of the particular clock transition. The resonance frequency divided by the resonance width is called the *quality factor* or simply *Q*. A high resonance frequency in combination with a narrow resonance width yields a high *Q*, i.e. a very stable clock signal. Apart from the *Q*-factor, the stability of an atomic oscillator is mainly determined by the sensitivity of the clock transition to environmental influences such as temperature, magnetic and electric field variations and quantum-physical effects such as collisions of the atoms.

Due to their good long-term stability, *cesium atomic frequency standard* are mainly used as primary frequency standards where accurate absolute frequency is required, such as national timing laboratories. The best, commercially available cesium beam frequency standards reach a frequency stability of $\sigma_y(\tau) \approx 3 - 4 \times 10^{-12}$ at $\tau = 10$ s averaging time and exhibit white frequency noise down to a level of approximately $\sigma_y(\tau) \approx 1 \times 10^{-14}$ beyond one day averaging time (Symmetricom Inc., 2012). Apart from these portable cesium clocks, several laboratory cesium frequency standards with superior performance have been developed, the most accurate of which are the so called fountain clocks. These clocks provide the best frequency stability in the long term and since they are based on the specific transition used for the definition of the SI second, they play an important role for the realization of the rate of the International Atomic Time (TAI). At subdaily averaging times the frequency stability of cesium fountains is comparable to active hydrogen masers (see below), but fountain clocks are usually not operated continuously.

Rubidium atomic clocks are usually considered as secondary standards, because they do not realize the definition of the SI second and their frequency tends to drift over time. The importance of rubidium clocks is due to the fact, that they can be built much smaller, cheaper and with lower power consumption than cesium or hydrogen frequency standards. For example, the first commercial chip-scale atomic clock (CSAC) is based on a rubidium gas cell. Despite its size of only 16 cm^3 , it offers a remarkable stability of $\sigma_y = 1.5 \times 10^{-10} \tau^{-\frac{1}{2}}$ (Symmetricom Inc., 2012). The short-term frequency stability of conventional Rb oscillators typically ranges from $\sigma_y(\tau) = 3 \times 10^{-11}$ to $\sigma_y(\tau) = 1 \times 10^{-12}$ at $\tau = 1$ s averaging time, depending on the particular design (e.g. Symmetricom Inc., 2012; Stanford Research Systems Inc., 2012). Therefore, the frequency stability of Rb oscillators is usually ranked between OCXOs and cesium atomic clocks. On the other hand the rubidium clocks on board of the latest generation of GPS satellites have demonstrated performance at the same level as a passive hydrogen maser (Montenbruck et al., 2011). Due to their portability and modest power requirements, several studies on the usage of Rb frequency standards for clock-aided GPS navigation applications have been performed (Bednarz and Misra, 2006; Misra, 1996). For clock modeling at the carrier phase level, which is investigated in this work, commercial rubidium clocks can usually not be used since their frequency signal does not meet the required stability (cf. Section 4.5).

The third type of microwave atomic clock is the *hydrogen maser* (H-maser). The word maser is derived from the abbreviation for Microwave Amplification by Stimulated Emission of Radiation. Hydrogen maser frequency standards can be divided into active and passive devices. The more popular active H-maser provides by far the most stable frequency of all commercial atomic clocks. Similar to a laser, the active maser is based on stimulated emission of radiation. Hydrogen atoms in a pre-selected energy state are injected into a microwave cavity, precisely tuned to the resonant frequency of the atomic transition. In this cavity the hydrogen atoms are stimulated to decay to a lower energy level and thereby emit phase

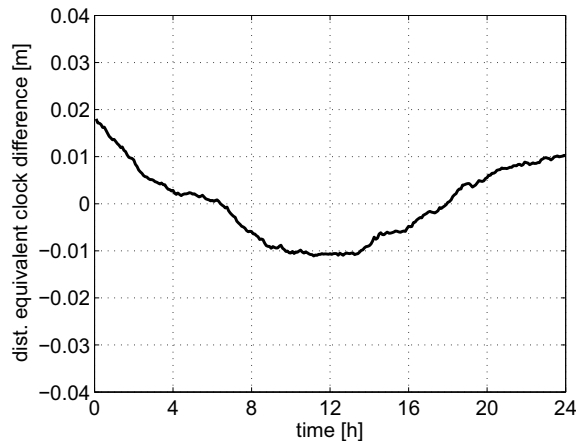


Figure 3.4: Time difference between two active hydrogen masers during a 24 hr period scaled to meters. A linear drift is removed. The time series was generated by integrating average fractional frequency differences over 5 min intervals; *Courtesy of Andreas Bauch (PTB)*

coherent radiation in the microwave domain which in turn stimulates the same transition in other atoms. If the losses are small and the atom density is high enough, a self-sustaining coherent oscillation starts. A small part of the radiation can then be extracted and amplified. A quartz crystal is locked to this stable cavity signal and forms the maser frequency output. Although the frequency of the hydrogen clock transition of approximately 1.4 GHz is lower than those of rubidium and cesium, the frequency produced by a hydrogen maser is generally more stable because its resonance width is very small, which results in a high Q-factor. A typical characteristic of the active H-maser is the white phase noise, which dominates the maser signal up to averaging times of 10-100 s. The Allan deviation of active hydrogen masers is typically around $\sigma_y(\tau) \approx 2 \times 10^{-13}$ at $\tau = 1$ s averaging time and reaches a floor of $\sigma_y(\tau) = 1-3 \times 10^{-15}$ at 1-2 hours averaging time. Due to this outstanding frequency stability for periods up to one day, active hydrogen masers are used for time tagging the observations of radio telescopes in Very Long Baseline Interferometry (VLBI) and as highly precise fly-wheel oscillators that are steered to cesium clocks in order to realize a time scale with the best stability at both short and long term. Active hydrogen maser frequency standards are the most important oscillators for the investigations presented in this work. This is not only because they provide the required frequency stability, but also because hydrogen masers are connected to GPS receivers at a number of IGS stations located at timing laboratories and VLBI sites. Unfortunately, the size, weight and power consumption generally impedes the usage of active hydrogen masers in mobile applications, not to mention the sensitivity to environmental influences.

In passive hydrogen masers, the clock signal does not oscillate by itself, but the atomic transition is stimulated by an external 1.42 GHz signal. This configuration allows to work with a lower atom density and a smaller and simpler cavity. Consequently, passive H-masers can be built smaller and cheaper than their active counterparts but their frequency stability is also significantly worse. For example, the model VCH1006 built by the Russian company Vremya CH, weighs around 30 kg and consumes 80 W of power. According to the manufacturer's specifications, the passive maser provides a short-term frequency stability of $\sigma_y(\tau) = 7 \times 10^{-13} \cdot \tau^{-\frac{1}{2}}$ for averaging times between 1 and 1000 s (Vremya-CH, 2012), thus being the most stable commercially available, portable frequency standard currently available. However, portable in this context means, that it can be easily transported from one laboratory to another, the usage of the maser in a navigation application is certainly limited by the environmental sensitivity and power requirements.

In Figure 3.4 the time difference between two active hydrogen maser frequency standards is depicted. At least one of the masers exhibits a significant frequency drift, which causes the quadratic shape of the time difference. From this figure it is clear that the time error of this type of oscillator varies smoothly from epoch to epoch and can well be approximated by a continuous function.

3.5.3 Optical atomic clocks

In recent years, progress in laser technology for cooling atoms and interrogation of optical transition frequencies enabled the development of a new generation of highly precise clocks, that operate at the frequency of visible or ultraviolet light. In addition, the realization of the *femtosecond frequency comb* has greatly facilitated the measurement of optical frequencies. Generally, there are two concepts of optical clocks under development today, namely single ion clocks and optical lattice clocks.

Single ion clocks take advantage of the low disturbances acting on an isolated ion that is confined in a Paul trap but have a low signal to noise ratio. By using many neutral atoms trapped in an optical lattice, the signal to noise ratio can be significantly increased (Gill, 2005). However, the operation of such lattice clocks is more complex. Various ions are currently investigated for the use in optical clocks. The most promising candidates are $^{88}\text{Sr}^+$, $^{199}\text{Hg}^+$, $^{171}\text{Yb}^+$ and $^{27}\text{Al}^+$. One of the best frequency stabilities to date ($\sigma_y = 4 \times 10^{-15} \tau^{-\frac{1}{2}}$) has been reported for a comparison between two optical clocks based on $^{199}\text{Hg}^+$ and $^{27}\text{Al}^+$ ions (Rosenband et al., 2008). For practical ground and space applications, currently single ion clocks are favored due to their higher technical maturity and simpler construction. However, as the technological development of optical lattice clocks is progressing, this might change in the future. Feasibility studies investigating the installation of optical clocks at ground stations of the ESA deep space network have already been performed (Gill et al., 2007). At the time of writing, however, the operation of optical clocks is still in an experimental phase and usage in practical applications such as GNSS cannot be expected within the next decade.

3.5.4 High-precision oscillators for space applications

Although the focus of this thesis is placed on ground clocks, some promising developments in the field of high-precision oscillators for space applications shall also be mentioned here. The first high-precision oscillator brought into space was a hydrogen maser within the Gravity probe A experiment. Although the actual flight-time was less than 2 hours, several relativistic effects could be successfully tested (Vessot et al., 1980). With the advent of satellite navigation systems such as GPS and GLONASS, numerous cesium and rubidium oscillators have been put into orbit with frequency stabilities around $\sigma_y(\tau) = 1 \times 10^{-11} \cdot \tau^{-\frac{1}{2}}$ and slightly better for the newer generation of GPS satellites (Senior et al., 2008). The latest big step with respect to the frequency stability of GNSS satellite clocks was the launch of the second Galileo test satellite GIOVE B in 2008, which carries for the first time a space-qualified passive hydrogen maser (PHM). Based on ground tests of this oscillator a frequency stability of $\sigma_y(\tau) = 6 \times 10^{-13} \cdot \tau^{-\frac{1}{2}}$ for averaging times between 10 and 10000 s has been reported (Waller et al., 2009). Although precise analysis of the in-orbit performance up to now suffer from the sparse ground tracking network, the stability of this clock seems to be well below its specifications of $\sigma_y(\tau) = 1 \times 10^{-12} \cdot \tau^{-\frac{1}{2}}$. It is interesting to note, that the rubidium clocks on board of the latest generation of GPS satellites (Block IIF) seem to achieve a very similar performance as the PHM on GIOVE B (Montenbruck et al., 2011).

Another project, that will bring high-precision oscillators into space is the ACES (Atomic Clock Ensemble in Space) mission (Salomon et al., 2001), which is to be installed on board of the International Space Station (ISS). The clocks under development within the framework of this mission are a space-qualified active hydrogen maser and a cold atom cesium clock with an expected outstanding frequency stability of $\sigma_y(\tau) = 3 \times 10^{-16}$ at one day averaging time.

Apart from the afore-mentioned atomic clocks, several space missions use or have been using so called ultra-stable oscillators (USO) to support measurement equipment and communication. A particularly interesting mission in this context is the Gravity Explorer And Climate Experiment (GRACE), which consists of two satellites in a near-polar low Earth orbit. Both GRACE spacecrafts are equipped with two high-quality GPS receivers that are connected to an USO with a frequency stability of $\sigma_y(\tau) = 1-3 \times 10^{-13}$ between 1 and 1000 s (Dunn et al., 2003). In Section 7.4 of this work, GPS data of the GRACE satellites will be used to analyze potential improvements of kinematic orbit determination through clock modeling of the onboard USO.

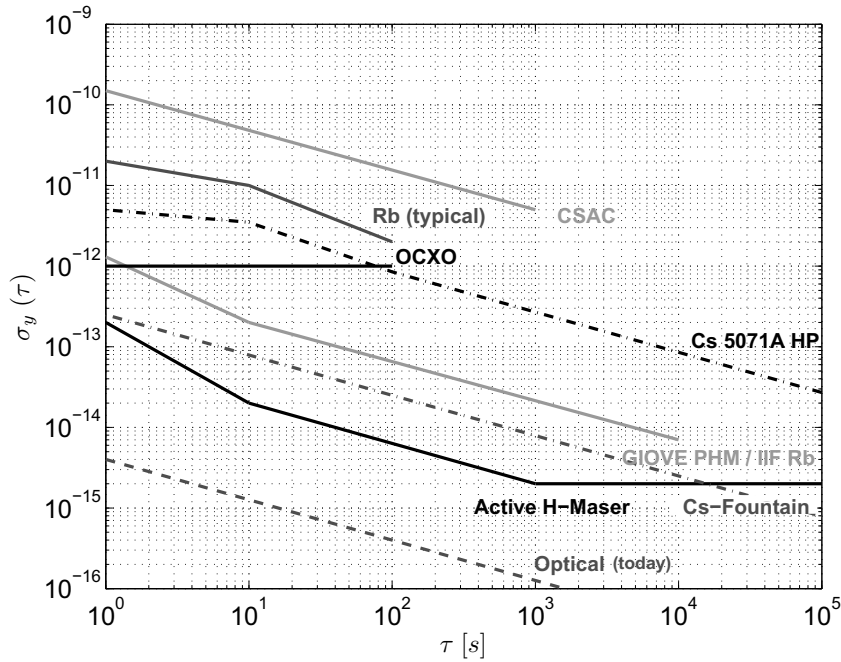


Figure 3.5: Allan deviation for selected high-precision frequency standards. The values for the oven-controlled quartz crystal oscillator (OCXO), the Chip-Scale Atomic Clock (CSAC) and the 5071A high-performance commercial cesium beam clock were taken from the Symmetricom website (Symmetricom Inc., 2012). The values for the rubidium standard are based on the specifications of the model PRS10 by SRS (Stanford Research Systems Inc., 2012). The frequency stability of the active hydrogen maser refers to the model VCH-1003A (Vremya-CH, 2012). The cesium fountain values correspond to the values for the difference between the fountains CSF1 and CSF2 of PTB given by Gerginov et al. (2010). Values of the ground test of the GIOVE B passive H-maser and the GPS Block IIF Rb standards are taken from Montenbruck et al. (2011). The frequency stability for the optical clock is based on Rosenband et al. (2008).

3.5.5 Summary of high-precision frequency standards

The typical frequency stability in terms of Allan deviations for different types of high-precision oscillators that have been described above, are shown in Figure 3.5. One can see a large dispersion of the frequency stability between the different oscillator types, spanning almost 4 orders of magnitude. Furthermore, we can see that the atomic frequency standards typically exhibit a slope of $-1/2$ between 10 s and a few hours, i.e. they are predominantly affected by white frequency noise at these time intervals. We will come back to this plot, when we will have defined the frequency stability requirements for clock modeling in GNSS. Finally, Table 3.2 shows typical spectral density coefficients h_α for different oscillator types. These values will be used later on to derive the process noise for the clock states in a Kalman filter based GNSS data analysis.

Oscillator type	h_0	h_{-1}	h_{-2}	source
Active H-maser	1×10^{-26}	3×10^{-30}	-	converted, Vremya-CH (2012)
Passive H-maser	1×10^{-24}	4×10^{-29}	-	converted, Vremya-CH (2012)
Rb	5.3×10^{-22}	-	1.2×10^{-31}	Vernotte et al. (2001)
USO	-	1.6×10^{-25}	1.4×10^{-29}	Vernotte et al. (2001)
TCXO	2×10^{-19}	7×10^{-21}	2×10^{-20}	Brown and Hwang (2005, p.431)

Table 3.2: Typical h_α coefficients for a number of high-precision oscillators

3.6 The time scales TAI, GPS Time and IGS Time

As discussed previously, GPS and other GNSS are based on one way ranging, thus requiring a synchronization of transmitter and receiver clocks with respect to a common time scale. Since the observed time offset of a particular clock can only be as good as the chosen time reference, the system time scale plays an important role in GNSS clock modeling when processing data of a single receiver. In contrast, for clock modeling in differential mode, only two or more stable receiver clocks are required, whereas the impact of the system time scale is eliminated.

The fundamental time scale for satellite geodesy and the current ITRF is Terrestrial Time (TT). As a uniform time scale, it can be used, for example, as the independent variable in the equation of motion of artificial Earth satellites. TT is defined as the time of an ideal clock on the rotating geoid and is realized by the International Atomic Time (TAI). By definition TT and TAI differ by an offset of 32.184 s. The realization of TAI is based on the comparison of a large number of globally distributed atomic clocks. For everyday usage and legal matters the Coordinated Universal Time (UTC) has been introduced. The rate of UTC agrees with TAI but additional leap seconds are inserted in order to keep the difference between UTC and the mean solar time UT1, which is related to the rotation of the Earth, below 0.9 s. When using GPS broadcast orbit and clock information the reference time scale is GPS time (GPST), which is derived from a limited number of atomic clocks in the GPS ground control segment and the GPS satellites themselves and which is steered to the UTC realization of the US Naval Observatory UTC(USNO). As opposed to UTC, GPS time is continuous, i.e. no leap seconds are inserted. Consequently, the nominal offset between GPS time and UTC is changing by a variable number of integer seconds whereas the offset between GPS time and TAI remains constant at 19 seconds, apart from inevitable differences due to their individual realizations. A comprehensive discussion of the various time scales and their applications is given e.g. by Montenbruck and Gill (2000) or Seeber (2003).

The practical realization of a time scale can either be the output signal of an individual clock or an ensemble average derived from the differences of several clocks. Examples for the first type are typically local UTC realizations such as UTC(PTB) which was realized by the primary cesium beam frequency standard CS2 for about 20 years until it was replaced by a steered hydrogen maser in February 2010. Ensemble time scales may either be formed in real-time by steering a single frequency standard based on observed differences to other clocks or it may be computed post facto, as a so called *paper time scale*. In the later case, there is no clock that shows this time. TAI, GPS time and the IGS time scales discussed below are such paper time scales.

Since November 2000 (GPS week 1087) the IGS provides clock products with 5 min resolution in a dedicated Clock RINEX file format. Initially the IGS clock products were linearly aligned to broadcast GPST on a daily basis. Subsequently, the IGS clock products were re-aligned with respect to the newly developed IGS rapid and final time scales (IGRT) and (IGST), respectively. These time scales are a weighted ensemble average of the IGS clock estimates. A detailed description of the Kalman filter based ensemble algorithm can be found in Senior et al. (2003). In essence, fractional frequency values for each clock are combined by the 2-state Kalman filter to form a frequency offset time series with respect to the original time scale which is GPST in this case. This time series is then integrated and subtracted from the original clock time series referenced to GPS time. However, before subtraction, the integrated time scale is loosely steered to GPS time. Consequently, the resulting time scale is more stable than any individual clock in the IGS network in the short term, but maintains a close link to GPS time in the medium to long run.

Due to the stable underlying time scales, the IGS products are expected to form an ideal basis for the clock modeling approach proposed in this work. However, PPP solutions with the ephemerides and satellite clock corrections of the IGS analysis center CODE, where a single selected H-maser clock from the IGS network serves as the time reference of the satellite clocks, showed comparable results. Thus the proposed clock modeling technique appears not to be limited to the use of IGS products.

Although the IGS time scale comprises cesium and rubidium clocks of both reference stations and GPS satellites, it is largely dominated by 15-25 well-maintained hydrogen maser ground clocks. Figure 3.6 shows the distribution of the stations in the IGS network that are nominally equipped with active

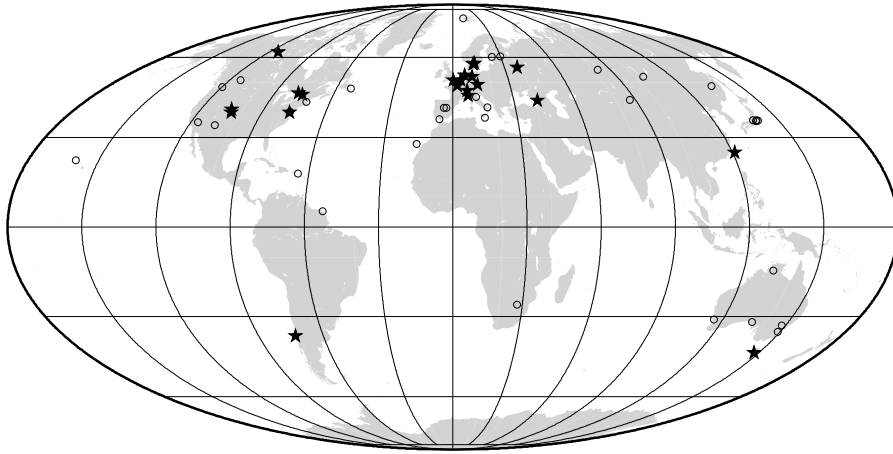


Figure 3.6: Distribution of H-maser clocks in the IGS reference station network as of March 2012. Solid stars indicate stations that usually provide excellent receiver clock stability and data quality and thus frequently get high weights in the IGS time scale algorithm

hydrogen maser clocks. Stations that reliably provide excellent frequency stability are marked by solid stars. The vast majority of H-maser stations are located in the northern hemisphere, especially in Central Europe and the US. Consequently, the global coverage considering the H-maser stations alone is very poor, although the overall number of H-maser stations in the IGS network is remarkable.

3.7 Clock time prediction and modeling errors

In addition to the characterization of the frequency stability, the Allan deviation can also be used to approximate the accumulated time error of a clock, i.e. the error of the predicted clock reading at some time in the future due to random frequency errors. This is important for many engineering applications including GNSS clock modeling.

Generally, the time error of a clock $x(t)$ with respect to an ideal reference time scale can be described by the following expression (Allan, 1987)

$$x(t) = x_0 + y_0 \cdot (t - t_0) + \frac{1}{2}d_0(t - t_0)^2 + \varepsilon, \quad (3.18)$$

with

- x_0 an initial time offset,
- y_0 a constant frequency offset,
- d_0 a constant frequency drift, and
- ε the integrated random frequency errors.

For a complete uncertainty evaluation of predicted clock time errors, the uncertainty of the initial time synchronization, frequency offset and drift values, which are derived from past measurements would need to be taken into account. In the case of clock modeling, however, the clock error is fitted and not predicted, i.e. the time and frequency offset are estimated and do not contribute to the residual error. Although there are types of oscillators or individual units with a frequency drift d_0 that can be treated constant over long time periods, often the frequency drift changes at shorter timescales or is very small. Therefore, we will neglect systematic frequency drift all together and focus on the random frequency error part ε . According to Allan (1987), the following relationship holds for the time prediction error $RMS_x(\tau_p)$ caused by random clock errors ε for the case of white and random-walk frequency noise:

Noise type	$RMS_x(\tau_p)$	asymptote
White PM	$\tau_p \cdot \sigma_y(\tau_p)/\sqrt{3}$	<i>constant</i>
Flicker PM	$\approx \tau_p \cdot \sigma_y(\tau_p)\sqrt{\ln \tau_p / \ln 2}$	$\sqrt{\ln \tau_p}$
White FM	$\tau_p \cdot \sigma_y(\tau_p)$	$\tau_p^{1/2}$
Flicker FM	$\tau_p \cdot \sigma_y(\tau_p)/\sqrt{\ln 2}$	τ_p
Random walk FM	$\tau_p \cdot \sigma_y(\tau_p)$	$\tau_p^{3/2}$

Table 3.3: Time prediction RMS calculation for different power-law noise types according to Allan (1987)

$$RMS_x(\tau_p) = \tau_p \cdot \sigma_y(\tau_p), \quad (3.19)$$

where σ_y is the Allan deviation and τ_p is the prediction interval. That means the time error due to random frequency fluctuations after a certain time interval is simply the Allan deviation at that time interval multiplied by the time interval itself. Due to multiplication with τ_p the asymptote of the time prediction error in a double logarithmic plot has a slope of $(1 - \alpha)/2$. Accordingly, the time prediction error for white frequency noise ($\alpha = 0$) is increasing with the square root of the prediction interval whereas for flicker frequency noise ($\alpha = -1$) the increase is linear. Note, that for other noise types the time prediction error has to be scaled with one of the noise-specific factors given in table 3.3. In particular, for the important case of flicker frequency noise, (3.19) is too optimistic by a factor of $(\ln 2)^{-\frac{1}{2}} \approx 1.2$.

The time prediction RMS is not to be confused with the so called time deviation (TDEV), which is mainly used to characterize time distribution systems. TDEV is based on the modified Allan deviation in order to distinguish between white and flicker phase noise and is computed as

$$TDEV(\tau) = \frac{\tau}{\sqrt{3}} \cdot \text{Mod}\sigma_y(\tau). \quad (3.20)$$

Due to the scaling with $1/\sqrt{3}$ the TDEV gives the same value as the classical standard deviation in the case of white phase noise. Though similar in shape to the time prediction RMS (3.19), the scaling of TDEV for power-law noise other than white phase noise is slightly wrong for predicting time errors.

Equation (3.19) can be used to determine the prediction interval for which the time error due to random instabilities of the clock frequency remains below a certain threshold. This in turn determines the process noise to be injected in the Kalman filter time update step or the maximum validity interval for one set of clock parameters in a batch adjustment. Although in the latter case, we have to take into account, that offset and drift are estimated from the data, which will absorb a significant part of the random clock variations. Figure 3.7 shows the evolution of the time error over an interval of one hour for 100 simulations of the time error of an active hydrogen maser scaled to meters. The time series were generated using the method proposed by Kasdin and Walter (1992) (cf. Section 3.8) with the coefficients h_α from Table 3.2. The standard deviation of the accumulated time error after one hour is approximately 10 ps or 3 mm equivalent propagation distance. This is in good agreement with the value obtained using the expression from Table 3.3 considering a flicker frequency noise floor of $\sigma_y(\tau) = 3 \times 10^{-15}$. If a linear trend is removed from each of the time series (Fig. 3.8), the residual time error can be considerably reduced. The

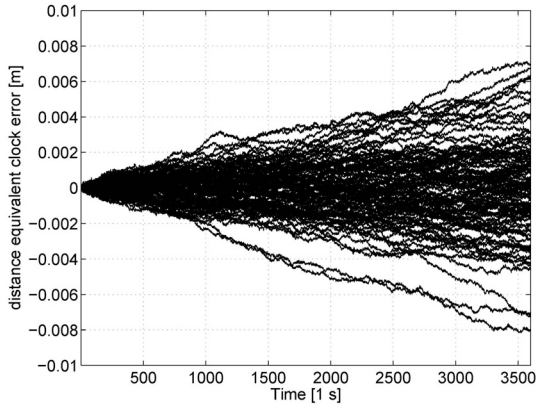


Figure 3.7: Accumulation of the time error during 1 hour for 100 simulations of the output signal of an active hydrogen maser scaled to meters; the standard deviation of the time error after one hour is approximately 3.0 mm (10 ps)

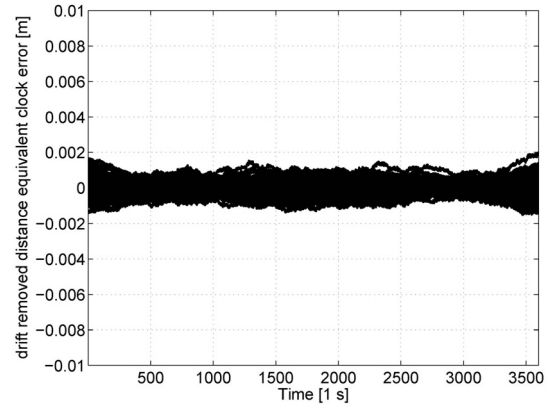


Figure 3.8: Residual time error of 1-hour linear fits to 100 simulations of the signal of an active H-maser scaled to meters; the std. deviation of the time error at the beginning and the end of the interval is ≈ 0.7 mm (2 ps)

standard deviation around the first and the last data point, where the deviation is usually the largest, is only about 2 ps or 0.65 mm, i.e. 4-5 times smaller than the time prediction error. Generally, this factor depends on the dominating noise type and the prediction interval. For practical usage in a batch least-squares adjustment, the receiver clock can be modeled by a sequence of piece-linear parameters. Due to the continuity constraints between consecutive linear segments, the constraints imposed by the model are slightly stronger than for independent linear fits applied here. This difference is, however, very small and will be discussed again in Section 4.4.1.

Finally, Figure 3.9 shows the accumulated time error against the prediction interval for different types of precise frequency standards as derived from (3.19). This figure corresponds to the Allan deviation plot (Fig. 3.5), but the slopes are shifted by +1 due to the multiplication with τ_p in (3.19).

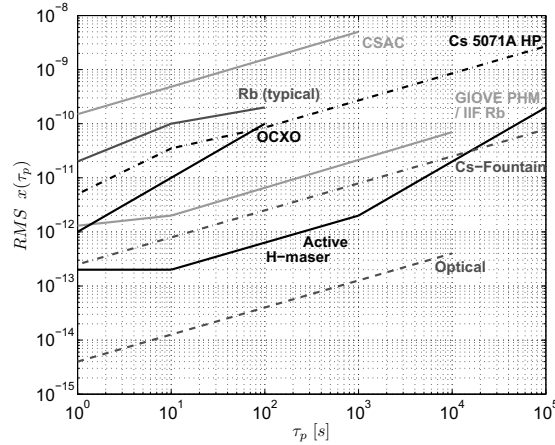


Figure 3.9: Typical prediction errors RMS_x for different high-precision oscillators. For references see Fig. 3.5.

3.8 Simulation of power-law noise in precision oscillators

In order to analyze the fit of the proposed clock models and for the generation of simulated observation data, actual time series of the oscillator signals are required. Ideally, we would like to use laboratory

measurements of the time error of a clock with respect to a reference oscillator of significantly higher accuracy. However, precise laboratory measurements, e.g. between hydrogen masers and cesium fountains, can only be carried out at timing laboratories and are primarily intended for internal use. In addition, for special or newly developed frequency standards no measurements may be (at least publicly) accessible at all, while the specifications in terms of Allan deviation are usually known from publications. Therefore, it is very helpful to have a tool for the simulation of colored or power-law noise time series based on given Allan deviation or spectral density parameters.

A popular approach to generate power-law noise has been proposed by Kasdin (1995). A detailed description of the noise generating algorithm, focusing on oscillator signal simulation, is given in Kasdin and Walter (1992). The basic idea is to convolve a white noise sequence w_k with an impulse response function b_k , which is derived from a generalization of the discrete transfer function for random walk noise $\beta = -2$ ($\alpha = 0$) to arbitrary β

$$H(z) = (1 - z^{-1})^{\beta/2}. \quad (3.21)$$

The corresponding discrete impulse response function b_k is found through a power series expansion of $H(z)$ and can be efficiently computed using the recursive relation

$$b_k = (k - 1 - \beta/2) \frac{b_{k-1}}{k}, \quad (3.22)$$

with $b_0 = 1$. The convolution is conveniently performed in the frequency domain through multiplication of the Fourier transforms of the impulse response and the white noise vector. The noise time series is then obtained via the inverse Fourier transform. For oscillator signal simulation the five afore mentioned power-law noise types with integer β are first generated separately and then added. The last problem is the determination of the scaling factor for the input white noise to match the intensity of the different noise processes as given by the coefficients h_α . This can be solved using Equation (39) of Kasdin and Walter (1992).

$$\sigma_w^2 = \frac{h_\alpha}{2(2\pi)^\alpha \tau_0^{\alpha-1}}. \quad (3.23)$$

Figure 3.10 shows the simulated time error of an active hydrogen maser. A comparison with the time differences of two real hydrogen maser frequency standards (Fig. 3.4) shows a good agreement of the overall variability. In addition, the Allan deviation of the simulated time series is in close agreement with the h_α values supplied to the noise generation function (Fig. 3.11).

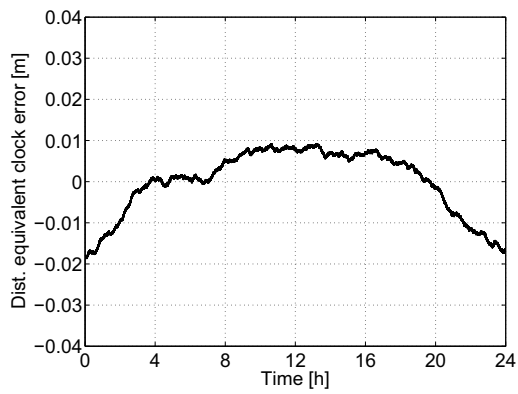


Figure 3.10: Simulated time errors of an active hydrogen maser during a 24-hour period scaled to meters with linear drift removed; the time series has been generated using the algorithm by Kasdin and Walter (1992) based on typical h_α coefficients

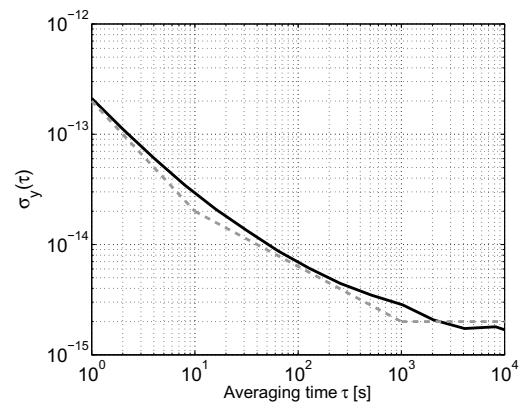


Figure 3.11: Allan deviation of simulated active hydrogen maser time errors based on typical coefficients h_α . The Allan deviation corresponding to the input noise coefficients is indicated by the dashed line.

4 Parameter Estimation and Clock Modeling

In this chapter the strategies to incorporate the additional information provided by a stable oscillator into the GNSS parameter estimation are discussed. The GNSS positioning problem is almost exclusively solved by least-squares adjustment either in a single step (batch) solution or in a sequential approach, e.g. a Kalman filter. Batch least-squares and sequential least-squares adjustment are theoretically equivalent and practically relevant estimation concepts that are used in GNSS software packages. The major advantage of the filtering approach is its real-time capability making it the method of choice in most navigation applications. In addition, the computation is often more efficient and the concept of process noise allows a better representation of the physical behavior of the time-varying parameters. On the other hand, classical batch least-squares adjustment, which is typically used for post-facto data analysis is more robust with respect to outliers in the observations. A more detailed comparison of the two approaches with respect to satellite orbit determination can be found in Montenbruck and Gill (2000). In view of their common usage, clock modeling will be analyzed for both, Kalman filtering and classical batch least-squares adjustment. However, the majority of the results presented in Chapters 6 and 7 were computed with the batch approach. In preparation of the derivation of the proposed clock models in Section 4.4 and the interpretation of the results, the fundamentals of least-squares adjustment and Kalman filtering are going to be introduced in the following.

4.1 Least-squares adjustment theory

Least-squares adjustment aims at finding an optimum solution for an overdetermined system of equations that describes the observations as a linear function of a number of unknown parameters by minimizing the sum of squared observation residuals. If the functional relationship between the observations and the parameters is non-linear, it can be linearized through a Taylor series expansion around a point given by the approximate values of the parameters \mathbf{x}^0 . The standard formulation of the least-squares problem is given by the *Gauß-Markov Model* (Koch, 1999). It consists of the *functional model*

$$E(\mathbf{l}) = \mathbf{f}(\mathbf{x}^0) + \mathbf{A} \hat{\mathbf{x}} \quad (4.1)$$

and the *stochastic model*

$$D(\mathbf{l}) = \mathbf{C}_u = \sigma_0^2 \mathbf{Q}_u = \sigma_0^2 \mathbf{P}^{-1}, \quad (4.2)$$

with

$E(), D()$	denoting the expectation value and dispersion operator, respectively,
\mathbf{l}	the $n \times 1$ vector of observations,
$\mathbf{f}(\mathbf{x}^0)$	the $n \times 1$ vector of modeled observations, computed from \mathbf{x}^0 ,
\mathbf{A}	the $n \times u$ design matrix containing the partial derivatives of the observations with respect to the parameters,
$\hat{\mathbf{x}}$	the $u \times 1$ vector of estimated parameter increments with respect to \mathbf{x}^0 ,
\mathbf{C}_{ll}	the $n \times n$ covariance matrix of the observations,
σ_0^2	the a priori variance factor or variance of unit weight,
\mathbf{Q}_{ll}	the $n \times n$ cofactor matrix of the observations, and
\mathbf{P}	the $n \times n$ observation weight matrix.

Introducing the $n \times 1$ vector of observation residuals \mathbf{v} with $E(\mathbf{v}) = 0$ and $D(\mathbf{v}) = D(\mathbf{l})$, we can formulate the *observation equations* based on (4.1) as

$$\mathbf{v} = \mathbf{A} \hat{\mathbf{x}} - \tilde{\mathbf{l}}, \quad (4.3)$$

with

$$\tilde{\mathbf{l}} = (\mathbf{l} - \mathbf{f}(\mathbf{x}^0)), \quad (4.4)$$

the vector of reduced observations often also called *observed-minus-computed*(o-c). It can be shown (e.g. Koch, 1999, p.158) that an optimum estimate of the parameter vector $\hat{\mathbf{x}}$ in the sense that it minimizes the weighted sum of squared residuals, i.e. $\min(\mathbf{v}^T \mathbf{P} \mathbf{v})$, is found through the so called normal equations

$$\mathbf{A}^T \mathbf{P} \mathbf{A} \hat{\mathbf{x}} = \mathbf{A}^T \mathbf{P} \tilde{\mathbf{l}}, \quad (4.5)$$

where the $u \times u$ matrix $\mathbf{N} = \mathbf{A}^T \mathbf{P} \mathbf{A}$ is called the *normal equation matrix* and the $u \times 1$ vector $\mathbf{n} = \mathbf{A}^T \mathbf{P} \tilde{\mathbf{l}}$ the *right-hand side* of the normal equations. Solving (4.5) for the parameter increments gives

$$\hat{\mathbf{x}} = (\mathbf{A}^T \mathbf{P} \mathbf{A})^{-1} \mathbf{A}^T \mathbf{P} \tilde{\mathbf{l}} = \mathbf{N}^{-1} \mathbf{n}. \quad (4.6)$$

According to the laws of error propagation the cofactor matrix of the parameters is the inverse of the normal equation matrix

$$\mathbf{Q}_{xx} = (\mathbf{A}^T \mathbf{P} \mathbf{A})^{-1}. \quad (4.7)$$

Other important quantities are the adjusted observations $\hat{\mathbf{l}}$ and residuals $\hat{\mathbf{v}}$ and their cofactor matrices, which are given by the following expressions

$$\hat{\mathbf{l}} = \mathbf{A} \hat{\mathbf{x}}, \quad \mathbf{Q}_{\hat{l}\hat{l}} = \mathbf{A} \mathbf{Q}_{xx} \mathbf{A}^T, \quad (4.8)$$

$$\hat{\mathbf{v}} = \mathbf{A} \hat{\mathbf{x}} - \tilde{\mathbf{l}}, \quad \mathbf{Q}_{\hat{v}\hat{v}} = \mathbf{Q}_{ll} - \mathbf{Q}_{\hat{l}\hat{l}}. \quad (4.9)$$

Using the weighted sum of squared residuals $\Omega = \mathbf{v}^T \mathbf{P} \mathbf{v}$ the *a posteriori variance factor*

$$\hat{\sigma}_0^2 = \frac{\hat{\mathbf{v}}^T \mathbf{P} \hat{\mathbf{v}}}{n - u} \quad (4.10)$$

can be computed. Furthermore, the weighted sum of squared residuals Ω may be used to test the solution for deficiencies in the functional or stochastic model based on the hypothesis $\hat{\sigma}_0 = \sigma_0$. The χ^2 -distributed test quantity is

$$T = \frac{\Omega}{\sigma_0^2} = \frac{(n-u)\hat{\sigma}_0^2}{\sigma_0^2} \sim \chi_{1-\alpha;f}^2. \quad (4.11)$$

Given the degree of freedom of the solution $f = n - u$ and the confidence level α , the test can be evaluated (Koch, 1999, p. 286). If the test is accepted and the degree of freedom is large, the estimated a posteriori variance factor can be used to compute the covariance matrices of the parameters, the residuals and the adjusted observations

$$\mathbf{C}_{xx} = \hat{\sigma}_0^2 \mathbf{Q}_{xx}, \quad \mathbf{C}_{vv} = \hat{\sigma}_0^2 \mathbf{Q}_{vv}, \quad \mathbf{C}_{\hat{t}} = \hat{\sigma}_0^2 \mathbf{Q}_{\hat{t}}. \quad (4.12)$$

The above equations form the basis of the parameter estimation of the batch processing module of the developed GPS processing software. The data processing is based on undifferenced pseudorange and carrier phase observations and the vector of unknowns comprises four different types of parameters, namely coordinates, tropospheric zenith delays, carrier phase ambiguities and receiver clock parameters. Because the receiver clock offsets generally need to be estimated at every epoch, the number of parameters and therefore the size of the normal equation matrix quickly becomes very large. Consequently, the memory requirements and the computational burden for the matrix inversion may pose serious problems. The situation is even worse, when kinematic coordinates are to be estimated, because this introduces 3 parameters at every observation epoch, instead of 3 coordinates for the entire observation session. Figure 4.1 illustrates the structure of the normal equation matrix for a 6-h static PPP solution with 5-minute observation intervals in which the unknown parameter vector consists of 3 coordinates, 13 piece-wise linear troposphere parameters, 25 carrier phase ambiguities and, in the lower right sub-matrix, 72 receiver clock offsets, one for every observation epoch.

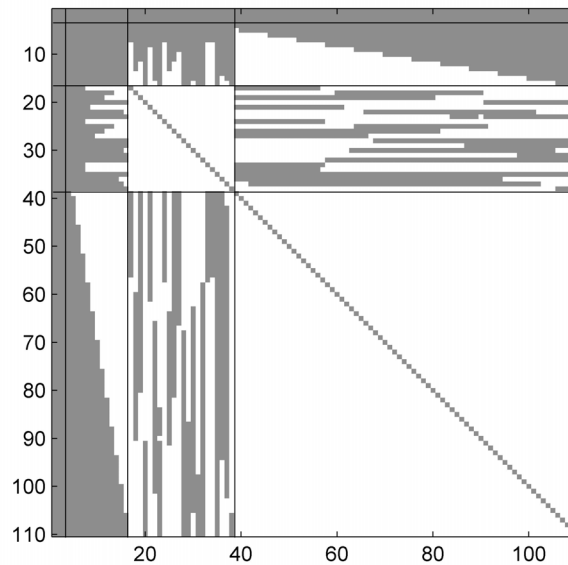


Figure 4.1: Structure of the normal equation matrix of a 6-h static PPP solution; the sequence of parameters is: receiver coordinates (3), zenith wet delay parameters (13), carrier phase ambiguities (25) and receiver clock offsets for every observation epoch (72)

One way to circumvent the problems associated with a large number of epoch-specific parameters is to pre-eliminate these parameters from the normal equation system. Due to the importance of this procedure for the understanding of the processing and the analysis of the impact of bias modeling in Section 4.3, it is derived in the following. Introducing a parameter vector consisting of global parameters \mathbf{x}_1 and epoch parameters \mathbf{x}_2

$$\hat{\mathbf{x}} = \begin{bmatrix} \hat{\mathbf{x}}_1 \\ \hat{\mathbf{x}}_2 \end{bmatrix}, \quad (4.13)$$

the system of normal equations for this *partitioned model* reads

$$\begin{bmatrix} \mathbf{A}_1^T \mathbf{P} \mathbf{A}_1 & \mathbf{A}_1^T \mathbf{P} \mathbf{A}_2 \\ \mathbf{A}_2^T \mathbf{P} \mathbf{A}_1 & \mathbf{A}_2^T \mathbf{P} \mathbf{A}_2 \end{bmatrix} \begin{bmatrix} \hat{\mathbf{x}}_1 \\ \hat{\mathbf{x}}_2 \end{bmatrix} = \begin{bmatrix} \mathbf{A}_1^T \mathbf{P} \tilde{\mathbf{l}} \\ \mathbf{A}_2^T \mathbf{P} \tilde{\mathbf{l}} \end{bmatrix} \quad (4.14)$$

or shortened

$$\begin{bmatrix} \mathbf{N}_{11} & \mathbf{N}_{12} \\ \mathbf{N}_{21} & \mathbf{N}_{22} \end{bmatrix} \begin{bmatrix} \hat{\mathbf{x}}_1 \\ \hat{\mathbf{x}}_2 \end{bmatrix} = \begin{bmatrix} \mathbf{n}_1 \\ \mathbf{n}_2 \end{bmatrix}. \quad (4.15)$$

Assuming that \mathbf{N}_{22}^{-1} exists, the second set of equations can be solved for $\hat{\mathbf{x}}_2$, i.e.

$$\hat{\mathbf{x}}_2 = \mathbf{N}_{22}^{-1}(\mathbf{n}_2 - \mathbf{N}_{21}\hat{\mathbf{x}}_1), \quad (4.16)$$

and the resulting expression can be inserted into the equation for $\hat{\mathbf{x}}_1$. In this way, a new reduced normal equation system is obtained

$$(\mathbf{N}_{11} - \mathbf{N}_{12}\mathbf{N}_{22}^{-1}\mathbf{N}_{21})\hat{\mathbf{x}}_1 = \mathbf{n}_1 - \mathbf{N}_{12}\mathbf{N}_{22}^{-1}\mathbf{n}_2, \quad (4.17)$$

or

$$\bar{\mathbf{N}}\hat{\mathbf{x}}_1 = \bar{\mathbf{n}}. \quad (4.18)$$

The weighted sum of squared residuals $\Omega = \mathbf{v}^T \mathbf{P} \mathbf{v}$ can be computed from the weighted sum of observed-computed values $\tilde{\mathbf{l}}$ as

$$\mathbf{v}^T \mathbf{P} \mathbf{v} = \tilde{\mathbf{l}}^T \mathbf{P} \tilde{\mathbf{l}} - \mathbf{x}_1^T \bar{\mathbf{n}}_1 \quad (4.19)$$

with

$$\tilde{\mathbf{l}}^T \mathbf{P} \tilde{\mathbf{l}} = \tilde{\mathbf{l}}^T \mathbf{P} \tilde{\mathbf{l}} - \mathbf{n}_2^T \mathbf{N}_{22}^{-1} \mathbf{n}_2. \quad (4.20)$$

The procedure described above preserves the impact of the pre-eliminated parameters $\hat{\mathbf{x}}_2$ on the solution, without explicitly calculating their values. That means, the estimates of the global (non-epoch-specific) parameters $\hat{\mathbf{x}}_1$ are the same as if the complete system (4.14) would have been solved in one step. However, for the investigations in this work, the values of the pre-eliminated (clock) parameters are also required and the pre-elimination step is only used to reduce the size of the main normal equation system comprising the global parameters. After this normal equation system has been solved, the epoch parameters are computed in a so called back-substitution step. This can be done according to Eq. (4.16).

According to e.g. Heck (1975), the cofactor matrix \mathbf{Q}_{22} of the pre-eliminated parameters can be computed as

$$\mathbf{Q}_{22} = \mathbf{N}_{22}^{-1} + \mathbf{N}_{22}^{-1} \mathbf{N}_{12}^T \mathbf{Q}_{11} \mathbf{N}_{12} \mathbf{N}_{22}^{-1}. \quad (4.21)$$

Pre-elimination and back-substitution of clock offsets and kinematic coordinates may be performed very efficiently on an epoch-by-epoch basis, because these parameter types are generally not mathematically correlated across epochs. This is also reflected by the diagonal structure of the submatrix containing the clock parameters in Figure 4.1. Consequently, we may proceed as follows: at every observation epoch the matrix N_{11} is set up and the matrices referring to the epoch-specific parameters N_{12} and N_{22} are appended. Then the epoch-specific part is pre-eliminated and the resulting reduced normal equation

matrices N_{11} are accumulated. Thus for epoch-wise pre-elimination, the maximum size of the matrix N_{22} is 4×4 when both, kinematic coordinates and epoch-wise receiver clock offsets are estimated. The largest matrix to be stored is $u_1 \times u_1$, where u_1 denotes the number of global parameters.

In case of many non epoch-specific parameters, that are valid only during certain periods and/or for specific satellites, such as troposphere parameters and carrier phase ambiguities, the manipulation of the normal equation matrix N_{11} using (4.17) may become very time-consuming. In order to speed up the computation, only those elements in the normal equation matrix and the right-hand side that are active during the current epoch should be updated.

A final remark concerns the incorporation of absolute and relative constraints into the least-squares adjustment. Constraints are usually applied to stabilize the solution if the observability of a parameter is weak, e.g. because the parameter interval is too small to allow a reliable estimation. In this situation constraints, that are based on a priori knowledge as for example the typical temporal variations of the parameter type, can improve the estimates.

Constraining parameters with respect to a specific value is called *absolute constraining*. In most cases this is the a priori value, used in the computation of the reduced observation vector \tilde{l} . In this case the parameter increment is constrained to zero and the absolute constraint can be expressed by

$$0 + v = x_i, \quad D(v) = \sigma_v^2, \quad (4.22)$$

where σ_v is the precision of this pseudo-observation, which is used to balance the a priori information with respect to the information from the least-squares adjustment of the actual observations. Instead of appending (4.22) to the design matrix, it can be conveniently applied at the normal equation level by adding the value σ_0^2/σ_v^2 to the main diagonal element of the normal equation matrix referring to the parameter x_i , i.e.

$$N_{i,i} = N_{i,i} + \sigma_0^2/\sigma_v^2. \quad (4.23)$$

In analogy, constraining parameters with respect to other parameters is called *relative constraining*, i.e. the difference between the parameters is constrained to zero. Consequently, the relative constraints can be expressed by the following pseudo-observation

$$0 + v = x_i - x_j, \quad D(v) = \sigma_v^2, \quad (4.24)$$

which corresponds to adding the 2×2 matrix

$$\begin{bmatrix} \sigma_0^2/\sigma_v^2 & -\sigma_0^2/\sigma_v^2 \\ -\sigma_0^2/\sigma_v^2 & \sigma_0^2/\sigma_v^2 \end{bmatrix} \quad (4.25)$$

to the elements $N_{i,j}$ of the normal equation matrix referring to the parameters x_i and x_j , i.e.

$$N_{i,j} = N_{i,j} + \sigma_0^2/\sigma_v^2 \quad \text{for } i = j \quad \text{and} \quad N_{i,j} = N_{i,j} - \sigma_0^2/\sigma_v^2 \quad \text{for } i \neq j \quad (4.26)$$

In the developed PPP software module, absolute constraints are used to constrain the slope of the piece-wise linear troposphere parameters to zero thus limiting the temporal variation. This temporal variation is usually described as a random walk process with a certain process noise $\sigma_{RW,trop}$. As we have seen in Section 3.7 the RMS prediction error of a random walk process (e.g. white FM) is growing with the square root of time. If not indicated otherwise a standard value of $\sigma_{RW,trop} = 5 \text{ mm}/\sqrt{h}$ is used throughout this work. Although there is no rigorous conversion between the process noise σ_{RW} and the standard deviation σ_v of the absolute constraints, the relationship can be approximated by simply assuming $\sigma_v = \sigma_{RW,trop} = 5 \text{ mm}/\sqrt{h}$. Note that the absolute constraints correspond to relative constraints when the nodes instead of the slopes are used as parameters of the piece-wise linear model.

Relative constraints are used for ambiguity fixing with respect to a reference ambiguity and are essential to limit the temporal change of the clock drift based on the frequency stability of the receiver oscillator. The constraints imposed on the clock parameters are discussed in detail in Section 4.4.1, where the functional and stochastic clock model for the least-squares adjustment is introduced.

4.2 Kalman filtering

In the conventional least-squares adjustment algorithm all observations and parameters for a certain time interval are processed in a single step. Due to the growing processing load as the number of observations and parameters increases, a sequential processing scheme for the estimation is often preferable. Sequential least-squares adjustment is closely related to the so called Kalman filter. In simple terms, the Kalman filter is a sequential least-squares solution augmented with the possibility to incorporate a dynamical model of the parameters. That means, the filter includes a so called time update step, i.e. a prediction of the state and the covariance of the parameters based on previous estimates and a given model of the parameter dynamics.

4.2.1 Kalman filter theory

Neglecting deterministic control inputs, the linear dynamic system of the parameters can be modeled by the following first-order differential equation

$$\dot{\mathbf{x}} = \mathbf{F}\mathbf{x} + \mathbf{w}, \quad (4.27)$$

with

- \mathbf{x} the parameter state vector,
- \mathbf{w} a vector with process noise,
- \mathbf{F} the dynamics matrix.

For time invariant systems, i.e. if the dynamics matrix \mathbf{F} contains only constant coefficients, a general solution of (4.27) is given by (e.g. Gelb, 1974, p. 66)

$$\mathbf{x}(t) = \Phi(t, t_0)\mathbf{x}(t_0) + \int_{t_0}^t \Phi(t, \tau)\mathbf{w}(\tau) d\tau \quad (4.28)$$

where the state transition matrix $\Phi(t, t_0)$ can be derived from the dynamics matrix \mathbf{F} using the matrix exponential

$$\Phi(t, t_0) = e^{\mathbf{F} \cdot (t-t_0)} = \mathbf{I} + \mathbf{F} \cdot (t-t_0) + \frac{1}{2!}\mathbf{F}^2 \cdot (t-t_0)^2 + \dots \quad (4.29)$$

For discrete time epochs k the solution (4.28) is expressed by the following difference equation

$$\mathbf{x}_k = \Phi_{k-1}\mathbf{x}_{k-1} + \mathbf{w}_k, \quad (4.30)$$

where

$$\mathbf{w}_k = \int_{t_{k-1}}^{t_k} \Phi(t, \tau)\mathbf{w}(\tau) d\tau \quad (4.31)$$

denotes system or process noise, that follows a normal distribution $N(\mathbf{0}, \mathbf{Q}_w)$. The process noise represents the stochastic disturbances of the dynamic system model.

This approach is very well suited to describe the behavior of high-precision oscillators. A very simple, yet efficient, two-state model of the clock behavior and the associated time update steps are described in Section 4.4.2.

The classical Kalman filter equations can treat only linear problems. The GNSS positioning problem, however, is non-linear in the receiver coordinates. Non-linear estimation problems are typically solved using the so called extended Kalman filter (EKF), in which the linearization is carried out around the latest estimates of the filter. Therefore, the EKF algorithm does not require precise approximate receiver coordinates. Introducing bad a priori coordinates will of course result in sub-optimal state estimates at the start of the filter. However, after a few epochs the estimated receiver coordinates have usually improved to a point where linearization errors are not significant.

The recursive extended Kalman filter algorithm essentially consists of three steps that are typically performed at every observation epoch k . In order to avoid confusion we will depart from the typical notation of the elements of the Kalman filter and use a notation consistent with the batch least-squares adjustment described in Section 4.1. In the first step, the *Kalman gain matrix* \mathbf{K}_k is calculated

$$\mathbf{K}_k = \tilde{\mathbf{Q}}_{x,k} \mathbf{A}_k (\mathbf{Q}_{l,k} + \mathbf{A}_k \tilde{\mathbf{Q}}_{x,k} \mathbf{A}_k^T)^{-1}, \quad (4.32)$$

with

- $\tilde{\mathbf{Q}}_{x,k}$ the state cofactor matrix of the previous epoch predicted for the current epoch,
- \mathbf{A}_k the design matrix, containing the partial derivatives of the observations with respect to the parameters, and
- $\mathbf{Q}_{l,k}$ the observation cofactor matrix.

The gain matrix can be thought of as a weighting function, that balances the information contained in the new observations with respect to the previously estimated states of the parameters, predicted for the current epoch.

Using the Kalman gain matrix, a new estimate of the state vector $\hat{\mathbf{x}}$ and its cofactor matrix $\hat{\mathbf{Q}}$ can be computed using the observations \mathbf{l}_k in the so called *measurement update* step

$$\hat{\mathbf{x}}_k = \tilde{\mathbf{x}}_{k-1} + \mathbf{K}_k \mathbf{d}_k, \quad (4.33)$$

$$\hat{\mathbf{Q}}_{x,k} = (\mathbf{I} - \mathbf{K}_k \mathbf{A}_k) \tilde{\mathbf{Q}}_{x,k}, \quad (4.34)$$

with

$$\mathbf{d}_k = \mathbf{l}_k - \mathbf{A}_k \tilde{\mathbf{x}}_{k-1}, \quad (4.35)$$

which is called the vector of *innovations* and represents the discrepancy between the observations of the current epoch \mathbf{l}_k and the system state $\tilde{\mathbf{x}}_{k-1}$ predicted for the current epoch and transformed into the observation space through multiplication with the design matrix \mathbf{A}_k . In combination with the corresponding cofactor matrix

$$\mathbf{Q}_{d,k} = \mathbf{Q}_{l,k} - \mathbf{A}_k \tilde{\mathbf{Q}}_{x,k-1} \mathbf{A}_k^T, \quad (4.36)$$

the innovations are well suited to identify problematic data such as outliers, cycle slips and clock jumps that are frequently encountered in GNSS data analysis (e.g. Niemeier, 2002, p. 387).

After processing all measurement data of the current epoch, the state vector and its cofactor matrix are predicted to the next epoch based on the dynamic model in the so called *time update* step

$$\tilde{\mathbf{x}}_{k+1} = \Phi_k \hat{\mathbf{x}}_k, \quad (4.37)$$

$$\tilde{\mathbf{Q}}_{x,k+1} = \Phi_k \hat{\mathbf{Q}}_{x,k} \Phi_k^T + \mathbf{Q}_{w,k}, \quad (4.38)$$

Process type	State difference equation
random constant	$x_{k+1} = x_k$
random walk	$x_{k+1} = x_k + w_{k+1}$
random ramp	$x_{1,k+1} = x_{1,k} + (t_{k+1} - t_k) \cdot x_{2,k} + w_{1,k+1}$ $x_{2,k+1} = x_{2,k} + w_{2,k+1}$

Table 4.1: Scalar state difference equations for different stochastic processes according to Strang and Borre (1997, p. 524)

Parameter type	System model	σ_0	σ
Static coordinates	Random constant	100 m	0 m
Kinematic coordinates	Random walk	100 m	100 m
Receiver clock time offset	Random ramp	$3 \cdot 10^5$ m	cf. 4.4.2
Receiver clock frequency offset	Random walk	300 m/s	cf. 4.4.2
Tropospheric <i>zwd</i>	Random walk	0.5 m	$0.005 \text{ m}/\sqrt{h}$
Carrier phase ambiguities	Random constant	1000 m	0 m

Table 4.2: PPP state variables and corresponding stochastic system model parameters used in this work

where Φ_k is the state transition matrix and $\mathbf{Q}_{w,k}$ the cofactor matrix of the process noise, introduced above. The time update step completes the Kalman filter cycle of epoch k . Starting with the computation of the new Kalman gain matrix (4.32), the process is repeated for the next epoch and so forth, until the measurement update of the last epoch is reached.

In the PPP approach used for this work, the state vector comprises four different types of parameters, namely three receiver coordinates, one wet tropospheric zenith delay, one carrier phase ambiguity for each GPS satellite in view and two receiver clock states describing the time and frequency offset of the receiver oscillator. Thus the size of the state vector is typically between 10 and 15, depending on the number of carrier phase ambiguities at a certain epoch. The state transition matrix and the process noise depend on the chosen system model for the state variables. For the PPP analysis in this work, random constant, random walk and random ramp system models (Gelb, 1974, p. 79 ff.) are considered. The corresponding discrete state difference equations are given in Table 4.1.

Apart from the random ramp model of the receiver clock, which is discussed in Section 4.4.2, $x_{k+1} = x_k$ holds, i.e. the state transition matrix is an identity matrix. In the case of the random constant model no process noise is added in the time update step, whereas for the random walk process, a suitable standard deviation σ has to be specified. Furthermore, initial values x_0 with corresponding standard deviations σ_0 need to be specified in order to start the Kalman filter loop at the first epoch and whenever a new ambiguity is added, because a new GPS satellite is observed. Table 4.2 summarizes the employed parameter types along with their system model and standard deviations. Note, that due to the large process noise added to the coordinates in the kinematic case, the position is estimated independently for every observation epoch.

4.2.2 Numerical stability

Kalman filtering is often associated with numerical instabilities due to computer round-off, especially when using single precision arithmetic, and so called square root methods have been developed to overcome this problem (Bierman, 1977). However, when using double precision arithmetic, a simple mean value operation that enforces the symmetry of the cofactor matrix $\hat{\mathbf{Q}}_x$ after each measurement update

$$\hat{\mathbf{Q}}_{x,k} = \frac{1}{2}(\hat{\mathbf{Q}}_{x,k} + \hat{\mathbf{Q}}_{x,k}^T), \quad (4.39)$$

or usage of the *Joseph form* for the measurement update of the cofactor matrix

$$\hat{\mathbf{Q}}_{x,k} = (\mathbf{I} - \mathbf{K}_k \mathbf{A}_k) \tilde{\mathbf{Q}}_{x,k} (\mathbf{I} - \mathbf{K}_k \mathbf{A}_k)^T + \mathbf{K}_k \mathbf{Q}_{l,k} \mathbf{K}_k^T \quad (4.40)$$

can avoid round-off problems (Brown and Hwang, 2005). Another source of numerical instability is the usage of very large initial variances or inappropriate units of the parameters. Both will lead to a large range of values within the covariance matrix, which can give rise to round-off errors (Grewal and Andrews, 2001). This problem can generally be avoided by (a) proper selection of units, e.g. the clock error should be scaled to meters through multiplication by the speed-of-light instead of using seconds, and (b) very large initial variances should be avoided by introducing adequate approximate values, e.g. ms clock jumps should be detected and corrected prior to the measurement update and approximate values of the carrier phase ambiguities based on the pseudorange observations should be introduced.

4.2.3 Smoothing of the filter output

Due to the sequential processing of the observation data, a Kalman filter can only use observations from the starting time t_0 of the filter up to a certain time t for the generation of the state estimates at time t . In contrast, a post processing batch least-squares solution can include all observations up to the end T of the data set including those after t and may thus provide better estimates. In order to overcome this limitation of the filter solution, for post processing applications the filter can be run in forward and backward direction. The estimates of both runs can then be rigorously combined to form an improved estimate that is based on all observations of the data set. This process is called smoothing or more precisely fixed-interval smoothing because the start time t_0 and end time T of the data set are “fixed”. Only filter states that are driven by a significant amount of process noise can be improved through smoothing and are therefore called “smoothable” (Gelb, 1974, p. 163). In GNSS analysis, the tropospheric zenith delay, kinematic coordinates and clock parameters are smoothable states, whereas random constants like static coordinates and carrier phase ambiguities are not smoothable. As a consequence, the final results of the latter parameters are obtained already upon completion of the forward run.

For this work, the fixed interval smoothing procedure described by Gelb (1974) has been implemented. In this approach the smoothed state vector at every epoch k is obtained as the weighted sum of the state estimates from the forward $\mathbf{x}_{k,f}$ and backward $\mathbf{x}_{k,b}$ filter run. The weights are given by the corresponding cofactor matrices $\mathbf{Q}_{k,f}$ and $\mathbf{Q}_{k,b}$. Consequently, the smoothed state estimates can be computed as

$$\bar{\mathbf{x}}_k = (\mathbf{Q}_{k,f}^{-1} + \mathbf{Q}_{k,b}^{-1})^{-1} (\mathbf{Q}_{k,f}^{-1} \mathbf{x}_{k,f} + \mathbf{Q}_{k,b}^{-1} \mathbf{x}_{k,b}) \quad (4.41)$$

and the corresponding cofactor matrix is

$$\bar{\mathbf{Q}}_k = (\mathbf{Q}_{k,f}^{-1} + \mathbf{Q}_{k,b}^{-1})^{-1}. \quad (4.42)$$

In order to compute the smoothed state estimates during the backward run of the filter, the estimates \mathbf{x}_f and the covariance matrices \mathbf{Q}_f of the forward run need to be available for every epoch k . The memory requirements therefore depend on the size of the state vector. For a PPP solution, the additional memory usage is moderate, since the maximum size of smoothable states is 6.

4.3 Continuous receiver clock modeling versus epoch-wise clock elimination

Due to the presence of receiver and satellite clock offsets, GNSS observations are always biased. Processing of observation differences that are free of clock offsets is thus a popular strategy in GNSS data analysis. Alternatively, the clock offsets can be estimated for every observation epoch. Since in batch processing the number of clock parameters may become very large, explicit estimation is usually replaced by a pre-elimination and back-substitution scheme as outlined in Section 4.1. According to the *Fundamental Differencing Theorem* (Lindlohr and Wells, 1985) bias elimination through observation differencing is equivalent to explicit bias estimation as independent white noise parameters, i.e. without any a priori information regarding the bias itself or its temporal variation. This has been discussed on a theoretical basis by several authors. A thorough proof of the theorem can be found, e.g., in Schaffrin and Grafarend (1986), whereas a particular compact derivation is given by Kuang et al. (1996).

In the following the difference between modeling and epoch-wise estimation of the receiver clock bias is going to be discussed. Receiver clock modeling as it is proposed in this work, aims at exploiting the additional information concerning the frequency stability provided by high-precision oscillators in order to improve the parameter estimates from the least-squares adjustment. In this context Kuang et al. (1996) show, that clock bias elimination through observation differencing can cause a loss of information because it prohibits the inclusion of a priori knowledge about the receiver clock parameters. In summary, Kuang et al. (1996) argue that if we had precise a priori knowledge of the clock offset of the receiver from some external source, the height accuracy could be significantly improved by imposing corresponding constraints on the clock parameters. Although this is an interesting finding, it is of little practical use since even if we had a very precise clock we would need a continuous calibration of the receiver clock with respect to the GPS system time, which is impossible to achieve at the required level of accuracy with the current system architecture. Rather than having absolute information about the satellite and receiver clock errors, we only know that the time error of stable clocks does change within certain bounds from one epoch to the next.

Note, that the situation is different when the GNSS data is processed in differential mode, because in this case only “absolute” values of the relative receiver clock offset are required. In fact, Macias-Valadez et al. (2012) show, that by using one receiver with multiple antennas and permanently calibrating the signal delays in the antenna cable, the differential receiver clock offset between two antenna sites may be calibrated externally in an absolute sense. However, this method can only be applied for relative positioning and short baselines. In all other cases, at least some clock parameters have to be estimated and constraints may be imposed only between these parameters and not on the parameter values themselves.

In order to examine the impact of constraints between consecutive receiver clock parameters on the precision of static and kinematic positioning results, let us consider a simple pseudorange solution covering two epochs. Assuming the receiver uses an oscillator that provides a highly stable frequency with negligible drift, i.e. the accumulated time error of the oscillator between the two epochs is smaller than the uncertainty of the receiver clock estimates based on the observation data, the receiver clock offset may either be determined for both epochs independently or estimated as a common parameter for both epochs. In the following, first *static positioning* is examined, while the kinematic case will be discussed later on in this section. Introducing the all-ones vector

$$\mathbf{e} = \begin{bmatrix} 1 & 1 & \dots & 1 \end{bmatrix}^T \quad (4.43)$$

of length n , representing the partial derivatives of the observations of n satellites with respect to the receiver clock error in units of meters and the $n \times 3$ design matrices \mathbf{A}_i containing the partial derivatives with respect to the receiver coordinates at epoch i

$$\mathbf{A}_i = \begin{bmatrix} \mathbf{u}_1 & \mathbf{u}_2 & \dots & \mathbf{u}_n \end{bmatrix}^T, \quad (4.44)$$

where

$$\mathbf{u}_j = \begin{bmatrix} \frac{X_r - X^j}{\|X_r - X^j\|} & \frac{Y_r - Y^j}{\|Y_r - Y^j\|} & \frac{Z_r - Z^j}{\|Z_r - Z^j\|} \end{bmatrix}^T \quad (4.45)$$

are the unit vectors pointing from the satellite position \mathbf{X}^j to the receiver position \mathbf{X}_r . In this notation the design matrix of the complete system for a *static receiver* in the case of epoch-wise independent clock estimation reads

$$\mathbf{A} = \begin{bmatrix} \mathbf{A}_1 & \mathbf{e}_1 & 0 \\ \mathbf{A}_2 & 0 & \mathbf{e}_2 \end{bmatrix} \quad (4.46)$$

and in the case when only one common clock offset is estimated for both epochs

$$\tilde{\mathbf{A}} = \begin{bmatrix} \mathbf{A}_1 & \mathbf{e}_1 \\ \mathbf{A}_2 & \mathbf{e}_2 \end{bmatrix}. \quad (4.47)$$

The parameter vectors read

$$\mathbf{x} = \begin{bmatrix} X_r & Y_r & Z_r & \delta t_{r,1} & \delta t_{r,2} \end{bmatrix}^T \quad (4.48)$$

and

$$\tilde{\mathbf{x}} = \begin{bmatrix} X_r & Y_r & Z_r & \delta t_r \end{bmatrix}^T, \quad (4.49)$$

respectively. The corresponding normal equation matrices are

$$\mathbf{N} = \begin{bmatrix} \mathbf{A}_1^T \mathbf{A}_1 + \mathbf{A}_2^T \mathbf{A}_2 & \mathbf{A}_1^T \mathbf{e}_1 & \mathbf{A}_2^T \mathbf{e}_2 \\ \mathbf{e}_1^T \mathbf{A}_1 & n_1 & 0 \\ \mathbf{e}_2^T \mathbf{A}_2 & 0 & n_2 \end{bmatrix} \quad (4.50)$$

and

$$\tilde{\mathbf{N}} = \begin{bmatrix} \mathbf{A}_1^T \mathbf{A}_1 + \mathbf{A}_2^T \mathbf{A}_2 & \mathbf{A}_1^T \mathbf{e}_1 + \mathbf{A}_2^T \mathbf{e}_2 \\ \mathbf{e}_1^T \mathbf{A}_1 + \mathbf{e}_2^T \mathbf{A}_2 & n_1 + n_2 \end{bmatrix}. \quad (4.51)$$

According to the explanations in Section 4.1, parameters or parameter groups can be pre-eliminated from the normal equation system using (4.17). The term

$$\Delta \mathbf{N}_{11} = \mathbf{N}_{12} \mathbf{N}_{22}^{-1} \mathbf{N}_{21} \quad (4.52)$$

quantifies the influence of the pre-eliminated parameters on the remaining parameters. For example, small values of the elements in $\Delta \mathbf{N}_{11}$ indicate that the pre-eliminated (clock) parameters contribute little to the uncertainty of the remaining (coordinate) parameters. Using the *matrix inversion lemma* (e.g. Koch, 1999, p. 34), the cofactor matrix of the coordinates including the contribution of the pre-eliminated clock bias parameters can be written as

$$(\mathbf{N}_{11} - \Delta \mathbf{N}_{11})^{-1} = \mathbf{N}_{11}^{-1} + \mathbf{N}_{11}^{-1} \mathbf{N}_{12} (\mathbf{N}_{22} - \mathbf{N}_{12}^T \mathbf{N}_{11}^{-1} \mathbf{N}_{12})^{-1} \mathbf{N}_{12}^T \mathbf{N}_{11}^{-1} = \mathbf{N}_{11}^{-1} + \mathbf{D} \quad (4.53)$$

It can be shown that the expression \mathbf{D} is always positive-semidefinite which in turn means that $tr(\mathbf{D}) \geq 0$ (van Diggelen, 2009). Because of

$$tr(\mathbf{A} + \mathbf{B}) = tr(\mathbf{A}) + tr(\mathbf{B}) \quad (4.54)$$

(e.g. Koch, 1999, p. 40) we obtain

$$\text{tr} \left((\mathbf{N}_{11} - \Delta \mathbf{N}_{11})^{-1} \right) = \text{tr} (\mathbf{N}_{11}^{-1} + \mathbf{D}) = \text{tr}(\mathbf{N}_{11}^{-1}) + \text{tr}(\mathbf{D}) \geq \text{tr} (\mathbf{N}_{11}^{-1}). \quad (4.55)$$

Thus, every pre-eliminated parameter will either cause an increase of the diagonal elements in the cofactor matrix of the estimated parameters or leave them unchanged. The latter case is worth a closer look. As stated in Teunissen (2003, p.93) additional parameters \mathbf{x}_2 do not affect the estimates of the primary parameters \mathbf{x}_1 if and only if the column space of their design matrix \mathbf{A}_2 is orthogonal to the column space of \mathbf{A}_1 . This is equivalent with the condition $\mathbf{A}_1^T \mathbf{P} \mathbf{A}_2 = \mathbf{N}_{12} = 0$, i.e. completely uncorrelated parameter groups. In GNSS data analysis, the correlation of the horizontal coordinate components and the receiver clock offset is generally small, while the height coordinate and the tropospheric zenith delay are typically highly correlated with the receiver clock parameters. Thus, mainly the latter parameter types should improve, if fewer clock parameters are estimated.

In principle, reducing the number of clock parameters should always improve the precision of correlated parameters provided that the actual receiver clock variations are still adequately represented by the model, i.e. the constraints imposed on the clock are not too optimistic. If the number of clock parameters is too small or the constraints are too tight, the parameter vector may become biased while this is not the case if the number of parameters is too large (Koch, 1999, pp 179-180). Thus, reducing the number of clock parameters has to be done with great care.

After this rather general discussion of the impact of the pre-eliminated bias parameters, let us go back to Equation (4.52) for a *geometrical interpretation* of the contribution of the receiver clock offsets to the normal equations of the coordinate parameters. During the pre-elimination of the clock parameters from the normal equation systems with epoch-wise clock offsets (4.50) and one common clock offset (4.51), the following $\Delta \mathbf{N}_{11}$ expressions are obtained

$$\Delta \mathbf{N}_{11} = \frac{1}{n_1} \mathbf{A}_1^T \mathbf{e}_1 \mathbf{e}_1^T \mathbf{A}_1 + \frac{1}{n_2} \mathbf{A}_2^T \mathbf{e}_2 \mathbf{e}_2^T \mathbf{A}_2 = \frac{1}{n_1} \mathbf{w}_1 \mathbf{w}_1^T + \frac{1}{n_2} \mathbf{w}_2 \mathbf{w}_2^T \quad (4.56)$$

$$\Delta \tilde{\mathbf{N}}_{11} = \frac{1}{n_1 + n_2} (\mathbf{A}_1^T \mathbf{e}_1 + \mathbf{A}_2^T \mathbf{e}_2) (\mathbf{e}_1^T \mathbf{A}_1 + \mathbf{e}_2^T \mathbf{A}_2) = \frac{1}{n_1 + n_2} (\mathbf{w}_1 + \mathbf{w}_2) (\mathbf{w}_1^T + \mathbf{w}_2^T), \quad (4.57)$$

where

$$\mathbf{A}_i^T \mathbf{e}_i = (\mathbf{e}_i^T \mathbf{A}_i)^T = \mathbf{w}_i \quad (4.58)$$

is the sum of all satellite-to-receiver unit vectors at epoch i . The resulting vector \mathbf{w}_i is pointing into the average direction of all observations, i.e. approximately the local nadir direction, independent of the receiver location. Comparing (4.56) and (4.57), it becomes obvious, that the two models yield identical results when the vector \mathbf{w}_i does not change between the epochs. In practice, the changing satellite geometry will of course lead to variations of \mathbf{w}_i over time and (4.57) will always be smaller than (4.56). However, the variations of \mathbf{w}_i are generally small. Figure 4.2 shows the angle between \mathbf{w}_i and the nadir direction with and without elevation-dependent weighting. For such variations, the difference between the elements referring to the height component in (4.57) and (4.56) is around 0.9 % for the unweighted and only 0.3 % for the weighted case.

Furthermore, we can see, that (4.57) approaches zero when the sum of all \mathbf{w}_i approaches zero. For the vertical component, this would only be the case if satellites from below the GPS antenna could be observed, which is generally not possible.

In summary, it can be concluded that estimating the clock offset parameter using multiple epochs does not improve the precision of static positioning as long as the average direction of the observations does not change significantly.

Now, let us have a look at the corresponding expressions for *kinematic positioning*, i.e. epoch-wise coordinate estimation. In the kinematic case the design matrix \mathbf{A} for two epochs and epoch-wise clock estimation reads

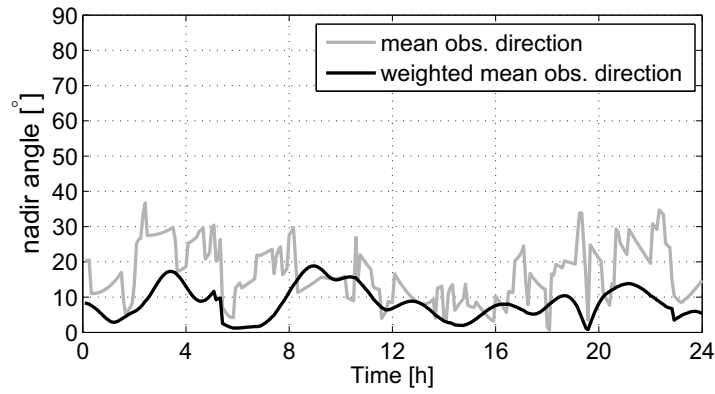


Figure 4.2: Nadir angle of (weighted) average direction of all observations for a mid-latitude station (IGS station WTZR)

$$\mathbf{A} = \begin{bmatrix} \mathbf{A}_1 & 0 & \mathbf{e}_1 & 0 \\ 0 & \mathbf{A}_2 & 0 & \mathbf{e}_2 \end{bmatrix} \quad (4.59)$$

and

$$\tilde{\mathbf{A}} = \begin{bmatrix} \mathbf{A}_1 & 0 & \mathbf{e}_1 \\ 0 & \mathbf{A}_2 & \mathbf{e}_2 \end{bmatrix}, \quad (4.60)$$

if only one common clock offset is estimated for both epochs. The normal equation matrices for the kinematic case are

$$\mathbf{N} = \begin{bmatrix} \mathbf{A}_1^T \mathbf{A}_1 & 0 & \mathbf{A}_1^T \mathbf{e}_1 & 0 \\ 0 & \mathbf{A}_2^T \mathbf{A}_2 & 0 & \mathbf{A}_2^T \mathbf{e}_2 \\ \mathbf{e}_1^T \mathbf{A}_1 & 0 & n_1 & 0 \\ 0 & \mathbf{e}_2^T \mathbf{A}_2 & 0 & n_2 \end{bmatrix} \quad (4.61)$$

and

$$\tilde{\mathbf{N}} = \begin{bmatrix} \mathbf{A}_1^T \mathbf{A}_1 & 0 & \mathbf{A}_1^T \mathbf{e}_1 \\ 0 & \mathbf{A}_2^T \mathbf{A}_2 & \mathbf{A}_2^T \mathbf{e}_2 \\ \mathbf{e}_1^T \mathbf{A}_1 & \mathbf{e}_2^T \mathbf{A}_2 & n_1 + n_2 \end{bmatrix}. \quad (4.62)$$

If the clock parameters are pre-eliminated from (4.61) and (4.62), their contributions $\Delta \mathbf{N}_{11}$ to the normal equations of the coordinate parameters are

$$\Delta \mathbf{N}_{11} = \begin{bmatrix} \frac{1}{n_1} \mathbf{A}_1^T \mathbf{e}_1 \mathbf{e}_1^T \mathbf{A}_1 & 0 \\ 0 & \frac{1}{n_2} \mathbf{A}_2^T \mathbf{e}_2 \mathbf{e}_2^T \mathbf{A}_2 \end{bmatrix} = \begin{bmatrix} \frac{1}{n_1} \mathbf{w}_1 \mathbf{w}_1^T & 0 \\ 0 & \frac{1}{n_2} \mathbf{w}_2 \mathbf{w}_2^T \end{bmatrix} \quad (4.63)$$

and

$$\Delta \tilde{\mathbf{N}}_{11} = \frac{1}{n_1 + n_2} \begin{bmatrix} \mathbf{A}_1^T \mathbf{e}_1 \mathbf{e}_1^T \mathbf{A}_1 & \mathbf{A}_1^T \mathbf{e}_1 \mathbf{e}_2^T \mathbf{A}_2 \\ \mathbf{A}_2^T \mathbf{e}_2 \mathbf{e}_1^T \mathbf{A}_1 & \mathbf{A}_2^T \mathbf{e}_2 \mathbf{e}_2^T \mathbf{A}_2 \end{bmatrix} = \frac{1}{n_1 + n_2} \begin{bmatrix} \mathbf{w}_1 \mathbf{w}_1^T & \mathbf{w}_1 \mathbf{w}_2^T \\ \mathbf{w}_2 \mathbf{w}_1^T & \mathbf{w}_2 \mathbf{w}_2^T \end{bmatrix} \quad (4.64)$$

When inspecting Equations (4.63) and (4.64), two important observations can be made:

Firstly, the estimation of only one clock parameter for multiple epochs introduces mathematical correlations between the coordinates of different epochs (4.64), whereas the coordinates are truly independent

when the clock offset is estimated epoch-by-epoch (4.63). The correlations induced by the relative clock constraints are significant and may need to be considered when the kinematic coordinates are used in subsequent processing steps, such as velocity or acceleration determination. However, we have to keep in mind that in PPP, correlations across epochs always exist due to the estimation of tropospheric zenith delays and carrier phase ambiguities. An example of inter-epoch correlations for estimated kinematic coordinates with and without clock modeling is given in Section 7.2.2. This example indicates an increase of the correlations up to approximately 30% for the vertical positions while the temporal correlations of the horizontal position estimates is in fact slightly reduced.

Secondly, the factor $1/(n_1 + n_2)$ in (4.64) is important, because it scales all elements of the $\Delta\mathbf{N}_{11}$ matrix. Consequently, as the number of epochs and therefore the number of observations used for the determination of one clock parameter increases, its contribution to the uncertainty of the coordinates at a specific epoch decreases. Thus, if the number of epochs used to determine a common clock parameter is large, $\Delta\mathbf{N}_{11}$ is approaching zero, i.e. the theoretical case in which no clock offsets are estimated at all.

4.4 Functional and stochastic models for clocks in GNSS data analysis

After having reviewed the parameter estimation approaches in the GNSS data analysis and the differences between continuous and epoch-wise clock estimation, some specific parameterizations of the clock synchronization error are discussed in the following section.

4.4.1 A clock model for use in a batch least-squares adjustment

As discussed in Chapter 3, GNSS receiver clock modeling at the carrier phase precision level is currently almost exclusively restricted to hydrogen maser frequency standards. Therefore, the obvious first step is to look at the parametrization of clocks in Very Long Baseline Interferometry (VLBI) analyses, where this oscillator type is used to synchronize remote radio telescopes at the ps precision level. Clock models based on second-order polynomials are most frequently employed in VLBI data analysis, because the quadratic term accounts for the significant frequency drift commonly found in H-maser signals (Tesmer, 2004). In Weinbach and Schön (2011), a single quadratic polynomial has also been successfully used to model the clock of a GNSS receiver driven by an active hydrogen maser over a 24-hour interval. However, the parametrization with a second-order polynomial cannot capture small subdaily variations of the frequency drift that are not uncommon for hydrogen masers. It is therefore common practice to model remaining clock variations using additional piece-wise linear corrections at 1- to 6-hour intervals (Ryan et al., 1993; Tesmer, 2004). Alternatively, a piece-wise linear model with relative constraints can be employed directly (Schmid, 2009). The fact that in this case the clock constraints have to be relaxed to some extent in order to account for the constant part of the frequency drift, does normally not degrade the solution noticeably since the drift is generally very small ($<1 \times 10^{-15}/\text{day}$). More importantly, and in contrast to a quadratic model, small changes in frequency drift can be modeled very well by the piece-wise linear approach. If nevertheless an exceptionally large frequency drift exists, it can be easily removed by fitting a quadratic polynomial to the clock time series before the main adjustment step.

Alternatively, more sophisticated approximation functions such as cubic splines (de Boor, 1978) could be used to model the clock behavior. However, despite resulting in a differentiable clock offset function, splines do not provide significant advantages. In addition, the spline approximation highly depends on the knot spacing, which is difficult to derive from the given frequency stability of the oscillator.

Due to its simplicity and flexibility, the piece-wise linear parametrization was selected for the modeling of clocks in the batch adjustment module of the developed PPP software.

There are different ways of implementing the piece-wise linear parameter estimation. In the simplest approach, the time-varying parameter to be estimated $c(t)$ is described by individual offsets d and slopes m that are set up separately for every linear segment j of length Δt with starting time $t_{0,j}$

$$c_j(t) = d_j + m_j \cdot (t - t_{0,j}), \quad t_{0,j} < t < t_{0,j} + \Delta t, \quad (4.65)$$

which can be connected by additional continuity constraints at the interval boundaries, expressed by the following pseudo-observation with a small variance $\sigma_{\varepsilon, cont}^2$

$$0 + \varepsilon = d_j + m_j \cdot \Delta t - d_{j+1}, \quad D(\varepsilon) = \sigma_{\varepsilon, cont}^2. \quad (4.66)$$

Alternatively, the continuity at the interval boundaries can be modeled directly, e.g., by

$$c_j(t) = d_1 + \sum_{k=1}^{j-1} m_k \Delta t + m_j \cdot (t - t_{0,j}) \quad (4.67)$$

or with less correlations using the values d_j at the interval boundaries as parameters

$$c_j(t) = d_j \left(1 - \frac{t - t_{0,j}}{\Delta t}\right) + d_{j+1} \left(\frac{t - t_{0,j}}{\Delta t}\right). \quad (4.68)$$

In case of strong continuity constraints (4.66), all three implementations are equivalent. Considering n piece-wise linear segments, the number of parameters to be set up in the normal equations when using (4.65) is $2 \cdot n$ while in the cases (4.67) and (4.68) it is only $n+1$. Therefore, the implementations according to (4.67) or (4.68) are generally preferable. Despite the larger number of parameters, the first approach has been implemented for clock modeling, simply because it is slightly easier to introduce jumps in the piece-wise linear function. In contrast, the tropospheric zenith delay which is always continuous is modeled according to (4.67). In both implementations, (4.65) and (4.67), it is possible to constrain the drift parameters of consecutive segments using pseudo-observations of the form

$$0 + \varepsilon = m_{j+1} - m_j, \quad D(\varepsilon) = \sigma_{\varepsilon, slope}^2 \quad (4.69)$$

with a variance $\sigma_{\varepsilon, slope}^2$ that is a function of the temporal stability of the stochastic process, e.g., the tropospheric zenith delay or the time offset of the receiver clock. Consequently, the constraints imposed on the clock drift can be adjusted by varying either the length of the piece-wise linear segments, or the constraints between consecutive drift parameters. Choosing suitable values for the interval length and drift constraints thus allows the estimation of an arbitrarily smooth sequence of clock parameters. Figure 4.3 shows a schematic view of the piece-wise linear parametrization.

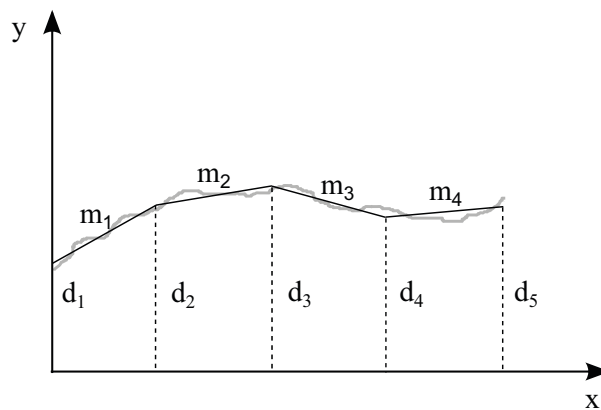


Figure 4.3: Schematic view of the piece-wise linear approximation of a random-walk process

In order to validate the piece-wise linear clock parametrization, the approximation error of the model has been tested by fitting the piece-wise linear function to a number of simulated clock time series. Figure 4.4 shows the difference between the simulated signal of an active hydrogen maser and the piece-wise linear model for 96 parameter intervals covering one hour of data each. Due to a slightly worse fit, the first

and the last segment were neglected. The dispersion is generally largest in the middle of the modeling interval, where it reaches an RMS error of approximately 0.7 mm (2.2 ps) for this example. This value is well below the observation noise of the GPS L_3 carrier phase observations projected onto the epoch-wise receiver clock estimates. Thus, a 1-hour spacing of the piece-wise linear segments appears to be adequate for the modeling of the time error of H-maser clocks.

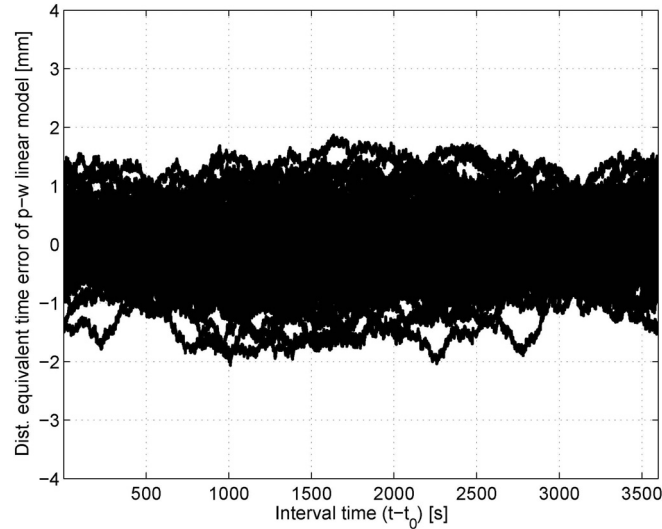


Figure 4.4: Approximation error of a 1-hour piece-wise linear model with respect to a simulated H-maser time signal for 96 intervals, the standard deviation in the middle of the interval is approximately 0.7 mm \approx 2.2 ps

Again, it has to be emphasized that not only the oscillator signal alone and its frequency stability determines the evolution of the GPS receiver clock offset but also the electric hardware delays in the whole system consisting of the receiver unit, the antenna, the antenna cable and the frequency distribution path. These additional aspects are discussed in Chapter 5. When the delay variations of these components are significant, the clock constraints have to be relaxed accordingly.

4.4.2 A clock model for use in a Kalman filter

The most simple model to account for GPS clock errors in the Kalman filter is to set up one state variable for each clock and allow for arbitrary increments by adding large amounts of noise during the covariance update step. Generally, there is no problem in proceeding this way as long as the process noise is large enough to account for all variations of the clock offset. However, when using such a one-state model, we cannot take advantage of a stable clock. If we want to use the information concerning the frequency stability of the oscillator we have to employ at least a two-state model consisting of a time offset x_p and a frequency offset x_f . In some cases also a third state, describing a linear frequency drift, may be justified (Hutsell, 1995). In addition to an initial time synchronization error, the time offset at a given epoch is the integral of the frequency offset from the initial epoch to this epoch. This is expressed by the following system of first-order differential equations

$$\begin{bmatrix} \dot{x}_p \\ \dot{x}_f \end{bmatrix} = \begin{bmatrix} 0 & 1 \\ 0 & 0 \end{bmatrix} \begin{bmatrix} x_p \\ x_f \end{bmatrix} + \begin{bmatrix} w_p \\ w_f \end{bmatrix}. \quad (4.70)$$

This model is also referred to as *random ramp*, where x_p is the random ramp process and x_f represents the slope of the ramp (Strang and Borre, 1997), which itself is modeled here as a random walk. Since the dynamics matrix in (4.70) is time-invariant, the state transition matrix Φ depends only on the time interval Δt and reads

$$\Phi = \begin{bmatrix} 1 & \Delta t \\ 0 & 1 \end{bmatrix}. \quad (4.71)$$

As described in Section 4.2, the precision of the predicted states must be propagated in time by updating the parameter cofactor matrix \mathbf{Q}_x . This is done according to the laws of error propagation and the given temporal stability of the state variables during the prediction interval reflected by the process noise cofactor matrix $\mathbf{Q}_{w,k}$

$$\mathbf{Q}_{x,k} = \Phi_{k-1} \mathbf{Q}_{x,k-1} \Phi_{k-1}^T + \mathbf{Q}_{w,k}. \quad (4.72)$$

For the clock states the process noise matrix $\mathbf{Q}_{w,k}$ essentially depends on the frequency stability of the oscillator at hand, which in turn is usually expressed in terms of Allan variances or power spectral density coefficients h_α . Using the relations in Table 3.1, the coefficients h_α can be derived from the Allan variance of a specific oscillator.

More specifically, the process noise cofactor matrix $\mathbf{Q}_{w,k} = E(\mathbf{w}\mathbf{w}^T)$ is derived from the spectral density matrix containing the spectral amplitudes of the noise S_p and S_f , that drives the time and frequency offset, respectively

$$\mathbf{Q}(t) = \begin{bmatrix} S_p & 0 \\ 0 & S_f \end{bmatrix}. \quad (4.73)$$

Using the relationship (4.31), we can write for the cofactor matrix

$$\mathbf{Q}_{w,k} = \int_{t_{k-1}}^{t_k} \Phi(\tau) \mathbf{Q}(t) \Phi(\tau)^T d\tau. \quad (4.74)$$

Inserting Φ and $\mathbf{Q}(t)$ into (4.74) and integrating over a time step Δt yields

$$\mathbf{Q}_w = \begin{bmatrix} S_p \Delta t + S_f \frac{(\Delta t)^3}{3} & S_f \frac{(\Delta t)^2}{2} \\ S_f \frac{(\Delta t)^2}{2} & S_f \Delta t \end{bmatrix}. \quad (4.75)$$

The major problem consists in the determination of the spectral amplitudes of the process noise. A common method is to neglect the flicker noise contribution and try to approximate the clock behavior by white and random walk frequency noise only (Herring et al., 1990). With this approximation we may write (Zucca and Tavella, 2005)

$$\sigma_y^2(\tau) \approx \frac{S_p}{\tau} + \frac{S_f \tau}{3} \quad (4.76)$$

or with Brown and Hwang (2005)

$$S_p \approx \frac{h_0}{2} \quad \text{and} \quad S_f \approx 2\pi^2 h_{-2}. \quad (4.77)$$

Another model to compute the elements of the process noise matrix from the h_0 , h_{-1} and h_{-2} coefficients was given by van Dierendonck et al. (1984) as

$$\mathbf{Q}_w = \begin{bmatrix} \frac{h_0}{2} \Delta t + 2h_{-1} \Delta t^2 + \frac{2}{3} \pi^2 h_{-2} \Delta t^3 & \frac{h_0}{2} + 2h_{-1} \Delta t + \frac{2}{3} \pi^2 h_{-2} \Delta t^2 \\ \frac{h_0}{2} + 2h_{-1} \Delta t + \frac{2}{3} \pi^2 h_{-2} \Delta t^2 & \frac{h_0}{2\Delta t} + 4h_{-1} + \frac{8}{3} \pi^2 h_{-2} \Delta t \end{bmatrix}. \quad (4.78)$$

This matrix was derived by van Dierendonck et al. (1984) using the impulse response of the different processes and it includes an approximation of the impact of flicker frequency noise (h_{-1}), which cannot

be modeled exactly by a finite order state model. Because the inclusion of a flicker term is deemed important, while the information concerning the random-walk frequency noise cannot always reliably be determined, expression (4.78) has been adopted in this work.

Note, that the elements $\mathbf{Q}_{w,12}$ and $\mathbf{Q}_{w,22}$ of (4.78) given in the original paper were corrected according to (Brown and Hwang, 2005, p.430).

In practice, even in the case of epoch-wise independent receiver clock estimation, a two-state model is often preferable because the clock parameter increments during the measurement update step are much smaller than for a one-state model and as a result numerical instabilities are avoided. Alternatively, the size of the clock parameter increments can of course be reduced by introducing approximate receiver clock estimates, e.g. from a preliminary pseudorange solution.

4.5 Frequency stability requirements for clock modeling

After having reviewed the statistical measures to describe the frequency and time stability of precision oscillators and the parameter estimation approaches, we can now come back to the fundamental question: how stable does an oscillator have to be to enable clock modeling at the precision level of the GPS carrier phase observations?

Generally, clock modeling is reasonable only when the accuracy of the time offset predicted by the model is better than the accuracy of the clock offset estimated from the data epoch by epoch without constraints. Of course, the accuracy of the clock estimates depends not only on the receiver tracking noise but also on the observation geometry and the entire range of errors affecting the GPS signals. In practice, the accuracy of the receiver clock estimates is significantly affected by errors in the satellite positions and clock offsets as well as residual troposphere modeling errors and multipath effects. Since we want to avoid a degradation of the solution through the addition of clock constraints under all circumstances, the lower bound of the precision of the epoch-wise clock offsets has to be used. Therefore, only the measurement noise and the satellite geometry are considered in the following approximation, whereas systematic error sources such as multipath are neglected. According to (4.7), the cofactor matrix of the parameters \mathbf{Q}_{xx} is related to the cofactor matrix of the observations \mathbf{Q}_{ll} by

$$\mathbf{Q}_{xx} = (\mathbf{A}^T \mathbf{Q}_{ll}^{-1} \mathbf{A})^{-1}. \quad (4.79)$$

The corresponding covariance matrix is obtained by scaling the cofactor matrix with the noise level of the observations given by the variance factor σ_0^2

$$\mathbf{C}_{xx} = \sigma_0^2 \mathbf{Q}_{xx}. \quad (4.80)$$

Assuming that the random variability of the observations is correctly reflected by the given stochastic model, the mapping of the random observation noise, in terms of its standard deviation σ_0 , onto the receiver clock estimates is thus completely described by the corresponding diagonal element of the parameter cofactor matrix q_{tt} . In the case of kinematic positioning, the square root of this value, $\sqrt{q_{tt}}$, is also referred to as *Time Dilution Of Precision* (TDOP). The TDOP is a function of the satellite geometry and varies with respect to receiver location, number of satellites in the constellation, the elevation mask as well as potential obstructions. Empirical analysis in the course of this work showed that the lower bound of the TDOP is approximately 0.5 for equatorial to mid-latitude stations and 0.7 in the polar regions. These values apply to equal weighting of the observations. In practice, an elevation-dependent weighting of the observations, which accounts for the increased troposphere modeling deficiencies and multipath errors at low elevations is frequently applied. A simple and widely used weighting function is

$$p(e) = \sin^2 e, \quad (4.81)$$

where e is the elevation angle of the observation. When applying this weighting scheme, the TDOP is increased to approximately 1.6 for an equatorial observing site and to 2.5 for a station near the poles. In contrast to the average TDOP values, the minimum TDOP was found to depend only weakly on the chosen elevation cut-off angle.

The carrier phase observation noise is traditionally assumed to be around 1% of the carrier wavelength, i.e. around 2 mm for the GPS L_1 and L_2 signals. As pointed out in Section 2.3.1, forming the ionosphere-free linear combination amplifies the noise of the individual L_1 and L_2 observations by a factor of 3, yielding a standard deviation of approximately 6 mm. Modern receivers, however, are providing carrier phase observations with 1 mm standard deviation and below. Consequently, 3 mm ionosphere-free observation noise seems to be a reasonable choice for the L_3 observation noise at high elevations. This value was also confirmed by analyzing post-fit PPP carrier phase residuals at high elevations for a number of IGS stations.

In summary, the lowest attainable precision of the receiver clock offsets in kinematic PPP with elevation-dependent weighting can be approximated by

$$\sigma_{CLK,min} \approx TDOP_{min} \cdot \sigma_{L3} = 1.6 \cdot 3 \text{ mm} = 4.8 \text{ mm} = 16 \text{ mm}. \quad (4.82)$$

As stated above, elevation-dependent weighting is very common for terrestrial applications mainly because of troposphere modeling deficiencies at low elevations. In contrast, observations recorded by a space-borne GPS receiver are not affected by tropospheric delays. In addition, experience with JPL's BlackJack GPS receiver in several low Earth orbiter (LEO) missions has shown that the multipath and tracking noise increase due to the lower signal-to-noise ratio of observations near the antenna horizon are moderate (Montenbruck and Kroes, 2003), thus justifying an equal weighting of the observations over the entire elevation range. This in turn, yields a minimum TDOP smaller than 1. Considering also the low overall carrier phase observation noise of the BlackJack receiver, 1-2 millimeter precision of the receiver clock offsets appear to be feasible for a space-borne GPS receiver during periods with good satellite coverage. We will come back to this point in Section 7.4, where clock modeling for the receivers on board of the GRACE satellites is investigated.

So far, only kinematic positioning has been discussed, because in this case the concept of TDOP is well established. However, the mapping of the observation errors onto the receiver clock estimates for a static receiver is described in the same way by the respective element of the cofactor matrix q_{tt} . For a static receiver with elevation-dependent weighting the minimum value of $\sqrt{q_{tt}}$ ranges between approximately 0.5 around the equator to 0.6 near the poles. Consequently, the precision of the receiver clock estimates obtained in a static solution is typically 3-4 times better than for a kinematic solution.

When neglecting systematic observation errors, the observation noise projected onto the receiver clock estimates $\sigma_{t,rx}$ can be expressed by an Allan deviation with $\sigma_y(1s) = \sigma_{t,rx}$ and a slope of -1 in a log-log plot, i.e. white phase noise. In Figure 4.5 this GPS receiver clock "observation noise" for kinematic pseudorange and carrier phase solutions is plotted along with the Allan deviations of a number of high-precision frequency sources that were already discussed in Section 3.5.

As a rule of thumb, clock modeling is reasonable for time intervals, where the Allan deviation of the oscillator's random frequency errors is below the GPS observation noise projected onto the receiver clock estimates. Inspecting the figure, it becomes clear, that currently only hydrogen maser and fountain clocks can be modeled over extended periods in GPS positioning based on carrier phase observations. In addition, high-performance OCXO can potentially be modeled over short time intervals. Finally, the great potential of optical frequency standards for clock modeling in GNSS applications is evident.

4.6 Clock jump detection and modeling

So far we have discussed clock modeling for the case, that the frequency standards operate according to their specifications. In most situations this is an absolutely legitimate assumption. However, during

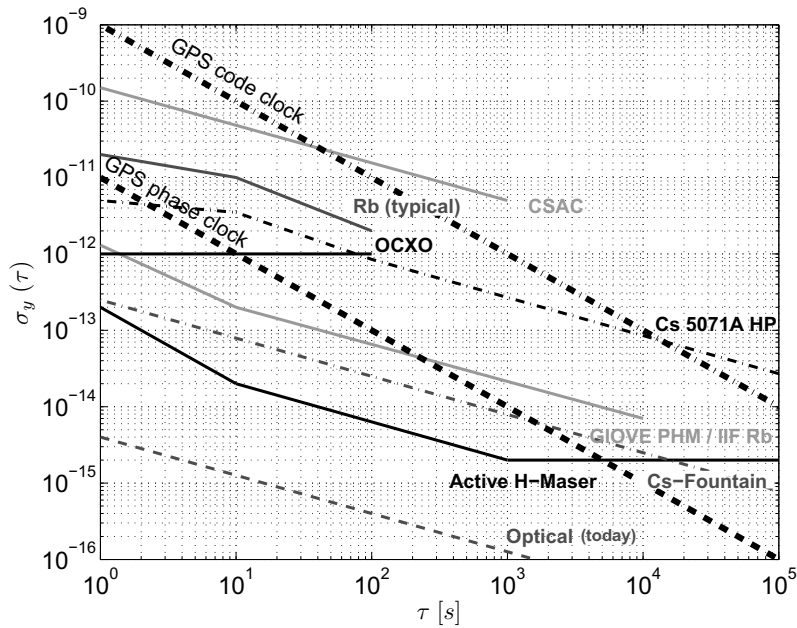


Figure 4.5: Allan deviation for selected high-precision frequency standards. The two bold dashed lines with a slope of -1 indicate an approximation of the lower bound of the GPS observation noise for ionosphere-free code and carrier phases, projected onto the epoch-wise receiver clock estimates in a kinematic positioning solution. For references regarding the frequency stabilities of the different clocks see Figure 3.5.

the practical operation of high-end atomic clocks, technical problems leading to a temporal interruption or degradation of the clock signal are not uncommon. There are numerous potential sources that may corrupt the clock signal, such as power outages, environmental influences, failure of electronic components causing a loss-of-lock of the clock signal or significant modulation sidebands, etc.. In addition, the GNSS receiver may lose lock of the clock signal or deliberately introduce jumps in order to maintain a certain degree of physical time synchronization. For a reliable clock modeling it is therefore essential, that the processing software is able to detect jumps and periods of bad clock performance and switch into epoch-wise clock synchronization mode, if necessary.

In the *batch least-squares adjustment*, the detection of bad receiver clock behavior is generally difficult because all epochs are processed in a single step. Therefore, an iterative procedure had to be adopted. Large discontinuities are detected in a preprocessing step by analyzing the mean time-differenced pseudorange observations. This procedure relies on the availability of good approximate receiver coordinates. Therefore, this very simple preprocessing procedure is limited to static and pseudo-kinematic positioning, truly kinematic data would probably need to be preprocessed by some kind of parameter estimation, e.g. a filter approach similar to the Kalman filter algorithm described below. Smaller clock jumps that cannot be detected during preprocessing, must be identified at the level of the carrier phase post-fit residuals along with remaining small cycle slips. In either case, a detected clock jump must be accounted for by splitting the piece-wise linear clock interval at the epoch of the jump and omitting the corresponding continuity constraint. If the clock jump was detected in the post-fit residuals, the parameter estimation must be iterated until no further clock jumps or cycle slips can be identified.

In the *Kalman filter*, clock jumps can be detected by analyzing the vector of innovations \mathbf{d} , cf. (4.35). Using the corresponding cofactor matrix \mathbf{Q}_{dd} , the squared sum of residuals of the epoch can be computed

$$\Omega = \mathbf{d}^T \mathbf{Q}_{dd} \mathbf{d} \quad (4.83)$$

and tested against an a priori variance factor σ_0 in an epoch-wise compatibility test using the test quantity

$$T = \frac{\Omega}{\sigma_0^2} \sim \chi_{1-\alpha;f}^2, \quad (4.84)$$

with f being the degree of freedom, i.e. the number of observations of the current epoch (Niemeier, 2002, p. 387ff). If the test fails and the majority of the innovations are affected by a similar offset, a clock jump is likely to have occurred. If a clock jump has been identified in this way, it can be generally accounted for, by adding a large amount of process noise to the clock states. Special cases arise for the so called “ms”-jumps and other receiver-specific jumps of known size. These can of course be corrected, based on their deterministic value.

The described jump detection procedure is usually very reliable, however, if the receiver is kinematic, the redundancy for the clock jump detection may be low because 4 parameters have to be estimated at each epoch. For periods with bad satellite observation geometry small clock jumps can therefore be difficult to detect.

Often clock jumps are accompanied by a tracking interruption and thus missing epochs. This has to be taken into account by the data screening algorithm. As a precaution, clock discontinuities are currently introduced for every data gap. Based on the experience with the data processing for this work, it was found that cases where the continuity of the clock across data gaps is maintained are relatively rare.

In general, the identification of a gradual degradation or periodic deviations of the clock signal are much more challenging than the detection of jumps. Thus, further work is required to develop integrity tests for the clock signal, in particular when it comes to kinematic applications.

5 Stability of Receiver Hardware Delays

In Section 4.5 the frequency stability of different high-precision frequency sources with respect to the requirements for GNSS clock modeling was analyzed. It could be shown that even with today's frequency standards clock modeling over significant time intervals should be feasible. Furthermore, we have seen that optical clocks can potentially be modeled for a period of one day and beyond. However, a major problem associated with clock modeling in practice are delay variations in the GNSS receiver system. In conventional geodetic GNSS analysis, signal delays in the antenna, the antenna cable and the receiver are comfortably absorbed by the estimated epoch-wise independent receiver clock offsets. This is the reason why there have been relatively few studies that address the variability of these hardware delays in the geodetic community. In contrast, timing users of GNSS have to carefully calibrate all delays of the satellite and clock signals in order to accurately compare the PPS timing signals generated by distant clocks¹. Therefore, it is thanks to this user-group that we have some knowledge about the temperature sensitivity of the GNSS receiver components at all (e.g. Overney et al., 1997; Powers et al., 1998; Larson et al., 2000). The number of studies in this field is, however, rather scarce. In particular, information on the temperature sensitivity of the latest antenna and receiver generation is hardly available.

In this chapter some of the work carried out in the field of hardware delay measurements in the past will be reviewed and new experimental results for more recent GNSS equipment will be added. Finally, an error budget for the different components is given and recommendations for limiting the temperature-induced delay variations are formulated.

5.1 Types of hardware delay variations

In a typical receiver setup with an external oscillator we can identify four basic components that may be affected by electric delay variations (Rieck et al., 2003; Schildknecht and Springer, 1998):

- The GNSS antenna consisting of the antenna element and the Low Noise Amplifier (LNA),
- the antenna cable,
- the GNSS receiver, and
- the power splitters and amplifiers used to distribute the GNSS and clock signals.

Note, that other important sources of clock instabilities, such as shock, vibration, magnetic field changes, etc., that are likely to occur in real navigation applications have been neglected in this analysis, because the hydrogen maser clocks analyzed in this work are not portable. For pseudorange-based navigation a number of studies addressed the impact of these errors on the clock performance. However, different conclusions are drawn regarding the impact of the errors in practice. While van Graas et al. (2011) observed a degradation of the clock performance by a factor of up to 30 in a test flight environment compared to laboratory measurements, Bednarz and Misra (2006) report a relatively small degradation on the order of 60 % for 1 min predictions of a commercial rubidium clock on board of a rough-riding pick-up truck.

¹A good example for the importance of hardware delay stability in time synchronization systems can be seen in the claim of the OPERA group to have possibly measured the velocity of a Neutrino beam, as being higher than the speed of light. This caused commotion in the scientific community and the media throughout the world. Eventually, the results were disproved and one of the two potential errors identified in the subsequent investigations of the timing system was tracked down to a loose plug in the fiber-optic link connecting the underground laboratories with the GPS receiver on the surface (Reich, 2012).

5.2 Antenna effects

Information on the temperature-induced delay variations in GNSS antennas are scarce. This is because it is difficult to measure. If the antenna is put into a climate chamber, the real GNSS signals cannot be received anymore, but if simulated signals were used, the sensitivity of the transmitter antenna would need to be measured first. Therefore, past investigations aimed at stabilizing the antenna with respect to temperature changes using special heating installations or focused on the antenna's low noise amplifier (LNA) alone. Based on experiments with temperature stabilized and not stabilized GPS antennas, Petit et al. (1998) showed a significant impact of temperature variations on the hardware delay variations of the antenna and the antenna cable. They suspected a significant temperature sensitivity of the antenna unit but could not rigorously separate the effects of the antenna cable. In contrast, Rieck et al. (2003) performed a temperature sensitivity analysis with the LNA of an Ashtech choke ring antenna. They reported a very low temperature coefficient of less than 0.2 ps per Kelvin. An alternative approach is to compare estimated receiver clock differences with local air temperature differences at sites with well-behaved hydrogen maser frequency standards. This method is based on the assumption, that the difference between the hydrogen maser clocks at two or more sites can be modeled by a straight line or a low-order polynomial and that the antenna is the only element in the receiver system that is subject to temperature-induced delay variations. If these conditions hold, the temperature coefficients of the antennas at two stations A and B can be derived from the estimated receiver clock differences Δt_{AB} by least-squares adjustment using the following functional model proposed by Ray and Senior (2001)

$$\Delta t_{AB} + v = k_A \cdot T_A - k_B \cdot T_B + k_0 + k_1 \cdot t, \quad (5.1)$$

with

Δt_{AB}	the observed time difference between the receiver clocks at station A and B,
k_A, k_B	the temperature coefficient of station A and B,
k_0, k_1	the relative receiver clock offset and drift parameters,
T_A, T_B	the temperature readings near the antenna at station A and B and
t	the observation time.

For the 2400 km baseline between the IGS stations USNO and AMC2, located in Washington D.C. and Colorado Springs, Ray and Senior (2001) derived an upper limit of 2 ps/K for the short term (i.e. subdaily) temperature sensitivity of the Dorne Margolin antenna type used at both observing sites.

The same approach can also be applied in single station mode using the PPP method described in Section 2.5. In this case we do not compare two receiver clocks but rather one receiver clock with respect to the GNSS system timescale as introduced via the satellite clock corrections. Thanks to the excellent stability of the IGS rapid and final timescales, being the weighted mean of a large number of clocks including more than 15 H-masers, this represents no limitation of the method when IGS products are used.

Figure 5.1 shows the PPP derived receiver clock offsets for IGS station WTZR during GPS week 1580 (April 2010) together with the local temperature recordings. At first glance, no correlation between the two time series can be identified. The long term trend of the receiver clock time series, which is mainly caused by frequency drift of the maser and the IGS timescale, can be approximated well by a third-order polynomial. Thus by adapting the model (5.1) through addition of higher-order polynomial coefficients and removal of the second station, the temperature sensitivity k_A of the outdoor equipment of the station, including the antenna, can be derived using the following model

$$\Delta t_{A,IGST} + v = k_A \cdot T_A + k_0 + k_1 \cdot t + k_2 \cdot t^2 + k_3 \cdot t^3. \quad (5.2)$$

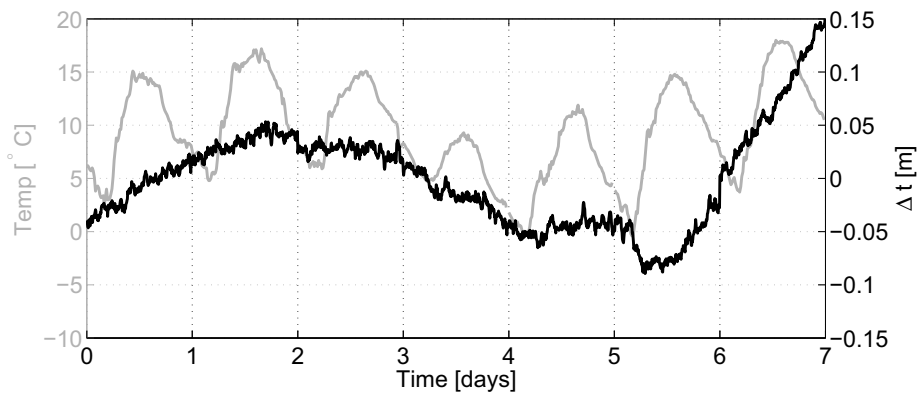


Figure 5.1: PPP receiver clock time series and local air temperature records for the IGS station WTZR during GPS week 1580 (April 2010)

Based on the data of the IGS station WTZR for GPS week 1580 (Fig. 5.1), a temperature coefficient of the signal delay of $-0.65 \text{ mm/K} \pm 0.08 \text{ mm/K}$ ($-2.2 \text{ ps/K} \pm 0.3 \text{ ps/K}$) is obtained for the Leica AR25 antenna and the portion of the antenna cable that is exposed to the outside temperature variations. This is in good agreement with the upper bound of 2 ps/K reported by Ray and Senior (2001) for a Dorne Margolin type antenna given above. For comparison, a significant temperature coefficient of the signal delay of $-4 \text{ mm/K} \pm 0.14 \text{ mm/K}$ ($-13.1 \text{ ps/K} \pm 0.5 \text{ ps/K}$) is obtained for the IGS station PTBB. However, this larger temperature sensitivity can be attributed primarily to 20 m of outside running RG 214 cable.

Of course the described procedure provides only a rough estimate of the upper limit of the temperature sensitivity due to the small time interval and the limited temperature range. It shows however, that for the frequently used Leica AR25 reference station antenna, the temperature sensitivity is not a limiting factor for clock modeling intervals up to one hour, since during this time interval the temperature variation will be always well below 10° C .

5.3 Cables and distribution amplifiers

In various studies it has been shown, that temperature-related delay variations in the antenna cable can be an important error source for precise time and frequency comparisons based on GPS carrier phases (e.g. Larson et al., 2000; Bruyninx et al., 1999). The temperature-induced electrical delay change of a coaxial cable is comprised of the physical length change and a change of the signal propagation velocity due to the temperature-dependence of the dielectric constant of the material used in the cable. Table 5.1 compiled by E. Burt and E. Powers of the USNO and accessible through the NRL website on IGS timing activities summarizes the temperature coefficients for a number of coaxial cables. The temperature coefficient for the commonly used cable type RG-58 with solid polyethylene (PE) dielectric has been added according to the results reported by Overney et al. (1997). Obviously, the impact of the antenna cable can be greatly reduced, when a foam dielectric, e.g. HELIAX[®]-type, antenna cable is used instead of a standard coaxial cable using a solid PE dielectric.

Hardware delay variations are most critical for time transfer. In contrast, for clock modeling only fast delay changes up to a few hours have to be limited, while seasonal and even diurnal variations are generally absorbed by the remaining clock parameters. Using a suitable cable type and keeping the length of the antenna cable short (e.g. $< 50 \text{ m}$) should reduce the delay variations of the antenna cable to a level, that does not compromise clock modeling.

Like any other equipment in the signal path, the addition of power splitters is a potential source of temperature sensitivity. However, no systematic investigations have been reported up to now. The same is true for the amplifiers used to distribute the clock signal in the laboratory. Apart from Bruyninx et al.

cable type	dielectric	v_{rel}	min $ps/^{\circ}C/m$	max $ps/^{\circ}C/m$	L1 loss [dB/100m]	L2 loss [dB/100m]
RG-58	solid PE	0.66	-0.42	-0.42	-	-
RG-142	solid PE	0.69	-0.36	-0.24	-	-
RG-213	solid PE	0.66	-0.42	-0.42	-	-
RG-214	solid PE	0.66	-0.40	-0.22	-	-
RG-223	solid PE	0.66	-0.76	-0.76	-	-
RG-393	solid PE	0.69	-0.35	-0.087	-	-
FSJ1-50A	foam	0.84	-0.028	0.036	24.8	21.7
FSJ2-50	foam	0.83	-0.036	0.036	17.0	14.3
FSJ4-50B	foam	0.81	-0.008	0.025	15.2	13.2
LDF2-50	foam	0.88	-0.031	0.023	14.8	12.9
LDF4-50A	foam	0.88	0.027	0.061	9.75	8.5
LDF5-50A	foam	0.89	0.019	0.045	4.97	4.56

Table 5.1: Temperature coefficients, relative velocity of propagation and signal attenuation for a number of coaxial cable types that can be used as GPS antenna cables

(2000) who reported a temperature sensitivity on the order of several 100 ps/ $^{\circ}C$ for such a distribution amplifier, there is no evidence that a properly functioning amplifier operated in a well temperature-stabilized environment adds significant noise to the oscillator signal.

5.4 Receiver effects

The hardware delay stability of the GPS receiver unit itself is probably the most critical factor for the success of clock modeling and for high-precision time and frequency transfer. Therefore, a number of studies exist that address the temperature sensitivity of the receiver delays. In a comprehensive study Fonville et al. (2007) found very large differences concerning the temperature sensitivity for a number of GPS receivers, ranging from 3 to 300 ps/ $^{\circ}C$ for the L1 and L2 carrier phases. In addition they showed, that the temperature sensitivity of the carrier phase tracking and the code tracking may be very different. Unfortunately, information about the temperature sensitivity of the receiver delays is usually not provided by the manufacturers. Thus, new receiver units should ideally be tested for their temperature sensitivity by the user. However, it seems as if for most receiver types, temperature effects can be reduced to a negligible level when the receiver is operated in a well temperature-stabilized environment. In order to identify potential remaining receiver effects in the case of almost perfect temperature stabilization an experiment has been set up in which a number of recent geodetic receiver models were operated side by side using a common external frequency source. The tested receiver types are listed in Table 5.2. The primary objectives of this receiver test can be summarized by the following questions:

- Are there significant differences with respect to the handling of the external clock signal among different receivers?
- What is the ultimate stability of the receiver hardware in a temperature-stabilized environment?

Experimental setup In order to be able to control the distance-dependent errors (e.g. atmospheric propagation delays) and site-specific errors (e.g. multipath) on the GPS observations, the receivers were operated in zero and short baseline configurations (Fig. 5.3). In addition, the usage of a common frequency reference (common clock) has the unique advantage that the differential receiver clock offset is known (in theory) to be constant as long as the receivers are locked to the signal of the external

Rec ID	model	type	clock input signals
JAV	JPS Legacy	geodetic	frequency
LEI	Leica GRX1200GGPro	geodetic	frequency
TRM	Trimble NetRS	geodetic	frequency
GTR	Dicom GTR50	timing	1 PPS + frequency

Table 5.2: Receiver types used in the experimental test of the hardware delay stability

oscillator. The 10 MHz reference frequency and the 1 PPS signal were derived from an active hydrogen maser VCH-1003A. The maser frequency was distributed using an HPDA-15RM-E amplifier by Spectra Dynamics. In the zero-baseline setup, the receivers were connected to the same antenna via one signal splitter (Model ALDCBS, GPS Networking Inc.), in case of the short baseline two identical signal splitters were used to connect the receivers to two antennas approximately 4.3 meters apart on the roof of the Kopfermann Bau at PTB (Fig. 5.2). The receivers were operated in a laboratory, which is temperature-stabilized to 0.5 K. In order to minimize outdoor temperature influences in the short baseline experiment, HELIAXTM-type antenna cables (FSJ2-50, Andrew Corp.) were employed. In both experimental setups we used Leica AX1202 antennas.

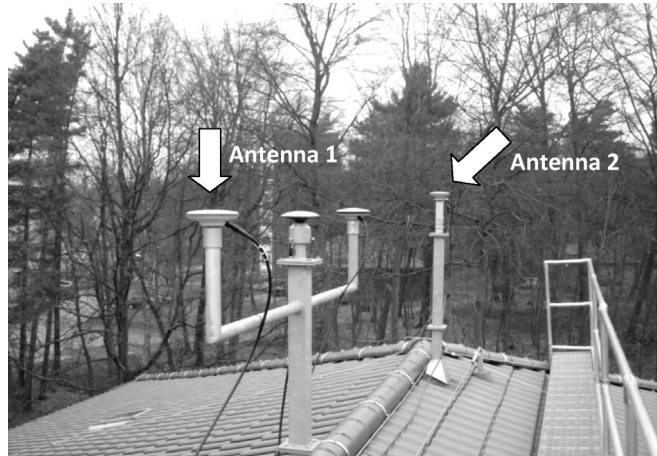


Figure 5.2: Antenna installations for the zero and short baseline receiver tests on the roof of the Kopfermann-Bau at PTB, Braunschweig

Data processing methodology The data processing follows a common-view approach based on single differences of the observations and has been applied in a similar way previously by Bruyninx et al. (1999). In the special case of zero and short baselines, the formation of single differences allows it to eliminate almost all error sources affecting the GPS signal. Starting with the observation equation for carrier phase observations (2.2) and dropping the frequency index i , the differences between the observations of one satellite j observed simultaneously by two receivers A and B can be written as

$$\Delta L_{A,B}^j = \Delta \rho_{A,B}^j + c \cdot \Delta \delta t_{A,B} + \Delta T_{A,B} + \Delta I_{A,B} + \Delta \lambda (\Delta n_{A,B}^j + \Delta \alpha_{A,B}) + \Delta \varepsilon_{L_{A,B}}. \quad (5.3)$$

Note, that the satellite clock offset δt^j , the relativistic effect δt_{rel} and the satellite hardware delay α^j are eliminated. In the special case of a very short baseline (SBL), all atmospheric propagation delays and orbit errors also cancel, because they can be considered identical for both receivers. The geometric term $\Delta \rho_{A,B}^j$ can be computed from accurately known satellite and receiver coordinates and removed from the single differences. This yields the reduced single difference observations $\Delta \bar{L}_{A,B}^j$. Implicitly, the geometric term also accounts for the fact that the two receivers may observe at slightly different times.

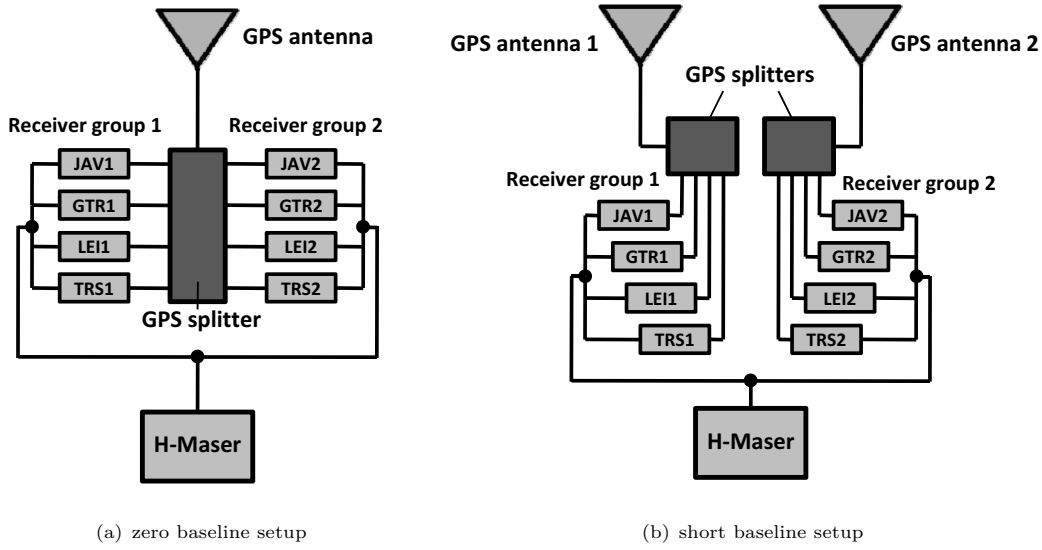


Figure 5.3: Experimental setup of the zero and short baseline, common clock receiver tests

The difference may be as large as 1 ms since the clock of most geodetic receivers is kept in the range of ± 0.5 ms with respect to GPS time. During this time the satellites move several meters. By computing the satellite position for the actual time of transmission and removing the computed distance from the raw phase observation we can account for these position differences. The receiver antenna phase center variations can either be eliminated by using identical antennas, properly oriented, or by applying suitable calibration values (Wübbena et al., 2000). That means, in addition to the differential receiver clock error, the differential hardware delay and the constant ambiguity term only site-dependent errors $\Delta mp_{A,B}$ (mainly multipath effects) and measurement noise remain in the single differences of a *short baseline*

$$\Delta \bar{L}_{A,B}^j = \Delta L_{A,B}^j - \Delta \rho_{A,B}^j = c \cdot \Delta \delta t_{A,B} + \Delta \lambda (\Delta n_{A,B} + \Delta \alpha_{A,B}) + \Delta mp_{A,B} + \Delta \varepsilon_{L_{A,B}}. \quad (5.4)$$

By choosing identical antennas and antenna cables of equal length and with low temperature sensitivity, the differential effect of temperature variations in the short baseline experiment can be reduced to a negligible level.

Assuming furthermore an identical receiver tracking behavior with respect to multipath, this effect can be eliminated, or at least strongly mitigated, on the zero baseline. In addition, the differential hardware delays are reduced to the difference of the delays in the short cables driving the signal from the antenna splitter to the receiver and the path of the signal inside the receiver. Because the cables connecting the antenna splitter with the receivers are located in the temperature-stabilized laboratory, the differential delay should stay constant, regardless of the antenna and antenna cables in use. Consequently, the expression for single difference observations of a *zero baseline* reduces to

$$\Delta \bar{L}_{A,B}^j = c \cdot \Delta \delta t_{A,B} + \Delta \lambda (\Delta n_{A,B} + \Delta \alpha_{A,B}) + \Delta \varepsilon_{L_{A,B}}. \quad (5.5)$$

Inspecting (5.5), it can be noted that every variation of the single differences exceeding the measurement noise must be attributed to the handling of the external frequency inside the receiver, provided that no cycle slips occur.

In summary, by forming single differences we obtain, for every satellite in view, an estimate of the differential receiver clock error biased by the differential hardware delay (identical for all satellites) and a satellite-specific integer number of carrier phase cycles. We can now reduce the single differences to their common fractional part by subtracting a rounded number of carrier phase cycles and average these reduced single differences of all satellites. In order to assure good data quality a cut-off angle of 30°

has been applied. This averaging gives the final estimate of the differential receiver clock error that is analyzed in the following.

Due to the influence of the ionosphere for distances greater than a few tens of kilometers, generally the ionosphere-free linear combination L_3 must be used to compare distant clocks. Because of its importance in practical applications we will show results based on L_3 observations. Furthermore, the L_3 linear combination is an indicator of the consistency of the L_1 and L_2 observations and facilitates a direct comparison with the results obtained by Precise Point Positioning. Since the carrier phase ambiguities of the L_3 linear combination are not integers, the L_1 and L_2 ambiguities are fixed separately before forming the ionosphere-free linear combination.

Zero baseline results In the following we will show results obtained by processing 7 days of zero baseline, common clock data following the processing scheme outlined above. This setup can be regarded as the ideal case since both satellite and clock signals as well as environmental effects are identical for all receivers and thus cancel when between-receiver single differences (SD) are formed. The data were recorded between the 24th and the 30th of December 2008. Figures 5.4-5.7 show the differential receiver clock errors between pairs of receivers of the same type connected to the same oscillator and antenna. Consequently, we expect to see a constant time difference with random observation noise. Interestingly, significantly different patterns can be observed for the individual receiver types.

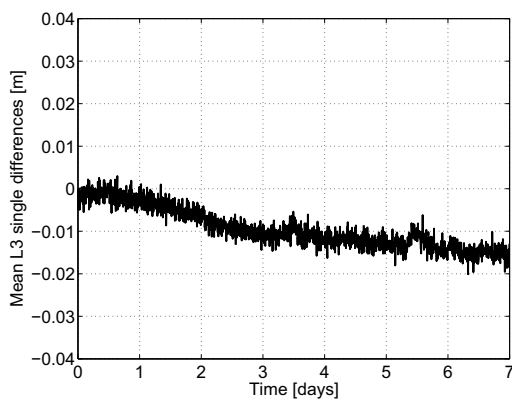


Figure 5.4: Differential L_3 carrier-phase receiver hardware delays for a pair of JPS Legacy receivers

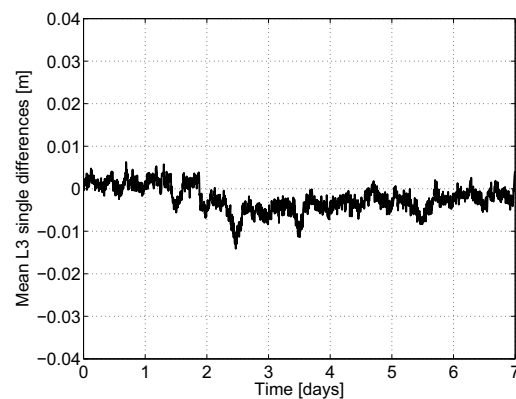


Figure 5.5: Differential L_3 carrier-phase receiver hardware delays for a pair of Leica GRX1200GGpro receivers

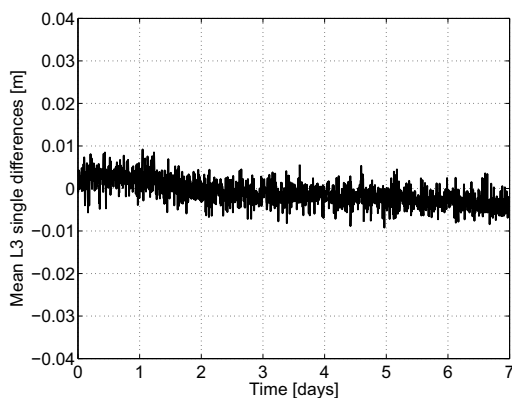


Figure 5.6: Differential L_3 carrier-phase receiver hardware delays for a pair of Trimble NetRS receivers

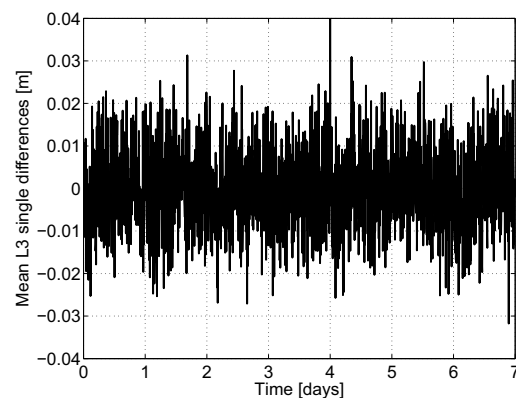


Figure 5.7: Differential L_3 carrier-phase receiver hardware delays for a pair of DICOM GTR50 timing receivers

The differential receiver clock errors of the two JPS receivers (Fig. 5.4) show the expected 3 mm (10 ps) high-frequency observation noise and a small non-linear drift leading to an accumulated time difference of approximately 1.5 cm (50 ps) after one week (Fig. 5.4). The two small peaks coincide with a brief tracking interruption of both receivers due to a power failure of the receiver feeding the antenna. This caused a jump in the single differences by a satellite-specific integer number of cycles.

The differential receiver clock error of the Leica receivers, shown in Figure 5.5, is not as smooth as that of the JPS receivers. Several small variations with an amplitude of up to 6 mm (20 ps) exceeding the measurement noise can be observed. The variations occur each day around the same time but with varying amplitude. The time difference accumulated after one week is almost negligible for this receiver type. Note, that two clock jumps in the Leica data were removed before plotting. According to the Leica support, this clock jump problem has been fixed in a later firmware version.

The Trimble NetRS receivers show both, a smooth and stable receiver clock behavior but also a small drift. The measurement noise is comparable to that of the JPS receivers. Note however, that the Trimble receivers can perform slightly better when Trimble antennas are used, because these antennas have a higher gain (50 dB) than the Leica antennas (40 dB) used in this experiment.

Finally, the DICOM GTR50 receivers exhibit a measurement noise that is about 4 times higher, compared to the other receivers. In contrast to the geodetic receivers, which simply lock their internal oscillator to the external frequency, this receiver type measures the time of its internal clock with respect to an external 1 PPS signal using a time interval counter (TIC). In the receiver specifications the manufacturer only guarantees a measurement resolution of better than 50 ps for the TIC. Based on the described zero baseline common clock data set the standard deviation of the receiver clock offsets was found to be approximately 25 ps on L1 and L2. No drift can be identified in the GTR50 data. Additional technical details regarding the GTR50 receiver can be found in Feldmann (2011).

Figures 5.8 and 5.9 show the Allan deviation and the modified Allan deviation of the differential receiver clock time series, respectively. Since all receivers use the same frequency signal, the impact of the external oscillator is eliminated. Thus, we should see only the measurement noise and potentially differential hardware delay variations. As expected, the Allan deviation (Fig. 5.8) for all receivers exhibits a -1 slope, which indicates white and/or flicker phase noise. The Allan deviation for the three geodetic receiver types is similar and reaches a frequency stability of $\sigma_y(\tau) = 1\text{-}2 \times 10^{-16}$ at one day averaging time, while the noise level of the GTR50 timing receiver is almost one order of magnitude higher.

The modified Allan deviation can be used to distinguish between white and flicker frequency noise. Inspecting Figure 5.9, we can see, that all receivers exhibit white phase noise (slope -3/2) up to averaging times of a few thousand seconds. While the timing receiver shows this behavior over the entire range of averaging times, the slope of the geodetic receivers eventually flattens, which possibly indicates flicker phase contributions or frequency drift.

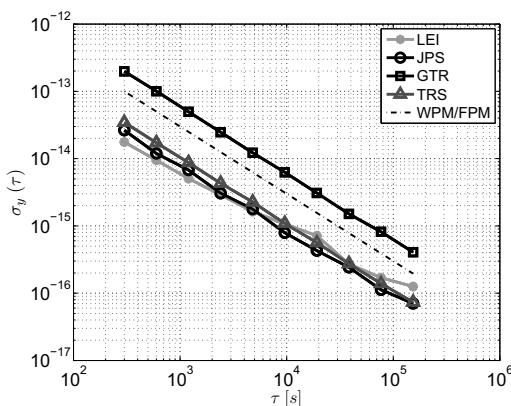


Figure 5.8: Allan deviation of the pairwise differential receiver hardware delays

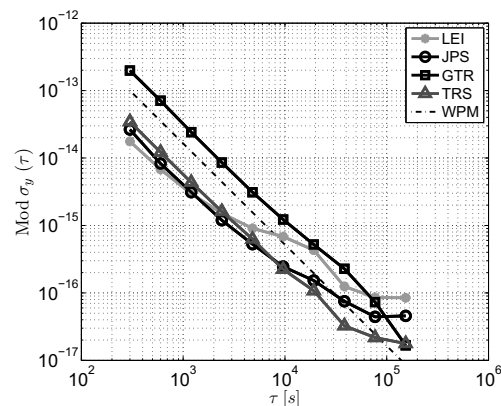


Figure 5.9: Modified Allan deviation of the pairwise differential receiver hardware delays

Up to this point only pairs of receivers of the same type were compared. In the next step, single differences between different receiver types were analyzed. Since the signal processing of receivers of different manufacturers can be regarded largely independent, this comparison is better suited to test if the receivers' internal clocks are properly related to the input frequency.

Figure 5.10 indicates that the Leica and the Trimble receiver clock estimates agree generally quite well. The drift of approximately 2 cm (66 ps) during the whole observation period is only slightly larger than the drift observed in the clock offsets between receivers of the same type. In addition we can observe clear daily variations with amplitudes up to 1 cm (33 ps) that are caused by the Leica receiver. In contrast, when comparing a JPS and a Trimble receiver, a drift of 6 cm (200 ps) during the 7 days of test data is found (Fig. 5.11). The same effect can be observed when the JPS receiver is compared to the Leica and the DICOM receivers. The drift found in the difference between the two JPS receivers (Fig. 5.4) is much smaller, probably because both receivers are affected similarly. This indicates a problem with this type of receiver or certain receiver settings. The differences between the DICOM and the Trimble receivers (Fig. 5.12) are dominated by the noise of the TIC of the DICOM receiver, but no drift can be identified.

We may conclude that the Leica, Trimble and DICOM receivers provide comparable receiver clock offsets, whereas the JPS receivers exhibit a small frequency bias with respect to the reference signal. Such a bias is generally not a problem for clock modeling but may adversely affect long-term time and frequency comparisons.

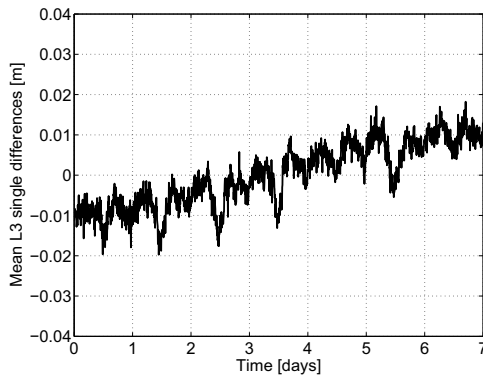


Figure 5.10: Differential L_3 carrier-phase hardware delays between a Leica GRX1200 and a Trimble NetRS receiver

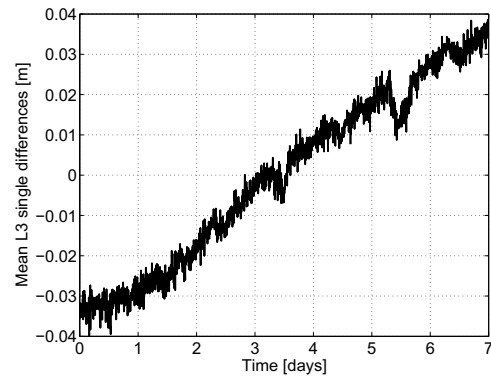


Figure 5.11: Differential L_3 carrier-phase hardware delays between a JPS Legacy and a Trimble NetRS receiver

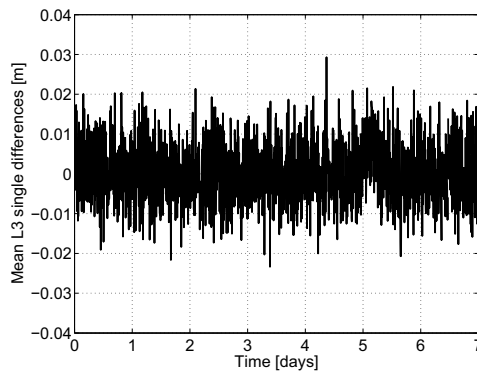


Figure 5.12: Differential L_3 receiver hardware delays between a DICOM GTR50 and a Trimble NetRS receiver

Short baseline results Although not directly related to the hardware delay stability discussed in this chapter, it is instructive to have a look at the influence of station-specific effects, e.g. multipath, by comparing the differential clock offsets derived from zero and short baseline data. Figure 5.13 shows the differential receiver clock error for the two Legacy receivers on a short baseline. This Figure may be compared to the zero baseline results shown in Figure 5.4. In Figure 5.14 the corresponding Allan deviations for the two JPS receivers are plotted. The Allan deviation for the short baseline is limited to averaging times $\tau < 20000$ s because only a 24-hour data set of short baseline data was available. Nevertheless, it becomes clear that the noise level of the L_3 clock estimates is increased by a factor between 2 and 3, resulting in a corresponding shift of the Allan deviation (Fig. 5.14). Extrapolation of the Allan deviation yields $\sigma_y(\tau) = 3 \times 10^{-16}$ at one day averaging time for a short baseline. This can be regarded as the lowest achievable Allan deviation at this averaging time using GPS L_3 observations obtained with current receivers.

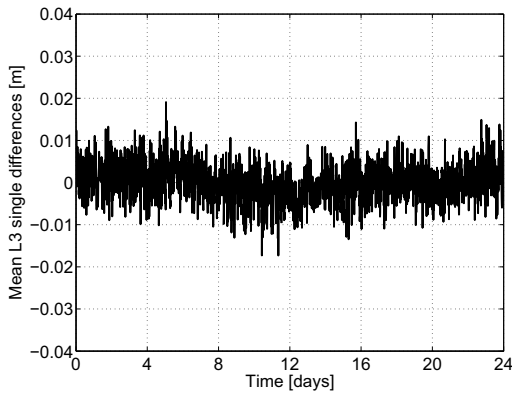


Figure 5.13: Differential L_3 carrier-phase clock error for two JPS Legacy receivers on a short baseline

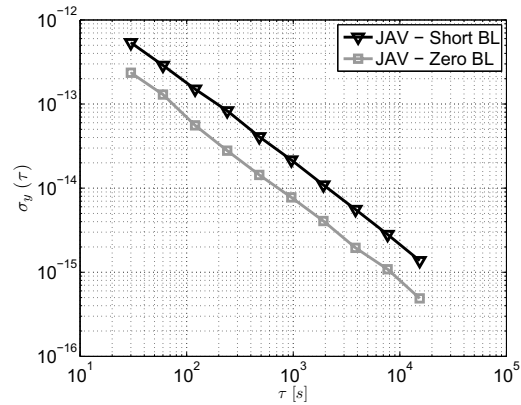


Figure 5.14: Allan deviations of the differential receiver clock error for two JPS Legacy receivers on a zero and a short baseline

5.5 Summary and recommendations

With respect to hardware delay stability three potential error sources were identified. The GNSS antenna, the signal distribution system and the receiver unit. While typical geodetic GNSS antennas appear to introduce only small delay variations due to ambient temperature changes (< 2 ps/ $^{\circ}$ C), the effect of delay variations in the antenna cable can be very significant. However, cable types with a low temperature sensitivity exist and are capable of reducing the impact of diurnal temperature variations over distances of at least 10-20 m to a negligible level. For the receiver unit, a proper temperature stabilization is deemed essential. Residual effects were found to be mostly drift-like, thus representing no limitation for clock modeling.

In summary, we may conclude, that by a proper equipment selection (e.g. antenna cables) and temperature control of the receiver unit and distribution amplifiers, the hardware delay variations can usually be reduced to a level, at which they do not compromise the modeling of the receiver clock.

6 PPP-based Clock Comparisons

The aim of the investigations presented in this chapter is to gain an understanding of the behavior of PPP-derived GPS receiver clock offsets, when the receiver is connected to an external hydrogen maser frequency standard and to assess the remaining error sources. However, usage of PPP for precise clock comparisons is an interesting field of research in its own right at the intersection of fundamental physics and geodesy. Therefore, the state-of-the-art of PPP-based, also called “geodetic”, time and frequency comparisons is covered in some detail in the following. For additional information regarding geodetic time and frequency transfer using IGS products the reader is referred to a comprehensive article by Ray and Senior (2005).

6.1 Fundamentals of GNSS time and frequency transfer

Apart from accurate ITRF coordinates and tropospheric zenith delays, the PPP algorithm provides us with a very precise estimate of the receiver clock offset with respect to the timescale imposed by the fixed satellite clock corrections. By forming differences between PPP receiver clock time series of two stations, the impact of the reference timescale is eliminated. The resulting time series is thus the time difference between the receiver clocks superposed by tracking noise, site-dependent effects such as multipath, unmodeled atmospheric delays and GPS satellite orbit and clock errors.

In the early days of GPS time and frequency transfer, clock comparisons were carried out in differential mode, using C/A code receivers (Allan and Weiss, 1980). Due to the limitations given by the requirement of common satellite visibility, this, so called *common-view*, technique was supplemented by dual frequency ionosphere-free pseudorange (P3) observations and the *all-in-view* approach (Weiss et al., 2005). In the latter approach all visible satellites at both stations are used to compute independent receiver clock offsets which are subsequently subtracted to obtain the clock differences. The PPP method can therefore be regarded as a refined all-in-view solution, that makes use of the highly precise carrier phase observations.

For geodetic applications, usually only the GPS carrier phase observations are used, because of their high precision of a few mm. Unfortunately, the carrier phases are ambiguous due to the unknown number of cycles for the first observation of each satellite track. Referring back to the carrier phase part of the PPP observation equations (2.14), it can be noted that the equation is actually singular, because of the linear dependence of the receiver clock parameter and the ambiguities. In other words, an arbitrary shift of the receiver clock error can be compensated by modifying all carrier phase ambiguities accordingly. In contrast, no such ambiguity exists for the pseudorange observations. Consequently, carrier phase observations alone cannot be used for time transfer, i.e. for the determination of the time difference between two remote clocks. They may, however, be used to monitor the evolution of the clock difference for the length of the analysis batch, which is usually denoted as *frequency transfer*. The PPP approach is a combination of code and carrier phases. As such it allows for both, time and frequency transfer, but at a different level of precision. While the frequency transfer precision in any carrier phase connected analysis batch is determined by the precision of the carrier phase observations, the absolute values, i.e. the actual time differences between the clocks, are determined by the average of the pseudorange observations. For accurate time transfer not only the use of pseudorange data is essential but also the calibration of the signal delays in the time and frequency distribution systems, the antenna cables and the GPS receiver units. The limited accuracy of this calibration usually dominates the uncertainty of PPP-based time transfer. For the proposed approach of clock modeling the absolute values of the receiver clock offsets are of minor interest as long as they are changing predictably. In the following,

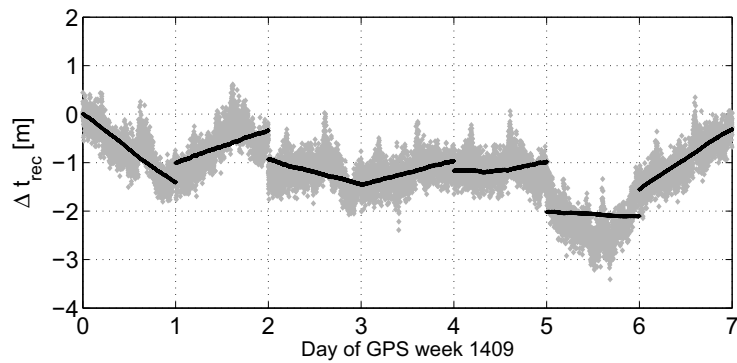


Figure 6.1: GPS receiver clock error with respect to IGS final timescale derived from P3 pseudoranges (gray) and PPP (black) for the IGS station YELL (Yellowknife, Canada) during GPS week 1409 (Jan 2007)

we will therefore only discuss frequency transfer and neglect any calibration issues. For information on the calibration procedure the reader is referred to, e.g., Petit et al. (2001) and Feldmann (2011). Figure 6.1 illustrates the relationship between a pseudorange-only (P3) and a PPP solution for the receiver clock offset of IGS station YELL with respect to the IGS timescale during GPS week 1409. The different noise levels of the two methods and the fact, that the precise PPP clock estimates are leveled by the less precise pseudorange observations are evident. The latter gives rise to large discontinuities between the PPP receiver clock estimates of independent daily computing batches, which are known as *day-boundary jumps*. These jumps are caused by the discontinuity of the carrier phase observations and the same jumps occur, when the receiver loses carrier phase lock simultaneously on all satellites. However, day-boundary jumps are an artifact of the daily processing scheme and several methods have been proposed to remove them, because they cause a bias in the computed Allan deviation (e.g. Dach et al., 2002; Guyennon et al., 2009). On the other hand, day-boundary jumps can also be used to analyze the actual accuracy of the receiver clock estimates as determined by the pseudorange observations (Ray and Senior, 2003). For the analysis in this work weekly receiver clock time series were computed in a single batch and are therefore not affected by day-boundary jumps.

6.2 Achievable precision

Assuming an observation noise of approximately 3 mm or 10 ps for the ionosphere-free linear combination of the GPS carrier phases, the receiver clock error can usually be estimated with a slightly higher precision, i.e. around 2 mm (cf. Section 4.5). Assuming furthermore a white or flicker noise behavior of the receiver clock estimates, the lower bound of the measurement noise, i.e. neglecting all environmental influences, in terms of an Allan deviation for the difference of two clocks can be approximated by $\sigma_y(\tau) = 1 \times 10^{-11}/\tau$. That means that an Allan deviation of $\sigma_y(1 \text{ h}) = 2.8 \times 10^{-15}$ and $\sigma_y(1 \text{ day}) = 1.2 \times 10^{-16}$ can be expected under ideal conditions. Similar values have been reported for short baseline experiments (Defraigne, 2011), where a constant relative receiver clock error can be established by connecting multiple receivers to a common oscillator as it was done in the receiver tests, described in Section 5.4. However, when comparing clocks over longer distances the noise of the PPP-derived clock differences is significantly higher. In order to analyze the distance-dependence of the frequency transfer precision, PPP clock differences between 10 globally distributed IGS stations equipped with well-maintained H-maser frequency standards were computed (Fig. 6.2).

Figure 6.3 shows the Allan deviations of the clock differences in all possible combinations. The individual PPP receiver clock offsets were computed in a 7-day continuous batch processing for GPS-week 1580 (April 2010). For reference the typical Allan deviation of an active H-maser signal and the lower bound for the short baseline frequency transfer accuracy discussed above are added. Up to approximately 1 to 2 hours the impact of the frequency instability of the maser is negligible, thus, the Allan deviation should

exclusively reflect the measurement noise contained in the PPP receiver clock estimates. Obviously, the receiver clock differences do not exhibit the expected white or flicker phase noise, i.e. the slopes of the Allan deviations do not equal -1 but rather a value between -1 and -1/2. For several clock differences, the Allan deviation for averaging times beyond 20000 s is increasing. This is due to a relatively large frequency drift of the hydrogen maser at station YELL.

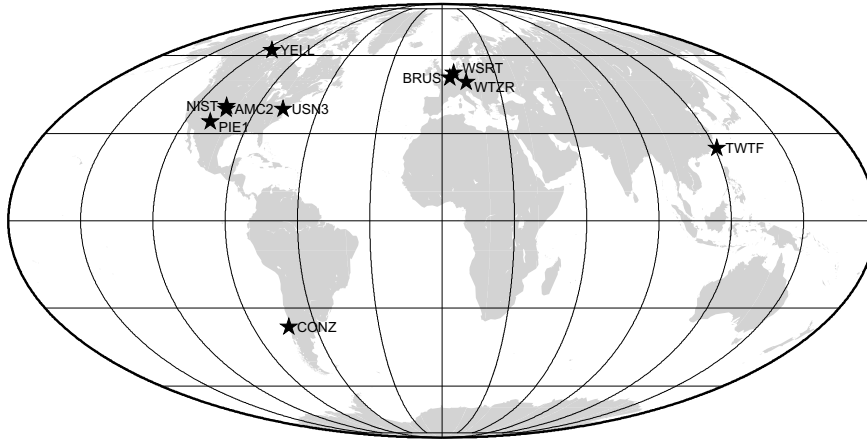


Figure 6.2: Global distribution of IGS stations with hydrogen maser frequency standards used in the evaluation of the PPP frequency transfer precision.

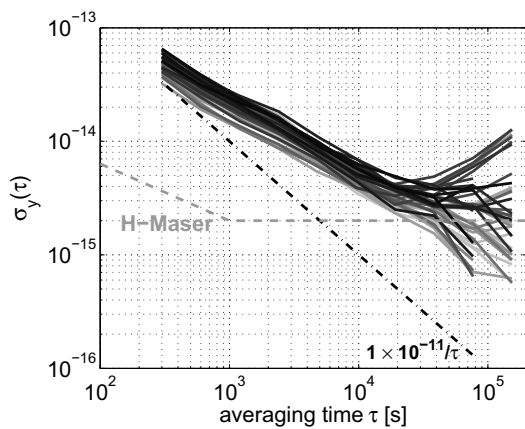


Figure 6.3: Allan deviation of 45 PPP-based H-maser clock differences over regional and intercontinental distances. For reference the Allan deviation for a short baseline clock comparison and a typical H-maser signal are included.

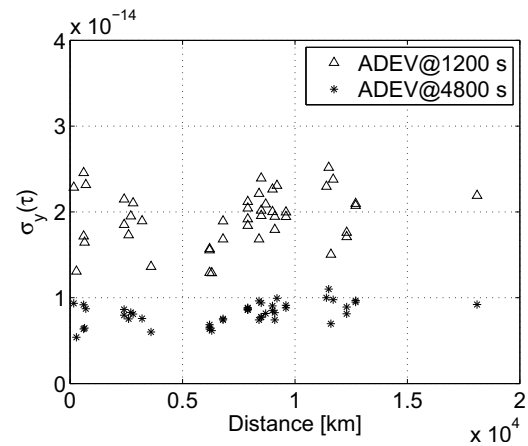


Figure 6.4: Allan deviation at $\tau=1200$ s and $\tau=4800$ s for 45 PPP-based clock differences between 10 globally distributed IGS-stations equipped with H-maser frequency standards plotted against the inter-station distance.

The distances between the stations range from 160 km for the stations NIST and AMC2 to 18000 km for the stations TWTF and CONZ. In order to see, whether the Allan deviation of the clock differences depends on the distance between the stations, the Allan deviations at $\tau=1200$ s and $\tau=4800$ s was plotted against the inter-station distance (Fig. 6.4). No significant distance-dependence can be observed, at least for inter-station distances exceeding 160 km. In other words, station- or receiver-specific characteristics are generally more important for the frequency transfer precision than distance-dependent effects such as orbit modeling errors.

6.3 Remaining error sources

Among the reasons for the degraded performance of carrier phase clock comparisons over regional and global distances compared to short baselines, is the influence of *unmodeled tropospheric delays* and to a lesser degree higher-order ionospheric effects. As discussed in Section 2.5.1, the distribution of water vapor in the troposphere is highly variable in space and time, while troposphere models and mapping functions usually assume azimuthal symmetry, at most supplemented by linear gradients. Thus, our ability to model the delays induced by small scale water vapor inhomogeneities is very limited. This situation is particularly unfavorable for time and frequency transfer because both, clock and troposphere parameters have to be estimated with a high temporal resolution and exhibit significant mathematical correlations. The correlations between station height, troposphere and receiver clock estimates have been studied by different authors in the past (e.g. Rothacher and Beutler, 1998). Based on analytical considerations using the simulation method of Geiger (1988), Dach et al. (2003) report a correlation coefficient between clock offsets and tropospheric zenith delay parameters of -0.98 for an elevation cut-off angle of 15° and elevation-dependent weighting at an equatorial site (cf. Tab. 2.1). According to their study the correlation coefficient can be reduced to -0.91 by lowering the cut-off angle to 5° . On the other hand, in Weinbach and Schön (2010) it is shown, that for an elevation cut-off angle of 5° , an error of 1 cm in the zenith wet delay causes a shift in the clock offset of 2.4 cm which is almost twice as high as for a 15° cut-off angle. That means, the improved observability of the tropospheric zenith delay by using observation data at low elevations is accompanied by an increased sensitivity of the receiver clock estimates with respect to small modeling errors.

All results in this work were computed using the global mapping function (GMF) (Boehm et al., 2006a) in combination with an a priori hydrostatic zenith delay zhd calculated with the model of Saastamoinen using pressure values taken from the GPT model (Boehm et al., 2007). This mapping function and the a priori zhd are long-term mean fits to numerical weather model (NWM) data and do not consider the actual meteorological conditions during the observation session. Thus mapping functions and zhd explicitly derived for the observation time as they are provided by the Vienna mapping functions (VMF1) (Boehm et al., 2006b) should generally improve the solution. However, a comparison of PPP receiver clock estimates obtained with GMF and VMF1 mapping functions and GPT- and NWM-based zhd values revealed primarily different offsets but no significant subdaily time variations of the receiver clock estimates (Weinbach and Schön, 2010). This is probably due to the relatively low temporal resolution of only 6 hours of the VMF1 data and the azimuthal symmetry assumed in both mapping functions.

In summary, we may conclude that unmodeled short-term tropospheric delay variations will propagate to a significant degree into the receiver clock estimates. However, due to the difficulty to precisely measure the tropospheric delay with high spatial and temporal resolution the exact impact of this error source is largely unknown.

Another important source of non-white noise in the receiver clock estimates are effects of *signal multipath* in the antenna vicinity. In contrast to orbit and troposphere modeling errors, the impact of multipath is not distance-dependent but site-specific. Multipath influences can usually be identified by comparing the residuals of the observations on consecutive days. Due to the fact that the GPS satellite geometry for a static observer repeats after approximately 23 h and 56 minutes, the geometry between the transmitter, receiver and reflector and thus the impact of multipath should be almost identical on consecutive days. Differences do obviously arise when the antenna environment changes or the properties of the signal reflecting surface are altered, e.g. by rain and snow. Since the receiver clock offset is estimated for every observation epoch, the impact of multipath effects can usually be observed not only in the observation residuals but also in the receiver clock estimates themselves. Figure 6.5 shows the PPP receiver clock estimates of IGS station WTZR for 3 consecutive days between March 31 and April 2, 2010. Most of the systematic variations are similar in all three time series. This is a strong indicator for multipath effects, because the H-maser clock variations, unmodeled tropospheric propagation delays and short-term temperature variations on different days can be regarded as largely uncorrelated.

Various strategies have been proposed in the past to mitigate the impact of multipath. Some investigations indicate, that placing microwave absorbing material around and under the antenna can reduce the

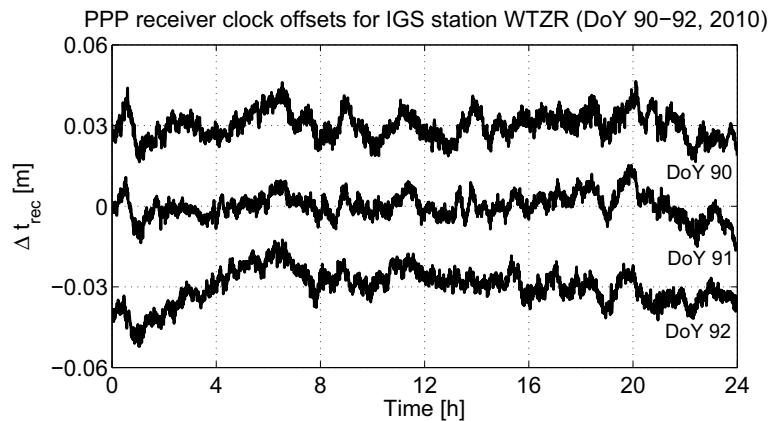


Figure 6.5: PPP receiver clock estimates of the IGS station WTZR for 3 consecutive days in April 2010. The time series are offset by 3 cm for better visibility.

impact of multipath from near the antenna, which is usually the most critical component (Ning et al., 2011). However, very few stations have been equipped in this way, which limits a conclusive analysis. Dilßner (2007) used a GPS antenna mounted on a moving robot to calibrate the multipath influence of a nearby reference station. He could show significant improvements but unfortunately the robot procedure is very laborious and has not been made operational. One of the more practical and promising approaches is the usage of carrier phase residual maps (Iwabuchi et al., 2004). These residual maps are generated by averaging a large number of carrier phase residuals in elevation- and azimuth-dependent grid cells. In this way repeatable errors of observations from a certain direction can be corrected. It would be interesting to see if the repeating variations in the receiver clock time series can be reduced with this approach. Unfortunately, long time spans of observation data have to be processed to obtain an adequate coverage of the antenna hemisphere with carrier phase residuals. This has prohibited a thorough test of this approach in the context of this work.

6.4 The impact of ambiguity fixing

It is well known, that one of the limitations of the conventional PPP approach is the missing possibility to fix the carrier phase ambiguities to integer values. In order to study the impact of ambiguity fixing on time and frequency transfer using PPP, several days of ambiguity-fixed PPP receiver clock estimates have been generated, following the strategy outlined in Section 2.5.2. Figure 6.6 shows epoch-wise estimated receiver clock offsets for the IGS station WTZR with and without ambiguity fixing. The estimated receiver clock time series are practically identical apart from a slightly different linear drift. This is in line with the finding by Dach et al. (2003), that time transfer results within one computing batch are not affected by the introduction of integer ambiguities from a double-difference solution. The small difference of the drift estimates is probably related to the fact, that ambiguity-fixed PPP is essentially a carrier phase-only solution. Similar and even larger drifts between PPP and phase-only solutions have been reported by other authors like, e.g., Defraigne et al. (2007) or Matsakis et al. (2006). Due to such drifts one or the other solution can develop a significant bias with respect to independent two-way satellite time transfer (TWSTFT) clock comparisons over longer time intervals. However, it remains unclear whether PPP or the phase-only solutions are more stable in the long term. Apart from long-term drift issues, the estimation of float ambiguities in the PPP approach seems to represent no significant disadvantage for time and frequency transfer compared to an ambiguity-fixed solution, because the observation sessions are typically very long. Nevertheless, one advantage of using ambiguity-fixed PPP for clock comparisons can be seen in the fact that day-boundary jumps are multiples of the narrow-lane wavelength $\lambda_c = 10.7$ cm and can thus easily be removed if longer continuous time series of clock differences are to be generated (Delporte et al., 2008).

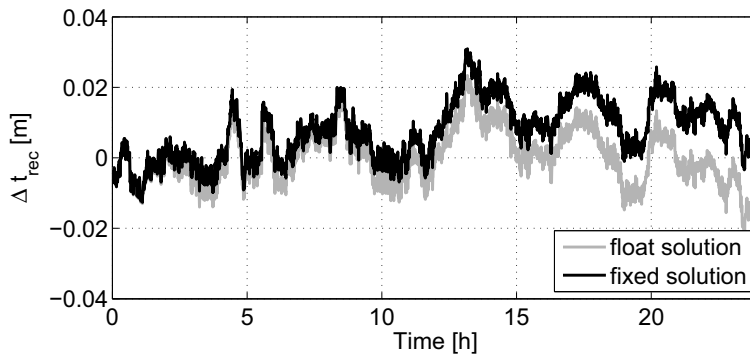


Figure 6.6: Float and fixed PPP receiver clock offsets of the IGS station WTZR on February 26, 2010. A linear drift of 20.7 cm/h has been removed from both time series. The time series of the fixed solution has been shifted to match the first epoch of the float solution.

6.5 Summary and alternative time and frequency transfer methods

It has been shown that PPP is a valuable tool for remote time and frequency comparisons of precision frequency standards. This was also acknowledged by the BIPM, through the *TAI PPP pilot experiment*, that was initiated in April 2008. Starting with September 2009, PPP time links are included in the routine generation of TAI (Petit et al., 2011). Theoretically, the Allan deviation of the measurement noise of PPP-derived receiver clock differences should be around $\sigma_y(1\text{ h}) = 1 \times 10^{-11} \tau^{-1}$, i.e. a level of 1×10^{-15} should be achievable after 3-4 hours. A comparable performance can be realized on very short baselines. However, over longer distances a significant increase of random-walk noise is observed, which leads to 2-5 times longer averaging times required to reach the 1×10^{-15} level.

In view of the developments in the area of atomic fountain clocks that have led to frequency stabilities in the 10^{-16} range, it will become increasingly difficult to compare these clocks even with the PPP approach, because very long averaging times are needed. Note, that in order to provide a reasonable sample size, the observed time series of clock differences should be at least 4-5 times as long as the longest averaging time for which the Allan deviation is to be computed. For optical clocks the situation is even more challenging and GPS-based methods seem to be inappropriate for clock comparisons at the 10^{-17} level.

The most promising method to compare optical clocks to date is via optical fiber (e.g. Grosche et al., 2009; Predehl et al., 2012). However, this technique requires a complex and expensive infrastructure and intercontinental fiber connections are not yet feasible. Therefore, one of the goals of the Atomic Clock Ensemble in Space (ACES) mission (Salomon et al., 2001) is to provide a very precise microwave link that would admit fountain and optical clock comparisons over inter-continental distances. However, expensive ground infrastructure will allow only few institutions to use the ACES link and the planned mission duration is only 3 years. Therefore, GPS observations and the PPP method will probably remain the backbone of precise time and frequency transfer for the next decade. Unfortunately, the room for improvement of the PPP time and frequency transfer technique appears to be rather small. Although the identified systematic effects might be slightly mitigated with improved observation modeling and additional GNSS satellites will reduce the effective receiver clock measurement noise, an improvement by more than a factor of 2-3 seems to be unlikely.

The fact that the Allan deviation of hydrogen maser clock comparisons for averaging times up to several hours is dominated by measurement noise and site-dependent effects, indicates a negligible influence of the oscillator at these time intervals. Therefore, linear clock modeling appears to be feasible for time intervals up to one hour and beyond. Furthermore, the additional colored noise observed at longer averaging times, probably caused by atmospheric influences, allows to extend the clock modeling interval. Problematic, however, are occasional receiver clock excursions as have been observed for example for the Ashtech ZXII receiver of the IGS station USN3 on April 7, 2010 (Fig. 6.7).

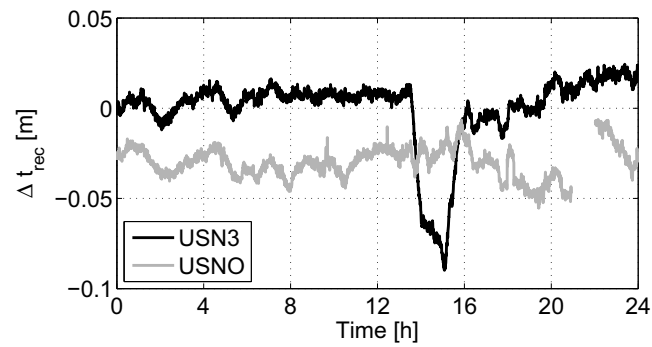


Figure 6.7: PPP receiver clock estimates for the IGS stations USN3 and USNO on April 7, 2010. Both receivers are connected to the same steered hydrogen maser that generates UTC(USNO)

Both receivers shown in the figure are connected to the highly stable USNO master clock, but in contrast to the receiver USNO, the receiver USN3 shows a pronounced deviation from the expected linear trend between 13:00-16:00. During such periods of suspicious receiver behavior the clock must not be modeled. However, due to the gradual increase of the error the identification of such a clock behavior is much more challenging than the detection of sudden jumps (cf. Section 4.6).

7 Analysis of the Impact of Receiver Clock Modeling

In the previous chapters, the parameterization and technical feasibility of clock modeling in GNSS data processing were discussed. In addition, the impact of a reduction of the number of clock parameters was investigated based on algebraic considerations. In this chapter, the question how GNSS solutions can be improved by clock modeling is analyzed empirically. This allows us to validate the proposed functional and stochastic clock models and to quantify the potential benefits in terms of the RMS reduction of the coordinate and troposphere parameter time series.

In a first step, the influence of different clock models on the coordinate part of the cofactor matrix will be analyzed for a simple case of point positioning, i.e. if only receiver clock parameters and coordinates are estimated. Both, static and kinematic coordinate estimation are considered. The aim of this analysis is to quantify the impact of the observation geometry and different numbers of clock parameters on the precision of the position estimates independent of observation noise and additional parameters. Subsequently, we will test the proposed clock models within a PPP solution based on simulated observation data. This allows us to assess the impact of clock modeling considering the full PPP parameter set including troposphere and ambiguity parameters independently of the systematic errors found in real observation data. Finally, clock modeling is applied to PPP with real observation data from several IGS stations equipped with hydrogen maser frequency standards. A separate section covers the impact of receiver clock modeling on GPS-based kinematic orbit determination for a low Earth orbiter (LEO). The Gravity Recovery and Climate Experiment (GRACE) mission is considered as a case study, because it combines a geodetic dual-frequency GPS receiver and an ultra-stable (quartz) oscillator (USO) on board of two LEOs. The impact of clock modeling on the kinematic positioning of the spacecraft is analyzed using simulated and real observation data.

7.1 Empirical analysis of the parameter cofactor matrix

In order to investigate the impact of different receiver clock parameterizations on the precision of the estimated receiver coordinates and troposphere parameters numerically, a simulation study has been performed. As discussed in Section 4.5 the mapping of the random observation noise onto the parameters is fully described by the parameter cofactor matrix (4.7). In the first instance only coordinate and clock parameters are considered, while in Section 7.1.3 tropospheric zenith delay parameters are added. Using satellite positions from the IGS precise ephemeris file for February 26, 2010, cofactor matrices for a near-polar, a mid-latitude and an equatorial site were computed. The weights of the observations were determined according to the sinus of their elevations e , i.e. the observation weight matrix has the form

$$\mathbf{P} = \text{diag} (\sin^2 e_1, \dots, \sin^2 e_n) . \quad (7.1)$$

The resulting cofactor matrix has been transformed into the local north, east, up coordinate system and scaled with the variance factor $\sigma_0^2 = (0.002 \text{ m})^2$. Thus the square roots of the diagonal elements approximately reflect the formal standard deviations of the parameters for a carrier phase based solution.

Three different approaches to clock modeling have been analyzed. In the conventional approach (E) a new receiver clock offset is estimated for every observation epoch. In the second scenario (X) no clock offset is estimated at all. This rather theoretical case assumes perfect synchronization of the receiver clock with the timescale of the satellite clocks (e.g. GPST or IGST). In reality this is very difficult to

Model ID	Description
X	No clock parameter
E	Clock offset every epoch
P	Offset + drift model

Table 7.1: Clock models considered for the investigation of the parameter covariance matrix

achieve since even the most stable atomic frequency standard will gain a non-negligible time error at some time after successful synchronization. Practically, one would need another method to continuously calibrate the receiver clock with superior accuracy. Nevertheless, it is interesting to consider this case since it marks the highest attainable accuracy for GNSS with clock modeling. The third and more realistic approach is to estimate a set of two parameters, consisting of a clock offset and a clock drift, for a certain time interval (P). As we have seen in the previous chapter, using such a linear model to describe the receiver clock error of a GNSS receiver connected to a hydrogen maser frequency standard is reasonable for periods up to one hour and more. The three approaches are listed in Table 7.1.

It has to be emphasized that similar investigations on the mutual relationship of height, clock and troposphere estimates have first been carried out on an analytical basis by Geiger (1988) and Santerre (1991) and were later revisited, e.g., by Rothacher and Beutler (1998) (cf. Section 2.2). However, the analysis presented in the following, differs in several aspects from these previous works: 1) A clear distinction is made between kinematic and static coordinate estimation, 2) the effect of clock modeling over multiple epochs is considered in addition to the cases with epoch-wise and without clock estimation and 3) the analysis is based on an exemplary 24-hour satellite geometry and not on an analytical model assuming a uniform satellite distribution between a minimum and maximum satellite elevation.

7.1.1 Static positioning

In a first step, the impact of clock modeling in static positioning mode will be analyzed. Figure 7.1 shows the standard deviation of the coordinates in the local north, east and up direction for the solution with epoch-wise receiver clock estimation for an equatorial, a mid-latitude, and a near-polar site, respectively. Static solutions of different lengths have been computed and the resulting standard deviations have been averaged over the entire 24-hour interval. The x-axis indicates the number of 30-s epochs contributing to one set of coordinate and clock parameters in the clock modeling case. Note, that 96 consecutive static solutions, covering 15 minutes of observation data each, have been averaged in the 30-epoch case, thus making the quoted standard deviations largely independent of a particular satellite geometry. It can be noted, that the standard deviations of the static coordinate components decrease approximately with the square root of the number of observation epochs contributing to one set of coordinates. Furthermore, we see, that the standard deviation of the vertical component for the equatorial and mid-latitude site is approximately 2 times larger than the standard deviations of the horizontal components. For the near-polar site this ratio is almost 5. These are the typical precision ratios of vertical and horizontal position estimates GNSS users are familiar with. If in contrast, no receiver clock offset had to be estimated (Fig. 7.2), the vertical component of the receiver position would be more precise than the horizontal position or at least equally precise for stations in the polar regions. Finally, if we had to estimate only one receiver clock offset and one drift parameter (P) for the interval of the static solutions, we would get the same values as in the case with epoch-wise clock estimation (Fig. 7.3). At first sight, this result is quite remarkable since the number of parameters in solution P is considerably reduced. However, we could expect such a behavior, since the static height estimate depends on the absolute level of the receiver clock error. With the 2 parameter clock model, however, only the evolution of the receiver clock offset is constrained but not its absolute values (cf. Section 4.3).

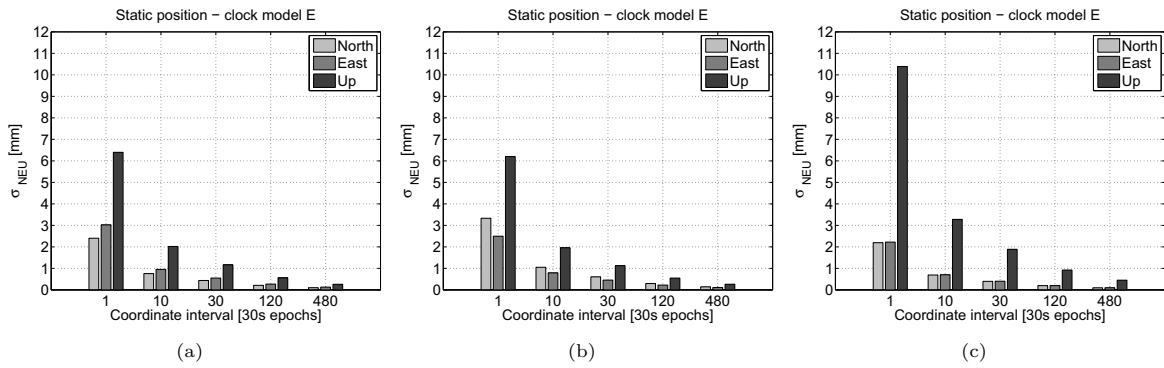


Figure 7.1: Formal standard deviations of the static receiver coordinates if clock offsets are estimated for every observation epoch for (a) an equatorial (b) a mid-latitude, and (c) a near-polar site

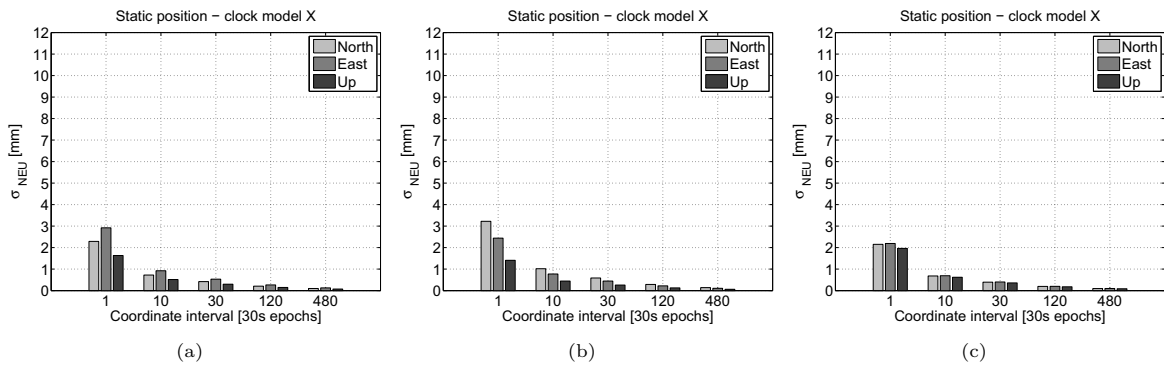


Figure 7.2: Formal standard deviations of the static receiver coordinates if no clock offsets are estimated for (a) an equatorial (b) a mid-latitude, and (c) a near-polar site

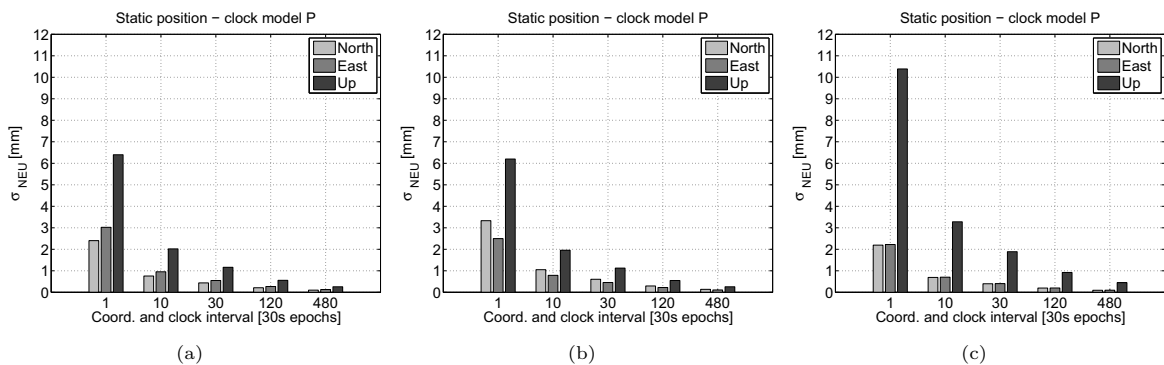


Figure 7.3: Formal standard deviations of the static receiver coordinates if only one clock offset and one clock drift (linear model) are estimated for (a) an equatorial (b) a mid-latitude, and (c) a near-polar site

7.1.2 Kinematic positioning

In a second step, the impact of clock modeling on kinematic positioning has been investigated. Here, coordinates are estimated for every 30-s observation epoch. The same holds for the receiver clock offsets in scenario “E”. In contrast, for case “P” only one offset and one drift parameter is estimated for the entire analysis batch size, denoted here as “session length”. Again, the standard deviations shown are average values over the entire 24-hour data set. Inspecting Figures 7.4 and 7.5 we notice, that the standard deviations for epoch-wise clock estimation (E) and the case without clock parameters (X) are independent of the chosen batch size. This is of course due to the fact that coordinates are estimated for every observation epoch. Consequently, the results are identical to the static case with one observation epoch.

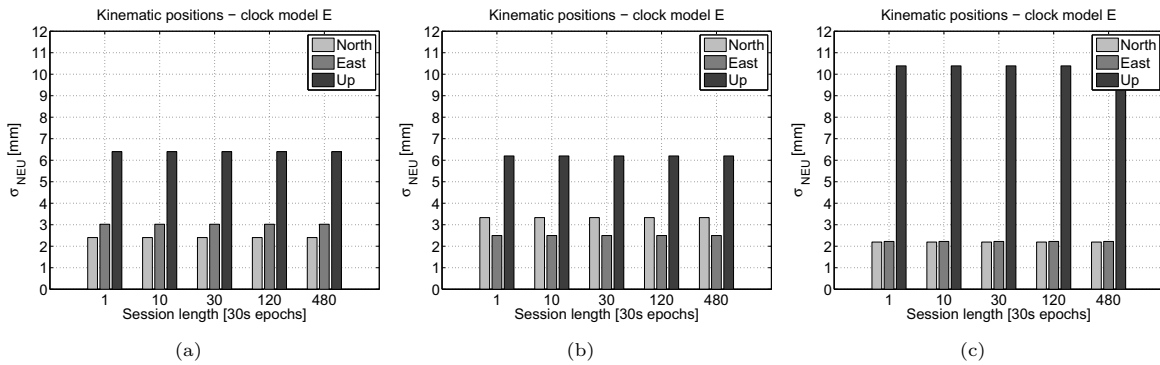


Figure 7.4: Formal standard deviations of the kinematic receiver coordinates if clock offsets are estimated independently for every observation epoch for (a) an equatorial (b) a mid-latitude, and (c) a near-polar site

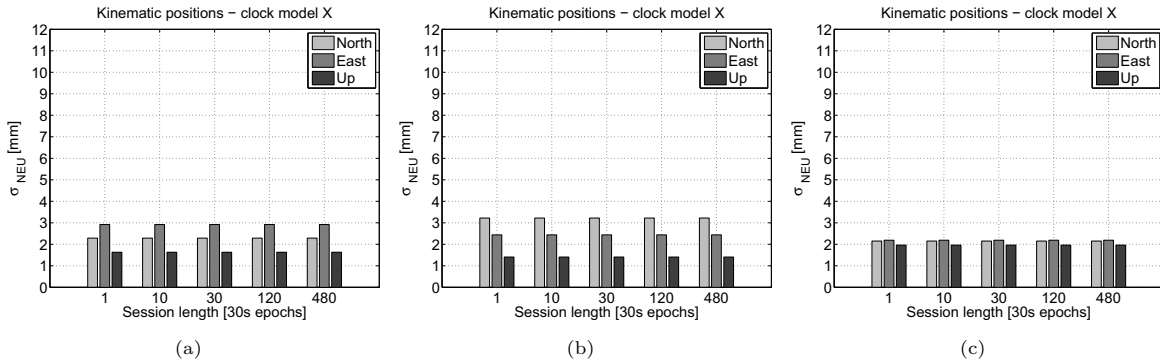


Figure 7.5: Formal standard deviations of the kinematic receiver coordinates if no clock offsets are estimated for (a) an equatorial (b) a mid-latitude, and (c) a near-polar site

In contrast, for the proposed two-parameter clock model the standard deviations of the height coordinate are decreasing as the length of the batch interval and thus the number of epochs contributing to one set of clock parameters increases (Fig. 7.6). When the clock parameter interval is as large as 4 hours or 480 epochs the standard deviation of the height coordinate is virtually as small as in the case without clock parameters (model X). In addition, it can be noted that 90% of the reduction is achieved up to a clock modeling interval of 120 epochs. Beyond this interval length the additional improvement is rather small. On the other hand, using only 10 epochs instead of only one to estimate the receiver clock offset the standard deviation of the kinematic height estimates is improved by a factor of two compared to the case with epoch-wise clock offsets. More generally, the difference of the standard deviations $\sigma_{u,P}$ of the height component with respect to the clock-free case ($\sigma_{u,X}$) decreases approximately with the square root of the number of epochs n contributing to one set of clock parameters, i.e.

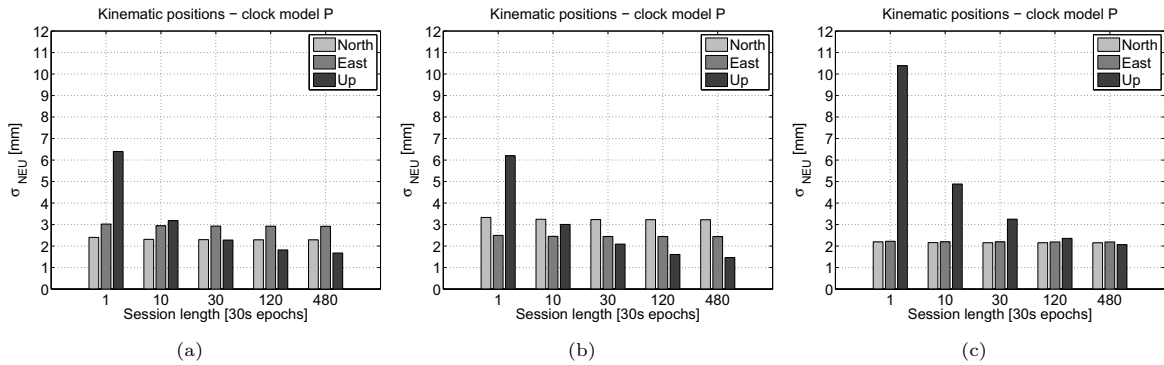


Figure 7.6: Formal standard deviations of the kinematic receiver coordinates if only one clock offset and one clock drift are estimated for (a) an equatorial (b) a mid-latitude, and (c) a near-polar site

$$\sigma_{u,P}(n) \approx \frac{\sigma_{u,E} - \sigma_{u,X}}{\sqrt{n}} + \sigma_{u,X} \quad (7.2)$$

In view of the findings regarding the impact of clock modeling on the precision of kinematic coordinates in Section 4.3 this behavior could be expected. In summary, we may conclude that the kinematic solution is improved, because clock modeling suppresses unrealistically large receiver clock variations. In other words, a better separation is achieved through a different temporal resolution of the parameter types.

7.1.3 Troposphere estimation in static positioning

In the next step, a tropospheric zenith delay parameter has been considered in addition to the static coordinates and receiver clock parameters. The partial derivatives of the observations with respect to the wet zenith delay (zwd) were computed using the Global Mapping Function (Boehm et al., 2006a). In a batch least-squares adjustment, the zwd is typically modeled by a sequence of piece-wise constant or piece-wise linear parameters with intervals between 15 minutes and 2 hours. For reasons of convenience a piece-wise constant parametrization has been implemented for this investigation. Based on the results of the previous sections, the impact of clock modeling is expected to depend on the length of the interval of the piece-wise constant parameters. Therefore, the precision of the zwd estimates are analyzed for a parameter spacing of 1 hour, 15 minutes and 30 seconds. The results for a mid-latitude site are depicted in the Figures 7.7 to 7.9.

At first glance, there seems to be no difference between epoch-wise receiver clock estimation (a) and the proposed 2-parameter clock model (c). Comparing Figure 7.7(a) and Figure 7.1(b), we can see that the addition of the zwd parameters strongly degrades the height precision, while the horizontal coordinate components are hardly affected. The zwd parameters themselves can be determined more precisely than the height coordinates. If no clock parameters would need to be estimated (b) the height precision is only slightly degraded down to the level of the horizontal coordinate components.

Despite the obvious similarities between the subfigures (a) and (c), we can identify an important difference between the two in Figure 7.9. While in the solution with epoch-wise clock estimation the standard deviations of the zwd s approach a constant value of approximately 2 mm for a batch size of 30 epochs and beyond, they continue to decrease in the case with clock modeling almost down to the level of the case without clock parameters (b). This becomes more obvious when looking at the numbers summarized in Table 7.2. A similar trend can also be observed for the cases with 15-minute and 1-hour zwd sampling, but the effect is too small to be visible in Figure 7.9 and is of no practical relevance.

In summary, we can conclude that much like the kinematic height coordinates, the standard deviation of zwd estimates with very high temporal resolution can be improved through clock modeling. In other words, small high-frequency fluctuations of the zwd estimates caused by the simultaneous estimation

of epoch-wise receiver clock offsets can be suppressed. This is usually of little interest for geodesists since meteorological conditions and therefore significant *zwd*s changes can be assumed to occur slowly, thus justifying parameter spacings of 15 minutes and more. However, if small (few mm) high-frequency fluctuations in the tropospheric (zenith) delay are to be studied, e.g. to characterize the turbulent energy in the atmosphere (Vennebusch et al., 2011), the usage of a high-precision oscillator in combination with a suitable clock model in the adjustment may prove beneficial.

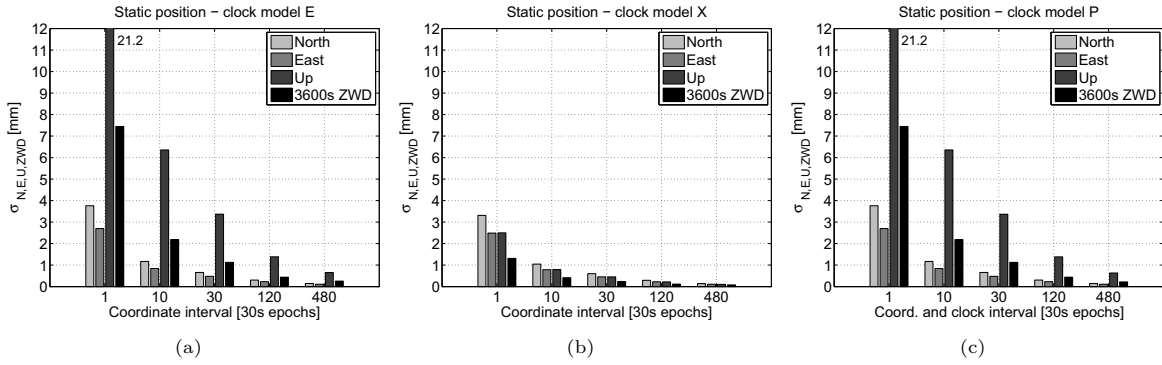


Figure 7.7: Formal standard deviations of static receiver coordinates and piece-wise constant *zwd* estimated every 3600 s for a mid-latitude site if (a) clock offsets are estimated for every observation epoch (b) no clock offsets are estimated and (c) only one clock offset and one clock drift are estimated

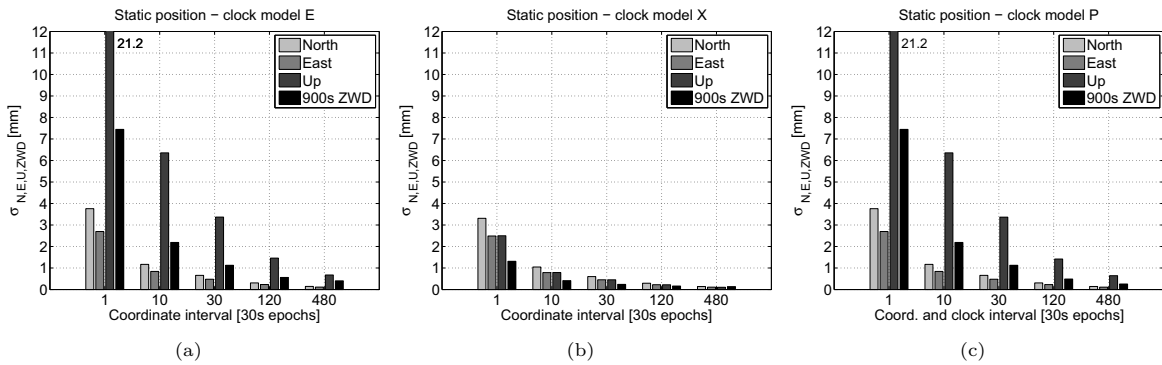


Figure 7.8: Formal standard deviations of the static receiver coordinates and piece-wise constant *zwd* estimated every 900 s for a mid-latitude site if (a) clock offsets are estimated for every observation epoch (b) no clock offsets are estimated and (c) only one clock offset and one clock drift are estimated

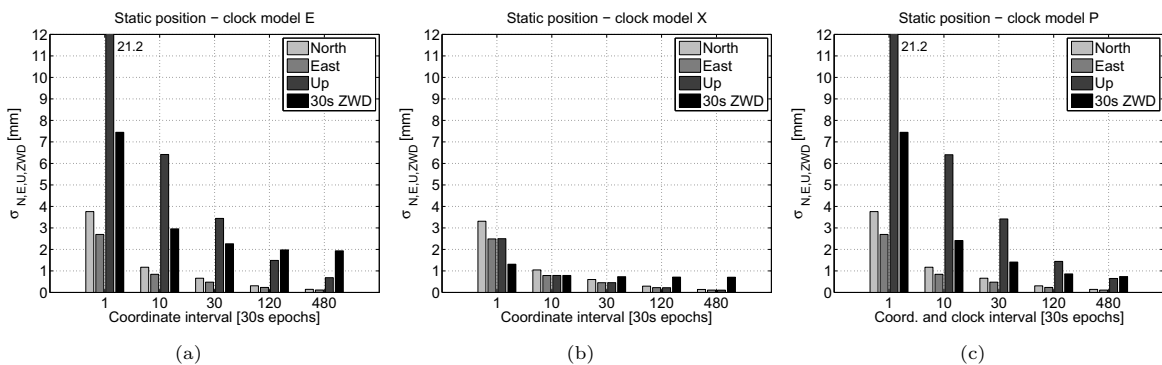


Figure 7.9: Formal standard deviations of the static receiver coordinates and piece-wise constant *zwd* estimated every observation epoch (30 s) for a mid-latitude site if (a) clock offsets are estimated for every observation epoch (b) no clock offsets are estimated and (c) only one clock offset and one clock drift are estimated

Batch size [30s epochs]	$\Delta t_{zwd} = 1h$			$\Delta t_{zwd} = 900s$			$\Delta t_{zwd} = 30s$		
	E [mm]	X [mm]	P [mm]	E [mm]	X [mm]	P [mm]	E [mm]	X [mm]	P [mm]
1	7.45	1.31	7.45	7.45	1.31	7.45	7.45	1.31	7.45
10	2.19	0.71	2.19	2.19	0.71	2.19	2.96	0.79	2.41
30	1.13	0.24	1.13	1.13	0.24	1.13	2.26	0.73	1.41
120	0.44	0.12	0.44	0.56	0.16	0.48	1.97	0.71	0.86
480	0.25	0.08	0.22	0.40	0.14	0.25	1.93	0.71	0.74

Table 7.2: Average standard deviations of troposphere estimates for 120-, 30- and 1-epoch piece-wise constant parameter intervals, different static coordinate intervals (batch sizes) and different receiver clock parametrizations

7.1.4 Absolute versus relative positioning

In principle, the same results as for absolute positioning should apply to relative positioning. In the latter case receiver clock modeling can be carried out at the single difference level. In analogy to their findings for a point positioning scenario, Kuang et al. (1996) state that differential receiver clock errors will be absorbed primarily along the average directions of the vectors pointing from the midpoint of the baseline to the observed GNSS satellites. Consequently, this direction coincides approximately with one of the principal axes of the error ellipsoid of the baseline components.

In Santerre and Beutler (1993), a method for improved differential height determination on short baselines is described, that is based on the elimination of the differential receiver clock bias. By using two antennas that are connected to a single receiver, the observations of both antennas are related to the same oscillator, so that the differential receiver clock offset can be assumed constant. Of course, this approach depends on the calibration of the delays of the GNSS signals on their way from the antenna to the receiver, which has to be realized with an accuracy of a few picoseconds. This challenging problem could not be solved at the time when the method was proposed by Santerre and Beutler. 18 years later such a real-time calibration system based on a GPS-over-fiber link was successfully demonstrated by Macias-Valadez et al. (2012). The results they show for a short baseline with differential receiver delay calibration are very similar to the findings for PPP with receiver clock modeling presented in this work.

7.2 PPP results with simulated data

In addition to the investigation of the elements of a simplified cofactor matrix in the previous section, the impact of clock modeling was studied with simulated observation data. The simulated data were processed with the same PPP software, that is later used for the analysis of real GPS data, thus facilitating the identification of possible error sources in real GNSS applications. Furthermore, the PPP processing includes additional carrier phase ambiguity parameters, which have been neglected in the analysis of the cofactor matrix. Finally, the PPP-derived zwd and kinematic coordinate time series allow insights into the temporal behavior of these parameters with and without clock modeling.

In order to limit the number of plots, only one exemplary mid-latitude observation site is shown in this section. Based on the GPS satellite geometry on February 26, 2010, a 24-hour data set of artificial observations with 30-s spacing has been generated for the IGS station WTZR in South-Eastern Germany. Normally distributed random noise with $\sigma_P = 0.2$ m and $\sigma_\phi = 0.002$ m multiplied with the elevation-dependent scaling factor $1/\sin(e)$ has been added to the synthetic L_1/L_2 pseudorange and carrier phase observations, respectively. Tropospheric delays and receiver clock offsets were assumed to be zero.

7.2.1 Static PPP results with simulated data

The static PPP solution has been studied with respect to coordinates and troposphere parameters. Based on the results of Section 7.1, we expect the impact of clock modeling on the precision of the static coordinates to be negligible. In contrast, troposphere estimates with high temporal resolution and weak relative constraints should be improved with clock modeling. In order to have a representative sample size for the investigation of the static coordinate repeatability, 100 daily observation files with a reduced observation sampling of 300 s and independent observation noise were simulated and then processed with the developed batch least-squares PPP module. The spacing of the zwd parameters was set to 30 minutes with relative constraints $\sigma_{zwd,rel}$ of 3.5 mm/h between the slopes of consecutive linear segments (cf. (4.67),(4.69)). In the first solution the receiver clock offset was estimated epoch-wise independently. In a second solution it was modeled as a piece-wise linear function with 1-hour intervals and relative constraints between consecutive clock drifts $\sigma_{clk-drift,rel}$ of 5 ps/h (cf. (4.65)-(4.69)).

Figure 7.10(a) shows the estimated receiver clock with and without clock modeling. An individual offset was removed from each of the 100 clock time series. Otherwise, the mean of each clock time series would scatter between -4 and +4 cm, because the absolute time offset of the PPP receiver clock is solely determined by the less precise pseudorange observations. This offset is, however, irrelevant for the estimation of coordinate and troposphere parameters since it is completely compensated by the carrier phase ambiguities that are estimated in the PPP solution. The variations of the clock error are much smaller for the piece-wise linear clock parametrization than for the epoch-wise independent clock estimation. A slightly degraded accuracy of the piece-wise linear clock offset can be noted at the day boundaries, where the carrier phase ambiguities can be less well determined.

Figure 7.10(b) shows the differences of the estimated daily, static height coordinates with respect to the value used in the simulation. Although the height estimates of individual solutions differ by up to 1 mm, no obvious differences in the overall scatter can be identified. This is also supported by the statistical measures given in Table 7.3, where the standard deviations of the height component are almost identical for the solution with and without clock modeling. As expected, both solutions, yield the same coordinate precision.

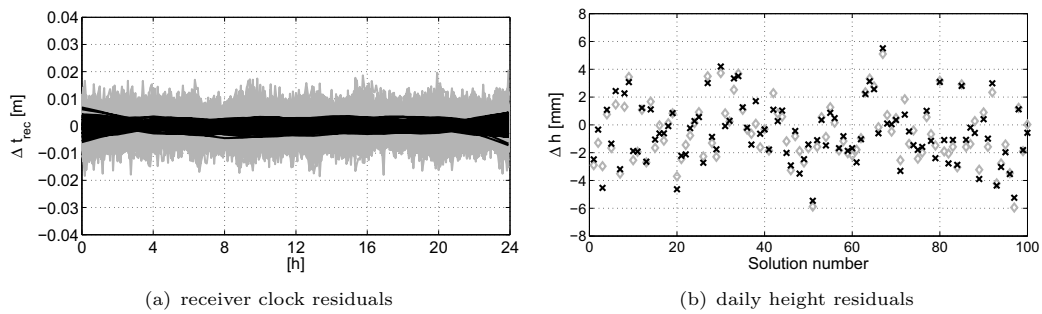


Figure 7.10: Offset removed receiver clock (a) and height residuals (b) of 100 simulated daily observation files for the IGS station WTZR on Feb. 26, 2010 with epoch-wise (gray) and 1-h piece-wise linear (black) clock estimation

clock parametrization	mean ΔN [mm]	std ΔN [mm]	mean ΔE [mm]	std ΔE [mm]	mean ΔU [mm]	std ΔU [mm]
epoch-wise	0.35	0.67	0.05	1.56	-0.58	2.15
1-h piece-wise lin.	0.34	0.63	0.03	1.48	-0.60	2.13

Table 7.3: Mean and standard deviation of the estimated static receiver coordinates based on 100 simulated 24-h observation files for the IGS station WTZR on February 26, 2010

For the analysis of high-resolution troposphere parameters, a single static PPP solution with 30-s observation data has been computed, in which the spacing of the zwd parameters was reduced to 5 minutes.

Due to the large number of zwd parameters and the varying GPS satellite geometry over 24 hours, the processing of a single day of data is deemed to provide a sufficient sample size. In Figure 7.11, an example of the estimated zwd with and without clock modeling is shown. Since no tropospheric delays were added to the simulated observations, the zwd should be zero. The relatively high temporal resolution of 300 s for the troposphere parameters was selected in order to demonstrate a significant impact of the clock modeling. Indeed, a reduction of the variations of the zwd can be noted in the unconstrained case, when clock modeling is applied (Fig. 7.11(a)). However, it is common practice to impose physically reasonable constraints on the evolution of the troposphere parameters if the parameter interval is smaller than 1 hour (Dach et al., 2007). Usually, the temporal variation of the zenith wet delays is expressed in the form of a random-walk process noise σ_{RW} as applied in Kalman filtering. Typical values are in the range of 2-10 mm/ \sqrt{h} and a frequently reported standard value is $\sigma_{RW} = 5$ mm (Schüler, 2001; Bosser et al., 2010). When constraining the variations of the wet tropospheric zenith delay pessimistically with $\sigma_{RW,zwd} = 8$ mm/ \sqrt{h} , i.e. $\sigma_{zwd,rel} = 2.3$ mm for a 300 s spacing of the piece-wise linear parameters, the reduction of the zwd variations through clock modeling becomes almost negligible (Fig. 7.11(b)).

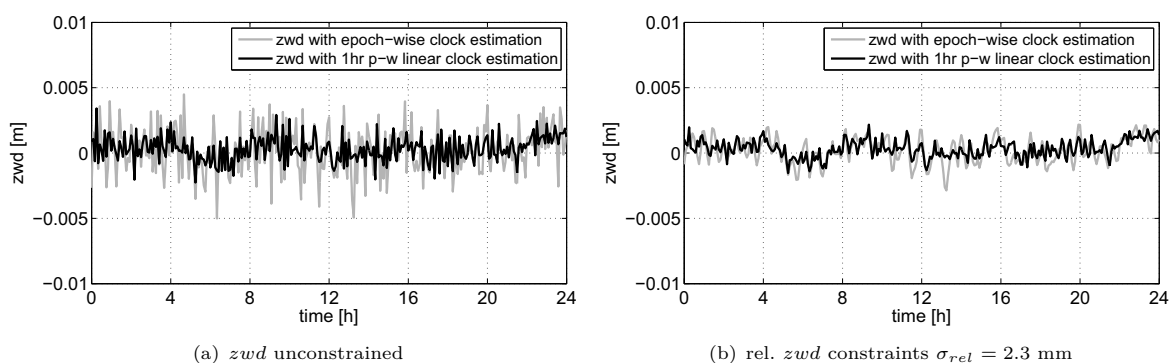


Figure 7.11: Residual 300-s piece-wise linear zwd for the IGS station WTZR based on simulated data with and without clock modeling for February 26, 2010

7.2.2 Kinematic PPP results with simulated data

In the next step, the simulated observation data were processed in kinematic mode. Both, results obtained by the batch least-squares adjustment and the Kalman filter will be shown. According to the findings in Section 7.1, we expect a significant improvement of the precision of the kinematic height coordinates, when clock modeling is applied.

Kinematic PPP using batch least-squares adjustment

The simulated observation data were first processed in a standard batch least-squares adjustment. Kinematic coordinates and epoch-wise clock parameters were pre-eliminated from the main normal equation system according to the procedure outlined in Section 4.1. After solving the reduced normal equation system, these parameters are recovered in a back-substitution step. In accordance with the data simulation no a priori tropospheric corrections were applied, but piece-wise linear zenith delay parameters, mapped with the wet part of the global mapping function (GMF) were estimated. The spacing of the zwd parameters was 30 minutes and the slope in each linear segment was constrained to zero with a standard deviation of σ_{zwd} of 3.5 mm, which corresponds approximately to a random walk process noise of $\sigma_{RW,zwd} = 5$ mm/ \sqrt{h} .

Figure 7.12 shows the kinematic position residuals with respect to the station coordinates that were used in the simulation for the case of epoch-wise independent clock estimation. In line with the findings of Section 7.1 the different precision levels of the parameters can be identified. As expected the height

component exhibits the largest scatter. Due to the varying satellite geometry the noise level of the kinematic position residuals is slightly changing over the 24-hour observation interval.

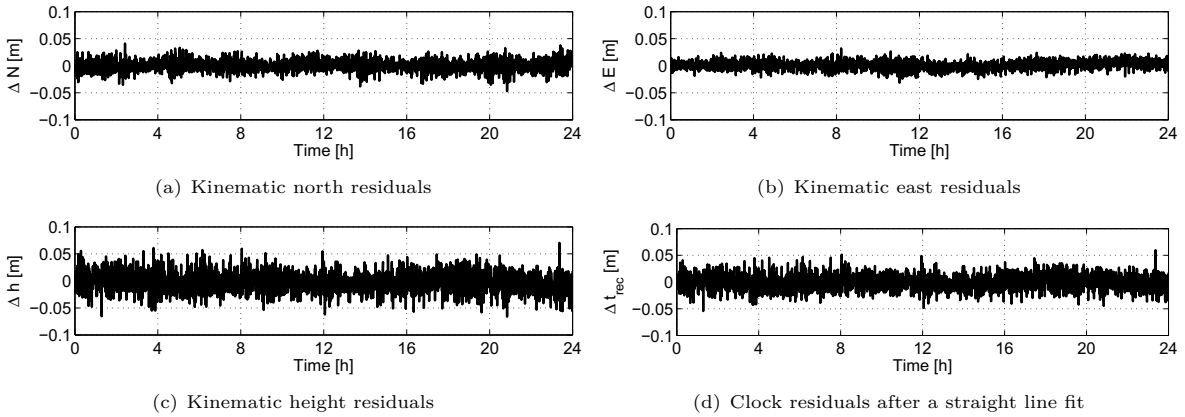


Figure 7.12: Kinematic PPP position and clock residuals for the IGS station WTZR based on simulated data and epoch-wise independent clock estimation on February 26, 2010

For comparison, Figure 7.13 shows the kinematic position residuals of a PPP solution in which the receiver clock offset was modeled by a sequence of 24 piece-wise linear segments of 1 hour length each, and the slopes of consecutive segments were constrained with $\sigma_{clk,drift} = 5$ ps/h relative to each other. The latter value reflects the accumulated time error of an active hydrogen maser due to random frequency fluctuations. As expected, the variations of the kinematic height coordinates are reduced by over 70 % from $\sigma_h = 17.8$ mm to $\sigma_h = 4.7$ mm while the horizontal components are essentially unaffected. In Figure 7.14 the zwd and ambiguity estimates are plotted. While the variation of the 30-min piece-wise linear zwd estimates can be slightly reduced when the receiver clock is modeled, the ambiguities are partly shifted, but their scatter is hardly reduced.

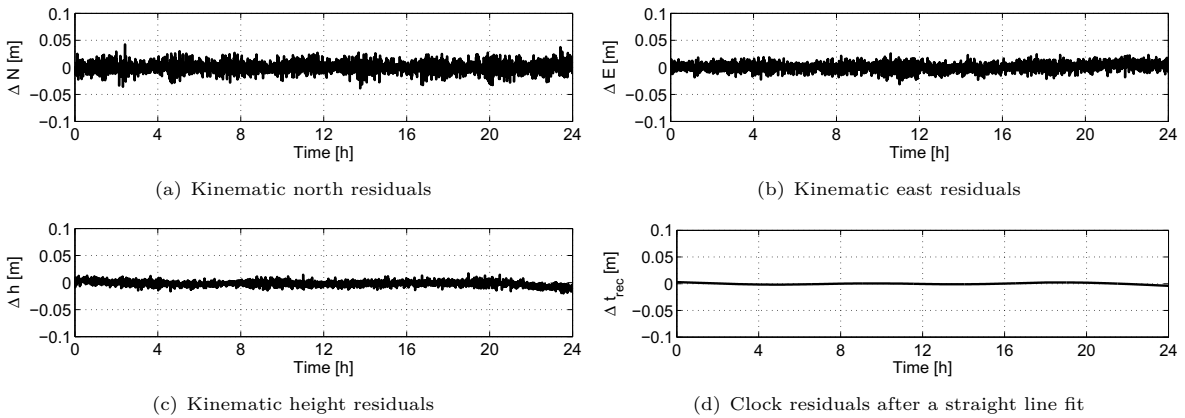


Figure 7.13: Kinematic PPP position and clock residuals for IGS station WTZR based on simulated data and 1-hour piece-wise linear clock estimation on February 26, 2010

Due to the constraints imposed by the piece-wise linear receiver clock model less observation noise is absorbed into the parameters and the residuals become larger. Consequently, the weighted sum of squared carrier phase residuals increases by 18 % from 15081 m^2 to 17879 m^2 . At the same time, the degree of freedom $n - u$ is increased due to the reduction of the number of clock parameters and the relative constraints imposed on these parameters. In sum, this results in an a posteriori variance factor very close to one, i.e. the a priori variance factor. This agreement is expected, since the functional and stochastic model perfectly fit the simulated data. Therefore, the same agreement is also achieved with epoch-wise clock estimation.

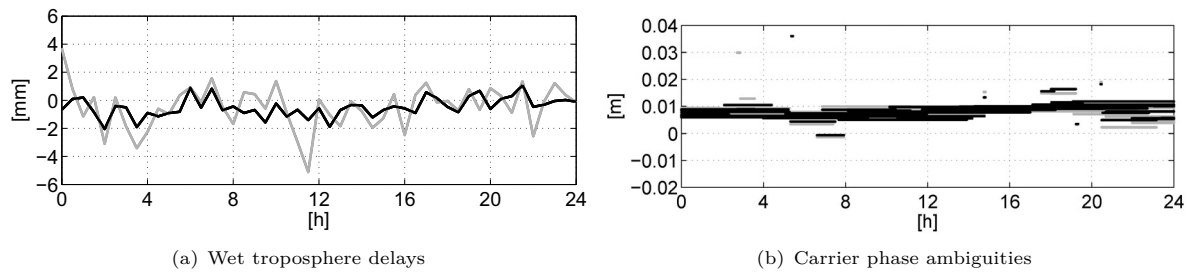


Figure 7.14: Estimated 30-minute zenith wet delays and carrier phase ambiguities for IGS station WTZR based on simulated data with (black) and without (grey) clock modeling (February 26, 2010)

The algebraic investigation of the kinematic positioning solution in Section 4.3 indicated a significant impact of clock modeling on the inter-epoch correlation of the kinematic coordinates. In order to analyze this temporal correlation, the correlation coefficients between consecutive kinematic coordinates have been extracted from the cofactor matrix. Because the kinematic coordinates are usually pre-eliminated from the normal equation system and recovered in a back-substitution step, a dedicated cofactor matrix has been computed for which the observation interval was reduced to 300 s and the partial derivatives of the kinematic coordinates refer to a local north, east, up coordinate system. Due to the reduced observation interval, the troposphere parameter interval was increased to 1 hour. Figure 7.15 shows the correlation coefficients of consecutive kinematic coordinates in the north, east and up direction. An increased temporal correlation of the kinematic height coordinates is evident, when clock modeling is applied. The average correlation coefficient increases from 0.38 to 0.69, i.e. it almost doubles. The inter-epoch correlations are particularly high at the day boundaries, where the float carrier phase ambiguities are less well determined. For the horizontal components, a small reduction of the temporal correlation can be observed. It is interesting to note, that the east component exhibits a much stronger temporal correlation than the north component. Generally, these correlations have to be kept in mind when the kinematic positions are introduced into further processing steps, such as the determination of velocities and accelerations.

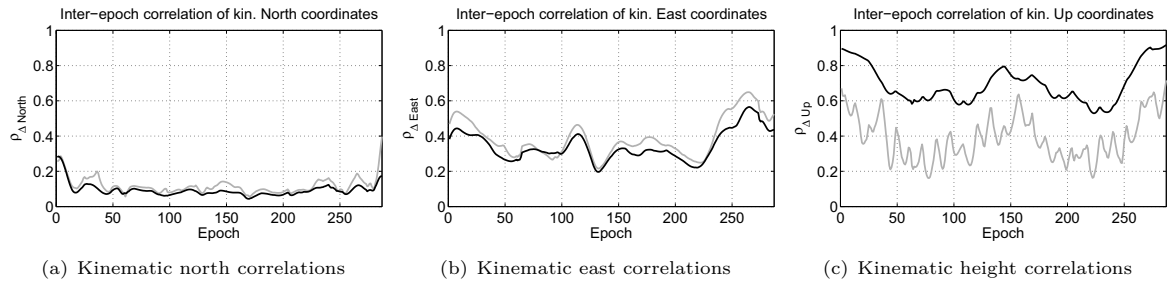


Figure 7.15: Inter-epoch correlations of kinematic PPP coordinates for simulated data of IGS station WTZR with epoch-wise independent (grey) and 1-hour piece-wise linear (black) clock estimation on February 26, 2010

Kinematic PPP using Kalman filtering

In order to validate the 2-state clock model, described in Section 4.4.2, the same simulated data set for the IGS station WTZR has been processed with the Kalman filter PPP processing module. The coordinates were treated as kinematic by adding 100 m process noise to the covariance matrix of the coordinate states during each time update. In order to make the results comparable to the batch solution, the state estimates of the forward and backward run of the filter were combined to form optimally smoothed estimates as outlined in Section 4.2.3. The h_α coefficients for an active hydrogen maser and a TCXO, which are required to calculate the process noise matrix \mathbf{Q}_w (4.78) of the clock states are taken from Table 3.2.

Figure 7.16 shows the position and clock residuals for a PPP solution that assumes a frequency stability of the receiver clock corresponding to a temperature compensated crystal oscillator (TCXO). When using the TCXO specifications (cf. Tab. 3.2), the process noise added in the time update step is much larger than the carrier phase observation noise, so that this case can be regarded as epoch-wise independent clock estimation. Consequently, the variations of the parameter time series are very similar to the results of the batch least-squares adjustment with epoch-wise clock estimation (Fig. 7.12).

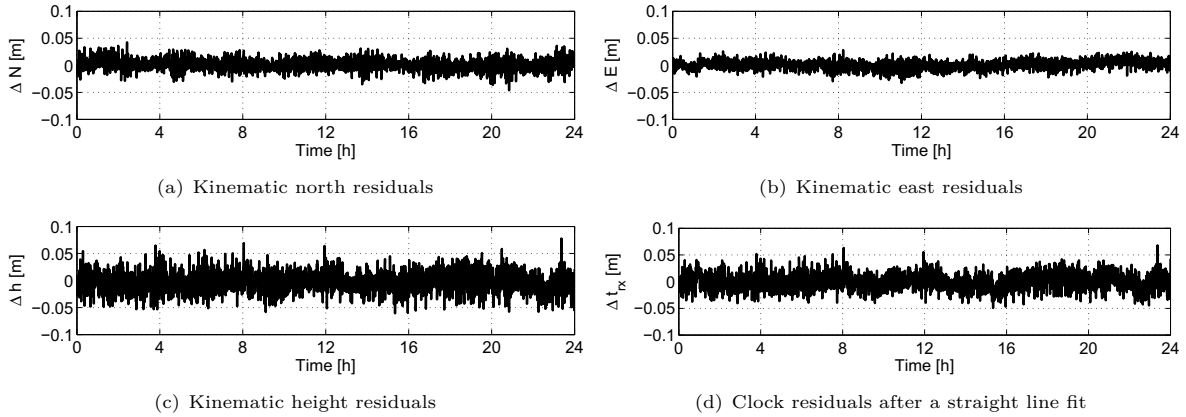


Figure 7.16: Kalman filter kinematic PPP position and clock residuals for IGS station WTZR based on simulated data and frequency-state process noise according to TCXO specifications (February 26, 2010)

Figure 7.17 shows the position and clock residuals for a PPP solution with clock process noise according to typical active hydrogen maser specifications (cf. Tab 3.2). A clear filtering effect can be observed in the receiver clock estimates and the kinematic height coordinates. However, still systematic variations up to 2 cm exist.

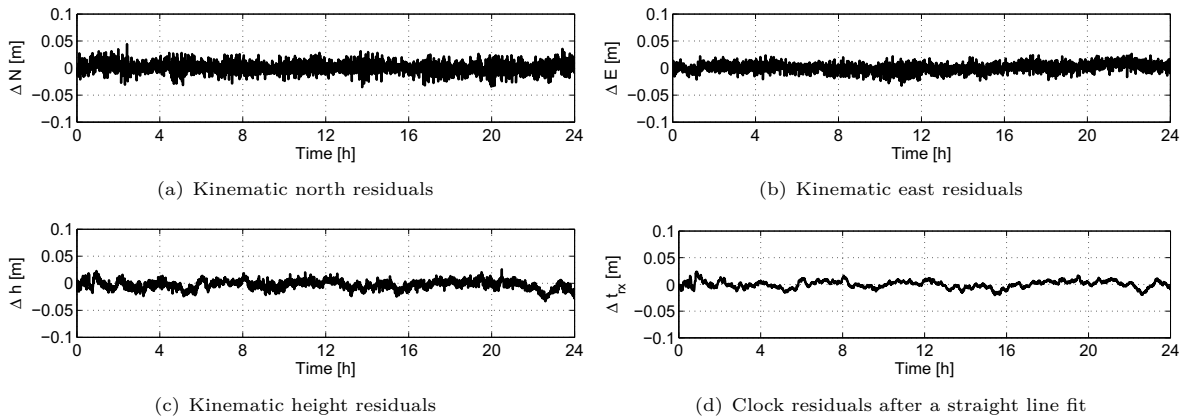


Figure 7.17: Kalman filter kinematic PPP position and clock residuals for IGS station WTZR based on simulated data and clock process noise according to H-maser specifications (February 26, 2010)

In another solution, the process noise added to the clock states was reduced to zero, that means the time and frequency offset of the receiver clock are treated as random constants (Fig. 7.18). Interestingly, the remaining variations can almost completely be suppressed. The latter scenario represents the largest achievable improvement through clock modeling. Of course one may argue, that this is only possible because no clock errors were added when the data was simulated. However, an analysis of simulated data that include a simulated hydrogen maser clock error lead to the same conclusion. Consequently, the utility of the process noise matrix given by (4.78) appears to be limited for the intended purpose. In practice, the process noise can be chosen significantly smaller. The suboptimal performance of the

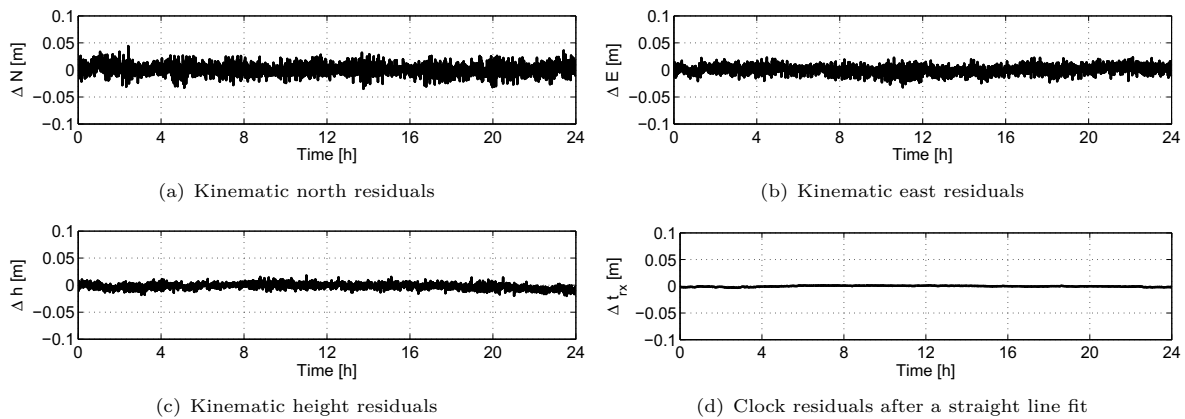


Figure 7.18: Kalman filter kinematic PPP position and clock residuals for IGS station WTZR based on simulated data and zero clock process noise (February 26, 2010)

theoretical process noise matrix is probably caused by the pronounced correlations between the clock parameters, the kinematic height coordinates, and the troposphere parameters, which is not taken into account by the model.

7.3 PPP results with real data

In the first two sections of this chapter, the impact of clock modeling was analyzed based on simulations. In order to demonstrate the practical feasibility of the proposed clock models in real GNSS data analysis, PPP solutions with receiver clock modeling were computed for a number of reference stations of the IGS, that are equipped with hydrogen maser frequency standards. The observation data are again processed in static and kinematic mode. The results of the static positioning are assessed by analyzing the repeatability of daily coordinates. The estimated kinematic coordinates are evaluated with respect to the static coordinates given by the weekly IGS solution. Exemplary results are again shown for the IGS station WTZR.

7.3.1 Static PPP results with real data

Considering the results of the static PPP solution with simulated data, we do not expect to see any significant impact of receiver clock modeling on the repeatability of the daily coordinate estimates. However, in the simulations only normally distributed random observation errors are considered, whereas real GNSS data are always affected by significant systematic errors caused for example by multipath and unmodeled tropospheric delays. If clock modeling had the potential to mitigate such systematic errors, there could possibly be an improvement of the static PPP solution with real data.

Table 7.4 summarizes the repeatability of static PPP coordinate estimates throughout GPS weeks 1577-1580 with and without clock modeling for a number of IGS stations equipped with hydrogen maser frequency standards that are usually in very good condition. Obviously, the solutions with and without clock modeling yield almost identical results. Despite the additional systematic effects in the real observation data, the results are in close agreement with the simulation study. Due to the static coordinates, i.e. only one value per day, the constraint imposed on the evolution of the receiver clock offsets appears to be irrelevant, although the degree of freedom is significantly increased because only 25 instead of 2880 clock parameters are estimated. The computed receiver clock offsets of IGS station WTZR obtained with and without clock modeling for an exemplary day are shown in Figure 7.19. This example illustrates the fact that the piece-wise linear and epoch-wise independent clock estimation yield almost identical daily offsets and drifts and therefore also lead to a comparable height estimate.

station	# of days	Without clock modeling			With clock modeling		
		σ_N [mm]	σ_E [mm]	σ_U [mm]	σ_N [mm]	σ_E [mm]	σ_U [mm]
AMC2 (USA)	28	1.3	1.8	4.0	1.3	1.8	4.2
YELL (Canada)	28	1.5	1.9	4.9	1.5	1.8	5.0
CONZ (Chile)	28	1.5	1.6	3.7	1.6	1.6	3.7
PTBB (Germany)	28	1.0	1.6	4.1	1.0	1.6	4.0
WTZR (Germany)	28	1.2	1.2	2.9	1.2	1.2	2.8

Table 7.4: Repeatability of daily static receiver coordinates for a number of IGS stations with H-maser clocks based on GPS weeks 1577-1580 (March 28 - April 24, 2010)

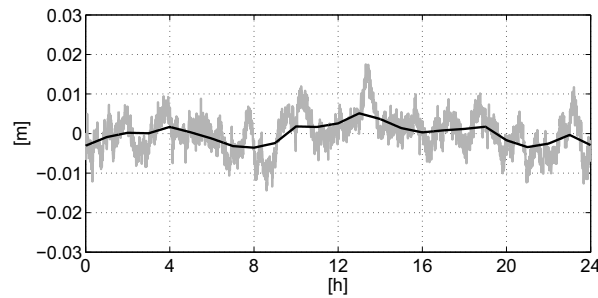


Figure 7.19: PPP-derived epoch-wise independent (gray) and 1-hour piece-wise linear (black) receiver clock offsets for IGS station WTZR on April 18, 2010

7.3.2 Kinematic PPP results with real data

Ideally, kinematic PPP should be validated with a truly kinematic receiver. Due to the limited portability of the oscillator types that meet the stability requirements for clock modeling in PPP, a real kinematic data set could not be recorded. Thus, apart from the GRACE kinematic orbit determination discussed in Section 7.4, the following analysis is based on static observation data, that is processed in kinematic mode, i.e. with epoch-wise independent coordinate estimation. This pseudo-kinematic positioning avoids some of the problems that can be encountered when processing data of kinematic receivers, such as large and varying viewing obstructions or complete signal interruptions. Another difference between kinematic and pseudo-kinematic positioning concerns the influence of the carrier phase wind-up effect (2.5.1). For truly kinematic receivers, the contribution of the receiver antenna rotations to the wind-up effect can reach very large values. Apart from the influence of code-carrier inconsistencies, the phase wind-up effect caused by a rotating receiver antenna can be absorbed by the epoch-wise estimated receiver clock offsets because it is identical for all satellites in view. When the receiver clock is modeled, this bias absorption is generally not possible. Thus, it is clear that for receiving antennas that are subject to significant rotations some external information on the orientation of the antenna element with respect to the ECEF coordinate system is required. The accuracy of this information should be accurate to better than 30° for the ionosphere-free linear combination (L_3) if sub-centimeter accuracy is strived for.

Kinematic PPP using batch least-squares adjustment

Figure 7.20 shows the (pseudo-)kinematic positioning residuals of the standard PPP approach with epoch-wise independent clock estimation for the IGS station WTZR. Compared to the simulated data set (Fig. 7.12), we can observe a similar level of high-frequency noise but additional systematic variations. While the east component is mainly affected by a very low frequency oscillation, the height component and the receiver clock offset exhibit more rapid variations with periods up to 4 hours and amplitudes up to

3 cm. The systematic variations in the north component do not exceed 1 cm. Because the WTZR receiver is connected to a H-maser in good condition and with low frequency drift, it can be well approximated to first order by a straight line. Thus the variations in Figure 7.20(d) are mainly caused by errors in the received GNSS signals. This is also supported by the similarity of the systematic variations in the receiver clock offsets and the height coordinate time series, which also reflects the strong correlation between these two parameter types. Note, that the slow oscillation of the kinematic east coordinate is an artifact of the parameter estimation with float ambiguities and can be avoided, when the carrier phase ambiguities are fixed to integers. In contrast, the more rapidly changing systematic variations, that can be observed in all components are primarily caused by residual troposphere modeling errors and site-dependent effects such as multipath and near-field effects.

When the clock is modeled by a sequence of piece-wise linear parameters with a spacing of 1 h, the high-frequency noise of the kinematic height estimates is significantly reduced (Fig.7.21). However, the systematic variations can only partly be suppressed. For completeness the carrier phase residuals and tropospheric zenith delays of both solutions are shown in Figures 7.22 and 7.23. The small increase of the carrier phase residuals that occurs when the receiver clock is modeled is hardly visible, because mainly the small residuals of satellites that are observed at high elevations are affected. For the piece-wise linear troposphere estimates a small smoothing effect can be noticed in the solution with clock modeling.

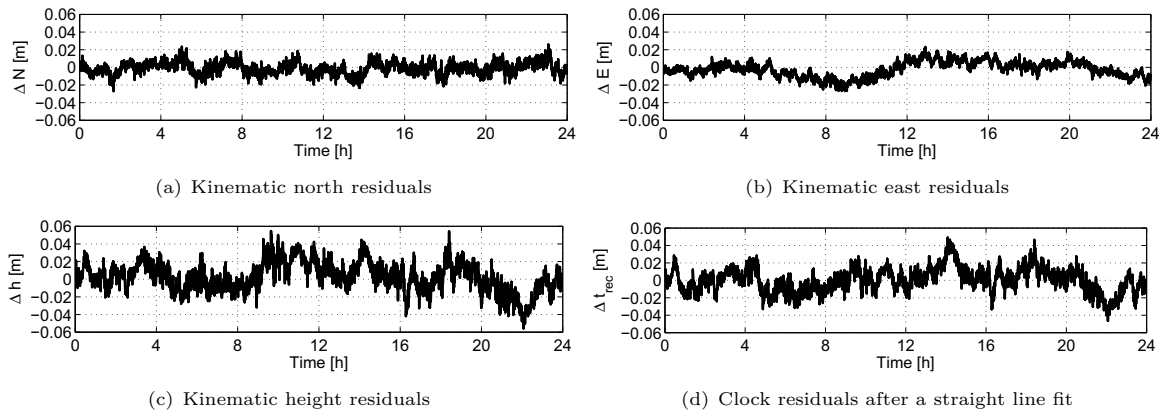


Figure 7.20: Kinematic PPP position and clock residuals for the IGS station WTZR based on real data and epoch-wise independent clock estimation on February 26, 2010

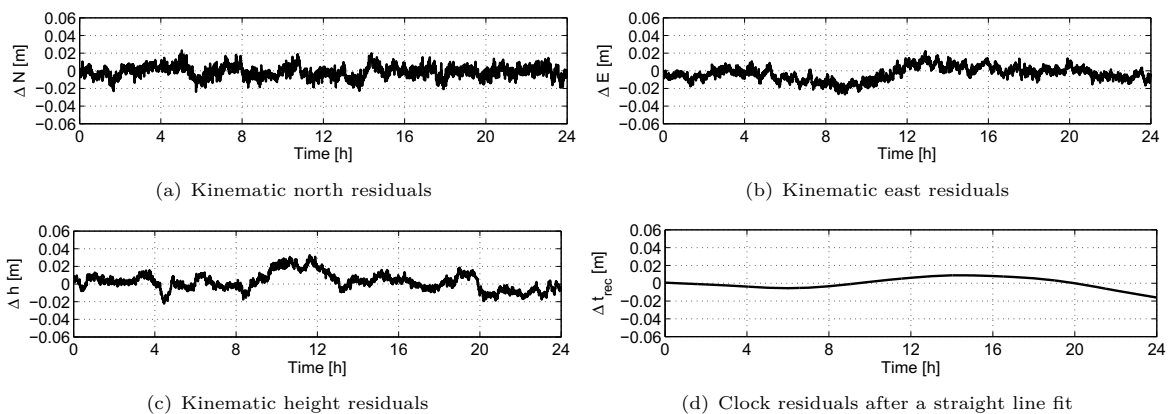


Figure 7.21: Kinematic PPP position and clock residuals for the IGS station WTZR based on real data and 1-hour piece-wise linear clock estimation on February 26, 2010

Since it does not make sense to compute the standard deviation of the non-stationary height time series (Fig. 7.20 and 7.21), the result of a moving average filter with a length of 5 epochs was first removed from the time series. The remaining high-frequency variations have a standard deviation of $\sigma_h = 1.5$ mm

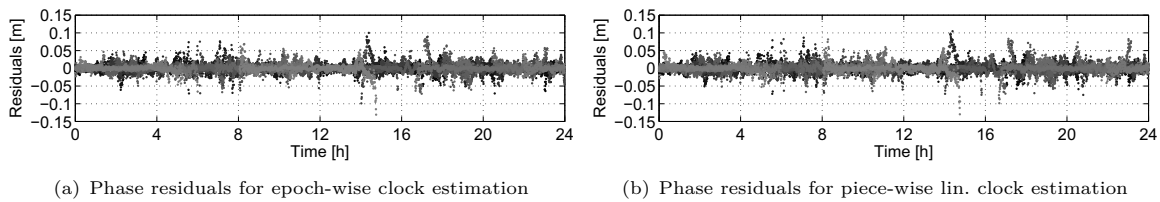


Figure 7.22: Carrier phase residuals of a kin. PPP solution for the IGS station WTZR on Feb. 26, 2010

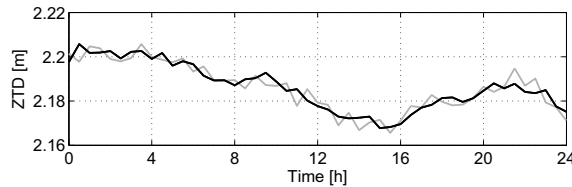


Figure 7.23: Estimated tropospheric zenith delays of a kin. PPP solution with (black) and without (gray) clock modeling for the IGS station WTZR on Feb. 26, 2010

and $\sigma_h = 4.5$ mm with and without clock modeling, respectively. This is an improvement of 65 % and in reasonable agreement with the expected reduction of about 70 % inferred from the simulation study. More important, however, is the finding, that also systematic effects can be reduced. This is clearly visible when the time window between 20:00 and 24:00 in Figures 7.20 and 7.21 are compared.

Table 7.5 shows the average RMS of daily kinematic solutions for five IGS stations equipped with well-maintained H-maser clocks over a period of 4 weeks. Despite the systematic effects, encountered in real GPS data analysis, the RMS improvement is consistently around 50 % for all stations.

station	# of days	RMS w/o clk modeling			With clk modeling			RMS ratio		
		N [mm]	E [mm]	U [mm]	N [mm]	E [mm]	U [mm]	N [%]	E [%]	U [%]
AMC2	28	8.8	8.6	22.3	8.0	8.3	11.9	8.4	2.9	49.5
PTBB	28	10.7	9.2	21.0	9.8	8.7	10.6	8.6	5.3	49.2
TWTF	25	10.0	9.4	26.3	8.5	9.2	12.4	15.1	2.9	52.8
CONZ	24	7.1	16.2	21.6	6.1	15.4	11.2	14.7	5.1	48.3
WTZR	28	9.2	9.6	22.4	8.4	8.8	11.0	7.5	8.6	50.6

Table 7.5: Average daily RMS of kinematic receiver coordinates for a number of IGS stations with H-maser clocks based on GPS weeks 1577-1580 and 30-s observation sampling

Generally, the propagation of systematic observation errors into the kinematic height coordinates can be reduced either by extending the interval of the piece-wise linear clock parameters or by increasing the relative constraints between them. Systematic variations at very low frequencies, however, can usually not be suppressed by clock modeling because even for hydrogen maser clocks a certain degree of mid- to long-term clock variations must be allowed. Only, practically drift-free oscillators like cesium fountains or optical clocks would allow to mitigate such low-frequency systematic effects.

For the example data set of IGS station WTZR the weighted sum of squared carrier phase residuals $\mathbf{v}^T \mathbf{P} \mathbf{v}$ increased from $5435 m^2$ to $6482 m^2$ when clock modeling was applied. Together with the increased degree of freedom due to the reduction of the number of clock parameters, this leads to the same a posteriori variance factor for the solutions with and without clock modeling. As expected, considering the results in Section 7.1, the horizontal coordinate components are practically not affected by the different clock parametrizations.

Kinematic PPP using a Kalman filter

In addition to the batch solution, the data of the IGS station WTZR were also processed with the Kalman filter algorithm. Figure 7.24 shows the kinematic PPP position residuals of the forward/backward smoothed filter solution with clock process noise based on TCXO specifications (cf. Tab. 3.2). As expected, similar systematic effects as for the batch least-squares solution can be observed. Especially for the height component and the receiver clock, the variations in the filter solution are, however, slightly more pronounced than in the batch solution. For the solution shown in Figure 7.25, the process noise

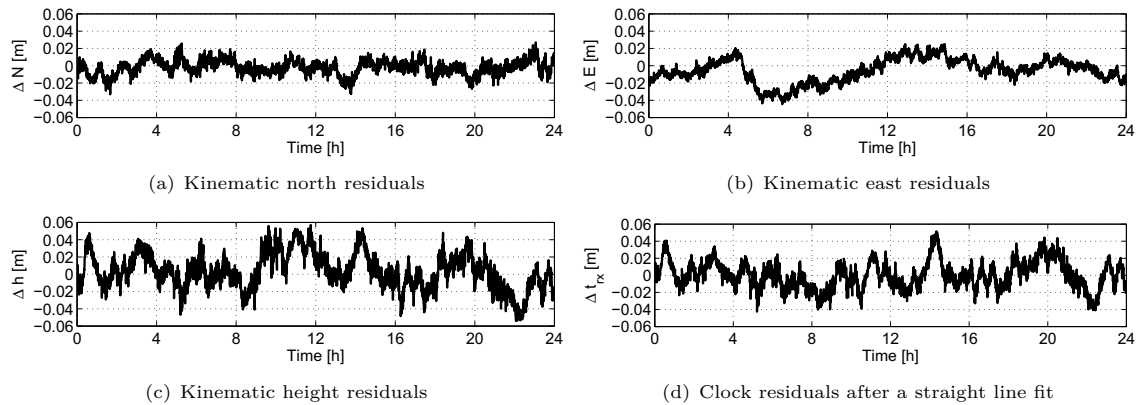


Figure 7.24: Kalman filter kinematic PPP position and clock residuals for the IGS station WTZR based on real data and clock-state process noise according to TCXO specifications (February 26, 2010)

applied to the clock states was reduced according to the specifications of an active hydrogen maser (cf. Tab. 3.2). The high-frequency noise of the kinematic height coordinates and the receiver clock time series in this solution is significantly reduced but the systematic variations are hardly affected. As in the

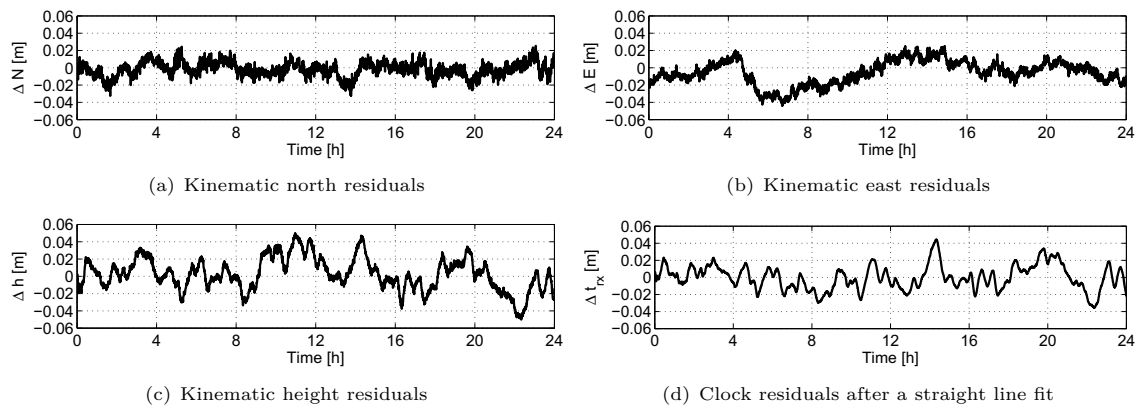


Figure 7.25: Kalman filter kinematic PPP position and clock residuals for the IGS station WTZR based on real data and clock-state process noise according to H-maser specifications (February 26, 2010)

case of simulated data, adding no process noise to the covariances of the clock states, results in a much smoother time series of the kinematic height estimates (Fig. 7.26).

In addition, for real data, a much better suppression of spurious variations at longer time scales is achieved. Although this solution is significantly over-constrained from the theoretical point of view, the kinematic height coordinates are actually closer to the truth. As already discussed for the simulated case this is probably related to the strong correlations between the kinematic coordinates, the tropospheric zenith delays and the receiver clock parameters. In combination with systematic errors in the observations, these correlations are responsible for the observed degradation of the estimated receiver

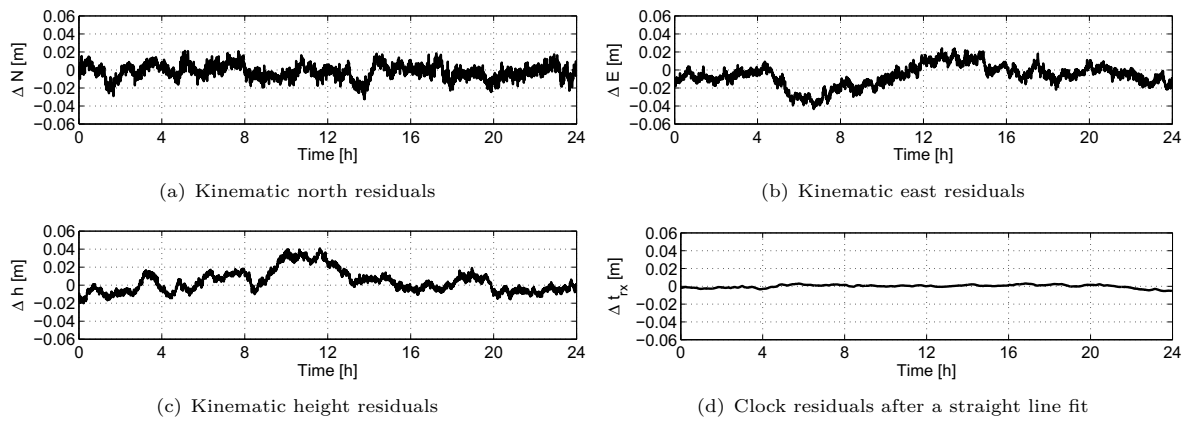


Figure 7.26: Kalman filter kinematic PPP position and clock residuals for the IGS station WTZR based on real data observed with a Leica GRX1200GGPro receiver and no clock state process noise (February 26, 2010)

clock time series. In practice, the process noise can be significantly reduced in order to achieve a higher degree of temporal decorrelation of the different parameter types. Suitable values can be determined by empirical analysis.

7.4 Receiver clock modeling for a LEO

In recent years, kinematic orbit determination of low Earth orbiters equipped with GPS receivers, such as CHAMP, GRACE and GOCE, has attracted much attention, especially for gravity field determination (e.g. Gerlach et al., 2003; Jäggi et al., 2011). In contrast to classical dynamic orbit determination approaches in which just six initial conditions of the satellite's equation of motion, often complemented by a few additional force model parameters, are determined, three independent coordinates are estimated at every observation epoch in the kinematic approach. Being a solution of the equation of motion, dynamic orbit determination relies on a detailed modeling of the physical forces acting on the spacecraft, in particular the gravity field of the Earth, atmospheric drag and solar radiation pressure. In order to reduce the impact of errors in these force models, additional empirical accelerations of the spacecraft can be estimated. Such an approach is called reduced-dynamic orbit determination and combines the knowledge about the laws of satellite motion with the geometrical strength and precision of GPS-based positioning (Wu et al., 1991). Independent of the orbit determination approach, additional receiver clock offsets and carrier phase ambiguities have to be estimated.

The main advantage of kinematic orbit determination can be seen in the fact that it is a purely geometric approach, i.e. the results are free from influences of any a priori gravity field model. However, kinematic orbits are much more sensitive to small errors in the observation modeling than reduced-dynamic orbits (Wu et al., 1991) and tracking of at least four GPS satellites at any time is necessary to compute a position and five satellites, if reliability is required. In view of the current tracking performance of spaceborne GPS receivers, this requirement regularly causes gaps in the computed kinematic trajectory, in particular for epochs, where bad observations have to be rejected. The most simple and efficient method for precise kinematic orbit determination of LEO satellites is the Precise Point Positioning (PPP) approach. The main difference compared to kinematic PPP for terrestrial applications is the rapid change of the observation geometry and the well defined attitude of the GNSS antenna, which facilitates the correction of the carrier phase wind-up effect. In addition, the size of the moving structure as well as the financial budget of a LEO mission allows to employ a high-quality oscillator. Space-qualified ultra-stable quartz, rubidium and, more recently, passive-hydrogen maser frequency standards are readily available and even more sophisticated and precise oscillators are currently under development. Therefore, kinematic LEO orbit determination is very well suited for the proposed method of PPP with receiver clock modeling. In fact the Gravity Recovery And Climate Experiment (GRACE) mission operates an ultra-stable oscillator (USO) in combination with a geodetic dual-frequency GPS receiver in low Earth orbit. In the following we will consider this mission as a case study and demonstrate the practical feasibility of clock modeling with real GRACE GPS data.

7.4.1 The GRACE mission

The Gravity Recovery And Climate Experiment (GRACE) consists of two identical satellites in a near-polar orbit at an altitude of approximately 500 km with an along track distance of approximately 220 km (Fig. 7.27). The primary observable for gravity field determination is the highly precise inter-satellite K-band microwave link that allows to measure the distance between the two spacecrafts with few μm accuracy. Furthermore, both spacecrafts are equipped with two dual-frequency BlackJack GPS receivers built by JPL. This receiver type behaves like a classical semicodeless geodetic receiver commonly found in the IGS network (Montenbruck and Kroes, 2003). In addition to tracking the GPS satellites the BlackJack receivers are also used to measure the K-band signal transmitted by the other GRACE spacecraft. The highly accurate determination of the inter-satellite distance is achieved through the dual one-way operation of the K-band link. This measurement configuration requires a synchronization of the two receivers to better than 150 ps during post-processing (Bertiger et al., 2003). Since both, the K-band ranging system (KBR) and the GPS receiver, share the same oscillator the GPS data can be used for this synchronization.

In Figure 7.28 the Allan deviation for a number of high-performance frequency sources is plotted including the GRACE USO with a frequency stability of $\sigma_y = 1 - 3 \times 10^{-13}$ for averaging times between



Figure 7.27: An artist's view of the GRACE twin satellites in orbit (Source: Astrium)

1 and 1000 s (Dunn et al., 2003). For reference, an approximation of the lower bounds of the L_3 and P_3 observation noise, projected onto the epoch-wise GRACE receiver clock estimates ($\sigma_{t,rx} = 3 \text{ mm} / 30 \text{ cm}$) are indicated by dashed lines with a slope of -1.

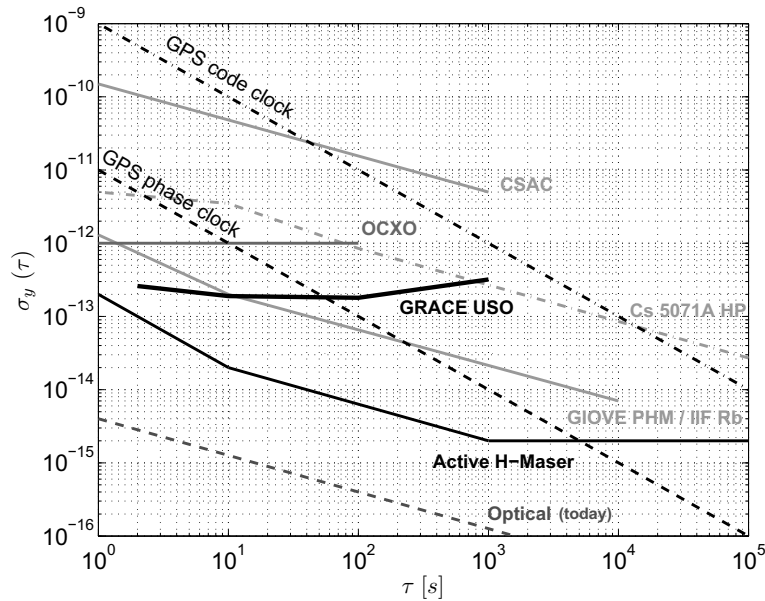


Figure 7.28: Frequency stabilities of selected precision oscillators including the GRACE USO (Dunn et al., 2003), dashed lines: Approximation of the GRACE GPS receiver L_3 and P_3 observation noise, projected onto the epoch-wise receiver clock estimates

Although the GRACE USO provide an extraordinary short-term frequency stability they do not achieve the performance offered by hydrogen maser frequency standards, in particular beyond 10 s averaging time. Based on this figure and the processing results, a spacing of only 60 seconds for the piece-wise linear parameters in combination with relative constraints of $\sigma_{m_i, m_{i+1}} = 6.2 \text{ ns/h} \cdot \Delta t$ between consecutive slopes were chosen. More precisely, the modified Allan deviation of the position differences with respect to the reduced-dynamic reference orbit, which is discussed later in this section, was used to optimize the relative drift constraints. The constraints are applied as pseudo-observation with an expectation value of zero and a standard deviation that is scaled to the piece-wise linear parameter interval of 60 s,

i.e. approximately $\sigma_{m_i, m_{i+1}} = 0.8$ ns/h. Due to these rather loose relative constraints and the small piece-wise linear intervals, the impact of the clock modeling is expected to be less pronounced than for the hydrogen maser clocks discussed in the preceding sections.

7.4.2 LEO data processing

Precise kinematic positioning of a LEO differs from kinematic PPP of a moving receiver on the Earth's surface mainly by the much more rapid change of observation geometry and the absence of non-dispersive atmospheric delays. A LEO at an altitude of 500 km orbits the Earth in approximately 95 minutes, i.e. around 15 times per day tracking a single GPS satellite for a maximum of 35 minutes. Figure 7.29 shows the satellite tracks observed by GRACE A on January 4, 2008.

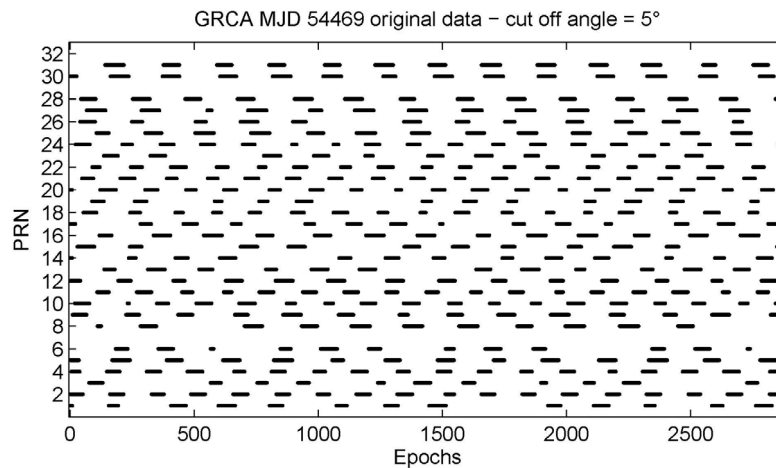


Figure 7.29: GPS satellites observed by GRACE A on January 4, 2008

Due to the short observation arcs and the increased ionospheric variability between consecutive observations, the data screening routines can have difficulties to detect small cycle slips and outliers. Therefore, the post-fit residuals have to be screened very carefully for undetected cycle slips and outliers in an iterative procedure. Alternatively, a preliminary dynamic or reduced-dynamic LEO orbit can be used to improve the detection of bad observations (Kroes, 2006).

During processing of data observed by the two GRACE satellites, it became clear, that the carrier phase observation residuals are only weakly elevation-dependent (Fig. 7.30(a)). This is probably due to the absence of tropospheric propagation delays for a receiver at LEO altitude. In contrast, the pseudorange observation residuals showed a clear increase at low elevations (Fig. 7.30(b)). Because the pseudorange observations in the PPP solution are essentially only used to resolve the singularity caused by the 1:1 correlation between carrier phase ambiguities and the receiver clock offsets, elevation-independent weighting has been applied for both, pseudorange and carrier phase observations.

7.4.3 Application of clock modeling to simulated GRACE GPS data

In a first step, the impact of clock modeling is again analyzed using simulated data. One day of synthetic GRACE A observation data with 30-s resolution were generated for January 4, 2008. Satellite and receiver clock offsets as well as tropospheric delays were assumed to be zero. GPS satellite positions were interpolated from the positions given in the CODE final ephemeris file. In order to closely match the real GRACE observation geometry only those GPS satellites and epochs were used, that are actually observed by the receiver on board of GRACE A on that particular day (Fig. 7.29). White noise with a standard deviation of 0.1 m for the pseudorange and 0.001 m for the phase observations was added. For the pseudoranges, the noise was multiplied by the elevation-dependent factor $1/\sin(e)$. The main

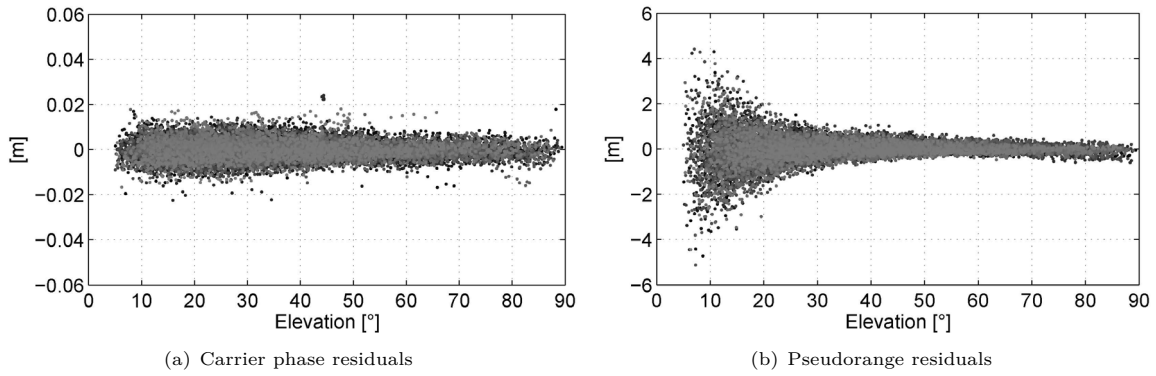


Figure 7.30: GRACE carrier phase and pseudorange observation residuals of a PPP solution with fixed integer ambiguities

advantages of using simulated observations are the independence of the data quality and the availability of a “true“ reference trajectory. In addition, the implementation of carrier phase ambiguity fixing is easy and its impact on the solution can be studied.

The differences of the kinematic LEO positions and the reference orbit are best analyzed in the orbital reference frame, i.e. in along-track, cross-track and radial direction. The transformation of the PPP-derived ECEF position residuals into the orbital frame is performed by first transforming the positions into an ECI frame and then applying a rotation matrix,

$$\mathbf{R}_{ECI \rightarrow orbitframe} = \begin{bmatrix} \mathbf{e}_1 & \mathbf{e}_2 & \mathbf{e}_3 \end{bmatrix}^T \quad (7.3)$$

that is composed of the unit vectors \mathbf{e}_1 pointing from the spacecraft to the origin of the ECI system, \mathbf{e}_3 , being orthogonal to \mathbf{e}_1 and the velocity vector of the satellite \mathbf{v} and \mathbf{e}_2 , that completes a right-hand coordinate system and points approximately into the direction of \mathbf{v} . Mathematically these relationships are expressed as

$$\mathbf{e}_1 = \frac{\mathbf{r}}{|\mathbf{r}|}, \quad \mathbf{e}_3 = \frac{\mathbf{e}_1 \times \mathbf{v}}{|\mathbf{e}_1 \times \mathbf{v}|}, \quad \mathbf{e}_2 = \mathbf{e}_3 \times \mathbf{e}_1. \quad (7.4)$$

Note, that only the position vector but not the velocity vector is obtained from the PPP solution. Therefore, the velocity vector has to be derived from the positions using a suitable interpolation approach. As a first approximation, simply the difference between neighboring orbit positions were used. More precise velocity estimates can be derived using higher-order interpolation polynomials. Strictly speaking, the velocities should be derived from the ECI positions. If ECEF velocities are used, the effect of Earth rotation has to be taken into account in the transformation from ECEF to ECI.

Figure 7.31 shows the position and clock residuals with respect to the values used in the simulation for a conventional PPP solution, i.e. with epoch-wise independent clock offsets. The first thing we notice is a distinct non-white noise behavior of the time series, although synthetic observation data with normally distributed random errors were used. The systematic deviations are caused by the large number of float ambiguities that need to be estimated in addition to the coordinates and clock parameters. The impact is most pronounced in the receiver clock time series. This is due to the high degree of mathematical correlation between the receiver clock offset and the carrier phase ambiguities. In fact, the (medium to long-term) separation of the two parameter types is governed by the less precise pseudorange observations. Furthermore, Figure 7.31 nicely illustrates the typical noise characteristics of the kinematic coordinate components. The radial component is much noisier than the along-track and cross-track components. The cross-track component shows the smoothest characteristic with small long-period deviations that are - in contrast to the other components - not correlated with the revolution period of approximately 90 minutes.

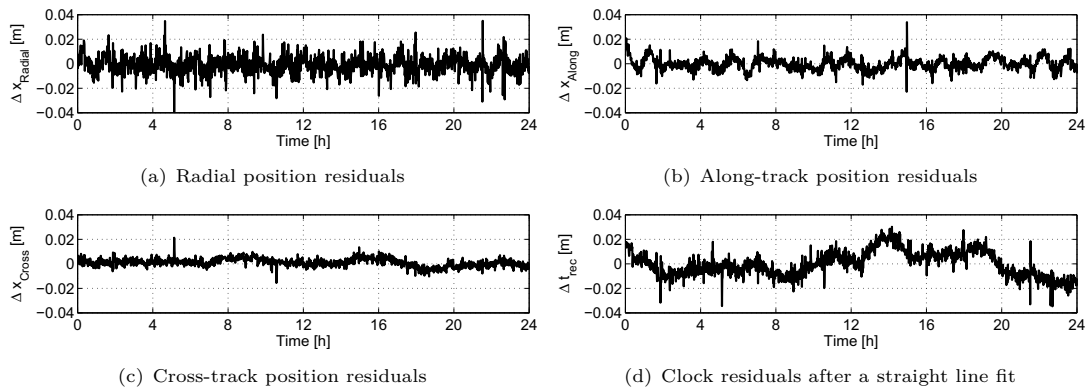


Figure 7.31: 30-s position and clock residuals of a kinematic PPP solution with epoch-wise independent clock estimation for a simulated data set based on the actual observation geometry seen by GRACE A on January 4, 2008

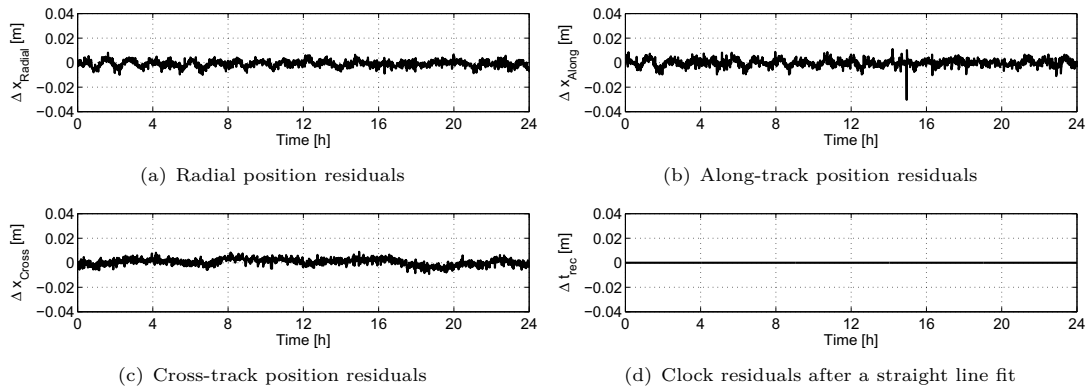


Figure 7.32: 30-s position and clock residuals of a kinematic PPP solution for a simulated data set based on the actual observation geometry seen by GRACE A on January 4, 2008, when only one offset and one drift parameter are estimated for the entire 24-hour data set

Comparing the results of the conventional approach of estimating epoch-wise independent clock offsets with the extreme case of estimating only one clock offset and one drift parameter (Fig. 7.32) for the entire day, we find a substantial reduction of the noise in the radial component, but also the along-track component is slightly improved. Furthermore, systematic variations in the radial and along-track components can be reduced. Apart from the reduction of some spikes, the cross track component seems to be hardly affected. In view of the results for the terrestrial PPP case, this behavior could be expected.

For the solution shown in Figure 7.33, the clock modeling interval was reduced to 60 s, according to the frequency stability of the GRACE ultra-stable oscillators. Obviously, much of the noise reduction in the radial component can already be achieved using this very short modeling interval. On the other hand, low-frequency variations, e.g. with the revolution period cannot be suppressed. The receiver clock time series is essentially a smoothed version of the epoch-wise receiver clock offsets.

In order to investigate the impact of the float ambiguities on the results, additional ambiguity-fixed PPP solutions have been computed for the simulated data set. Figure 7.34 shows the results that are obtained with epoch-wise clock offsets and Figure 7.35 shows the solution with 60-s piece-wise linear clock modeling. In both cases systematic effects have disappeared, while the high-frequency (random) noise is not noticeably affected. This demonstrates, that the systematic errors observed in the conventional PPP case are related to the estimation of float ambiguities. Due to the absence of systematic variations, the ambiguity-fixed solutions are well suited to compare the precision of the position estimates in terms of their RMS (Tab. 7.6). In the ideal case, i.e. when only one clock offset and one drift parameter for the entire 24-hour data set are estimated, the precision of the radial orbit positions can be improved by 66 %.

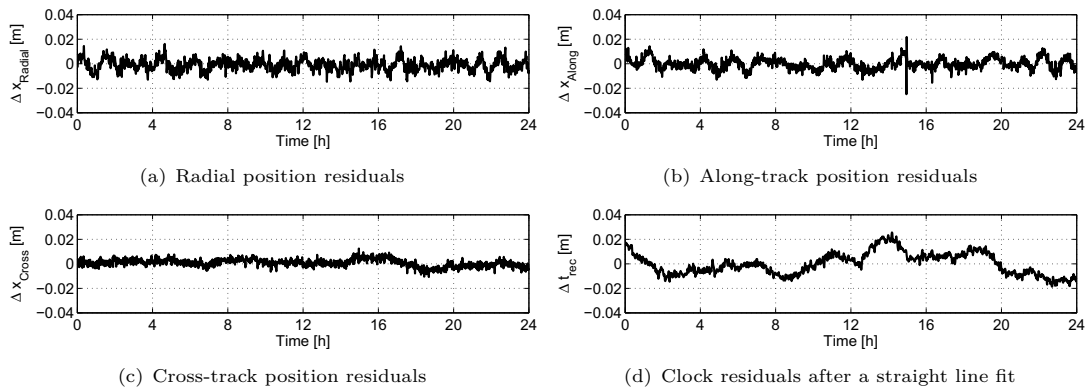


Figure 7.33: 30-s position and clock residuals of a kinematic PPP solution for a simulated data set based on the observation geometry seen by GRACE A on January 4, 2008, when the receiver clock is modeled by piece-wise linear parameters with 60-s spacing and 0.8 ns/h relative constraints between consecutive slopes

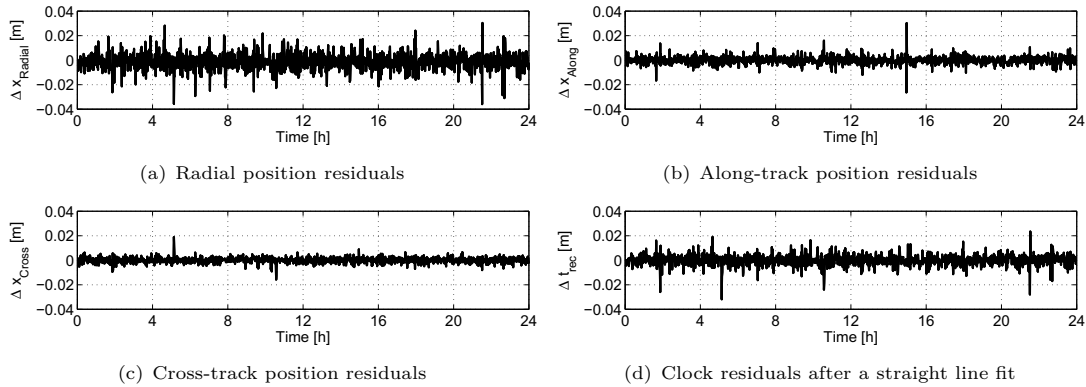


Figure 7.34: 30-s position and clock residuals of an *ambiguity-fixed* kinematic PPP solution with epoch-wise independent clock estimation for a simulated data set based on the actual observation geometry seen by GRACE A on January 4, 2008

When using a piece-wise linear clock model with a parameter spacing of only 60 s, the reduction of the radial RMS is still 47 %. That means that even for the GRACE USO a significant improvement of the radial orbit precision can be expected. With a 10-20 % reduction of the RMS significant improvements can also be observed for the along-track and cross-track components.

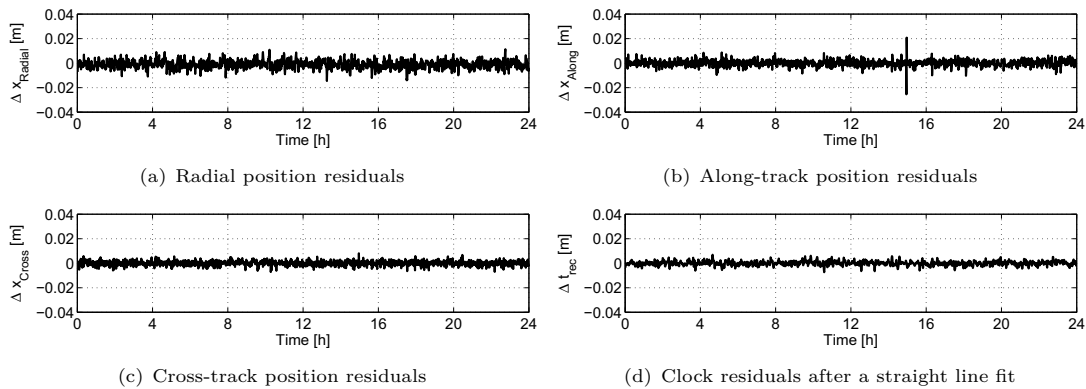


Figure 7.35: 30-s position and clock residuals of an *ambiguity-fixed* kinematic PPP solution for a simulated data set based on the observation geometry seen by GRACE A on January 4, 2008, when the receiver clock is modeled by piece-wise linear parameters with 60-s spacing and 0.8 ns/h relative constraints between consecutive slopes

	PPP	PPP + 60 s clock	PPP + 24 h clock	Improvement
Radial RMS	6.8 mm	3.6 mm	2.3 mm	47 / 66 %
Along-track RMS	3.2 mm	2.7 mm	2.5 mm	16 / 21 %
Cross-track RMS	2.4 mm	2.1 mm	2.0 mm	12 / 16 %

Table 7.6: RMS of ambiguity-fixed PPP position residuals with and without clock modeling for a simulated data set based on the observation geometry seen by GRACE A on January 4, 2008

7.4.4 Application of clock modeling to real GRACE GPS data

The processing of real GRACE GPS data is of course complicated by the presence of outliers and carrier phase cycle slips. In addition, the data editing algorithms need to cope with an increased variability of the ionospheric delay due to the rapid movement of the spacecraft. Nevertheless, the same data preprocessing steps that are used for terrestrial stations have been applied for the LEO data. That means that time differences of the geometry-free (L_4) and Melbourne-Wübbena linear combinations are used but the detection threshold for the L_4 time differences is increased to account for the larger changes in the ionospheric delay between consecutive observations. Consequently, small cycle slips and outliers cannot be reliably detected during the pre-processing. Fortunately, for a typical observation geometry with more than 5 GPS satellites, the least-squares solution exhibits a certain degree of robustness with respect to small outliers, which allows to identify the problematic data from the post-fit residuals. Apart from the identification of bad data points and cycle slips some LEO- or GRACE-specific processing aspects are worth to be discussed here.

The BlackJack receivers on board of the GRACE satellites provide two different carrier phase observation types on the L_1 frequency, denoted as L1 and LA in the experimental RINEX 2.20 format. While the L1 carrier phase is derived from the P-code tracking channel, the LA observable originates from the C/A code channel and exhibits a significantly lower noise level (Montenbruck and Kroes, 2003; Jäggi et al., 2008). Therefore, the LA observations were favored over the L1 observations.

During the processing of real GRACE data, typically 2-4 pseudorange observation arcs per day have to be corrected for a constant bias of 15.5 m. Such a bias is known to occur occasionally for all BlackJack GPS receivers and is probably caused by a receiver sampling error (Montenbruck and Kroes, 2003). Since the carrier phase observations are not affected, the identification of the biased satellite tracks is very easy from the post-fit residuals in a combined processing. For a pseudorange-only solution the identification is much more challenging. A detection during preprocessing is generally difficult, since the entire satellite track is usually affected in the same way so that any algorithm relying on time differenced observations will fail.

When using GPS data observed by a LEO, special attention also has to be paid to geometric corrections due to the changing orientation of the satellite with respect to the reference coordinate system. Most importantly, the offset of the physical antenna reference point (ARP) of the GPS receiver antenna with respect to the center of mass of the satellite has to be corrected. Furthermore, the offset of the frequency-dependent electrical phase center (PCO) of the receiving antenna has to be taken into account. The values of these corrections for the GRACE GPS antennas are taken from Montenbruck et al. (2009) and are quoted in Table 7.7.

In addition to the common PCO, the apparent phase center of the receiving antenna depends on the direction of the incoming signals. These small azimuth and elevation-dependent delays, known as phase center variations (PCV), have to be taken into account if cm-level accuracy is strived for. Usually, antenna PCVs are determined in a dedicated calibration procedure which was also carried out for the GRACE GPS antenna type. However, these values did not provide satisfying results during practical application (Montenbruck et al., 2009). This is possibly due to interactions of the receiver antenna with the spacecraft surface or other satellite components. Therefore, it has been suggested to derive corrections for the phase center variations from the in-orbit observation data. Jäggi et al. (2009) have

	x [mm]	y [mm]	z [mm]
ARP	0.00	0.00	-444.00
L_1 PCO	0.60	1.49	-7.01
L_2 PCO	0.86	0.96	22.29

Table 7.7: GRACE ARP and phase center offsets according to Montenbruck et al. (2009)

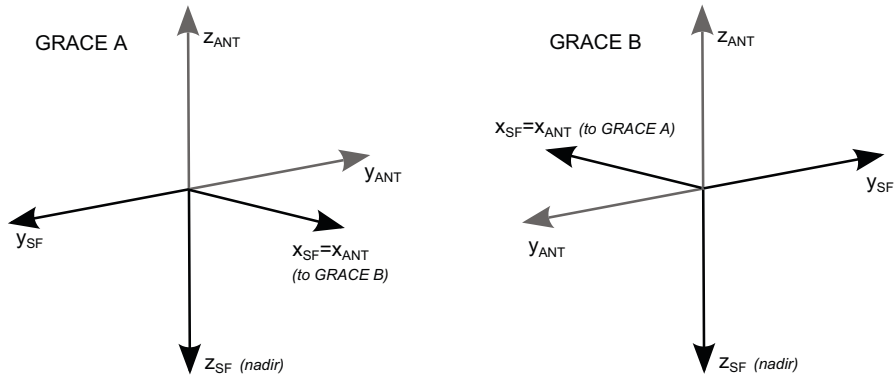


Figure 7.36: Spacecraft-fixed science reference frame (SF) and antenna reference frame (ANT) for the two GRACE satellites. Note, that the direction of flight corresponds to an azimuth of 90° for the trailing satellite GRACE A and 270° for the leading satellite GRACE B in the antenna reference frame

successfully applied such empirical PCV corrections based on averaged carrier phase residuals from kinematic orbit determinations covering one year of observation data on a $1^\circ \times 1^\circ$ grid. An advantage of this approach is that multipath effects caused by the spacecraft surface can also be reduced. The resulting phase center maps for GRACE A and B were kindly provided by Adrian Jäggi of the AIUB and used for this investigation.

As discussed earlier (cf. Section 2.5.1), phase wind-up errors caused by a rotating receiver antenna should be corrected generally in PPP and in particular if precise clock modeling is to be applied. The changing orientation of the GRACE GPS antenna may either be derived from the star camera observations on board the satellites or by assuming the nominal attitude of the spacecraft. In both cases the resulting receiver antenna phase wind-up effect can be easily computed and removed from the carrier phase observations. The accuracy requirement for this correction is moderate because small residual phase wind-up effects can still be absorbed by the carrier phase ambiguities and the remaining receiver clock parameters.

The offset of the ARP, the antenna PCO and the receiver antenna phase wind-up correction were computed based on the attitude given in the GRACE star camera (SCA1B) files. These files contain quaternions with 5-s resolution that describe the precise orientation of the GRACE science reference frame (SF) with respect to the quasi-inertial reference frame ICRF. Since the entire GPS processing is performed in the Earth-fixed reference frame (ITRF), corresponding transformations have to be applied to the offset vectors. Furthermore, the orientation of the antenna coordinate system with respect to the science reference frame has to be taken into account. The relationship is illustrated in Figure 7.36. In analogy to the conventions for terrestrial antennas the boresight vector is pointing to the zenith, i.e. the z-axis of the science reference frame changes sign. In order to maintain a right-hand coordinate system the direction of the y-axis is also inverted and the azimuth angle is counted clock-wise from the y-axis to the x-axis (Montenbruck et al., 2009; Jäggi et al., 2009).

In order to make optimal use of the USO frequency stability, the influence of relativistic effects on the LEO clock should be corrected for. The GRACE oscillators are subject to relativistic frequency shifts induced by the varying altitude and velocity of the satellites along their orbit. This gives rise to

periodic receiver clock variations on the order of several ns (Larson et al., 2007). However, the relativistic effects are removed from the observations before generating the Level 1B RINEX data that are used in this investigation (Bertiger, personal communication). Consequently, no additional relativistic clock corrections were applied to the LEO oscillator.

Code-only solution In a first attempt to analyze real GRACE GPS data, kinematic orbits based solely on ionosphere-free (P3) GRACE pseudorange data have been computed with and without clock modeling. While being identical in terms of the observation geometry the processing of the code-only solution is not complicated by the existence of carrier phase cycle slips. In addition, the accuracy of the position estimates can be assessed using the reduced-dynamic GRACE Level 1B orbits which are significantly more accurate than a pseudorange-only orbit. During processing of the data it became clear that the noise of the GRACE pseudorange data increases at low elevations (Fig. 7.30). Therefore, elevation-dependent weighting, according to $\sin^2(e)$, was applied in the pseudorange-only solution. Due to the higher noise level of the pseudorange observations the spacing of the piece-wise linear clock parameters was increased to 300 s, whereas the relative constraints of 0.8 ns/h between consecutive slopes was retained.

The results of the kinematic orbit determination based on pseudorange observation alone are displayed in Figures 7.37 and 7.38. The reduction of the noise in the radial direction when using the piece-wise linear clock model is striking. In contrast, the noise levels of the along-track and cross-track components are hardly affected. The number of outliers is, however, also considerably reduced.

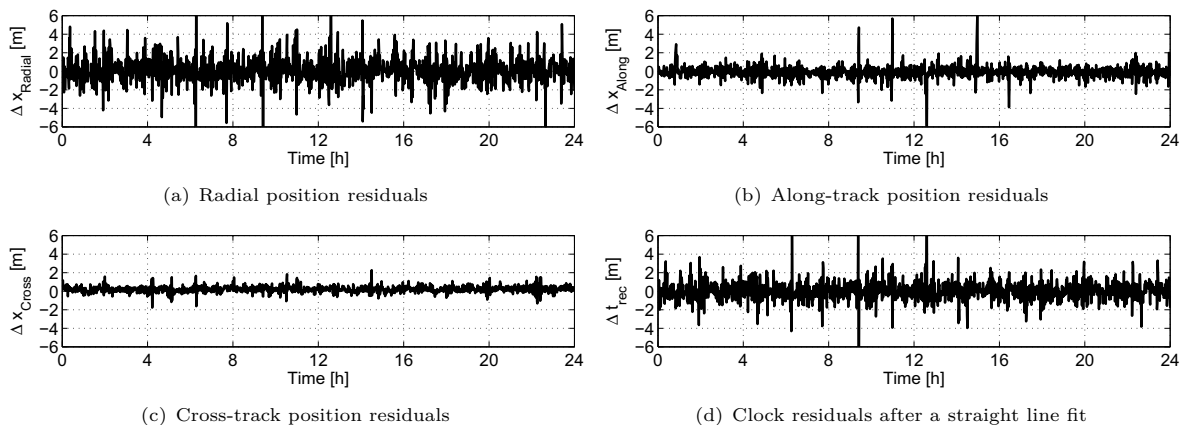


Figure 7.37: Pseudorange-only (P3) position and clock residuals with respect to the GRACE Level 1B orbit using epoch-wise independent clock estimation (GRACE A on January 4, 2008)

The RMS values of the time series are given in Table 7.8. The RMS of the radial position component is reduced by 75 % from 1.18 m to 0.29 m while the improvement of the along-track and cross-track components is only 3 % and 10 %, respectively. For the computation of the statistics, position estimates deviating by more than 3.15 m were rejected. This value corresponds approximately to the standard deviation of the position residuals in the case of epoch-wise independent clock offset estimation multiplied by a factor of three.

PPP solution The validation of the PPP-based kinematic LEO positions is generally difficult due to the absence of a reference orbit of significantly higher accuracy. In fact, the reduced-dynamic orbit produced by JPL that is provided as part of the GRACE Level 1B products, exhibits a similar accuracy as the computed kinematic orbit. Nevertheless, the reduced-dynamic orbit can serve as a reference for the analysis of high-frequency errors in the kinematic trajectory because it is smooth like the actual LEO orbit. This can be confirmed, for example, by comparing the inter-satellite distance from the reduced-dynamic orbits with the highly precise observations of the GRACE K-band link, which results in smoothly time varying residuals.

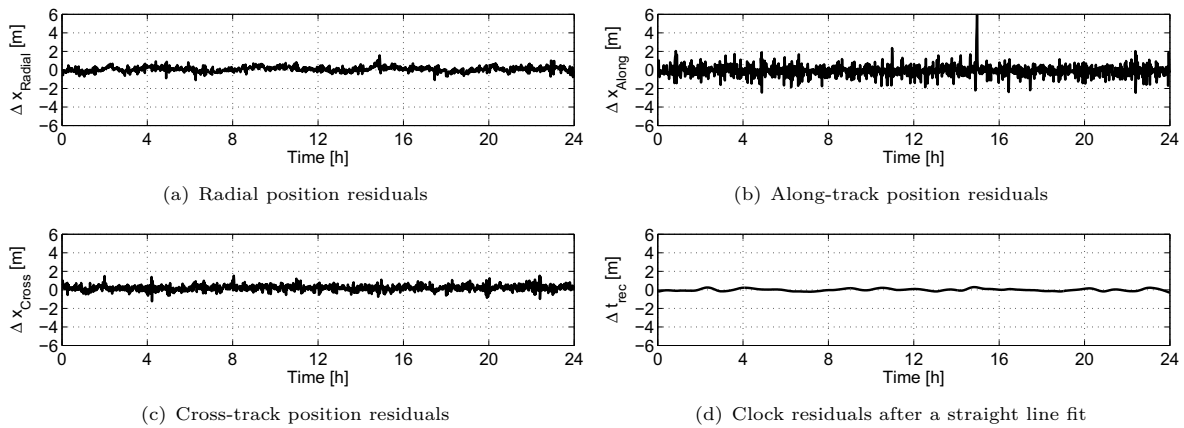


Figure 7.38: Pseudorange-only (P3) position and clock residuals with respect to the GRACE Level 1B orbit using a 300-s piece-wise linear clock model (GRACE A on January 4, 2008)

	SPP	SPP + clk model	Improvement
Radial RMS	1.18 m	0.29 m	75 %
Along-track RMS	0.60 m	0.58 m	3 %
Cross-track RMS	0.41 m	0.37 m	10 %
Completeness	98.96 %	99.86 %	

Table 7.8: RMS of pseudorange-only (P3) position residuals with and without clock modeling with respect to the L1B GRACE science orbit for GRACE A on January 4, 2008

Figures 7.39 and 7.40 show the position residuals with respect to the GRACE Level 1B orbits and the receiver clock residuals from a straight line fit for epoch-wise clock estimation and 60-s piece-wise linear clock modeling, respectively. Obviously, both solutions are dominated by systematic errors, predominantly at timescales close to the orbital period. These periodic variations may either be caused by modeling deficiencies in the PPP solution or the reference trajectory. As a consequence, no pronounced differences between the two solutions are notable besides a reduction of the number and size of outliers, when clock modeling is applied. Nevertheless, we expect a reduction of the radial position noise which is hidden by the large systematic fluctuations. This is also supported by the formal errors of the computed spacecraft positions shown in Figure 7.41. Note, that the formal errors of the receiver clock estimates hardly improve, when clock modeling is applied. This unexpected behavior can be explained by the fact that the standard deviations describe the absolute time offset which is governed by the less precise pseudorange observations independent of the improved subdaily variations. Nevertheless, the reduction of the formal errors of the radial component when using the piece-wise linear clock model is evident. The behavior of the formal errors is much more even, indicating that the largest improvements are achieved during periods with unfavorable observation geometry. As expected the impact on the formal errors of the along-track component is small and negligible for the cross-track component of the kinematic orbit. However, a number of outliers can be avoided.

In order to demonstrate the improved precision also in the time series of the position residuals, a high-pass filter can be applied. By subtracting a moving average filter with a length of 5 epochs, the systematic effects are largely removed and the high-frequency position errors, primarily caused by the random measurement noise, can be studied. Alternatively, the (modified) Allan deviation of the position residuals can be used to analyze the noise level at different (averaging) timescales (Fig. 7.42(a)). Care has to be taken though when analyzing time series like the one in Figure 7.39 because the estimate of the Allan deviation may be significantly biased by large outliers, that are caused, e.g., by epochs with very poor observation geometry. Therefore, outliers have been removed from the time series prior to the

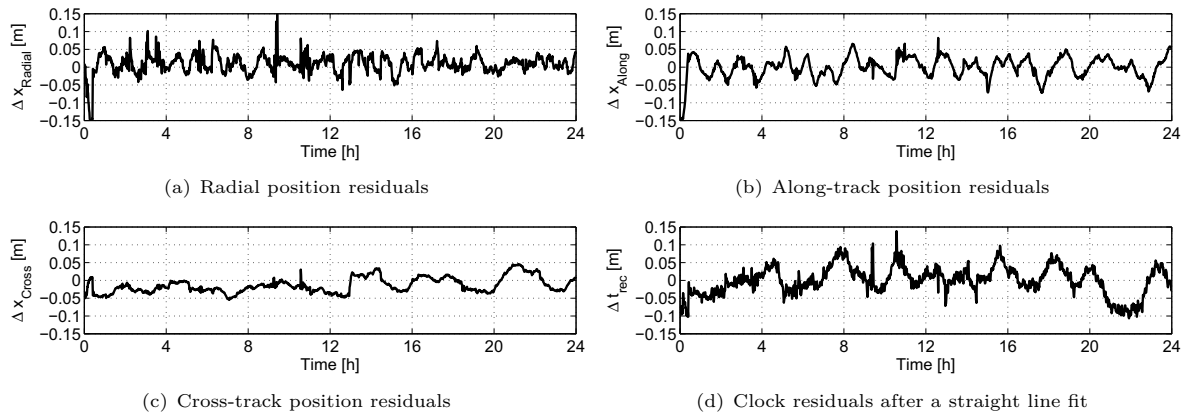


Figure 7.39: PPP position and clock residuals with respect to the GRACE Level 1B orbit when estimating epoch-wise independent receiver clock offsets (GRACE A on January 4, 2008)

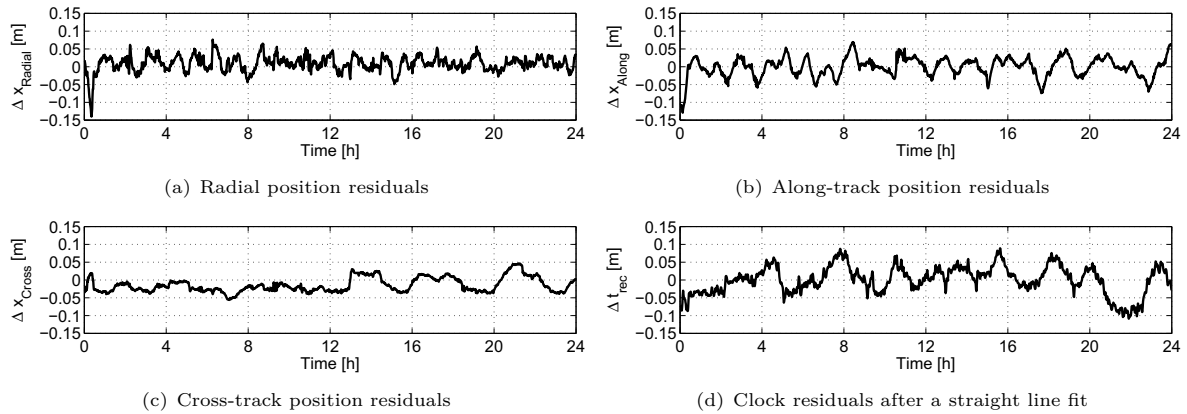


Figure 7.40: PPP position and clock residuals with respect to the GRACE Level 1B orbit when using a 60-s piece-wise linear receiver clock model (GRACE A on January 4, 2008)

calculation of the Allan deviation by applying an outlier rejection threshold of 3 cm to the high-pass filtered residual position time series. When inspecting the plot of the modified Allan deviation (Fig. 7.42(a)), a significant decrease of the noise level for short averaging times, i.e. close to the sampling frequency, can be observed when the piece-wise linear clock model is used. On the other hand, both approaches yield the same noise level at averaging times between approximately 700 s and 4000 s. This is where the systematic effects become dominant. Note, that the Allan deviation is not necessarily reduced through clock modeling. If the constraints on the clock evolution are overly optimistic, a degradation of the kinematic position will be the consequence. In Figure 7.42(b) the modified Allan deviation of the radial position residuals for clock modeling with linear segments of 300 s length has been plotted. Clearly, the imposed clock constraints are too strong and cause a degradation of the kinematic orbit. Thus, the modified Allan deviation of the position residuals proves to be a valuable tool to analyze the suitability of the applied clock constraints.

The Tables 7.9 and 7.10 list the modified Allan deviations of the kinematic position residuals at 60 s averaging time and different lengths of the piece-wise linear receiver clock interval for GRACE A and B, respectively. For comparison the results obtained with epoch-wise independent receiver clock estimation are shown in the first column. Although the differences between the modified Allan deviations for clock parameter intervals between 30 and 120 s are small, we can identify an optimum value at 60 s for both GRACE A and B. In a similar way the optimum value of the relative constraints between the slopes in consecutive linear intervals was found to be approximately 0.8 ns/h.

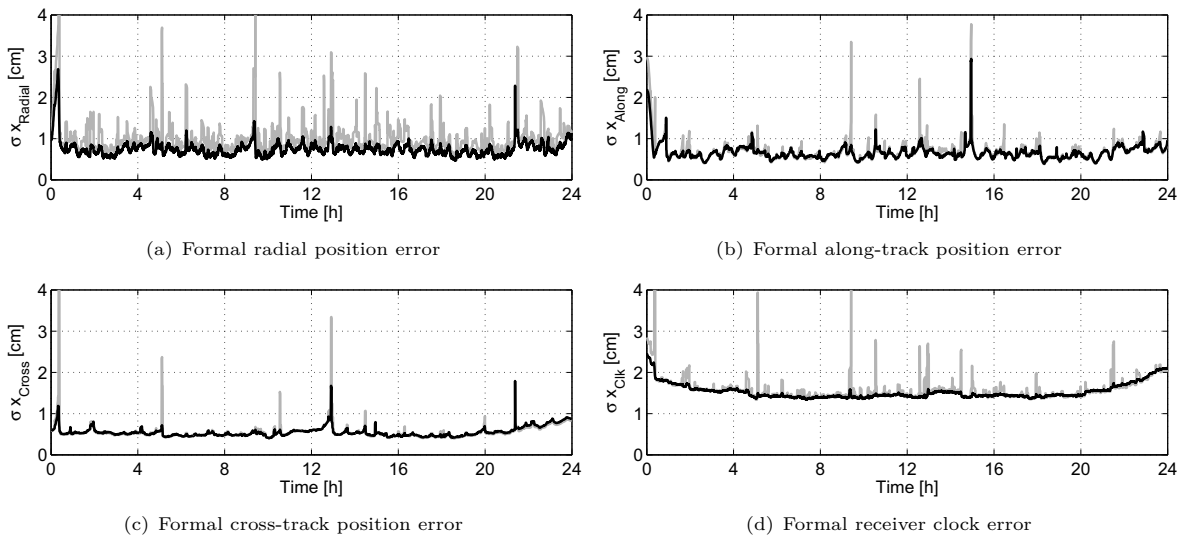


Figure 7.41: Formal PPP position errors using epoch-wise (grey) clock estimation or a 60-s piece-wise linear (black) receiver clock model (GRACE A on January 4, 2008)

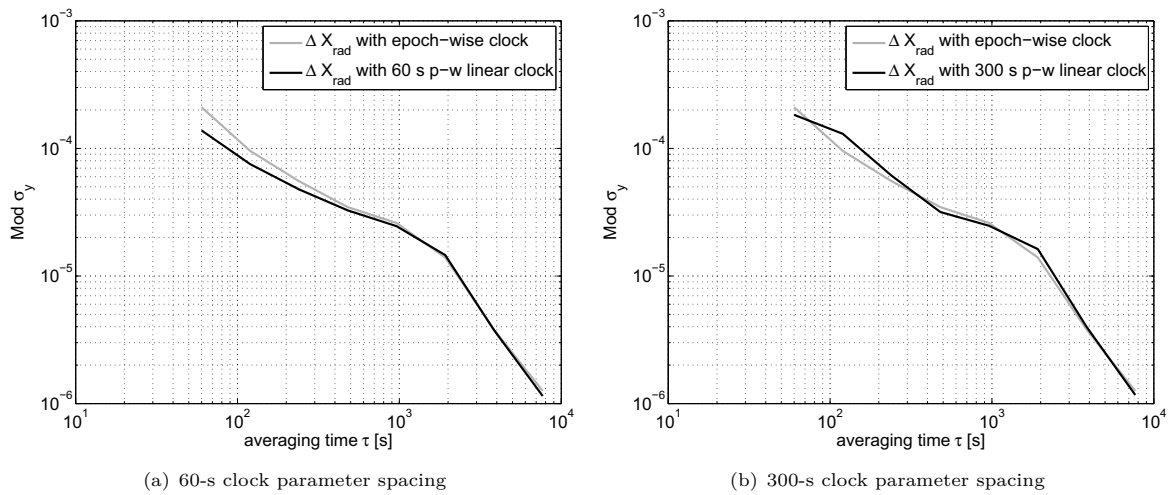


Figure 7.42: Modified Allan deviation of the kinematic PPP radial position residuals with respect to the GRACE Level 1B orbits based on epoch-wise (grey) and 60-s (300-s) piece-wise linear (black) receiver clock modeling (GRACE A on January 4, 2008)

PPP solution with fixed ambiguities As demonstrated in the PPP solution based on simulated data, periodic deviations as they are observed in the real data PPP position residuals can be caused by the large number of float ambiguities that are estimated in the PPP solution for a low Earth orbiter. Therefore, kinematic GRACE orbits with undifferenced ambiguity fixing have been computed for several days. The employed procedure for ambiguity fixing is described in Section 2.5.2.

In contrast to daily observation sessions of terrestrial receivers, where the fixing of the between satellite single difference ambiguities to integer values can usually be achieved by simple rounding, the usage of a bootstrapping procedure was found to be vital for the GRACE data. While the wide-lane ambiguities can still be fixed by rounding of the Melbourne-Wübbena linear combination, the narrow-lane ambiguities are fixed iteratively one at a time. That means, the normal equation system is recomputed and solved each time a narrow-lane ambiguity has been fixed, or more precisely heavily constrained, to an integer value. The resulting new ambiguity estimates and their cofactor matrix provide improved fractional parts and standard deviations of the remaining float ambiguities. Based on this new cofactor matrix

	Mod $\sigma_y(60\text{ s})$				
modeling interval	-	30 s	60 s	90 s	120 s
Radial	2.1×10^{-4}	1.4×10^{-4}	1.4×10^{-4}	1.5×10^{-4}	1.7×10^{-4}
Along-track	7.4×10^{-5}	7.6×10^{-5}	7.7×10^{-5}	7.7×10^{-5}	7.8×10^{-5}
Cross-track	6.0×10^{-5}	5.4×10^{-5}	5.3×10^{-5}	5.5×10^{-5}	5.5×10^{-5}

Table 7.9: Modified Allan deviation of the kinematic position residuals of GRACE A with respect to the reduced-dynamic GRACE L1B orbit for different clock modeling intervals

	Mod $\sigma_y(60\text{ s})$				
modeling interval	-	30 s	60 s	90 s	120 s
Radial	1.5×10^{-4}	0.9×10^{-4}	0.9×10^{-4}	1.0×10^{-4}	1.1×10^{-4}
Along-track	6.3×10^{-5}	5.4×10^{-5}	5.3×10^{-5}	5.4×10^{-5}	5.6×10^{-5}
Cross-track	5.0×10^{-5}	3.8×10^{-5}	3.8×10^{-5}	3.8×10^{-5}	3.9×10^{-5}

Table 7.10: Modified Allan deviation of the kinematic position residuals of GRACE B with respect to the reduced-dynamic GRACE L1B orbit for different clock modeling intervals

the ambiguity with the lowest standard deviation and a fractional part below 0.2 narrow-lane cycles with respect to the reference ambiguity is rounded to the nearest integer and constrained in the normal equation system. In this way the success rate of the ambiguity fixing can be significantly increased. Although all non-ambiguity parameters are pre-eliminated from the normal equation system before the iterative ambiguity fixing is started, the procedure is rather time-consuming because for a daily LEO observation file generally more than 400 ambiguities have to be fixed. That means at least 400 inversions of the 400×400 ambiguity cofactor matrix have to be performed. However, with the described integer bootstrapping typically more than 95 % of the single difference ambiguities could be fixed to their integer values.

Figures 7.43 and 7.44 show the position residuals of the kinematic orbit determination with fixed ambiguities with respect to the GRACE Level 1B orbit. A comparison with the PPP solutions based on float ambiguities (Fig. 7.39-7.40) reveals only minor differences. The large periodic deviations are hardly reduced. This is also reflected in the modified Allan deviation of the radial position residuals plot shown in Figure 7.45.

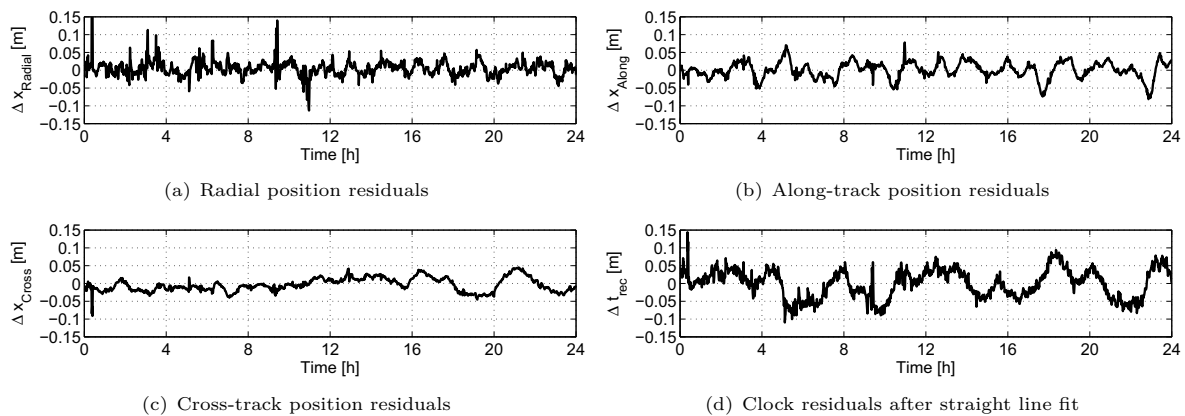


Figure 7.43: Ambiguity-fixed PPP position and clock residuals with respect to the GRACE Level 1B orbits when estimating epoch-wise independent receiver clock offsets (GRACE A on January 4, 2008)

Due to the fact that one of the single difference ambiguities was fixed to an arbitrary integer value, the receiver clock offsets are not determined by the less precise pseudorange observations. Consequently,

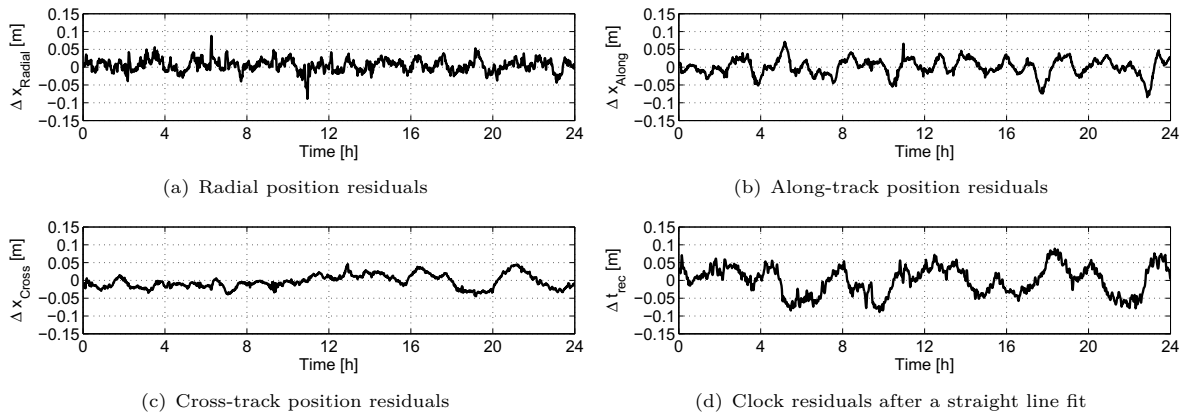


Figure 7.44: Ambiguity-fixed PPP position and clock residuals with respect to the GRACE Level 1B orbits using a 60-s piece-wise linear receiver clock model (GRACE A on January 4, 2008)

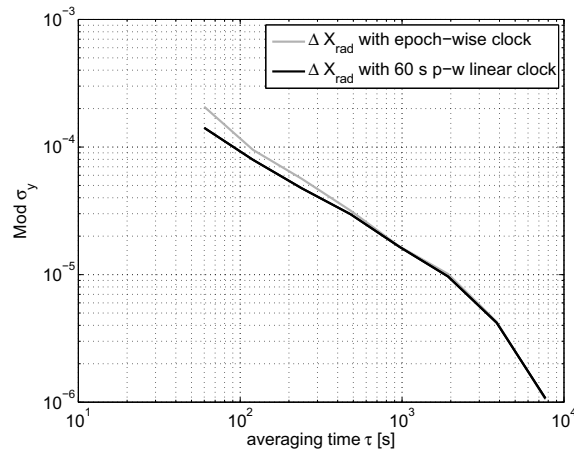


Figure 7.45: Modified Allan deviation of the ambiguity-fixed kinematic PPP radial position residuals with respect to the GRACE Level 1B orbits based on a) epoch-wise and b) 60-s piece-wise linear receiver clock modeling (GRACE A on January 4, 2008)

the formal errors of the clock parameters shown in Figure 7.46 reflect the inherent precision of the carrier phase observations and the reduction due to clock modeling becomes evident. Furthermore, no degradation of the formal errors of the position and clock estimates near the boundaries of the daily computing batch can be observed, because the fixed ambiguities do not contribute to the uncertainty of these parameters anymore.

A unique feature of the formation flying GRACE satellites is the highly precise inter-satellite K-band ranging system, which allows to measure the distance between the two spacecraft with μm precision. Figure 7.47 shows the difference of the inter-satellite distances computed from the kinematic orbits and the K-band observations.

The float solution is again dominated by systematic fluctuations, whereas the range residuals of the ambiguity-fixed kinematic orbits are closer to white noise. Therefore, the ambiguity-fixed solution is well suited to analyze the noise levels of the inter-satellite range derive from the kinematic solutions with and without clock modeling, respectively. However, apart from a reduction of the number of outliers the improvement through clock modeling appears to be rather small. The reduction of the RMS is in the range of 5-10% depending on the outlier rejection threshold. This result is not surprising, because the inter-satellite distance is hardly sensitive to radial orbit errors, which should show the largest improvement, when clock modeling is applied. In principle, the radial orbit errors could be checked

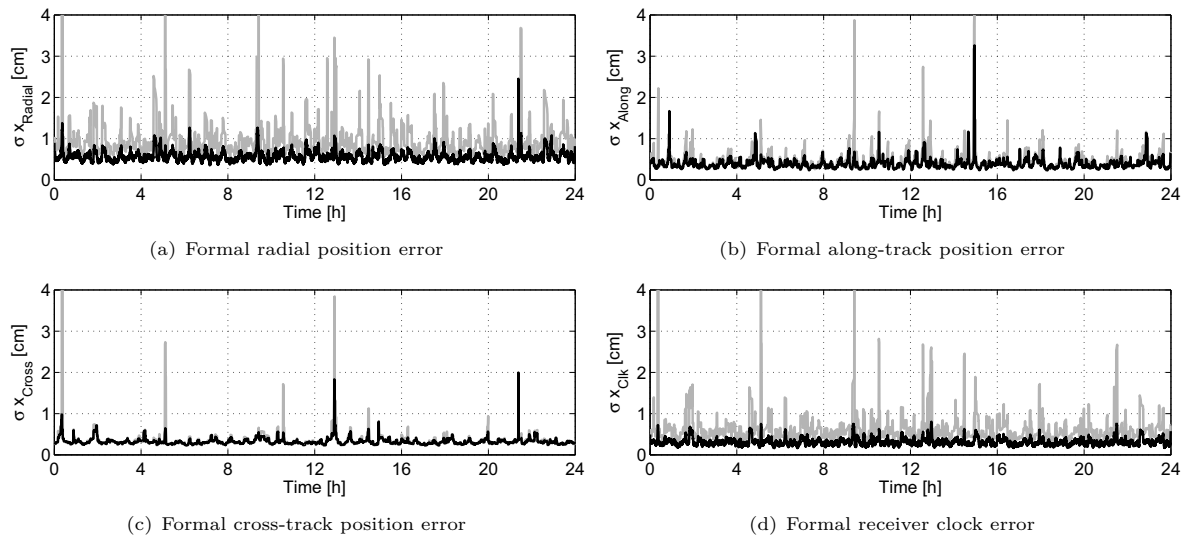


Figure 7.46: Formal position errors using epoch-wise (grey) clock estimation or a 60-s piece-wise linear (black) receiver clock model for an ambiguity-fixed PPP solution (GRACE A on January 4, 2008)

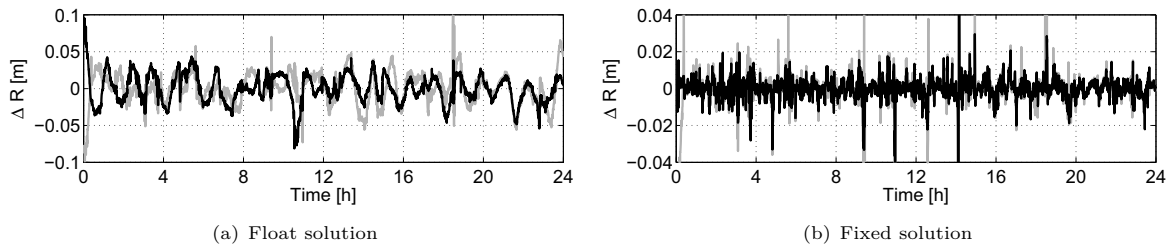


Figure 7.47: GRACE K-band range residuals with (black) and without (grey) clock modeling (January 4, 2008). Note the different scales.

with satellite laser ranging (SLR) observations but these do not provide the required accuracy up to now. Although the sensitivity of the K-band link to radial orbit errors is limited, the comparison of the inter-satellite distance with the K-band observations can be regarded as an independent validation of the employed ambiguity fixing procedure.

8 Conclusions

The three main objectives of this work, defined in the introduction, were (1) the determination of the technical requirements for GPS receiver clock modeling at the carrier phase precision level, (2) the derivation and validation of a suitable functional and stochastic clock model in the parameter estimation, and (3) the analysis of the benefits of clock modeling in different application scenarios. The most important findings are summarized in the following.

With regard to the *technical feasibility* it was shown that several types of oscillators exist that meet the level of frequency stability required for precise GPS clock modeling. By far the most important of these frequency standards are active hydrogen masers, not only because they provide an outstanding frequency stability, but also because of their common usage for the time tagging of the observations in VLBI and the generation of national UTC realizations. In turn, GNSS receivers are commonly used to synchronize the maser clocks at the VLBI sites and to compare local timescales to the international atomic time TAI. Due to this synergy a fairly dense network of GNSS receivers with H-maser exists at least in the Northern hemisphere. With the current expansion and modernization of the global VLBI network in the framework of the VLBI2010 initiative, this network is likely to improve in the future. Furthermore, it was demonstrated that clock modeling at the level of precision of the GPS carrier phase observations is generally possible using standard geodetic receiver equipment with external frequency input. However, proper temperature control of the receiver environment is mandatory. In addition, antenna cables exist, that mitigate the influence of outside temperature variations to a level at which they do not pose a problem for clock modeling. The temperature sensitivity of the antenna itself appears to be rather small, for typical high-quality geodetic antennas and does generally not limit the applicability of the proposed clock modeling approach.

Various *parametrizations of the receiver clock error* may be chosen that allow a continuous representation of the oscillator time offset. Due to its simplicity and flexibility a piece-wise linear clock model was selected and successfully applied for the batch least-squares adjustment used in this work. In addition, a simple 2-state model, consisting of the oscillator's phase and frequency offsets, was found to be adequate for precise GNSS receiver clock modeling in a Kalman filter based parameter estimation. Both approaches can be easily adapted to the specific frequency stability of different oscillator types. In the batch adjustment this can be achieved by varying the length of the linear modeling intervals and the relative constraints between the drifts in consecutive segments. In the Kalman filter approach the entries of the process noise matrix of clock states needs to be adapted. Although good approximate values for these processing parameters can be found with the help of the Allan deviation $\sigma_y(\tau)$ or the noise spectral density coefficients h_i of the oscillator at hand, some additional parameter tuning is generally required.

The *impact of clock modeling* was first investigated on a theoretical basis by analyzing the contribution of the clock parameters to the normal equations of the coordinate parameters for a simple pseudorange solution covering two epochs. It was shown, that in static positioning mode the impact of clock modeling depends on the variation of the average direction of all GNSS observations at the receiver site. Since this direction, provided that no significant obstructions exist, is always close to the local nadir direction, the impact of clock modeling on static coordinate estimates is very small. In contrast, the height component of kinematic coordinate estimates can be significantly improved when the receiver clock is modeled over multiple epochs instead of estimated for every epoch independently. In the next step, the elements of the cofactor matrix for an exemplary 24-hour GPS satellite geometry were analyzed for different geographic locations. This analysis confirmed the fact that static coordinates are almost not affected by the chosen clock model, while the precision of the kinematic height coordinates can be improved by a factor of 2.5 for equatorial and mid-latitude sites and up to a factor of 5 in the polar regions. Furthermore, it was found that the estimation of *zwd* parameters with high temporal resolution can

be stabilized through clock modeling. In addition, it was shown that if the receiver clock was perfectly synchronized with the system timescale, also in the static case, the accuracy of the vertical direction would improve. In fact, it would generally be better than the accuracy of the horizontal positions. Unfortunately, such an absolute synchronization is impossible to achieve with current GNSS architecture. Finally, the proposed clock models were validated with simulated and real observation data using a PPP software with clock modeling capability, that was developed in the framework of this thesis. Despite the systematic observation errors that exist in the real data, the RMS reduction of the kinematic PPP height estimates when clock modeling is applied, was found to be typically around 50% for real data compared to more than 70% reduction obtained with simulated data. This is due to the fact that some but not all of the spurious fluctuations of the kinematic height estimates with sub-hourly periods can be suppressed when receiver clock modeling is applied. In addition to ground-based GPS receivers, clock modeling was also successfully demonstrated for the two low Earth orbiting GRACE satellites. A unique feature of these satellites is the combination of a dual-frequency GPS receiver with an Ultra-Stable Oscillator (USO), that provides the required frequency stability for the proposed clock modeling approach. In analogy to the terrestrial case, the precision of the high-frequency kinematic radial spacecraft positions seems to be improved by almost 50% through clock modeling, when compared to a smooth reduced-dynamic orbit.

In general, clock modeling, as it has been investigated in the context of this work, proves beneficial only when parameters which are mathematically correlated with the clock parameters are to be estimated with very high temporal resolution such as kinematic height coordinates and high-frequency tropospheric zenith wet delays. This is because the constraints imposed by a clock model are only relative, i.e. between consecutive parameters, and not absolute. In other words, only the temporal evolution of the clock synchronization error is constrained and therefore only the temporal evolution of other parameters can be improved.

Although the demonstrated benefits of clock modeling for kinematic positioning are substantial, the applications that can be envisioned are currently limited, because of the lack of portable and affordable oscillators at the level of precision required for the proposed approach. High-precision frequency standards such as active hydrogen masers are expensive and stationary devices, weighting almost 100 kilogram, consuming more than 100 W of power and costing around 200 000 EUR. Even the considerably smaller passive hydrogen masers are too bulky and expensive for most kinematic applications, not to mention presumably serious environmental influences when the maser is moved around. Although significant progress has been achieved in the field of miniaturized and chip-scale atomic clocks, the frequency stabilities of these devices are currently still well over one order of magnitude above the requirements for clock modeling in carrier phase based positioning. However, the great success of the first commercially available CSAC introduced by Symmetricom Inc. in 2011 as well as the efforts to develop other miniaturized atomic clocks e.g. based on single $^{199}\text{Hg}^+$ and $^{171}\text{Yb}^+$ ions are promising and may eventually lead to miniaturized oscillators suitable for clock modeling in GNSS applications based on carrier phase observations.

The primary goals of this work were to assess the general technical feasibility of GNSS receiver clock modeling at the carrier phase precision level and to gain an understanding of the mechanisms through which constraints imposed on the receiver clock affect other parameters in the GNSS solution. The next step towards practical applications would require a more detailed investigation of the receiver and clock performance in a real navigation environment which is typically characterized by vibration and shock as well as temperature and magnetic field variations. More work is also required to extend the proposed receiver clock modeling from the GPS-only case investigated in this work to multi GNSS solutions. Due to the fact, that every GNSS has its own system timescale, additional system-specific clock offsets have to be considered in this case. Furthermore, the frequency-dependent hardware delays of the GLONASS observations require careful attention.

With the upcoming Galileo system, an entire constellation of GNSS satellites carrying highly precise oscillators will be available in the future. Apart from the obvious advantages of reduced clock prediction and interpolation errors this will be an interesting opportunity to study the impact of transmitter clock modeling on precise orbit determination. Furthermore, the Galileo satellites will broadcast, a highly precise broadband code signal on the E5 frequency. This signal will offer significantly improved pseudorange positioning and time transfer capabilities.

In the quest for ever increasing precision, accuracy and reliability of GNSS-based positioning, clock modeling is expected to gain in importance in the future. However, many applications will vitally depend on the availability of small and inexpensive high-precision oscillators with very low power consumption. In view of the recent progress in the field of clock technology, this limitation is likely to be overcome at least partly in the future. Thus, receiver clock modeling could become a viable extension of present GNSS processing strategies. At the moment, the additional effort required to install and operate sophisticated high-precision receiver oscillators is probably only acceptable for dedicated scientific investigations, such as high-frequency vertical deformation monitoring or kinematic aircraft and LEO positioning. However, the improved robustness and the possibility to compute a position with only 3 satellites in view, is also attractive for navigation in urban areas with severe obstructions.

Bibliography

- Allan, D. W. (1966). Statistics of atomic frequency standards. *Proceedings of the IEEE*, 54(2):221 – 230.
- Allan, D. W. (1987). Time and frequency (time-domain) characterization, estimation, and prediction of precision clocks and oscillators. *IEEE Transactions on Ultrasonics Ferroelectrics and Frequency Control*, 34:647–654.
- Allan, D. and Weiss, M. (1980). Accurate time and frequency transfer during common-view of a GPS satellite. *Proceedings of the 34th Annual Symposium on Frequency Control (SFC)*, pp. 334–336.
- Banville, S. and Tang, H. (2010). Antenna rotation and its effects on kinematic precise point positioning. In *23rd International Technical Meeting of the Satellite Division of the Institute of Navigation, Portland, OR, September 21-24, 2010*, pp. 2545–2552.
- Barnes, J., Chi, A. R., Cutler, L. S., Healey, D. J., Leeson, D. B., McGunigal, T. E., Mullen, J. A., Smith, W. L., Sydnor, R. L., Vessot, R. F., and Winkler, G. M. (1971). Characterization of frequency stability. *IEEE transactions on instrumentation and measurement*, 20:105–120.
- Bauch, A. (2007). Atomic frequency standards, properties and applications. In Hänsch, T., Leschiutta, S., and J., W. A., editors, *Proceedings of the international school of physics - Enrico Fermi*, pp. 287–315. Societa italiana di Fisica, Bologna.
- Bednarz, S. and Misra, P. (2006). Receiver clock-based integrity monitoring for GPS precision approaches. *IEEE Transactions on Aerospace and Electronic Systems*, 42(2):636 – 643.
- Bertiger, W., Dunn, C., Harris, I., Kruizinga, G., Romans, L., Watkins, M., and Wu, S. (2003). Relative time and frequency alignment between two Low Earth Orbiters, GRACE. *Proceedings of the IEEE International Frequency Control Symposium and PDA Exhibition Jointly with the 17th European Frequency and Time Forum*, pp. 273 – 279.
- Bevis, M., Businger, S., Herring, T. A., Rocken, C., Anthes, R. A., and Ware, R. H. (1992). GPS meteorology: Remote sensing of atmospheric water vapor using the Global Positioning System. *Journal of Geophysical Research*, 97:15,787–15,801.
- Bierman, G. J. (1977). *Factorization methods for discrete sequential estimation*. Academic Press, New York.
- Bock, H., Dach, R., Jäggi, A., and Beutler, G. (2009). High-rate GPS clock corrections from CODE: Support of 1 Hz applications. *Journal of Geodesy*, 83:1083–1094.
- Boehm, J., Niell, A., Tregoning, P., and Schuh, H. (2006a). Global Mapping Function (GMF): A new empirical mapping function based on numerical weather model data. *Geophysical Research Letters*, 33:L07304.
- Boehm, J., Werl, B., and Schuh, H. (2006b). Troposphere mapping functions for GPS and very long baseline interferometry from European Centre for Medium-Range Weather Forecasts operational analysis data. *Journal of Geophysical Research*, 111:B02406.
- Boehm, J., Heinkelmann, R., and Schuh, H. (2007). Short note: A global model of pressure and temperature for geodetic applications. *Journal of Geodesy*, 81:679–683.
- Bosser, P., Bock, O., Thom, C., Pelon, J., and Willis, P. (2010). A case study of using Raman LIDAR measurements in high-accuracy GPS applications. *Journal of Geodesy*, 84:251–165.
- Brown, R. G. and Hwang, P. Y. C. (2005). *Introduction to Random Signals and Applied Kalman Filtering*. John Wiley & sons, New York, 3rd edition.
- Brunner, F. K. and Gu, M. (1991). An improved model for the dual frequency ionospheric correction of GPS observations. *Manuscripta Geodaetica*, 16(3):205–214.
- Bruyninx, C., Defraigne, P., and Sleewaegen, J. (1999). Time and frequency transfer using GPS code and carrier phases: Onsite experiments. *GPS Solutions*, 3(2):1–10.
- Bruyninx, C., Defraigne, P., Dehant, V., and Paquet, P. (2000). Frequency transfer using GPS carrier phases: Influence of temperature variations near the receiver. *IEEE Transactions on Ultrasonics, Ferroelectrics and Frequency Control*, 47(2):522–525.
- Collins, P., Lahaye, F., Héroux, P., and Bisnath, S. (2008). Precise point positioning with ambiguity resolution using the decoupled clock model. In *Proceedings of ION GNSS 21st international technical meeting of the*

- satellite division, Savannah, US*, pp. 1315–1322.
- Dach, R., Beutler, G., Hugentobler, U., Schaer, S., Schildknecht, T., Springer, T., Dudle, G., and Prost, L. (2003). Time transfer using GPS carrier phase: error propagation and results. *Journal of Geodesy*, 77:1–14.
- Dach, R., Hugentobler, U., Fridez, P., and Meindl, M. (2007). *Bernese GPS Software Version 5.0*. Astronomical Institute, University of Bern.
- Dach, R., Schildknecht, T., Springe, T., Dudle, G., and Prost, L. (2002). Continuous time transfer using GPS carrier phase. *IEEE Transactions on Ultrasonics, Ferroelectrics and Frequency Control*, 49:1480–1490.
- de Boor, C. (1978). *A practical guide to splines*, volume 27 of *Applied mathematical science*. Springer-Verlag, New York.
- Defraigne, P. (2011). GNSS time and frequency transfer: state of the art and possible evolution. BIPM workshop on the development of advanced time and frequency transfer techniques 28–29 June, 2011.
- Defraigne, P., Bruyninx, C., and Guyennon, N. (2007). PPP and phase-only GPS time and frequency transfer. *Proceedings of the IEEE International Frequency Control Symposium 2007 jointly with the 21st European Frequency and Time Forum*, pp. 904–908.
- Delporte, J., Mercier, F., and Laurichesse, D. (2008). Time transfer using GPS carrier phase with zero-difference integer ambiguity blocking. *Proceedings of the 22nd European Frequency and Time Forum (EFTF)*.
- Dilßner, F. (2007). *Zum Einfluss des Antennenumfeldes auf die hochpräzise GNSS-Positionsbestimmung*. Dissertation, Wissenschaftliche Arbeiten der Fachrichtung Geodäsie und Geoinformatik der Leibniz Universität Hannover, Nr. 271.
- Dilßner, F. (2010). GPS IIF-1 satellite antenna phase center and attitude modeling. *Inside GNSS*, 5(6):59–64.
- Dow, J. M., Neilan, R. E., and Rizos, C. (2009). The International GNSS Service in a changing landscape of Global Navigation Satellite Systems. *Journal of Geodesy*, 83:191–198.
- Dunn, C., Bertiger, W., Bar-Sever, Y. E., Desai, S., Haines, B., Kuang, D., Franklin, G., Harris, I., Kruizinga, G., Meehan, T., Nandi, S., Nguyen, D., Rogstad, T., Thomas, J., Tien, J., Romans, L., Watkins, M., Wu, S., Bettadpur, S., and Kim, J. (2003). Instrument of GRACE. *GPS World*, 14(2):17–28.
- El-Sheimy, N., Hou, H., and Niu, X. (2008). Analysis and modeling of inertial sensors using Allan variance. *IEEE Transactions on Instrumentation and Measurement*, 57(1):140–149.
- Elgered, G., Davis, J. L., Herring, T. A., and Shapiro, I. I. (1991). Geodesy by radio interferometry: Water vapor radiometry for estimation of the wet delay. *Journal of Geophysical Research*, 96(B4):6541–6555.
- Feldmann, T. (2011). *Advances in GPS based Time and Frequency Comparisons for Metrological Use*. Dissertation, Leibniz Universität Hannover.
- Fonville, B., Powers, E., Kropp, A., and Vannicola, F. (2007). Evaluation of carrier-phase GNSS timing receivers for UTC/TAI applications. *39th Annual Precise Time and Time Interval (PTTI) Meeting, Long Beach, CA*, pp. 331–338.
- Fritsche, M., Dietrich, R., Knoefel, C., Ruelke, A., Vey, S., Rothacher, M., and Steigenberger, P. (2005). Impact of higher-order ionospheric terms on GPS estimates. *Geophysical Research Letters*, 32:1–5.
- Ge, M., Gendt, G., Rothacher, M., Shi, C., and Liu, J. (2008). Resolution of GPS carrier-phase ambiguities in Precise Point Positioning (PPP) with daily observations. *Journal of Geodesy*, 82(7):389–399. 10.1007/s00190-007-0208-3.
- Geiger, A. (1988). Simulating disturbances in GPS by continuous satellite distribution. *Journal of Surveying Engineering*, 114(4):182–194.
- Gelb, A. (1974). *Applied optimal estimation*. MIT Press, Cambridge.
- Gerginov, V., Nemitz, N., Weyers, S., Schröder, R., Griebisch, D., and Wynands, R. (2010). Uncertainty evaluation of the caesium fountain clock PTB-CSF2. *Metrologia*, 47(1):65–79.
- Gerlach, C., Földvary, L., Svehla, D., Gruber, T., Wermuth, M., Sneeuw, N., Frommknecht, B., Oberndorfer, H., Peters, T., Rothacher, M., Rummel, R., and Steigenberger, P. (2003). A CHAMP-only gravity field model from kinematic orbits using the energy integral. *Geophysical Research Letters*, 30(20):2037.
- Gill, P. (2005). Optical frequency standards. *Metrologia*, 42(3):125–137.
- Gill, P., Barwood, G. P., Klein, H. A., Margolis, H. S., Webster, S. A., Riehle, F., Peik, E., Schnatz, H., Sterr, U., Schäfer, W., Hejc, G., Pawlitzki, A., Portolés, D., Hammesfahr, J., Furthner, J., Moudrak, A., and Süß, M. (2007). Feasibility and applications of optical clocks as frequency and time references in ESA deep space stations. online. URL <http://esamultimedia.esa.int/docs/gsp/completed/C19837ExS.pdf>. ESA study 19837/06/F/V5.

- Grewal, M. S. and Andrews, A. P. (2001). *Kalman Filtering : Theory and Practice Using MATLAB*. John Wiley & sons, New York, 2nd edition.
- Grosche, G., Terra, O., Predehl, K., Holzwarth, R., Lipphardt, B., Vogt, F., Sterr, U., and Schnatz, H. (2009). Optical frequency transfer via 146 km fiber link with 10^{-19} relative accuracy. *Optics Letters*, 34(15):2270–2272.
- Gurtner, W. and Estey, L. (2007). RINEX: The Receiver INdependent Exchange format - Version 2.11. online. URL <http://igsb.jpl.nasa.gov/igsb/data/format/rinex211.txt>.
- Guyennon, N., Cerretto, G., Tavella, P., and Lahaye, F. (2009). Further characterization of the time transfer capabilities of Precise Point Positioning (PPP): The sliding batch procedure. *IEEE Transactions on Ultrasonics, Ferroelectrics and Frequency Control*, 56(8):1634–1641.
- Hauschild, A., Montenbruck, O., and Steigenberger, P. (2012). Short-term analysis of GNSS clocks. *GPS Solutions*, online first:1–13.
- Heck, B. (1975). Die Genauigkeit eliminiertes Unbekanntes. *Allgemeine Vermessungsnachrichten*, 10:345–348.
- Herring, T. A., Davis, J. L., and Shapiro, I. I. (1990). Geodesy by radio interferometry: The application of Kalman filtering to the analysis of very long baseline interferometry data. *Journal of Geophysical Research*, 95(B8):12561–12581.
- Hofmann-Wellenhof, B., Lichtenegger, H., and Wasle, E. (2008). *GNSS, Global Navigation Satellite Systems, GPS, GLONASS, Galileo and more*. Springer Wien / New York.
- Hoque, M. M. and Jakowski, N. (2007). Higher order ionospheric effects in precise GNSS positioning. *Journal of Geodesy*, 81(4):259–268.
- Hugentobler, U., Plattner, M., Bedrich, S., Heinze, M., Klein, V., and Voithenleitner, D. (2009). Optical clocks in future global navigation satellites. In *Proceedings of the 2nd International Colloquium on Scientific and Fundamental Aspects of the Galileo Programme*.
- Hutsell, S. T. (1995). Relating the Hadamard variance to MCS Kalman filter clock estimation. *Proceedings of the 27th Annual PTTI Systems and Applications Meeting, San Diego*, pp. 291–301.
- IGS (2012). IGS product table. website. URL <http://igsb.jpl.nasa.gov/components/prods.html>. last access 03-06-2012.
- IS-GPS-200D (2004). Interface Specifications - Navstar GPS space segment/navigation user interfaces. URL www.navcen.uscg.gov/pdf/IS-GPS-200D.pdf.
- Iwabuchi, T., Shoji, Y., Shimada, S., and Nakamura, H. (2004). Tsukuba GPS dense net campaign observations: Comparison of the stacking maps of post-fit phase residuals estimated from three software packages. *Journal of the Meteorological Society of Japan*, 82(1B):315–330.
- Jäggi, A., Beutler, G., Prange, L., Dach, R., and Mervart, L. (2008). Assessment of GPS-only observables for gravity field recovery from GRACE. In Sideris, M. G., editor, *Observing our Changing Earth*, volume 133 of *International Association of Geodesy Symposia*, pp. 113–123. Springer Berlin / Heidelberg.
- Jäggi, A., Dach, R., Montenbruck, O., Hugentobler, U., Bock, H., and Beutler, G. (2009). Phase center modeling for LEO GPS receiver antennas and its impact on precise orbit determination. *Journal of Geodesy*, 83:1145–1162.
- Jäggi, A., Bock, H., Prange, L., Meyer, U., and Beutler, G. (2011). GPS-only gravity field recovery with GOCE, CHAMP, and GRACE. *Advances in Space Research*, 47(6):1020 – 1028.
- Kasdin, N. J. (1995). Discrete simulation of colored noise and stochastic processes and $1/f^\alpha$ power law noise generation. *Proceedings of the IEEE*, 83(5):802–827.
- Kasdin, N. and Walter, T. (1992). Discrete simulation of power law noise (for oscillator stability evaluation). In *Frequency Control Symposium, 1992. 46th., Proceedings of the IEEE*, pp. 274 –283.
- Koch, K. R. (1999). *Parameter Estimation and Hypothesis Testing in Linear Models*. Springer Berlin / Heidelberg / New York.
- Kouba, J. (2009a). A guide to using International GNSS Service (IGS) products. online. URL <http://igsb.jpl.nasa.gov/igsb/resource/pubs/UsingIGSProductsVer21.pdf>.
- Kouba, J. (2009b). A simplified yaw-attitude model for eclipsing GPS satellites. *GPS Solutions*, 13:1–12.
- Kouba, J. and Héroux, P. (2001). Precise Point Positioning Using IGS Orbit and Clock Products. *GPS Solutions*, 5:12–28. 10.1007/PL00012883.
- Kroes, R. (2006). Precise relative positioning of formation flying spacecraft using GPS. Publications on Geodesy 61, Netherlands Geodetic Commission (NCG).

- Kuang, D., Schutz, B. E., and Watkins, M. M. (1996). On the structure of geometric positioning information in GPS measurements. *Journal of Geodesy*, 71:35–43.
- Larson, K. M., Levine, J., Nelson, L. M., and Parker, T. E. (2000). Assessment of GPS carrier-phase stability for time-transfer applications. *IEEE transactions on Ultrasonics, Ferroelectrics, and Frequency Control*, 47(2):484–494.
- Larson, K. M., Ashby, N., Hackman, C., and W.Bertiger (2007). An assessment of relativistic effects for low Earth orbiters: the GRACE satellites. *Metrologia*, 44(6):484.
- Laurichesse, D., Mercier, F., Berthias, J. P., Broca, P., and L., C. (2009). Integer ambiguity resolution on undifferenced GPS phase measurements and its application to PPP and satellite precise orbit determination. *Navigation, Journal of the Institute of Navigation*, 56(2):135–149.
- Lichten, S. M. and Border, J. S. (1987). Strategies for high-precision Global Positioning System orbit determination. *Journal of Geophysical Research: Solid Earth*, 92(B12):12751–12762.
- Lindlohr, W. and Wells, D. (1985). GPS design using undifferenced carrier beat phase observations. *Manuscripta Geodaetica*, 10:255–295.
- Lindsey, W. C. and Chie, C. M. (1976). Theory of oscillator instability based upon structure functions. *Proceedings of the IEEE*, 64(12):1652–1666.
- Loyer, S., Perosanz, F., Mercier, F., Capdeville, H., and Marty, J.-C. (2012). Zero-difference GPS ambiguity resolution at CNES-CLS IGS analysis center. *Journal of Geodesy*, 86:991–1003.
- Lyard, F., Lefevre, F., Letellier, T., and Francis, O. (2006). Modelling the global ocean tides: modern insights from FES2004. *Ocean Dynamics*, 56:394–415.
- Macias-Valadez, D., Santerre, R., Laroche, S., and Landry, R. (2012). Improving vertical GPS precision with a GPS-over-fiber architecture and real-time relative delay calibration. *GPS Solutions*, 16(4):449–462.
- Matsakis, D., Lee, M., Dach, R., Hugentobler, U., and Jiang, Z. (2006). GPS carrier phase analysis noise on the USNO-PTB baselines. *Proceedings of the IEEE International Frequency Control Symposium and Exposition 2006*, pp. 631–636.
- McCarthy, D. D. and Seidelmann, P. K. (2009). *Time from Earth rotation to atomic physics*. Wiley-VCH.
- Meindl, M., Schaer, S., Hugentobler, U., and Beutler, G. (2004). Tropospheric gradient estimation at CODE: Results from global solutions. *Journal of the Meteorological Society of Japan*, 82(1B):331–338.
- Melbourne, W. G. (1985). The case for ranging in GPS based geodetic systems. In Goad, C., editor, *Proceedings of the first international symposium on precise positioning with the Global Positioning System*, pp. 373–386, US Department of commerce, Rockville, Maryland.
- Mercier, F. and Laurichesse, D. (2007). Receiver/payload hardware biases stability requirements for undifferenced wide-lane ambiguity blocking. In *proceedings of the 1st Colloquium on Scientific and Fundamental Aspects of the Galileo Programme*.
- Misra, P. (1996). The role of the clock in a GPS receiver. *GPS world*, 7(4):60–66.
- Montenbruck, O. and Gill, E. (2000). *Satellite orbits: Models, methods, and applications*. Springer Berlin / Heidelberg / New York.
- Montenbruck, O. and Kroes, R. (2003). In-flight performance analysis of the CHAMP BlackJack GPS receiver. *GPS Solutions*, 7(2):74–86.
- Montenbruck, O., Garcia-Fernandez, M., Yoon, Y., Schön, S., and Jäggi, A. (2009). Antenna phase center calibration for precise positioning of LEO satellites. *GPS Solutions*, 13(1):23–34.
- Montenbruck, O., Steigenberger, P., Schönemann, E., Hauschild, A., Hugentobler, U., Dach, R., and Becker, M. (2011). Flight characterization of new generation GNSS satellite clocks. *Proceedings of the 24th International Technical Meeting of the Satellite Division of the Institute of Navigation (ION GNSS 2011)*, pp. 2959–2969.
- Niemeier (2002). *Ausgleichsrechnung*. de Gruyter, Berlin / New York.
- Ning, T., Elgered, G., and Johansson, J. M. (2011). The impact of microwave absorber and radome geometries on GNSS measurements of station coordinates and atmospheric water vapour. *Advances in Space Research*, 47(2):186–196.
- Orliac, E., Dach, R., Voithenleitner, D., Hugentobler, U., Wang, K., Rothacher, M., and Svehla, D. (2011). Clock modeling for GNSS applications. Poster presented at AGU Fall Meeting 2011, San Francisco, USA.
- Overney, F., Schildknecht, T., Beutler, G., Prost, L., and Feller, U. (1997). GPS time transfer using geodetic receivers: Middle term stability and temperature dependence of the signal delays. *Proceedings of the 11th European Frequency and Time Forum (EFTF)*, pp. 504–508.

- Petit, G. and Luzum, B., editors (2010). *IERS Conventions (2010)*. IERS Technical Note 36. Verlag des Bundesamts für Kartographie und Geodäsie, Frankfurt am Main.
- Petit, G., Thomas, C., Jiang, Z., Uhrich, P., and Taris, F. (1998). Use of GPS Ashtech Z12T receivers for accurate time and frequency comparisons. *Proceedings of the IEEE International Frequency Control Symposium*, pp. 306–314.
- Petit, G., Harmegnies, A., Mercier, F., Perosanz, F., and Loyer, S. (2011). The time stability of PPP links for TAI. *Proceedings of joint conference IFCS and EFTF 2011, San Francisco, CA*, pp. 1041–1045.
- Petit, G., Jiang, Z., White, J., Beard, R., and Powers, E. (2001). Absolute calibration of an Ashtech Z12-T GPS receiver. *GPS Solutions*, 4(4):41–46.
- Powers, E., P., W., Judge, D., and Matsakis, D. (1998). Hardware delay measurements and sensitivities in carrier phase time transfer. *Proceedings of the 30th Precise Time and Time Interval meeting (PTTI), Reston, VA*, pp. 293–305.
- Predehl, K., Grosche, G., Raupach, S. M. F., Droste, S., Terra, O., Alnis, J., Legero, T., Hänsch, T. W., Udem, T., Holzwarth, R., and Schnatz, H. (2012). A 920-kilometer optical fiber link for frequency metrology at the 19th decimal place. *Science*, 336(6080):441–444.
- Ramlall, R., Streter, J., and Schneck, J. F. (2011). Three satellite navigation in an urban canyon using a chip-scale atomic clock. *Proceedings of the 24th Int. Technical Meeting of the Satellite Division of the Institute of Navigation (ION GNSS), Portland, OR*, pp. 2937–2945.
- Ray, J. and Senior, K. (2001). Temperature sensitivity of timing measurements using Dorne Margolin antennas. *GPS Solutions*, 5(1):24–30.
- Ray, J. and Senior, K. (2003). IGS/BIPM pilot project: GPS carrier phase for time/frequency transfer and timescale formation. *Metrologia*, 40(3):270–288.
- Ray, J. and Senior, K. (2005). Geodetic techniques for time and frequency comparisons using GPS phase and code measurements. *Metrologia*, 42(4):215–232.
- Reich, E. S. (2012). Embattled neutrino project leaders step down. Nature online. URL <http://www.nature.com/news/embattled-neutrino-project-leaders-step-down-1.10371>.
- Remondi, B. W. (1991). NGS second generation ASCII and binary orbit formats and associated interpolation studies. *Proceedings of the XX. General Assembly of the International Union of Geodesy and Geophysics (IUGG), Vienna, Austria*.
- Rieck, C., Jarlemark, P., Jaldehag, K., and Johansson, J. (2003). Thermal influence on the receiver chain of GPS carrier phase equipment for time and frequency transfer. *Frequency Control Symposium and PDA Exhibition Jointly with the 17th European Frequency and Time Forum*, pp. 326–331.
- Riley, W. J. (2008). Handbook of frequency stability analysis. NIST special publication 1065.
- Rosenband, T., Hume, D. B., Schmidt, P. O., Chou, C. W., Brusch, A., Lorini, L., Oskay, W. H., Drullinger, R. E., Fortier, T. M., Stalnaker, J. E., Diddams, S. A., Swann, W. C., Newbury, N. R., Itano, W. M., Wineland, D. J., and Bergquist, J. C. (2008). Frequency ratio of Al⁺ and Hg⁺ single-ion optical clocks; Metrology at the 17th decimal place. *Science*, 319:1808–1812.
- Rothacher, M. and Beutler, G. (1998). The role of GPS in the study of global change. *Physics and Chemistry of The Earth*, 23(9-10):1029–1040.
- Rothacher, M. and Schmid, R. (2010). ANTEX: The ANTenna EXchange format, version 1.4. online. <http://igsceb.jpl.nasa.gov/igsceb/station/general/antex14.txt>.
- Rutman, J. (1978). Characterization of phase and frequency instabilities in precision frequency sources: Fifteen years of progress. *Proceedings of the IEEE*, 66(9):1048–1075.
- Ryan, J. W., Ma, C., and Caprette, D. S. (1993). NASA space geodesy program: GSFC data analysis, 1992. crustal dynamics project VLBI geodetic results, 1979 - 1991. Technical Memorandum 104572, NASA.
- Saastamoinen, J. (1973). Contributions to the theory of atmospheric refraction. *Bulletin Géodésique*, 107:13–34.
- Salomon, C., Dimarcq, N., Abgrall, M., Clairon, A., Laurent, P., Lemonde, P., Santarelli, G., Uhrich, P., Bernier, L., Busca, G., Jornod, A., Thomann, P., Samain, E., Wolf, P., Gonzalez, F., Guillemot, P., Leon, S., Nouel, F., Sirmain, C., and Feltham, S. (2001). Cold atoms in space and atomic clocks: ACES. *Comptes Rendus de l'Académie des Sciences - Series IV - Physics*, 2(9):1313 – 1330.
- Santerre, R. (1991). Impact of GPS satellite sky distribution. *Manuscripta Geodaetica*, 16:28–53.
- Santerre, R. and Beutler, G. (1993). A proposed GPS method with multi-antennae and single receiver. *Bulletin Géodésique*, 67:210–223.

- Schaffrin, B. and Grafarend, E. (1986). Generating classes of equivalent linear models by nuisance parameter elimination. *Manuscripta Geodaetica*, 11:262–271.
- Schildknecht, T. and Springer, T. (1998). High precision time and frequency transfer using GPS phase measurements. *Proceedings of the 30th Precise Time and Time Interval Meeting (PTTI)*, Reston, VA, pp. 281–292.
- Schmid, R. (2009). Zur Kombination von VLBI und GNSS. Deutsche Geodätische Kommission, Reihe C 636, Verlag der Bayerischen Akademie der Wissenschaften, München.
- Schmid, R. and Rothacher, M. (2003). Estimation of elevation-dependent satellite antenna phase center variations of GPS satellites. *Journal of Geodesy*, 77:440–446.
- Schüler, T. (2001). *On Ground-Based GPS Tropospheric Delay Estimation*. Dissertation, Universität der Bundeswehr München, Fakultät für Bauingenieur- und Vermessungswesen.
- Seeber, G. (2003). *Satellite Geodesy*. de Gruyter, Berlin / New York, 2nd edition.
- Senior, K., Koppang, P., and Ray, J. (2003). Developing an IGS time scale. *IEEE Transactions on Ultrasonics, Ferroelectrics and Frequency Control*, 50(6):585–593.
- Senior, K. L., Ray, J. R., and Beard, R. L. (2008). Characterization of periodic variations in the GPS satellite clocks. *GPS Solutions*, 12(3):211–225.
- Sesia, I. and Tavella, P. (2008). Estimating the Allan variance in the presence of long periods of missing data and outliers. *Metrologia*, 45(6):134.
- Stanford Research Systems Inc. (2012). website. URL www.thinksrs.com/products/. last access 22-04-2012.
- Stein, S. R. (1985). *Precision frequency control*, volume 2, chapter Frequency and Time - their measurement and characterization, pp. 191–232. Academic Press, New York.
- Strang, G. and Borre, K. (1997). *Linear Algebra, Geodesy, and GPS*. Wellesley-Cambridge Press, Wellesley MA.
- Sturza, M. (1983). GPS navigation using three satellites and a precise clock. *Navigation, Journal of the Institute of Navigation*, 30(2):122–132.
- Symmetricom Inc. (2012). website. URL <http://www.symmetricom.com/products/frequency-references/>. last access 22-04-2012.
- Tesmer, V. (2004). Das stochastische Modell bei der VLBI-Auswertung. Deutsche Geodätische Kommission, Reihe C 573, Verlag der Bayerischen Akademie der Wissenschaften, München.
- Teunissen, P. (2003). *Adjustment theory: An introduction*. Series on mathematical geodesy and positioning. Delft Univ. Press.
- van Dierendonck, A. J., McGraw, J. B., and Brown, R. G. (1984). Relationship between Allan variances and Kalman filter parameters. *Proceedings of the 16th Annual Precise Time and Time Interval (PTTI) Applications and Planning Meeting, Greenbelt, MD*, pp. 273–293.
- van Diggelen, F. (2009). *A-GPS: Assisted GPS, GNSS, and SBAS (GNSS Technology and Applications)*. Artech House, Boston / London.
- van Graas, F., Craig, S., and Pelgrum, W. (2011). Laboratory and flight test analysis of rubidium frequency reference performance under dynamics. *Proceedings of the 24th International Technical Meeting of the Satellite Division of the Institute of Navigation (ION GNSS)*, Portland, OR, pp. 2950–2958.
- Vennebusch, M., Schön, S., and Weinbach, U. (2011). Temporal and spatial stochastic behaviour of high-frequency slant tropospheric delays from simulations and real GPS data. *Advances in Space Research*, 47(10):1681 – 1690.
- Vernotte, F., Delporte, J., Brunet, M., and Tournier, T. (2001). Uncertainties of drift coefficients and extrapolation errors: Application to clock error prediction. *Metrologia*, 38(4):325–342.
- Vessot, R. F. C., Levine, M. W., Mattison, E. M., Blomberg, E. L., Hoffman, T. E., Nystrom, G. U., Farrel, B. F., Decher, R., Eby, P. B., Baugher, C. R., Watts, J. W., Teuber, D. L., and Wills, F. D. (1980). Test of relativistic gravitation with a space-borne hydrogen maser. *Phys. Rev. Lett.*, 45:2081–2084.
- Vremya-CH (2012). website. URL <http://www.vremya-ch.com/english/product/>. last access 22-04-2012.
- Waller, P., Gonzalez, F., Binda, S., Hidalgo, I., Tobias, G., Sesia, I., and Tavella, P. (2009). Overview and performances of Galileo on-board clocks. *Proceedings of the 2nd Int. Colloquium on the Scientific and Fundamental Aspects of the Galileo Programme, Padova*.
- Weaver, G., Garstecki, J., and Reynolds, S. (2010). The performance of ultra-stable oscillators for the Gravity Recovery And Interior Laboratory (GRAIL). *Proceedings of the 42nd Annual Precise Time and Time Interval (PTTI) Meeting*, pp. 369–379.

- Weinbach, U. and Schön, S. (2010). On the correlation of tropospheric zenith path delay and station clock estimates in geodetic GNSS frequency transfer. *Proceedings of the 24th European Frequency and Time Forum (EFTF), ESA/ESTEC, Noordwijk, The Netherlands*.
- Weinbach, U. and Schön, S. (2011). GNSS receiver clock modeling when using high-precision oscillators and its impact on PPP. *Advances in Space Research*, 47(2):229 – 238.
- Weiss, M. A., Petit, G., and Jiang, Z. (2005). A comparison of GPS Common-View time transfer to All-in-View. *Proceedings of the Joint IEEE Intl. Freq. Control Symposium and PTTI Systems and Applications Meeting, Vancouver, Canada*, pp. 324–328.
- Winkler, G. M. R. (1976). A brief review of frequency stability measures. *Proceedings of the 8th Precise Time and Time Interval Systems and Applications Meeting (PTTI), USNO, Washington*, pp. 489–527.
- Wu, J., Wu, S., Hajj, G., Bertiger, W., and Lichten, S. (1993). Effects of antenna orientation on GPS carrier phase. *Manuscripta Geodaetica*, 18:91–98.
- Wu, S. C., Yunck, T. P., and L., T. C. (1991). Reduced-dynamic technique for precise orbit determination of low Earth satellites. *Journal of Guidance, Control and Dynamics*, 14(1):24–30.
- Wübbena, G. (1985). Software development for geodetic positioning with GPS using TI-4100 code and carrier measurements. In Goad, C., editor, *Proceedings of First International Symposium on Precise Position with Global Positioning System*, pp. 403–412, US Department of Commerce, Rockville, Maryland.
- Wübbena, G. (1991). *Zur Modellierung von GPS-Beobachtungen für die hochgenaue Positionsbestimmung*. Dissertation, Wissenschaftliche Arbeiten der Fachrichtung Vermessungswesen der Universität Hannover, Nr. 168.
- Wübbena, G., Schmitz, M., Menge, F., Böder, V., and Seeber, G. (2000). Automated Absolute Field Calibration of GPS Antennas in Real-Time. In *Proceedings of the 13th International Technical Meeting of the Satellite Division of The Institute of Navigation (ION GPS 2000)*, pp. 2512–2522, Salt Lake City, UT, USA.
- Yousif, H. and El-Rabbany, A. (2007). Assessment of several interpolation methods for precise GPS orbit. *Journal of Navigation*, 60:443–455.
- Zeimetz, P. and Kuhlmann, H. (2008). On the accuracy of absolute GNSS antenna calibration and the conception of a new anechoic chamber. *Proceedings of the FIG Working Week 2008, 14.-19. June, Stockholm, Sweden*.
- Zhu, S. and Groten, E. (1988). Relativistic effects in GPS. In Groten, E. and Strauß, R., editors, *GPS-Techniques Applied to Geodesy and Surveying*, volume 19 of *Lecture Notes in Earth Sciences*, pp. 41–46. Springer Berlin / Heidelberg.
- Zucca, C. and Tavella, P. (2005). The clock model and its relationship with the Allan and related variances. *IEEE Transactions on Ultrasonics, Ferroelectrics and Frequency Control*, 52(2):289–296.
- Zumberge, J. F., Heflin, M. B., Jefferson, D. C., Watkins, M. M., and Webb, F. H. (1997). Precise point positioning for the efficient and robust analysis of GPS data from large networks. *Journal of Geophysical Research*, 102(B3):5005–5017.

Acknowledgments

First of all, I'd like to thank Steffen Schön for giving me the opportunity to work on the topic of GNSS clock modeling and his thoughtful guidance throughout the process of this thesis. Without his many ideas, steady support and encouragement but also the freedom he gave me to follow my own research interests, this work would not have been possible. I am also indebted to Markus Rothacher and Christian Heipke for their willingness to act as co-examiners. Markus Rothacher's advice was of particular importance for this work. Furthermore, I'd like to thank Andreas Bauch, Pascal Defraigne, Demetrios Matsakis, Urs Hugentobler, Adrian Jäggi and Rolf Dach for their valuable advice regarding atomic clocks, time and frequency transfer and kinematic orbit determination of low earth orbiters. The support of Thorsten Feldmann during the preparation of the receiver test at PTB was essential for this part of the work. Many thanks also go to my colleagues at the Institut für Erdmessung for their help and a great time in Hannover.

This work has been carried out in the framework of the Centre for QUantum Engineering and Space-Time research (QUEST). QUEST is a cluster of excellence funded by the Deutsche ForschungsGemeinschaft (DFG). It is a joint venture of the Leibniz Universität Hannover, the Max Planck Institute for Gravitational Physics, the Physikalisch-Technische Bundesanstalt (PTB) and several other research institutions. The outstanding support by the QUEST office in all administrative matters, especially by Birgit Ohlendorf, is gratefully acknowledged.

Above all I'd like to thank my wife Margarete for her understanding, persisting support and motivation throughout the ups and downs of this thesis.